

**INVESTIGATION OF EMBEDDABLE SENSORS & STUDY OF
THEIR PLACEMENT FOR SMART STRUCTURES**

BY

ASAD MUHAMMAD BUTT

A Dissertation Presented to the
DEANSHIP OF GRADUATE STUDIES

KING FAHD UNIVERSITY OF PETROLEUM & MINERALS

DHAHRAN, SAUDI ARABIA

In Partial Fulfillment of the
Requirements for the Degree of

DOCTOR OF PHILOSOPHY

In

MECHANICAL ENGINEERING

MAY, 2017

KING FAHD UNIVERSITY OF PETROLEUM & MINERALS

DHAHRAN- 31261, SAUDI ARABIA

DEANSHIP OF GRADUATE STUDIES

This thesis, written by **ASAD MUHAMMAD BUTT** under the direction of his thesis advisor and approved by his thesis committee, has been presented and accepted by the Dean of Graduate Studies, in partial fulfillment of the requirements for the degree of **DOCTOR OF PHILOSOPHY IN MECHANICAL ENGINEERING.**



Dr. SAMIR MEKID
(Advisor)



Dr. ZUHAIR GASEM
Department Chairman



Dr. KHURRAM QURESHI
(Member)



Dr. SALAM A. ZUMMO
Dean of Graduate Studies



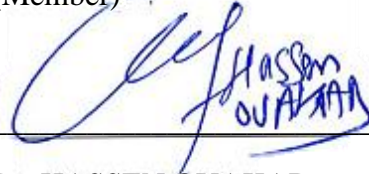
Dr. SAHEB NOUARI
(Member)

16/10/17

Date



Dr. YAGOUB AL NASSAR
(Member)



Dr. HASSEN OUAKAD
(Member)

© Asad Muhammad Butt

2017

Dedicated to the Muslims of the world in suffering, May Allah protect and return to them
their livelihoods

ACKNOWLEDGMENTS

I would like to thank first of all The Almighty Allah for bestowing upon me a privilege to seek knowledge and to travel away from home following in the saying of beloved prophet Muhammad (PBUH). Secondly my advisor Dr. Samir Mekid for accepting me for this challenging work and guiding me to the best of his abilities to pursue this dissertation along with my Thesis Examination Committee. I would likely to also acknowledge Dr. Khurram Qureshi for his valuable knowledge and assistance on fiber optic systems, Dr. Saheb Nouari, Dr. Yagoub Al Nassar and Dr. Hassen Ouakad for reviewing the thesis work. Following I would like to thank the Department of Mechanical Engineering (KFUPM), the chairman, the faculty and the staff for cooperating and assisting my work. A special thanks to KFUPM, Ministry of Higher Education and the Leadership of Kingdom of Saudi Arabia for giving me this opportunity to pursue a doctoral degree in the Kingdom and making my stay pleasant and accommodating.

Last but not the least my Family and Friends who are the inspiration for me to move forward and achieve higher in life and betterment of both Deen and Dunya. I would like to specially mention my parents who would really feel proud of their son's achievement and finally my wife Humera who has been supportive every instance and help me focus on my contribution to the scientific community through hard work, dedication and motivation.

TABLE OF CONTENTS

ACKNOWLEDGMENTS	V
TABLE OF CONTENTS	VI
LIST OF TABLES	XI
LIST OF FIGURES	XIV
NOMENCLATURE.....	XXI
LIST OF ABBREVIATIONS	XXIV
ABSTRACT	XXV
ملخص الرسالة	XXVII
CHAPTER 1 INTRODUCTION.....	1
1.1. Definition of a Smart Structure.....	5
1.2. Objectives	6
1.3. Research Plan.....	6
1.4. Chapter Organization.....	8
CHAPTER 2 LITERATURE REVIEW ON EMBEDDING PROCESSES & SENSORS PLACEMENT	9
2.1. Candidate Sensors for Embedding.....	9
2.1.1. Fiber Bragg Grating (FBG).....	9
2.1.1.1. Advantages of FBG	10
2.1.1.2. Disadvantages.....	12
2.1.2. Piezoelectric Sensors	12
2.1.2.1. Advantages	14

2.1.2.2. Disadvantages.....	14
2.2. Sensor Embedding Processes.....	15
2.2.1. Embedding in Metals	15
2.2.2. Embedding in Polymers and Composite Materials.....	25
2.3. Optimal Sensor Placement.....	28
2.4. Conclusion	31
CHAPTER 3 SENSOR CHARACTERIZATION & CALIBRATION	34
3.1. Characterization of Fiber Optics.....	38
3.1.1. Tensile Test (Corning SMF 28 Optical Fiber).....	38
3.1.2. Strain Response of FBG.....	43
3.1.3. Temperature Characterization of FBG.....	45
3.1.4. Pressure Test of FBG	49
3.1.5. Bend Test (Corning SMF 28 Optical Fiber)	53
3.2. FBG Calibration against LVDT.....	63
3.2.1....Objective	63
3.2.2. Problem Description	63
3.2.3. Test Description	64
3.2.4. Analytical Solution	64
3.2.5. Theoretical Displacement	65
3.2.6. Theoretical Strain (Gage Location)	66
3.2.7. Indirect Measurements.....	66
3.3. Conclusion	68

CHAPTER 4 SENSORS PLACEMENT TECHNIQUES	70
4.1. Optimum Sensors Placement	72
4.1.1. Optimization via Placement Index	72
4.1.2. Actuator Feasibility (PVDF Position, Gain and Shape Design)	80
4.1.3. Optimization via D-Optimal Method	82
4.2. Force Localization	86
4.3. System Equivalent Reduction Expansion Process (SEREP)	87
4.4. Comparison of SEREP to other Model Reduction Techniques	90
4.5. Conclusion	91
CHAPTER 5 SIMULATION RESULTS FOR STRUCTURAL EXAMPLES	93
5.1. Simulated Examples	95
5.2. Problem Formulation & Solution Flow Chart	96
5.3. Example 1: Clamped - Clamped Beam under Static & Forced Harmonic	99
5.3.1. Modal Identification	101
5.3.2. Strain Expansion	102
5.3.3. Force Identification (Position)	103
5.3.4. Force Identification (Magnitude)	105
5.3.5. Comparison between Optimal and Non-Optimal Solutions	107
5.3.6. Error Analysis	111
5.4. Example 2: Cantilever Beam under Impact	114
5.4.1. Displacement Comparison	118
5.4.2. Strain Comparison	123
5.4.3. Force Identification (Magnitude)	125

5.4.4. Force Identification (Position)	127
5.4.5. Error Analysis	128
5.5. Example 3: All Edges Clamped, Rectangular Plate under Forced Harmonic	129
5.5.1. Displacement Comparison	131
5.5.2. Strain Comparison	133
5.5.3. Error Analysis	136
5.5.4. Force Identification (Position)	136
5.5.5. Force Identification (Magnitude)	137
5.6. Conclusion	138
CHAPTER 6 EXPERIMENTAL STUDY	140
6.1. Experiment Strategy	142
6.2. Equipment/Hardware Details	144
6.3. VI Development & Data Acquisition	145
6.4. Frequency Response Function (Experimental)	146
6.5. Experimental Impact Test (Cantilever Beam)	149
6.5.1. Experimental Setup	149
6.5.2. Strain Results	151
6.5.3. Displacement Prediction	154
6.5.4. Force Identification (Position and Magnitude)	155
6.6. Experimental Impact Test (Clamped-Clamped Beam)	157
6.6.1. Strain Results	159
6.6.2. Displacement Prediction	162
6.6.3. Force Identification (Position and Magnitude)	163

6.7. Conclusion	165
CHAPTER 7 ANALYSIS, CONCLUSION & RECOMMENDATIONS	166
7.1. Analysis.....	166
7.2. Conclusion	168
7.3. Future Recommendations	169
REFERENCES.....	170
APPENDIX	180
VITAE	201

LIST OF TABLES

Table 2.1 Sensor characteristics on basis of their feasibility to be introduced in structures	14
Table 2.2 Comparison of the UC process for two different experiments	22
Table 3.1 Sensing capabilities of contemporary sensors	36
Table 3.2 Tensile test results Corning SMF 28.....	42
Table 3.3 Polyimide coated FBG properties.....	43
Table 3.4 Strain sensitivity vs. gage length.	44
Table 3.5 Test parameters for polyimide coated FBG.....	45
Table 3.6 Polyimide coated FBG properties.....	47
Table 3.7 Signal strength [dB] and output power [mW] for different fibers connected.	48
Table 3.8 Summary for Strain, Temperature and Pressure Sensitivity.....	53
Table 3.9 Power individual bends (Full Circle) – circular, signal loss with different bend radiuses from 30 - 5mm	56
Table 3.10 Power progressive bends (Full Circle) – circular, signal loss spiral pattern with progressive radiuses.....	58
Table 3.11 Bend shape comparison for power losses with bend radius 10 [mm] and power in 1.61 [mW] at 1550 [nm]	59
Table 3.12 Signal loss zigzag pattern with multiple bends at R=10mm, a) high power, b) low power.	61
Table 3.13 Load conversion from [g] to [N].....	65

Table 3.14 Analytical formulas for strain and displacement	66
Table 3.15 Data calculated for LVDT, Strain gage and FBG.....	67
Table 4.1 Comparison of different reduction techniques Guyan, IRS and SEREP	91
Table 5.1 Data for Beam and Plate examples	96
Table 5.2 Sensor position tabulated with respect to optimization schemes.....	100
Table 5.3 Modal Participation Factors at T [0 1.0] sec with sensors at (1, 3, 9, 11)	102
Table 5.4 Mode switching observed based on the MPF calculations for sensors at [1 3 9 11].....	102
Table 5.5 Static Force identification	104
Table 5.6 Displacement errors shown for different placement schemes	112
Table 5.7 Strain errors shown for different placement schemes.....	113
Table 5.8 Force errors shown for different placement schemes	113
Table 5.9 Force errors (RMS) after amplification, comparison between 10 and 100N dynamic load for sensors at.....	114
Table 5.10 Sensor position tabulated with respect to optimization schemes.....	118
Table 5.11 % RMS error at t = 0.1, 0.2 and 0.3 [sec]	129
Table 5.12 % RMS error (displacements) at Node 15 for T [0, 1.5] [sec]	129
Table 5.13 Sensor positions (coordinates) tabulated with respect to optimization schemes	130
Table 5.14 % RMS error at t = 0.1 [sec] for displacements and strains against different optimization schemes.....	136
Table 5.15 Mode shapes for structural examples.....	139

Table 6.1 Modal frequencies obtained from FEM against (a) 2D Beam Physics and (b)	
3D Solid Mechanics	149
Table 6.2 % RMS error for displacements at different times (Cantilever Beam).....	155
Table 6.3 % RMS error for displacements at different times (Clamped-Clamped	
Beam).....	163

LIST OF FIGURES

Figure 1.1 Nervous system analogy depiction	4
Figure 1.2 (a) A typical neuron. (b). Equivalent circuit of a dendrite or axon. (c): Perpendicular Active Fiber Composite Sensor Module	4
Figure 2.1 FBG structure	11
Figure 2.2 FBG working principle	11
Figure 2.3 PZT principle	14
Figure 2.4 RFID cast part with integrated RFID transponder (left) and design of a glass transponder (right)	16
Figure 2.5 Piezoelectric sensor of type SP505 7x7x32.4 mm ³ (left) and structural- mechanical calculation of a load of 1800 N (right)	17
Figure 2.6 (a) Unpacked 3D module, (b) Fully assembled module, (c) Installation in the test specimen	18
Figure 2.7 CAD representation of embedded sensor using UC process	19
Figure 2.8 Setup of the ultrasonic welding equipment and the embedding procedures ..	21
Figure 2.9 Results of different embedding techniques	21
Figure 2.10 (a) FBG embedded in a 42CrMo part, (b) radial cross-section of the part ..	24
Figure 2.11 Geometry of the tool system	24
Figure 2.12 Tool development with embedded FBG	24
Figure 2.13 Specimen preparation, a. wet layup cutout, b. laying down the FBG array in the middle of the carbon ply outer layer, c. curing process of panel, d. completed smart structure sandwich panel with embedded FBG sensor	26

Figure 2.14 FBG sensor line during the fabrication of Filament Wound Composite Vessel.....	26
Figure 2.15 FBG sensors embedded into 3D printed (a) Valero and (b) ABS scaffold ..	28
Figure 3.1 Loading state of an embedded optical fiber sensor	36
Figure 3.2 Optical fiber schematic and its SEM picture	39
Figure 3.3 Test samples for tensile test (post breakage)	40
Figure 3.4 Test setup for tensile test	40
Figure 3.5 Tensile test sample result for a bare optical fiber gage length 20 [mm]	42
Figure 3.6 Translation stage with fiber grips for strain response	43
Figure 3.7 Wavelength vs displacement trend for different gage lengths	44
Figure 3.8 Schematic for test setup.....	46
Figure 3.9 Lab setup showing connections and instruments/apparatus used.....	47
Figure 3.10 (a) Superimposed spectra of wavelength shift with varying temperature (°C) and effect on signal strength, (b) Linear response of wavelength shift to temperature variation	48
Figure 3.11 Pressure experimental setup	51
Figure 3.12 FBG strain measured with pressures reduced from 2600 [psi] (Test 1), 2850 [psi] (Test 2)	51
Figure 3.13 Compressive Strain vs Pressure (Error Plot ± 50 [psi])	52
Figure 3.14 Average strain response from the three tests with ± 7.63 [$\mu\epsilon$] error	52
Figure 3.15 Setup configuration of the fiber optic tests with light measurement.....	55
Figure 3.16 Bend pattern for (a) individual radiuses, (b) bending issue.....	56
Figure 3.17 Spiral pattern for progressive bend test	57

Figure 3.18 Percent loss [dBm] with various bend radiuses Individual Bends vs. Spiral Bends 1.53 [mW] Bare Fiber Power	58
Figure 3.19 Percent loss [dBm] with Full, Half and Quarter circle bend radius (10mm) at 1.53 [mW] Bare Fiber Power	59
Figure 3.20 Zigzag pattern for bending test.....	61
Figure 3.21 Percent loss [dBm] with increasing number of bends (Bend Radius 10 [mm]) at low and high power input	62
Figure 3.22 Comparison of power loss between Individual/progressive bends and the zig zag pattern on account of number of bends	62
Figure 3.23 Beam with strain gage locations highlighted, FBGs are placed in slot next to the strain gages.....	64
Figure 3.24 (a) Test setup for calibration, (b) instrumented beam with LVDT sensor on top	64
Figure 3.25 Load location on the cantilever beam.....	65
Figure 4.1 Load position on a clamped-clamped beam	81
Figure 4.2 (a) Actuator gain profile along the beam length, (b) Piezo electric actuator width profile to accomplish gains in (a)	82
Figure 4.3 Mode Shape Reduction from full set 'n' to active DOFs 'a'	89
Figure 4.4 Graphical representation of implemented scheme	92
Figure 5.1 Problem formulation Flow Chart (a) Placement Index and (b) D-Optimal Design	98
Figure 5.2 Problem solution Flow Chart.....	99

Figure 5.3 A clamped-clamped with cross locations identifying the position of D-Optimal sensors.....	100
Figure 5.4 Displacement comparison of Actual vs Expanded data at D-Optimal locations [1,3,9,11] (t=1.0 [sec]).....	101
Figure 5.5 Strain comparison of Actual vs Expanded data at D-Optimal locations [1,3,9,11] (t=1.0 [sec])	103
Figure 5.6 Minimum difference graphically illustrated for the Clamped-Clamped Beam example, highlighting node 6 as the position of load	105
Figure 5.7 Force calculated through SEREP results expanded on D-Optimal sites at node 6 (t=0.0-1.0 [sec]).....	106
Figure 5.8 Comparison of the expanded displacement solution with the actual displacement of beam for sensor schemes (a) D-Optimal (b) Modified D-Optimal and (c) Placement Index	107
Figure 5.9 Comparison of the expanded strain solution with the actual displacement of beam for sensor schemes (a) D-Optimal (b) Modified D-Optimal and (c) Placement Index	108
Figure 5.10 Comparison of the expanded force solution with the actual force on beam for sensor schemes (a) D-Optimal (b) Modified D-Optimal and (c) D-Optimal (3 sensors)	111
Figure 5.11 (a) Nodal representation of the cantilever beam, (b) Impact force of 42 [N]	116
Figure 5.12 (a-d) Characteristic loading functions for simple load pulses, (e) comparison of profiles	117

Figure 5.13 Sensors positions with respect to (a) D-Optimal, (b) Modified D-Optimal and (c) Placement Index.....	118
Figure 5.14 Comparison of the expanded displacement solution with the actual displacement of beam for sensor schemes (i) D-Optimal (ii) Modified D-Optimal and (iii) Placement Index at time (a) $t = 0.1$ [sec], (b) $t = 0.2$ [sec] and (c) $t = 0.3$ [sec]	120
Figure 5.15 Displacements with S2 OFF (Cantilever Beam under impact), $T [0-1.5]$ [s] (a) at Node 1, (b) at Node 34 and (c) at Node 52.....	122
Figure 5.16 Comparison of the expanded strain solution with the actual displacement of beam for sensor schemes (i) D-Optimal (ii) Modified D-Optimal and (iii) Placement Index at time (a) $t = 0.1$ [sec], (b) $t = 0.2$ [sec] and (c) $t = 0.3$ [sec]	124
Figure 5.17 Comparison of the expanded D-Optimal force solution with the actual force on beam and (b) Section forces developed at $t = 0.2$ [sec] along the beam length.....	126
Figure 5.18 Minimum difference check to locate applied load, transition from $t = 0.1$ [sec] to $t = 0.2$ [sec]	127
Figure 5.19 Minimum difference check to locate applied load at $t = 0.2$ [sec], comparison between (a) D-Optimal, (b) Modified D-Optimal and (c) Placement Index.....	128
Figure 5.20 Identification of sensor positions on the all sides clamped rectangular plate	130

Figure 5.21 Comparison of the expanded displacement solution with the actual displacement of beam for sensors schemes (a) Actual Solution (b) D-Optimal (c) Placement Index and (d) Random Positions at time $t = 0.1$ [s]	133
Figure 5.22 Comparison of the expanded strain solution with the actual displacement of beam for sensors schemes (a) Actual Solution (b) D-Optimal (c) Placement Index and (d) Random Positions at time $t = 0.1$ [s].....	135
Figure 5.23 Minimum difference check to locate applied load at $t = 0.1$ [s], comparison between D-Optimal and original location.....	137
Figure 5.24 Comparison of the expanded D-Optimal force solution with the actual force (450 x, 300 y) on all sides clamped plate, $T = [0,1]$ [sec]	138
Figure 6.1 Sensor positions, (a) D-Optimal sites, cantilever and (b) clamped-clamped beam with impact locations	141
Figure 6.2 Experimental development flow chart.....	143
Figure 6.3 NI OSI Explorer GUI displaying signature wavelengths of individual sensors in array and the effect of strain	146
Figure 6.4 Impact hammer and accelerometer used in experiment to generate FRF	147
Figure 6.5 (a) Force data and (b) acceleration data to produce (c) frequency response of the impact on the cantilever beam	148
Figure 6.6 Beam dimensions and sensor positions (cantilever).....	150
Figure 6.7 Complete experimental setup along with instrumented beam with embedded FBG array.....	150
Figure 6.8 Experimental impact force 20.07 [N]	151
Figure 6.9 FBG strains recorded at sensor position 1-4.....	152

Figure 6.10 (a-d), Comparison of experimental results to simulated (cantilever)	154
Figure 6.11 Expanded displacement profile from D-Optimal sensors at $t = 0.6$ [sec] ..	155
Figure 6.12 (a) Location identification at different times (b) Comparison of the expanded D-Optimal force solution with the actual force on beam at Node 15.....	157
Figure 6.13 Beam dimensions and sensor positions (clamped-clamped)	158
Figure 6.14 Instrumented clamped-clamped beam	158
Figure 6.15 Experimental impact force 28 [N]	159
Figure 6.16 FBG strains recorded at sensor position 1-4.....	160
Figure 6.17 (a-d), Comparison of experimental results to simulated (clamped-clamped)	162
Figure 6.18 Comparison displacements (Theoretical vs Experimental), clamped- clamped beam	163
Figure 6.19 (a) Location identification at different times (b) Comparison of the expanded D-Optimal force solution with the actual force on beam at Node 34.....	164

NOMENCLATURE

$[M]$:	Mass Matrix
$[D_{damp}]$:	Damping Matrix
$[K]$:	Stiffness Matrix
σ	:	Stress
ϵ	:	Strain
$\{\ddot{x}(t)\}$:	Acceleration as a function of time
$\{\dot{x}(t)\}$:	Velocity as a function of time
$\{x(t)\}$:	Displacement as a function of time
$\{f(t)\}$:	Force as a function of time
A	:	Nodal System Matrix (State Space)
B	:	Nodal Input Matrix (State Space)
C	:	Nodal Output Matrix (State Space)
D	:	Nodal Feed Forward Matrix (State Space)
B_0	:	Nodal Force Input Vector
C_{0q}	:	Nodal Displacement Vector
C_{0v}	:	Nodal Velocity Vector

ω_i	:	Natural Frequency (ith mode)
ξ_i	:	Damping Ratio (ith mode)
Φ	:	Mode Shape Matrix
Ψ	:	Modal Strain Matrix
$[A]$:	Strain Sensitivity Matrix
A_{mi}	:	Modal System Matrix (ith mode)
B_{mi}	:	Modal Input Matrix (ith mode)
C_{mi}	:	Modal Output Matrix (ith mode)
b_{mi}	:	Modal Input Vector
C_{mqi}	:	Modal Displacement Vector
C_{mvi}	:	Modal Velocity Vector
$\ G_i\ _2$:	Structure Transfer Function (ith mode) H_2 based
$\ G_i\ _\infty$:	Structure Transfer Function (ith mode) H_∞ based
$\ G\ _2$:	Structure Transfer Function (Total) H_2 based
$\ G\ _\infty$:	Structure Transfer Function (Total) H_∞ based
$\ b_{mi}\ _2$:	Input Gain
$\ c_{mi}\ _2$:	Output Gain

r	:	Number of Actuators
s	:	Number of Sensors
$\eta_{i(2,\infty)}^k$:	Placement Index (ith mode, kth sensor/actuator) for H_2 or H_∞
$H_{(2,\infty)}$:	Placement Index Matrix for H_2 or H_∞
a	:	Active Degrees of Freedom
d	:	Deleted Degrees of Freedom
λ_b	:	Bragg Wavelength
n_{eff}	:	Effective Refractive Index
Λ	:	Grating Period
E	:	Modulus of Elasticity
G.F	:	Gage Factor

LIST OF ABBREVIATIONS

OSP	:	Optimum Sensor Placement
FBG	:	Fiber Bragg Grating
SEREP	:	System Equivalent Reduction Expansion Process
PZT	:	Lead Zirconate Titanate
PVDF	:	Polyvinylidene-Di-Fluoride
MPF	:	Mode Participation Factor
MPF_{mass}	:	Mass Participation Factor
LVDT	:	Linear Variable Differential Transducer
OSA	:	Optical Spectrum Analyzer
FRF	:	Frequency Response Function
GUI	:	Graphical User Interface

ABSTRACT

Full Name : [Asad Muhammad Butt]

Thesis Title : [Investigation of Embeddable Sensors & Study of their Placement for Smart Structures]

Major Field : [Mechanical Engineering]

Date of Degree : [May 2017]

This work aims to investigate smart structures with embedded fiber optic strain sensors in order to identify unknown applied load (Static/Dynamic) magnitude and its location. The smart attribute of the structure is exhibited with strategically positioned minimum number of sensors. These positions are obtained from a) Placement Index & b) D-Optimal methods. Sensors positioning is based on the most significant strain information obtained through these methods. A comparison between the two methods showed that the D-Optimal method produced better prediction for force (magnitude and location). A full field expansion of displacement and strain data at the D-Optimal sites produced results in agreement with the full field theoretical displacements and strains. The expansion was applied with System Equivalent Reduction Expansion Process (SEREP) which preserves the true dynamic characteristics of the structural system. Based on these assessments, force predictions were demonstrated with simulated examples of beam and plate. The thesis work progresses with an initial understanding of a selected fiber optic strain sensor, Fiber Bragg Grating (FBG) due to numerous advantages it offers in comparison to its counterparts. The characterization study was performed for the FBG sensor that would exhibit conditions of tensile, compaction and thermal loads in embedded conditions and

would require drawing limits to the sensor's mechanical/thermal strain. Additional constraints related to geometry distortions of the fibers were investigated. The smart sensing in an aluminum beam was experimentally demonstrated through D-Optimal sensor distribution scheme followed by an impact force identification. This scheme was based on the inputs of the D-Optimal method and has allowed us to obtain sensors positions for FBGs embedded in metallic structures. It was deduced that the SEREP expansion from D-Optimal sensor sites produced results in agreement with the theoretical solution.

ملخص الرسالة

الاسم الكامل: أسد محمد بوت

عنوان الرسالة: التحقيق في أجهزة الاستشعار القابلة للتضمين ودراسة وضعها للهياكل الذكية

التخصص: قسم الهندسة الميكانيكية

تاريخ الدرجة العلمية: أيار، 2017

يهدف هذا العمل إلى تحقيق هياكل ذكية تحتوي على الياف بصرية مضمنة لتحسس الالتواءات وذلك للتعرف على مقدار ومكان تأثير الأحمال المؤثرة المجهولة (الساكنة والمتحركة). تم عرض صفة الذكاء للهيكل عن طريق تحديد استراتيجي لأقل عدد من المجسات. يتم الحصول على هذه المواقع عن طريق (مؤشر الموضع و ب) طريقة D-Optimal. يستند تحديد مواقع المجسات على معلومات الالتواءات الأكثر أهمية التي يتم الحصول عليها من خلال هذه الطرق. أظهرت المقارنة بين كلا الطريقتين أن D-Optimal أنتجت توقع افضل للقوى (مقدار وموقع). كما وأنتجت معلومات الالتواء والإزاحة على مجال واسع في مواقع D-Optimal إلى نتائج تتوافق جيد مع الالتواءات والإزاحات النظرية.

تم تطبيق التمدد عن طريق SEREP التي تحافظ على الخصائص الديناميكية الحقيقية للنظام الهيكلي. بناء على هذه التقييمات، عرضت توقعات القوة لأمتلة محاكاة مثل عارضة و صفيحة. يقدم العمل في هذه الأطروحة مع الفهم المبني لاختيار الالياف البصرية المستخدمة لتحسس الالتواءات، والياف FBG بسبب العديد من المزايا التي توفرها مقارنة مع نظائرها. تم إجراء دراسة التوصيف للياف FBG التي من شأنها أن تظهر ظروف الشد، والضغط والأحمال الحرارية في ظروف التضمين كما ويتطلب تحديد الالتواءات الميكانيكية والحرارية للمجس. تم التحقق أيضا من القيود الإضافية المتعلقة بالتشوهات الهندسية للياف. تم اثبات الاستشعار الذكي عمليا في عارضة ألومنيوم من خلال مخطط توزيع الاستشعار D-Optimal تلاها تحديد القوة المؤثرة. هذا المخطط يعتمد على المدخلات لطريقة D-Optimal و التي تسمح لنا الحصول على الموقع الأمثل للياف FBG المضمنة داخل الهياكل المعدنية. قد استنتج أن تمدد SEREP من المواقع التي تم تحديدها من طريقة D-Optimal أنتجت نتائج تتوافق بشكل جيد مع الحل النظري.

CHAPTER 1

INTRODUCTION

The vision and possibilities of having a smart and interactive system is expanding on a rapid pace supported by the possibility to fabricate miniaturized systems e.g. micro-electro-mechanical systems (MEMS) with embedded electronics and sensors. By smart we mean that the system has the capability to identify any change in stimulus from the environment and to identify the source of that change by its location and magnitude. The purpose to have embedded sensors provides advantages not only to retrieve information within the material/structure but also to keep the sensor protected from the harsh environment outside. Different materials e.g. polymers, ceramic, metals and composites have the potential to act as sensorial materials by hosting sensors. With the advancement in polymeric technologies (electroactive polymers and artificial muscles [1]) along with new age sensors being embedded within, one can imagine a material or a system responding the same way as a human nervous system [1,2]. Lead Zirconate Titanate (PZT) is an example from the ceramic material domain which acts as both sensor and actuator [3]. Similarly Fiber Optic sensors such as Fiber Bragg Grating (FBG) are also gaining attention due to their utility as a noninvasive sensor when combined with different embedding techniques [4–7]. Strain gages have been around as one of the oldest and reliable sensor when it comes to strain monitoring but pose enormous challenges when they are considered to be sensor choice for embedding purposes. A combination of sensing and actuation devices along with processing and control electronics help develop a smart material/structure. Different types

of smart materials have been discussed in [8] which illustrates the function and use of such materials for the development of a nervous material. A nervous material is a material that combines the actions of sensing, processing and responding. As the current scope is limited to the sensing part, one needs to define the type of measurand and the ways to sense them. This would define the limits for the smartness of a nervous material and provide grounds to make the existing materials or systems smart. Metals and metallic structures are one such example which require to be developed into smart systems because of their immense use. The areas dealing with composite manufacturing have used sensor embedding to their advantage as with the composite fabrication especially fiber reinforced polymers (FRPs) [9–11]. Sensor embedding is conveniently done due to lower fabrication temperatures and layered manufacturing style. Examples from aviation, automotive, civil and petro-chemical industries show immense potential for such smart materials/structures [12–14]. Application areas include military and aerospace e.g. shape morphing wings [15], robotics & biomedical e.g. robotic manipulators and advance prosthetics [16,17] and civil infrastructure monitoring [18].

Material strength and design are key issues in the development of smart structures. These characteristics should not be compromised when introducing smart features. The challenge to make existing metallic or polymeric structures smart arise from the fact that only a few sensors are compatible with the host material properties. The temperatures and the forces required to introduce sensors within said material are detrimental to the sensors. Literature shows various attempts to introduce sensors in metals either through casting, laser sputtering and ultrasonic consolidation [6,19,20,6]. On the other hand sensor placement in polymers/polymer based composites structures are illustrated in [4,5,7].

Another aspect is sensor design, which either means to build a sensor from the scratch or use off the shelf sensors. The selection is an important task as to what type of sensor would be required and the type of measurand we expect to investigate. Usually the strain information is the key to evaluate different structural properties when no direct means to measure are available such as accelerometers, Linear Variable Differential Transducers (LVDTs) etc. A major effort after sorting out embedding methods is spent to identify the location to install the strain sensors. Care is taken to place the sensors in critical locations depending on the structural geometry, material properties and boundary conditions. Placement schemes are discussed in detail the theoretical framework chapter and would discuss on various possibilities to introduce strain sensors to the smart structure.

The future generations of materials and structures are envisaged to behave more on biological analogy to human nervous system with distributed embedded sensor array architecture [21] and SMART (*Stanford Multi-actuator Receiver Transduction*) Layer concept [22] to develop a biologically inspired sensory system for aerospace vehicles and related systems. An Active Fiber Continuous Sensor (AFCS) was developed comprising piezoceramic ribbons made by CeraNova Corporation, that are cast in epoxy with electrode imprinted Kapton films on either side. Figure 1.2 (a) shows a typical neuron of a human nervous system, Figure 1.2 (b) shows the equivalent circuit of a dendrite or axon and Figure 1.2 (c) is the actual active fiber composite sensor module [21]. These sensors were embedded in testing coupons of laminated composite plate structures forming the ‘Smart Skin’. But when the same discussion comes to the metallic structures, their embedding techniques vary depending on the type of material to be introduced, their thickness, their composition and the temperature at which these sensors would be embedded in the

structure. We intend to develop such structures/materials with an attribute that terms them ‘*Smart*’. A smart structure/material is intended to identify an external affect through a sensorial system which is a part of the Nervous system and are limited to the function of sensing only. Whereas a nervous system as a whole has the capability to sense, infer and respond to an external stimuli through an action. Figure 1.1 depicts a nervous system analogy to a physical system.

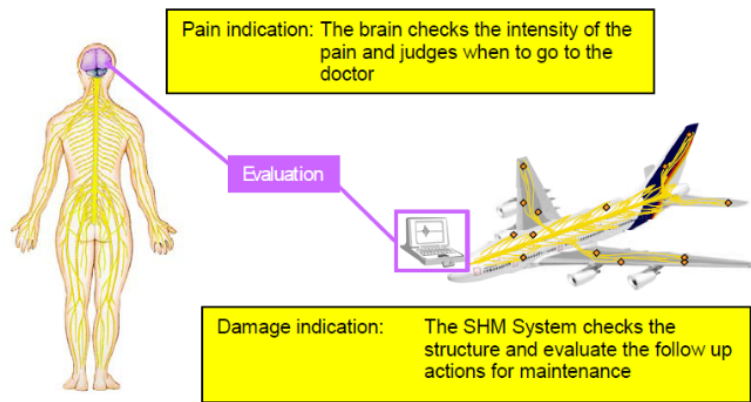


Figure 1.1 Nervous system analogy depiction [23]

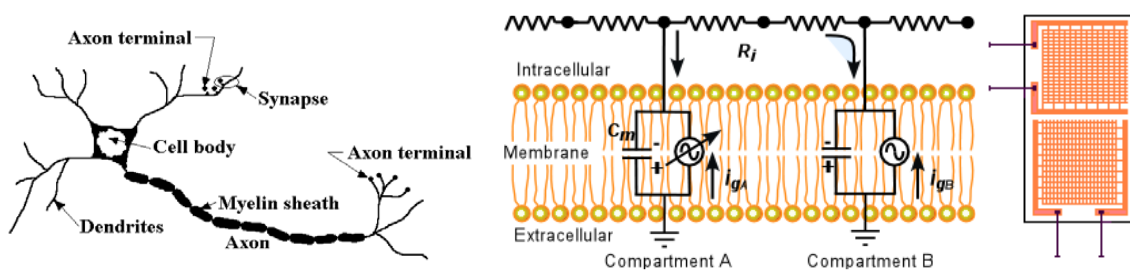


Figure 1.2 (a) A typical neuron. (b). Equivalent circuit of a dendrite or axon. (c): Perpendicular Active Fiber Composite Sensor Module [18].

The following section will define a Smart Structure and the role of the sensorial system in bringing smartness to the system/structure.

1.1. Definition of a Smart Structure:

A '*Smart Structure*' can be defined as structure that intends to evaluate a certain scenario through sensory means to either resist or change its response to an external stimulus. An important element of that structure is the '*Sensorial System*'. It is a system that has the ability to sense an external stimuli for example mechanical strain, temperature and pressure. Such a system is a subsystem that integrates with the nervous system to provide necessary information in order to produce adequate response through actuation. The system of nerves in a human body that sends messages are actually contributing to a sensorial system for controlling movement and feeling between brain and other parts of the body. Therefore a sensorial system is a system which can sense and later be inferred and responded by the rest of the nervous system to any external effect e.g. force, pressure or temperature. The capability to coordinate between the sensing and actuating through a central processing would increase the performance of such system. The power supply can be either supplied wired, charged wirelessly or harvested to charge batteries.

A smart structure can sense an external stimulus through change in heat, pressure, and chemical composition etc. with the entire material of the structure acting as sensing agent (Sensory Materials) or with the help of sensing elements added to it in the form of sensors. The nerve system for a sensorial material has to comprise of small intricate sensors. The term "Nervous" was first pitched in [24] explaining the ways optical fibers can be used as sensors distributed in a network to describe the health of the structure. Nervous

materials/structures can offer great benefits in the field of Structural Health Monitoring (SHM).

With the importance of the thesis subject highlighted in the passages above, we would now focus on defining the thesis objectives which when achieved would contribute towards development of such Smart Material/Structures.

1.2. Objectives:

The objective of the current research is to investigate the use of embeddable fiber optic sensors to extract applied unknown load in terms of its position and magnitude from an optimum configuration of sensors. Having the sensor in embedded state will serve our purpose to retrieve information within the material/structure and also keep the sensor protected from the harsh environment outside.

1.3. Research Plan:

The research plan was developed in order to investigate embeddable fiber optic sensor to give the structure a smart feature to identify and locate an unknown applied force. The following list details the structure of research with their expected outcomes.

- 1. Selection of Embeddable Sensors:** FBG sensor would be selected for the required application as it offers numerous benefits to its counterparts. The benefits will be discussed in the literature review.
- 2. Sensor Characterization & Calibration:** The sensor would be investigated for its performance under mechanical, thermal and pressure loads through a series of articulate tests

to acquire support data for design and implementation. Tests would also be conducted to observe the signal transmission effects under linear and circular layouts. This would serve as valuable information for both current and future scope of the work. Different layout templates would be tested with multiple bends to investigate the effect of bend radius on the light transmission. Calibration study would be carried out using strain gages and LVDT sensor on a sample cantilever beam. It would help us use the data from the characterization to see the relation between strain activity of strain gage in comparison to FBG sensor.

3. Theoretical Investigation for Optimal Sensor Placement: A detailed study based on the comparison of two optimal sensor placement techniques would be performed namely Placement Index and D-Optimal Design. Objective is to use the concepts from the control systems (H_2 & H_∞ norms), numerical techniques and system dynamics to help us achieve an optimal sensors distribution. A distribution that could deliver to us the position and magnitude of an unknown applied load to the smart structure through an accurate shape reconstruction of the structure. Sample problems with beam and plate will be investigated to identify the applied load and build a complete strain profile with limited selection of optimal sensors and associated expansion procedures.

4. Implementation on a Physical System: An experiment is designed with a cantilever and a clamped-clamped beam with embedded FBG sensors following the layout described by the optimal sensor position scheme. The objective is to investigate the validity of the proposed scheme.

1.4. Chapter Organization:

Chapter 2 details the previous attempts to embed various type of sensors into different materials. This is shown through an extensive literature review covering topics on available sensors suitable for embedding, their advantages and disadvantages, embedding techniques in metals and polymers and sensor placement studies.

Chapter 3 discusses various attempts on characterization for the fiber optic sensor to have a complete data on sensor performance under various conditions. It also details on the account of sensor calibration.

Chapter 4 focuses on the theoretical framework for the optimal placement of sensors.

Chapter 5 provides a comparison between two different design schemes namely, 1. Placement Index, and, 2. D-Optimal Design method that delivers the required results for identifying an applied load is discussed and implemented on examples of beam and plate.

Chapter 6 discusses the experimental results and inferences for the selected optimal layout with embedded FBG sensor in an aluminum beam.

Chapter 7 will discuss on the outcomes of the thesis, inferences, analysis and future recommendations.

CHAPTER 2

LITERATURE REVIEW ON EMBEDDING PROCESSES & SENSORS PLACEMENT

A literature review is presented here encompassing two attributes of research objectives;

1. To develop an understanding of the technology that has been developed in recent past to embed off the shelf sensors, looking into aspects of sensor and host selection and manufacturing aspects, 2. To study and suggest improvement in sensors placement with the desired objectives to identify applied loads (static/dynamic) along with its location. We would also like to see a full field displacement/strain profile with the reviewed placement schemes. We intend to build a knowledge base to assist us develop smart structures. The following paragraph 2.1. discusses a few candidate sensors suitable for embedding.

2.1. Candidate Sensors for Embedding:

Two sensors namely (1) Fiber Bragg Grating and (2) Piezo Electric sensors are investigated as candidate sensors for embedding.

2.1.1. Fiber Bragg Grating (FBG):

Fiber Optic Technology was first developed in the 1970s and became famous with its usage in communications but it has gained wide acceptance as a promising tool for strain and damage sensing. The book by Measures [23] discusses strain monitoring through fiber optic sensors and their application in composite structures. Professor Measures is a pioneer

in the field of fiber optic strain monitoring as evident from his early article entitled ‘Smart Structures with Nerves of Glass’ [24]. Fiber Optic sensors respond to strains like strain gages with the design based on the principal of changes in transmission of light through the optic channel. These changes are brought in intensity, phase, frequency, polarization, wavelength or mode due to external stimuli of forces, pressure or temperature. These sensors are highly sensitive and can detect minute variations. Out of various optical sensors, FBG is one of the most promising optical sensor for developing a sensorial material/structure.

FBG exploits spectrometry which is based on the modulation in the index of refraction along a short length of fibers. The main advantage of this technique depends on the sensed information encoded directly into the wavelength which is an absolute parameter of measurement and is independent of any variation. By grating at a slightly different frequency, wavelength division multiplexing is achieved. The Bragg grating type exploits spectroscopy, creating a large number of gratings with slightly different frequency of each.

2.1.1.1. Advantages of FBG:

FBGs being immune to electromagnetic interference (EMI) also offer smaller physical dimensions with lightweight characteristics. Such characteristics make them feasible for embedding offering minimum hindrance in the structural performance. With no wires, FBGs act as both sensing elements and the signal propagation conduit. They possess excellent resolution and range, resistance to water and corrosion, ability to be multiplexed, immunity to harsh weather conditions, compact sensor and harness size, and reasonable cost per channel. Wavelength encoded information feature of FBGs makes it an absolute

parameter measuring sensor. They offer a self-referencing, absolute measurement scheme as the information remains immune to power fluctuations in the optical path.

One of the main advantages of FBGs over other fiber sensor schemes are its low cost, good linearity, wavelength multiplexing capability, resistance to harsh environments and the transduction mechanism, which eliminates the need for referencing as in interferometric sensors [25]. Figure 2.1 is a depiction of the FBG structure and Figure 2.2 describes the FBG working principle.

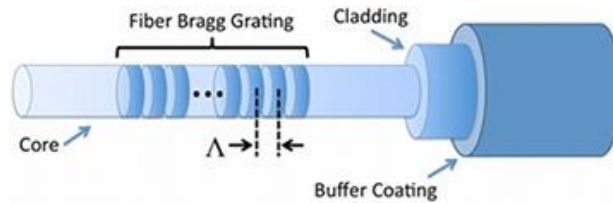


Figure 2.1 FBG structure [26]

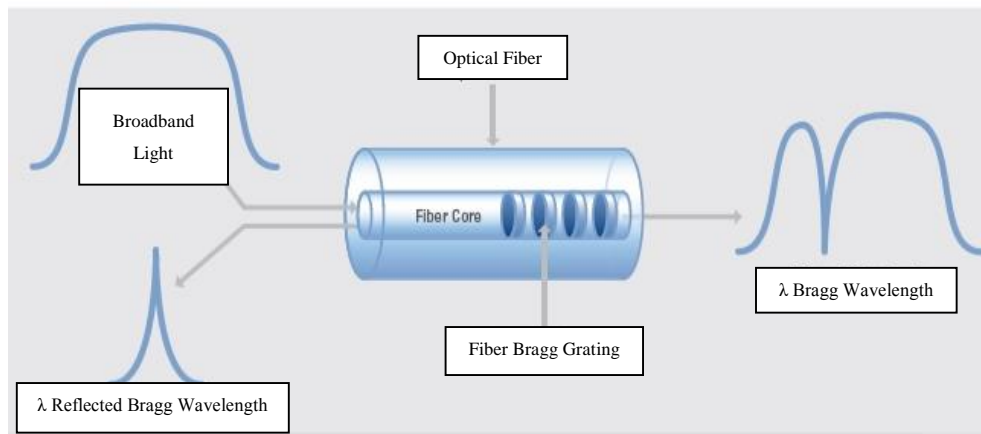


Figure 2.2 FBG working principle [26]

The reflected wavelength can be calculated by

$$\lambda_b = 2n\Lambda \quad (1)$$

In equation (1), λ_b is the Bragg wavelength, n is the effective refractive index of the fiber core, and Λ is the spacing between the gratings, known as the grating period.

2.1.1.2. Disadvantages:

One major drawback is that the optic unit for transmission and reception makes it challenging for the whole system to be embedded in the structure. Also the cost and maintenance issues would require careful assessment before progressing with the final design.

2.1.2. Piezoelectric Sensors:

Embedded or surface bonded piezoelectric sensors are another sensor type for evaluation of structures when miniaturization is concerned and they overcome difficulties encountered in traditional NDTs such as poor signal to noise ratio. They can remain permanently attached to the structures and have been used in composites for health monitoring during curing processes and also up to the end of their life. The use of piezoelectric element has been extensively explored in reference to the field of Structural Health Monitoring (SHM). Giurgiutiu describes usage of piezoelectric inserts named as PWAS (Piezoelectric Wafers Active Sensors) that can be implemented for various techniques of nondestructive evaluation [27]. Although techniques to evaluate structural health may seem simple with piezos but they offer challenges especially to quantitatively assess the situation. Piezoelectric sensors can be categorized into three main classes; (i) acoustic emission, (ii)

acousto-ultrasonics using piezoelectric transducers and (iii) electromechanical impedance based on whether they are to function as an active, passive or a mixed SHM system.

Lead Zirconate Titanate (PZT) sensors act upon application of force, piezoelectric transducers develop an output voltage and are frequently used as ultrasonic receivers, displacement transducers, acting as devices measuring acceleration, force and pressure. Piezoelectric transducers are made from piezoelectric materials which have an asymmetrical lattice of molecules which are distorted when a mechanical force is applied to it. The distortion orientates electric charges within the material, causing relative displacement of positive and negative charges. The charge displacement induces surface charges on the material of opposite polarity between the two sides. With electrodes implanted on to the surface, an output voltage can be measured across the electrodes.

Another application appeared using PZT as paints. Egusay and Iwasawaz in 1998 introduced a new concept of piezoelectric paint with their research at the Japan Atomic Energy Research Institute. This paint was presented as a continuous acoustic emission sensor. These paints are prepared using PZT ceramic powder bonded in an epoxy resin. Modal vibration sensing was performed using piezoelectric paints an integrated continuous health monitoring sensor [28]. The paint was applied on aluminum cantilever beams. Paint film thickness was varied from 25 to 300 μm . The film was evaluated in the frequency range from 0.3 to 1.0 MHz demonstrating good sensitivity. Figure 2.3 represents the PZT working principle.

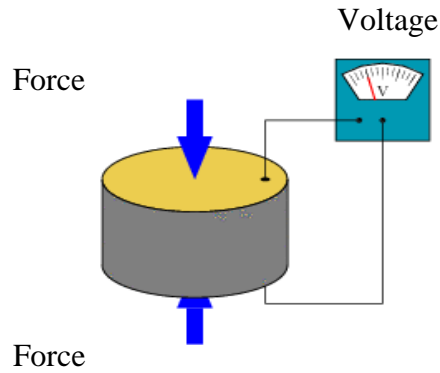


Figure 2.3 PZT principle [29]

2.1.2.1. Advantages:

PZT sensors are small and lightweight. They can perform as both sensor and actuator. Feasible for strain sensing and acoustic detection.

2.1.2.2. Disadvantages:

They are brittle due to their ceramic nature. The complexity of shape/geometry and the area of the structure being monitored make it difficult to identify sensor number and location, wiring issues, amplification, multiplexing and high computational effort. A number of research attempts are ongoing to find a remedy to this problem proposed in the form continuous sensors and artificial neural system.

The two mentioned sensors along with their characteristics and feasibility to be embedded in structures made from metals and polymers are tabulated in Table 2.1.

Table 2.1 Sensor characteristics on basis of their feasibility to be introduced in structures

Sensor Type	Flexible	Embeddable	
		Metals	Polymers
Piezo Electric	✗	✓	✓
Fiber Optic	✓	✓	✓

Here we have discussed the two promising sensors which have a better chance of being introduced in an embedded state. On one hand we have seen the advantages offered by optical sensors and on the other, the potential for piezoelectric sensors to be used in the development of smart structures. The next step involves looking at different developmental possibilities using these sensors. The following passage highlights the existing embedding technologies for the embeddable sensors in metals and composite structures.

2.2. Sensor Embedding Processes:

Sensor embedding processes are the methods or manufacturing techniques that are related to embedding sensors into the material. These can be classified as technologies related to the host material type namely (a) Metals and (b) Composite Materials as each material has its own requirement and associated difficulties for embedding. Next we discuss these techniques and look at aspects related to the feasibility of introducing sensors in an embedded state.

2.2.1. Embedding in Metals:

Embedding sensors in metals is a challenging task depending on the location of the sensor within the material. A sensor embedded in a state surrounded completely by the host material such that it exists at a depth below the subsurface level can be termed as Bulk Material Embedding. Whereas sensors located at subsurface levels can be introduced through a layering technique which we refer to here as Sub-surface Embedding. A literature review is provided in the light of both embedding techniques.

2.2.1.1. Embedding in Bulk Materials:

A technique has been shown in [19] to embed piezo sensors and RFID transponders into the cast product during casting process. As far as the RFID transponder is concerned a special glass encapsulated RFID device was used to protect it from the harsh casting environment. A glass transponder ‘Sokymat SID153 Hitag S 2048 bit was chosen. Its compact construction (2.12 mm of diameter and 12 mm length) is suited for the integration in thin walled casting structures. Its operating frequency is in the low band at 125 kHz to hold disturbances by the metallic environment as low as possible. The peak temperature of the transponder is 120°C for max. 100 h storage and 85°C for operational use. Figure 2.4 shows an RFID transponder embedded into a cast part. Figure 2.5 demonstrates embedding of a piezoelectric sensor in a mechanical structure.

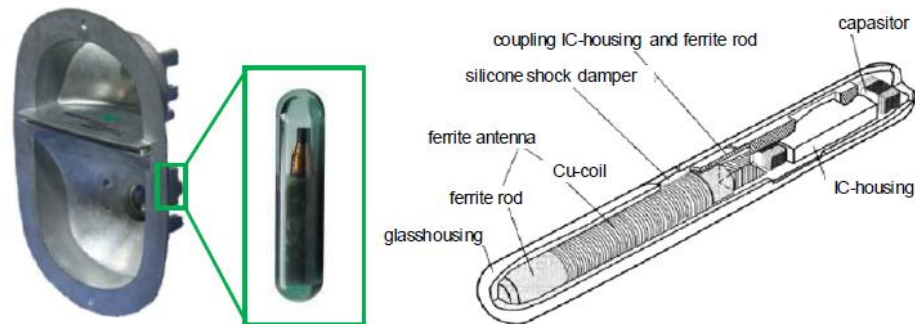


Figure 2.4 RFID cast part with integrated RFID transponder (left) and design of a glass transponder (right) [19]

The piezo-ceramic stack actuator type ‘CeramTec SP505 7x7x32.4 mm³’ was selected for the application due to the robust machining properties and high ability in generating the sensor signals. This sensor offers a storage and usage temperature from 40 up to 120 °C. The piezo sensor is further encapsulated in a high heat resistant polymer layer of 2mm

thickness. This layer in addition to thermal insulation provides shielding from mechanical damage caused by process based redensification compressions up to 2000 bars during solidification.

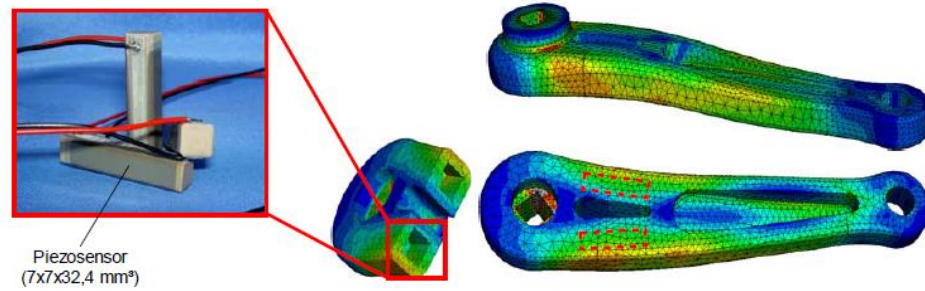


Figure 2.5 Piezoelectric sensor of type SP505 7x7x32.4 mm³ (left) and structural-mechanical calculation of a load of 1800 N (right) [19]

A method for development and evaluation of a miniature (1 cm³) embedded electronic module that can resolve temperature-compensated mechanical strain in three dimensions is described in [30]. The module is designed to be embedded into materials and to measure, in-situ. The module has been designed to deliver all nine components of strain to a PC via wired communications.

The module consists of three miniature, off-the-shelf, three-gauge, rectangular rosettes. These rosettes are assembled in a 3-D array to collect all components of strain. The cube structure has gauges on the outer faces and electronics on the inside. The electronics consists of signal conditioning circuitry, a 24-bit sigma-delta ADC, a microcontroller which sends the digital data directly to a PC, and an onboard temperature sensor for thermal compensation of the gauges. The module was encapsulated in epoxy and subjected to compressive and tensile testing. The result comparison to FE simulations revealed an

average of 7% difference between magnitudes and a standard deviation of 4%. Figure 2.6 (b) shows the 3D module for strain data collection.

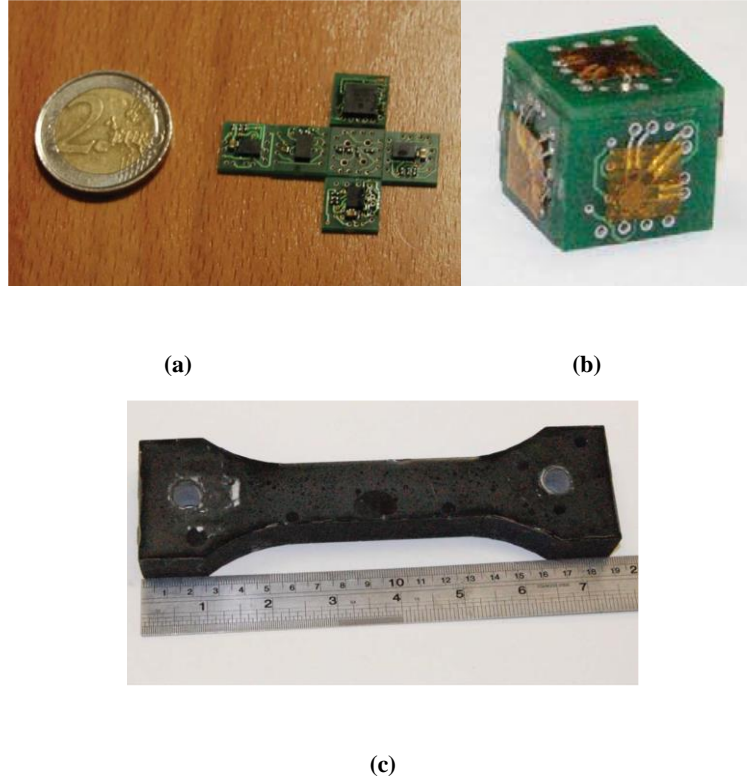


Figure 2.6 (a) Unpacked 3D module, (b) Fully assembled module, (c) Installation in the test specimen [30]

2.2.1.2. Embedding Sub-surface:

A method to embed off the shelf sensors into aluminum structure using Ultrasonic Consolidation (UC) at room temperature has been shown in [31–33]. Embedding sensors and electronics at 300°F to overcome the delamination issues resulted in optimal bonding, and the sensors used thus far have functioned normally. A Solidica UC SFF machine was

utilized at Utah State University for this purpose that is fed by aluminum tapes later on acting as layers for the structure.

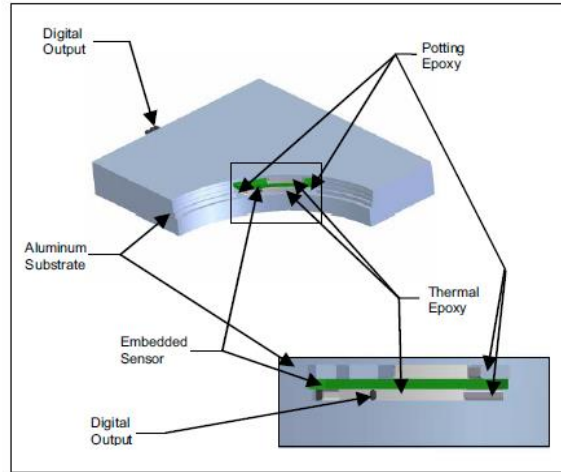


Figure 2.7 CAD representation of embedded sensor using UC process [31]

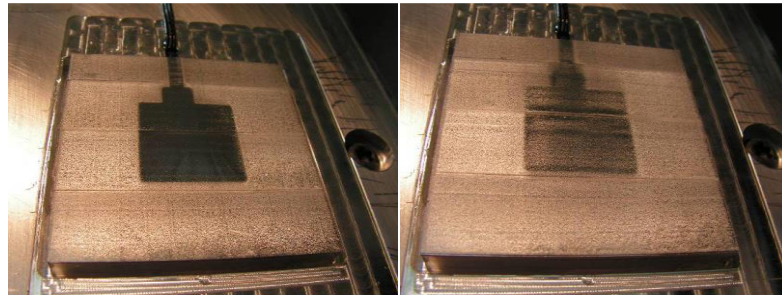


Figure 2. Multiple foil layers (10, 4 and 8) of aluminum applied through UC [31]

The USB interfaced sensor was introduced into a micromachined cavity surrounded by epoxy support. [6] refers to the study of the effects of protective coating properties on embedding process of FBG sensor in aluminum foil using ultrasonics. A comparison of performance was drawn among bare fibers, chemical nickel plated fibers and chemical-electro nickel fibers in the ultrasonic welding process. Results indicated that only chemical-

electro plated fibers and FBGs were successfully embedded in aluminum foils due to good protection and an appropriate matrix metal. The samples were loaded with a cyclic tensile load (0-40N). The chemical plating coating was about 3-5 μm in thickness and the chemical-electro plating coating had a thickness of 180 μm . This paper has discussed on the disadvantage of cladding the fiber by molten metal in previous attempts as it hampered the FBG performance and damaged the fiber. The FBG sensor has an operational temperature of around 200°C and also shown to go till 900 °C [34]. Figure 2.7 is CAD model showing features of the embedded sensor construction and Figure 2. Multiple foil layers (shows the layering effect of aluminum foil under UC method.

A similar technique using ultrasonic consolidation was employed in [6]. It was shown that bonding through ultrasonic occurs among the metal foil/metal coated fiber/metal foil sandwich when the pressure and ultrasonic vibration applied to this sandwich structure breaks up the surface oxide and interlocking, diffusion and plastic deformation occurs within the two metal foils. Figure 2.9 [6] illustrates the bonding characteristics between copper and aluminum foil with (i) bare fibers, (ii) chemical nickel plated fibers and (iii) chemical-electro nickel fibers. The welding parameters used were following: Static Force 0.45 MPa, welding time 0.09 s and vibration frequency 25 kHz. The copper/bare fiber/copper failed to form bonding between interfaces due to lack of bonding nature around the fiber. Examination through light transmission and intensity detection measurements showed that fiber integrity in the matrix was compromised. Rest of the experiments done with chemical and chemical-electro plating showed better results but chemical-electro nickel coating showed the best bonding characteristics with fiber integrity

and enhanced temperature sensitivity. Figure 2.8 depicts the schematics for ultrasonic welding and its results in Figure 2.9.

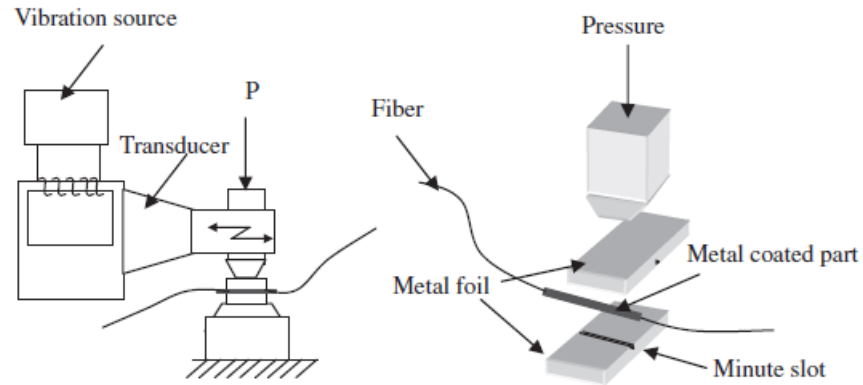
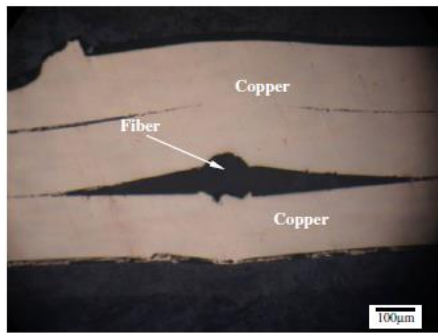
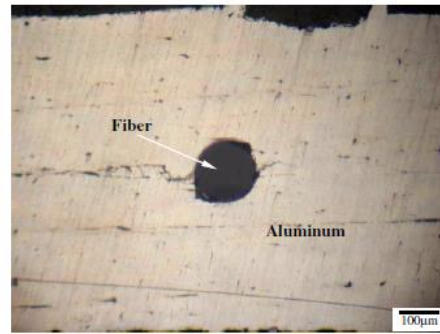


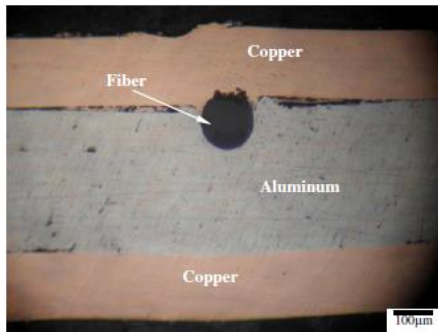
Figure 2.8 Setup of the ultrasonic welding equipment and the embedding procedures [6]



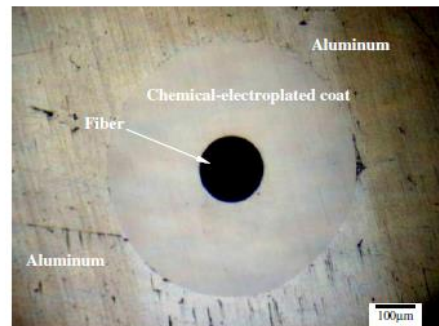
(a) Copper/fiber/copper structure



(b) Image of the cross section with magnification of 100x



(c) Copper/fiber/aluminum/copper structure



(d) Cross section of the Al/chemical electroplated fiber/Al

Figure 2.9 Results of different embedding techniques [6]

A discussion on investigation of embedding Ni coated FBG fiber within AA6061 matrices by Ultrasonic Welding for the formation of 3D smart metal structure is presented in [35]. Table 2.2 gives a comparison of UC process for the two experiments. The purpose to compare techniques from both research is to show similarity and also to look into advantages of varying conditions of weld and material type.

Table 2.2 Comparison of the UC process for two different experiments

Source	[35]	[6]
Material (Substrate)	Aluminum 6061 (TS = 113-117 [MPa]), (YS = 45-50 [MPa]) Elongation at Break (10-10.5[%])	Pure Aluminum Pure Copper
Material (Coating)	Ni	Ni
Thickness (Substrate)	0.4 [mm] foil Surface Roughness: 0.4 [μm] (R _a)	Pure Aluminum: 450 [μm] Pure Copper: 250 [μm] Slot Dimensions: 5x5 [μm]
Thickness (Coating)	140.3 [μm]	Ni-Chemical Plating: 3-5 [μm] Ni-Chemical Electro Plating: 180 [μm] Coating Length: 45 [mm]
FBG Characteristics	Cladding Diameter [125 μm] Central Wavelength [1540 nm] Temperature [30°C]	FBG Length: 20 [mm] Central Wavelength: 1538.74 [nm] Wavelength Shift (after Ni Plating): 1534.02 [nm] Wavelength Shift (after Ultrasonic Welding): 1530.20 [nm]
Weld Parameters	Power: 3.2 [kW] Frequency: 20 [kHz] Amplitude: 30 [μm] Welding Current: 12[A] Sonotrode: 125 [mm] tool steel Ending: 15x15 square Optimal Weld Time: 230 [ms]	Static Force: 0.45 [MPa] Frequency: 25 [kHz] Weld Time: 0.09 [s]
Temperature Sensitivity	(15 [pm/°C] coated, non-embedded) (17.9 [pm/°C] coated, embedded)	25 [pm/°C] with Ni (Total Diameter = 0.48 [mm]), (Central Wavelength = 1550 [nm])

The coating methods used in [35] have been proposed in [36,37] with optimum conditions for coating bare optic fibers through chemical and chemical-electroplating. After metallization, the fiber sensor was successfully embedded in the 42CrMo steel by brazing method with a Sn-Ag-Zn filler metal [37] shown in Figure 2.10.

The results showed that whether it is copper or nickel as conductive coating material through chemical plating, electroplating Ni afterwards showed better results in terms of sensor function with increased sensor sensitivity ($0.02179 \text{ nm}/^{\circ}\text{C}$) and fiber integrity. The above method of coating is claimed to be advantageous due to its simplicity, cost effectiveness and lower processing temperature.

Similar metallization process [36] involving chemical electroplating was investigated for thermal stress influence on the temperature sensing properties of the metalized and a physical-mathematical model for temperature sensing of FBG was presented. The sensor was introduced during casting of the host material (42CrMo). The metallization process [36] discussed would help us understand better conditions to deposit metal over the fiber optic sensor in order to provide a good bonding interface between the fiber and the metal host.

Another example is from smart tool development through FBG embedding for tool temperature and strain data. As illustrated in Figure 2.11 and Figure 2.12, FBG sensor embedding in a steel part by the process of a low temperature laser assisted maskless microdeposition (LAMM) of a silver ($1.7\text{-}2.3 \text{ }\mu\text{m}$) coated FBG followed by Ni electroplating in steel part is adopted [20]. The steel part is then further coated with WC-Co through laser solid free form method to investigate the FBG sensor characteristics when the part is used as a machining tool.

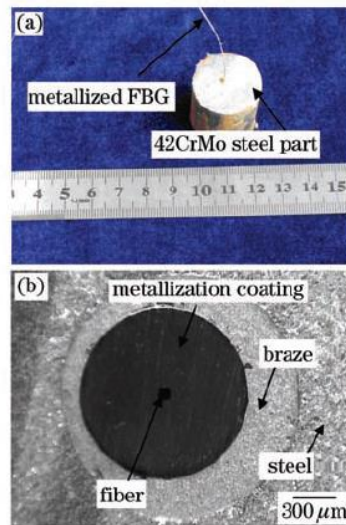


Figure 2.10 (a) FBG embedded in a 42CrMo part, (b) radial cross-section of the part [36]

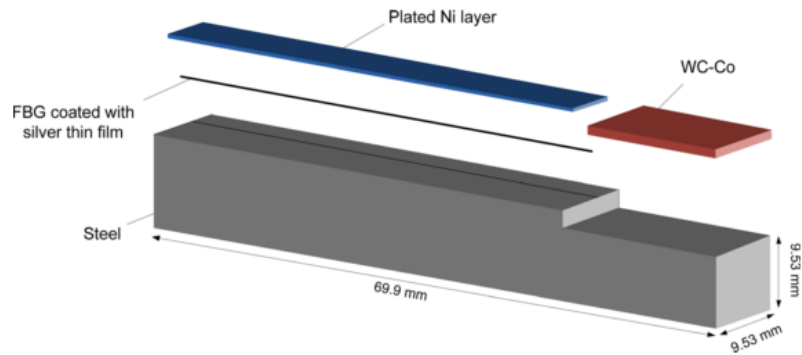


Figure 2.11 Geometry of the tool system [20]

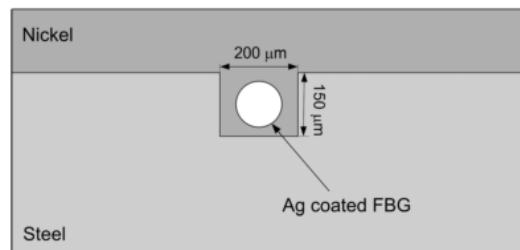


Figure 2.12 Tool development with embedded FBG [20]

In the work of [38] layered manufacturing technique was applied to embed FBGs in Ni, Stainless Steel, polymer and ceramic structures. This technique was specifically designed to be embedded near surface for rotating structures like blades in gas turbine engines for structural health monitoring. The layered manufacturing topics under discussion were Stereolithography (SLA), Fusion Deposition Modeling (FDM), Selective Area Laser Deposition (SALD), and Shape Deposition Manufacturing (SDM) processes. The above mentioned technologies allow us to explore the possibility of developing smart structures from these techniques and understand how they can be helpful for creating cost effective smart products.

2.2.2. Embedding in Polymers and Composite Materials:

A carbon fiber vertical stabilizer was embedded [4] with FBG sensors to monitor strain activity. The sensors were embedded during the layup process. The test coupons were developed to the size of 300x200x20 mm under the conditions of curing at 82.2°C for 90 minutes under 110 kPa as shown in Figure 2.13.

An embedding technique including a number of FBG sensors into filament wound pressure tanks are shown in [11]. The work considers multiplexing and in situ structural health monitoring of filament wound pressure tanks under hydrostatic tests using embedded FBG sensor arrays. From the experimental results, it was demonstrated that FBG sensors can be successfully adapted to filament wound pressure tanks for their structural health monitoring by embedding. See Figure 2.14 for details.

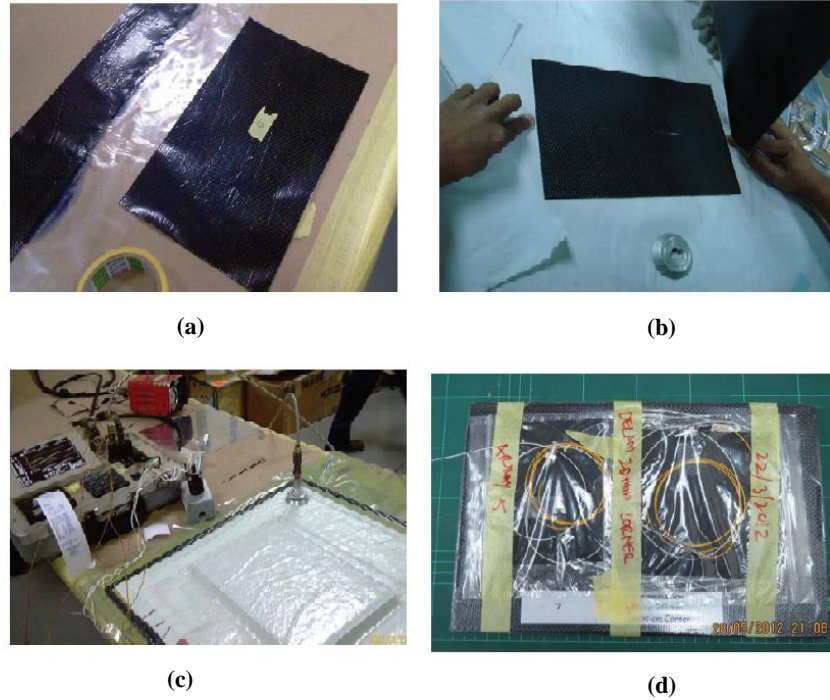


Figure 2.13 Specimen preparation, a. wet layup cutout, b. laying down the FBG array in the middle of the carbon ply outer layer, c. curing process of panel, d. completed smart structure sandwich panel with embedded FBG sensor [4]

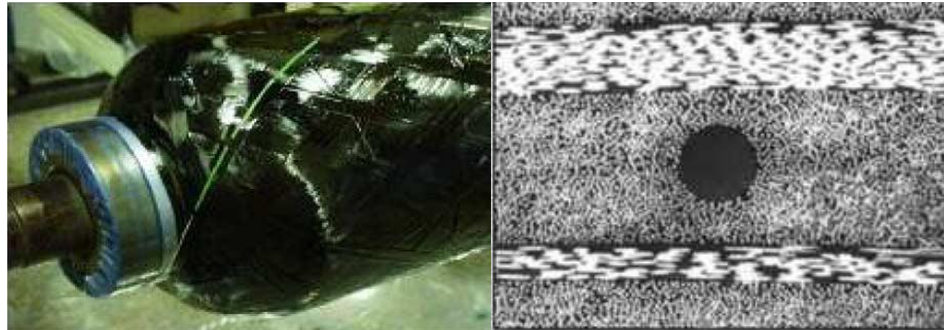


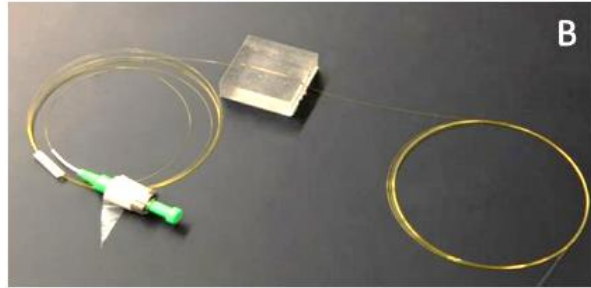
Figure 2.14 FBG sensor line during the fabrication of Filament Wound Composite Vessel [11]

[9] has shown to embed piezo-resistive strain sensor with circuitry to enable sensing of local strain through external resistance meter. The two in-situ piezoresistive sensors that are evaluated are; 1. Embedded Nickel Nanostrand (NiN) Nanocomposites, and, 2. Neat

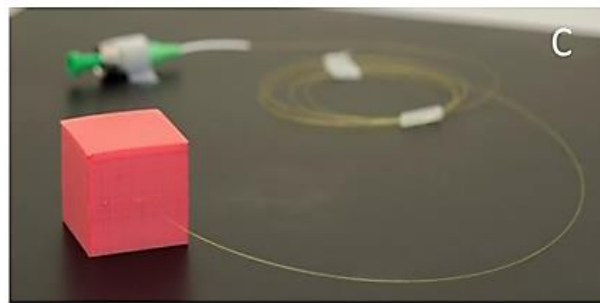
Prepreg Carbon Fiber. For the connecting circuitry, nickel coated carbon fibers and carbon fiber prepreg alone are compared as pseudowires to the piezoresistive sensor; the probing configuration of the external meter is also considered.

The previous attempts to embed optical devices and FBGs through 3D printing are reported in [7,39,40]. 3D printing referred here is a type of additive manufacturing technique and one of those techniques is Fused Deposition Modeling (FDM). This method of printing is both versatile and easy. The material for FDM is extruded from a high temperature head on to a plate which holds the 3D printed part. The optical elements are embedded by either the construction of those elements directly from the 3D printing process [39] or are introduced by interrupting the layering process and continued upon to have the sensor concealed/embedded (See Figure 2.15) [7,40].

After a detailed review on the current state of the art for embeddable sensors for smart structure development, we conclude that the choice of embedding procedure is restricted to the type of host material and the sensor chosen for embedding. Since the advantages of using fiber optic sensor weighs more in comparison to its counterparts, we choose to use fiber optic sensor for current study of embeddable sensors. For the current study we would introduce the fiber optic sensor into a metal beam by creating a slot compatible with fiber dimensions and giving it a sub-surface embedding by using epoxy to bury the sensor in the metal structure.



(a)



(b)

Figure 2.15 FBG sensors embedded into 3D printed (a) Valero and (b) ABS scaffold [40]

2.3. Optimal Sensor Placement:

Optimal sensor placement (OSP) is a term frequently used nowadays in current research [41–45] which aims at introducing sensors with optimum positions to a system in order to observe the system status. OSP is a very demanding objective to design Structural Health Monitoring (SHM) systems as some systems would like to be installed with sensors in fixed position throughout their life time. One of the possibility is to have them embedded inside the structure which needs careful observation as the sensors need to extract desired information such as strain, temperature and pressure from critical locations.

OSP problems have been implemented with swarm algorithms recently and have shown tremendous research potential. These algorithms have helped install minimum sensors for vibration observation in bridge structures [42,43]. Also damage selection through optimal sensor in a cantilever beam were studied in [46] and improvement in swarm algorithms was implemented with sonar sensors in [47]. Swarm optimization is a computational method that optimizes a problem through iterative procedures to improve a candidate solution with regards to a certain defined objective. The objective can be accurate shape reconstruction or identifying the applied input to the system. Swarm technique solves a problem by having a population of candidate solutions (called particles) and moving these particles around in the search space towards the best solution. These techniques are based on artificial intelligence and requires some times intensive computations. Similarly researchers have also incorporated genetic algorithm (GA) for optimal sensor placement schemes [41,48]. The genetic algorithm repeatedly modifies a population of individual solutions. At each step, the genetic algorithm selects individuals at random from the current population to be parents and uses them to produce the children for the next generation. Over successive generations, the population "evolves" toward an optimal solution.

Similarly earlier attempts on Placement Index solutions to find optimal sensor placement have been presented in [45,49]. The Placement Index solution leads to establish the most responsive sensors to an external input. The index is calculated on the basis of identifying the true response of the structure by implementing a set of possible sensors. The technique though a straightforward implementation through the Finite Element and State Space representation of the system, requires that input be known in terms of its location and magnitude. Whereas our requirement is to establish an optimal sensor arrangement that

does not require the input information beforehand. The potential of D-Optimal method for sensor/actuator placement studies are illustrated in [50,51]. The D-Optimal or the Determinant optimization is a numerical method that takes into account minimizing the prediction error for an input load. All of the mentioned techniques aim to identify the system's dynamic properties in terms of force or modal identification independently.

Force identification through system response is considered to be an inverse problem which in detail are reviewed in [52–56] and in general uses dynamic strain data in addition to inverse problem solving techniques to solve for the optimum sensor problem. Modal identification is also an advantage in addition to the force identification which have been independently studied in [41,57]. A benefit of using the sensor data for development of complete displacement and strain fields are presented in [58–60].

After analyzing the mentioned sensor placement schemes, we would like to incorporate the method(s) that would fulfil our objective to identify true load input with accurate description of the structure under consideration. We also require that the method is computationally less intensive and could use technique such as Finite Element Method (FEM) to give an insight into structural behavior in terms of strain, displacement, velocity and acceleration of the system. This would help us identify the load input using standard equation of motion of the excited structure. For this reason we have chosen to implement the Placement Index and the D-Optimal methods to test whether both or one of the schemes is more suitable for load input identification,

2.4. Conclusion:

This chapter gives an insight into candidate sensors for sensor embedding in different materials. The state of the art of sensor embedding processes is presented for different materials/structures made smart using latest manufacturing techniques. Each method of embedding is different based on sensor type, ease of manufacturing and conformity of a sensor to the host material. Sensor embedding in metals and polymers was reviewed in detail to understand and evaluate the existing methods for the development of the smart material/structure explained in the chapter 1. The literature review on embedding techniques highlights the difficulty to embed sensors into metals. And also possibilities to improve upon processes in polymer based structures especially in the field of additive manufacturing. So far, the observed shortcomings are the difficulty of embedding combined with challenges to strategically place these sensors.

Improvement in the existing methods or new fabrication techniques need to be discovered to develop on the concept of smart structures. One of them could be ultrasonic and layered manufacturing in metals. As for polymeric structures, 3D printing is an emerging solution which can be exploited to develop structures with complex geometries and complex sensory layout.

Optimal sensor placement is another issue to address once the fabrication method is justified. FBG stands out as a choice for the characteristic smart structure/material based on the merits and demerits of this optical sensor. Upon deciding the type of sensor, their placement also becomes another challenging task. The review on sensor placement help us

choose method(s) that could serve the purpose to make our structure smart by identifying an unknown load. Summarizing the above, following focus areas are highlighted:

1. Challenges related to sensor selection as we need miniaturize sensors not to hamper the structural performance with their sheer presence. Also the measurand quality being transmitted and the real time response through a reasonable actuation makes the problem research worthy and beneficial for future generation structural designs.
2. The embedding processes need to be easy and cost effective. The process needs to be scaled from small structures to large structures. Process simplification and ease would make it convenient to adopt this new form of technology for day-to-day usage designs.
3. The smart feature to identify an input load with minimum sensor number requires optimally placed sensors.
4. For future, methods need to be investigated for a better coordination between sensors and actuators. A modular scheme for such interaction needs to be studied for different structural modules joined together to form a structural assembly. This sort of design would allow us to depict a true nervous system behavior, as each structural module would act as a different organ of the structural body with same or different measurand collection feature interconnected with each other.

Since the current development is for sensorial structures. Only the issues related to sensing will be addressed in the following chapters. Besides manufacturing aspects, one of the challenging tasks is the sensor placement and the focus area for the thesis. Investigative methods will be explored in light of the literature review supportive of the placement

issues. It was found that most of the sensor placement methods rely on complex mathematical optimization procedures especially for force identification problem. There is a need to understand the sensor placement with respect to the structural behavior analysis. Finite element method (FEM) provides an in depth insight into structural problems specially when the structures are complex and analytical solutions do not exist. Two placement methods namely a) Placement Index and b) D-Optimal method have been selected based on sensor placement directly dealing with the FEM structure representation. We would like to observe the effectiveness of these methods in favor of force prediction. Based on the review we would now proceed to explore practical issues to deal with embeddable sensors.

CHAPTER 3

SENSOR CHARACTERIZATION & CALIBRATION

This chapter describes fiber optic sensor characterization along with an investigative method to determine the bend losses in optical fibers using different placement layouts. Following characterization studies, calibration procedure is explained in detail to setup a measurement system for the fiber optic sensor. Fiber optics have undoubtedly revolutionized the communication world with a wide spectrum of applications industry especially associated with fields of telecommunications, civil, mechanical and aerospace. Fiber optic sensing is yet another feat which enables users and industries to investigate critical problems where other conventional sensors fail to deliver. Aspects of failure would be, but not limited include handling of multiple sensors, their survivability and reliability. Examples of such applications are covered widely with fiber optic systems incorporated into aerospace [25,61] and civil structures [62] and have shown a promising future in the realm of Structural Health Monitoring (SHM). SHM is a discipline which supports nearly all engineering domains to investigate physical parameters critical to the operation. SHM widely depends upon the sensing technologies in terms of the advantages of miniaturization, compatibility, robustness and ease of installation. Fiber optic sensors meet the demand of all the mentioned qualities.

One of the genres of the fiber optic sensing elements is Fiber Bragg Grating (FBG). Light transmission through the FBG is reflected back with a signature wavelength acquired due to a grating period and refractive index. Any sort of mechanical or thermal strain will cause

the grating to expand or contract and hence the wavelength could shift either side of the signature wavelength when observed with an optical interrogator system. Many commercial devices which support FBG sensing have their own system limits to optical transmission and interrogation. Thus there is a requirement to investigate sensor performance with varying parameters of the system input. Conventional devices offer an observation span of 1510-1590 nm [63] whereas the optical input is also limited to device capability.

The previous attempts to embed optical devices and FBGs through 3D printing are reported in [7,40]. 3D printing referred here is a genre of additive manufacturing technique more technically termed as Fused Deposition Modeling (FDM). The optical elements are embedded by either the construction of those elements directly from the 3D printing process [39] or are introduced by interrupting the layering process and continued upon to have the sensor concealed/embedded [7,40].

The deployment of FBG sensors for large and complex mechanical structures can be challenging through embedding at the material subsurface or even inside the material. The embedding processes such as ultrasonic consolidation method in aluminum sheets; powder based aluminum alloy with compaction followed by sintering at 300-400°C was carried out in another study [33] whose results for characterization study is presented in this chapter. Rapid prototyping or 3D printing using polymer materials e.g. ABS, PLA was performed with optical fiber embedded as another route to embed sensors in polymeric structures under current study. Fiber embedding is performed while the printing is in progress. The host material/structure can have critical areas where the sensors need to be embedded in order to measure structural behavior. The FBG sensors embedded in various

locations require the fiber to bend according to the required placement with a single continuous fiber. The fibers can be subjected to high temperature, pressure and strains as shown in Figure 3.1.

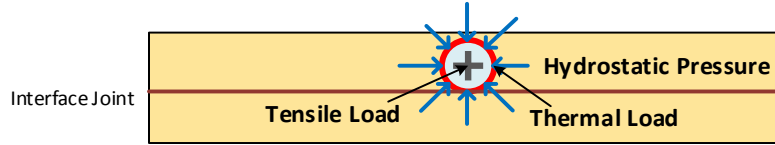


Figure 3.1 Loading state of an embedded optical fiber sensor

Table 3.1 gives a comparison for sensing capabilities between aforementioned sensors.

Table 3.1 Sensing capabilities of contemporary sensors [64]

<i>Technology</i>	<i>Strain Gage</i>	<i>PZT</i>	<i>FBG</i>
<i>Sensitivity</i>	0.003 [mV/ $\mu\epsilon$]	80 [pC/ $\mu\epsilon$]	1.2 [pm/ $\mu\epsilon$], 10 [pm/ $^{\circ}\text{C}$]
<i>Principle of Measurement</i>	absolute	relative	absolute
<i>Linearity</i>	0.05 [%]	1 [%]	< 0.5 [%]
<i>Connection</i>	Min 4 wires	2 wires	Single Mode Fiber
<i>Strain Limit</i>	$\pm 10,000$ [$\mu\epsilon$]	$\pm 1,000$ [$\mu\epsilon$]	$\pm 10,000$ [$\mu\epsilon$]
<i>Operating Temperature</i>	400 [$^{\circ}\text{C}$]	400 [$^{\circ}\text{C}$]	-40 ~ 800 [$^{\circ}\text{C}$]

The single mode fiber is embedded without its jacket inside the material as shown in Figure 3.2. It is composed of a silica core with a cladding and an extra coating totaling an average diameter of 270 μm . It can be re-coated and subject to tension and pressure caused by the embedding processes as the fiber is in direct contact with the material at elevated temperatures in all mentioned processes. Since the fiber is manually placed inside the

material with various geometries i.e. linear, circular with tight corners, it was logical to check aspects of integrity of the sensors to guarantee its use. Hence, with the increased complexity in verifying the performance of these materials, the characterization of the fibers becomes important. Fiber characterization is defined as a series of tests performed on optical fiber span to verify its integrity after being subject to geometry variation, load and temperature. It is worth noticing that the interrogator supplies fiber optics with low level power light e.g. average of 0.18 mW and hence with multiple FBGs in a serial configuration, a question arises whether the last FBG would still be able to receive enough power to measure and is there any limitation to it?

New design and applications require characterization customized to the needs of the customer or end user. Sensor calibration and characterization is an important step in developing new systems. For example usage of optical fibers is gaining tremendous attention in the field of aerospace, oil and gas and biomedical sector. The initial applications of fiber optic sensors for a variety of purposes specially in SHM of aerospace vehicles were proposed in [24] and there usage in oil and gas for well information and robotics application for a sensitive fingertip were investigated in [65] and [66] respectively. The novelty of design and application inspires us to use existing material characterization with customized test setups and investigation methods. Examples of implementing fiber characterization techniques to suit applications without hindering system performance and retaining sensor integrity were also studied. A metal coated optical fiber is investigated for its integrity and sensitivity to thermal changes in [36]. Pressure response studies were carried out in [65] whereas [68] offers insight into performing tests to identify tensile strength of tailored optical fibers. The sensor response to different measurand like force,

pressure, temperature and strains show the effectiveness of a sensor in a particular loading scenario. The following sections provide details for various characterization methods for fiber optic sensors to investigate sensor sensitivity and their mechanical strength.

3.1. Characterization of Fiber Optics:

Any embedded fiber optic with several FBGs inside a material is subject to external effects such as tensile pull, compression, pressure and temperature. The following tests will characterize the fiber in various aspects and show some limitations.

3.1.1. Tensile Test (Corning SMF 28 Optical Fiber):

The tensile tests were conducted on a Corning Single Mode Fiber (SMF 28) in order to evaluate the fiber strength in tensile loading. The fiber used is a standard single mode fiber used in fabricating different FBGs with various coatings. The fiber geometry details are presented in [69] and a typical schematic is shown in Figure 3.2. The fiber geometry is described below.

Coating Diameter [μm] = 245 ± 0.5

Cladding Diameter [μm] = 125 ± 0.7

Core Diameter [μm] = 8.2

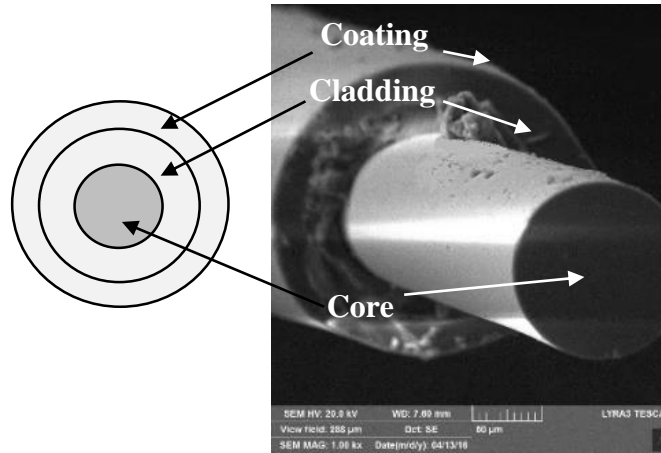


Figure 3.2 Optical fiber schematic and its SEM picture

3.1.1.1. Sample Preparation:

The test coupons were made out of cardboard material under design specifications from ASTM D 3379-75 (1989) [70]. The tests were conducted in batch of three for each type of bare and coated fibers with gage lengths of 20 mm and 30 mm respectively. The coupons grip area length was adjusted to fit in the BOSE ElectroForce ® Tensile Test Machine with a limit load of 225N (See Figure 3.4). The tests were conducted at room temperature and the displacement rate was 0.2 mm/min. The grips used were Titanium T/C fatigue grips GRP-TC-Ti450N-F with a grip width of 25 mm. Post breakage condition of samples are shown in Figure 3.3



Figure 3.3 Test samples for tensile test (post breakage)

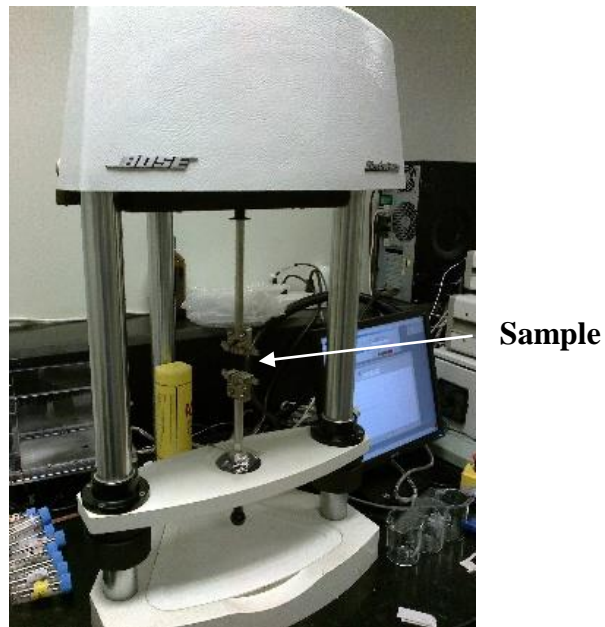


Figure 3.4 Test setup for tensile test

3.1.1.2. Test Results (Analysis and Errors):

The test results of the tensile test are shown in Figure 3.5 exhibiting linear relationship between force and strain with fiber breakage occurring at a pulling force of 6.5N (Sample 1). The fiber breakage point at failure for bare fiber specimen type varied by 20% when compared to coated fibers. The failure did not occur in the bond region and remained intact

during test. Nevertheless, the bare fibers experienced a brittle fracture whereas the coated fibers underwent excessive elongation after the fiber breakage inside. With three samples, two from each type (coated and uncoated) exhibited similar trends. Average test results are illustrated in Table 3.2. The average value of similar results suggests that bare fibers exhibit higher strength in the absence of coating with a higher modulus (Table 3.2). Whereas due to the shear between the cladding and the coating, the coated fiber experiences additional shear load and hence caused fiber to fail early. The other reason can be the reduction in effective stiffness of the system. The SMF 28 Data Sheet [69] suggested that the tensile limit is ≥ 0.7 GPa which is close to the test result with tensile limit of 0.63 GPa (See Table 3.2). Figure 3.5 depicts a sample data collected to calculate the ultimate tensile limit.

The tests concluded that there are some inconsistencies in the result due mainly to the gripping of the fibers but gives an approximation for the tensile limit of the fiber for both bare and coated conditions. The bare fibers exhibited the brittle failure with a steep slope (elastic modulus) and plastic strain introduced by the presence of acrylate CPC6 coating on the coated fiber.

The breaking values may slightly vary from one test to another due to the following observed errors during the tests.

- Non-alignment of the pull axis with the fiber length.
- Unequal gripping conditions.
- Bonding inconsistency between fiber and the epoxy.
- Inconsistent slippage between cladding and the core.

- Excessive load while pulling out/separating the fiber from the protective jacket.

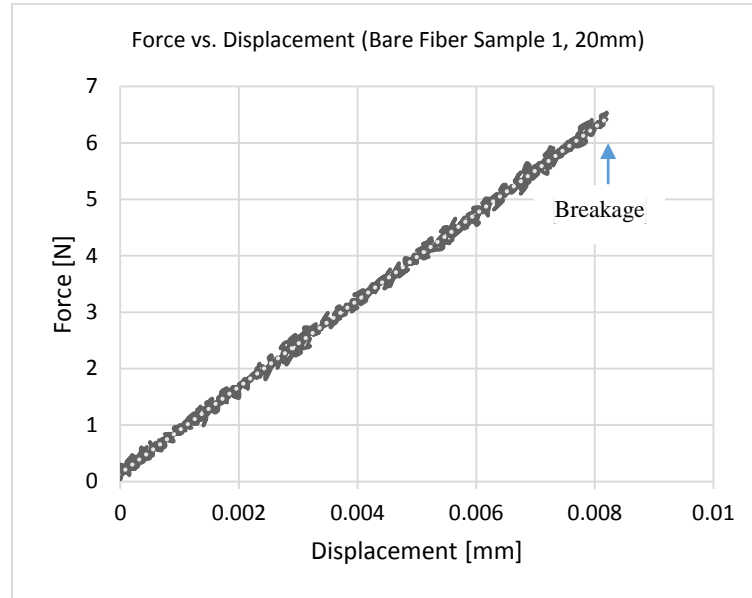


Figure 3.5 Tensile test sample result for a bare optical fiber gage length 20 [mm]

Table 3.2 shows a set of test results for bare fiber and coated fibers. Three repeated tests were performed for each fiber type. The results are in close agreement to those published by manufacturers and other references [68,71].

Table 3.2 Tensile test results Corning SMF 28

<i>Fiber Optic Sample Type</i>	<i>Gage Length [mm]</i>	<i>Initial Position [mm]</i>	<i>Break Position [mm]</i>	<i>Initial Load [N]</i>	<i>Break Load [N]</i>	<i>Slope Elastic [N/mm]</i>	<i>Stress [N/m²]</i>	<i>Strain [mm/mm]</i>	<i>E [N/m²]</i>
<i>Bare Fibers</i>	20	-6.31	-6.09	-0.02	7.86	39.39	6.33E+08	0.01	5.84E+10
	<i>Average Bare fibers Young's Modulus = 58.38 [GPa], UTS = 0.63 [GPa]</i>								
<i>Coated Fibers</i>	30	-6.31	-5.52	0.00	9.86	15.69	2.03E+08	0.03	8.12E+09
	<i>Average Coated fibers Young's Modulus = 8.12 [GPa], UTS = 0.20 [GPa]</i>								

3.1.2. Strain Response of FBG:

In addition to the acrylate coated fiber, a similar polyimide coated FBG was tested for strain response using a translation stage (Figure 3.6). The details of the FBG are given in Table 3.3.

Table 3.3 Polyimide coated FBG properties

Centre Wavelength	1544.075 [nm]
Bandwidth at 3dB	0.211 [nm]
SLSR	16.63 [dB]
Reflectivity	96.26 [%]
Grating Length	10 [mm]

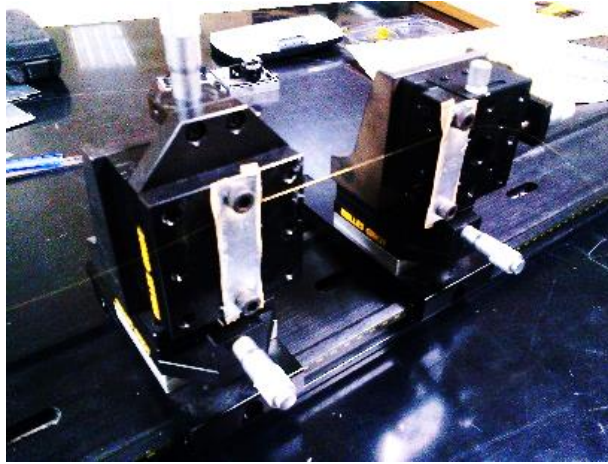


Figure 3.6 Translation stage with fiber grips for strain response

The FBG was tested with gage lengths of 100, 110 and 120 mm. One end of the fiber was fixed while the other end was movable through micrometer screws. Each time a displacement of 0.01 mm was assigned and the strain response was recorded at the Optical Spectrum Analyzer (OSA). The fiber was pulled uniaxially between the grips. Any chance of misalignment was taken care of to avoid erroneous results. Figure 3.7 shows results observed for different gage lengths.

Table 3.4 Strain sensitivity vs. gage length.shows the strain sensitivity to gage length.

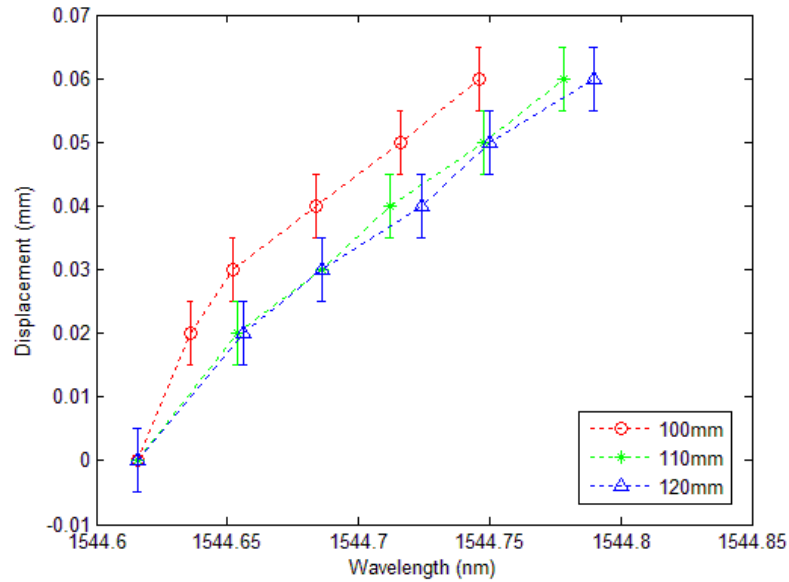


Figure 3.7 Wavelength vs displacement trend for different gage lengths

Table 3.4 Strain sensitivity vs. gage length.

S/No.	Gage Lengths [mm]	Sensitivity [nm/ μ strain]
1	100	2.85E-04
2	110	3.25E-04
3	120	3.60E-04

The error bars shown in Figure 3.7 depicts the error caused due to human error in reading the micrometer of Least Count (LC) 0.01 mm, and possible gradual slippage at the gripping points of the fiber explaining the non-linearity. The analysis reveals that the sensitivity of the FBG tends to decreases with increasing gage lengths. This type of sensitivity determinations helps us evaluate Gage Factor. Gage Factor (G.F.) is defined as $GF = \frac{\Delta\lambda/\lambda}{\varepsilon}$ where $\Delta\lambda$ is the change in wavelength and λ is the nominal wavelength. ε is the strain experienced during the test.

3.1.3. Temperature Characterization of FBG:

The other aspect of FBG characterization includes the evaluation of the maximum temperature to failure of a single mode FBG along with the evaluation of the optical transmission fiber. The FBG inscribed SMF 28 is polyimide coated with properties shown in Table 3.5 Test parameters for polyimide coated FBG [9]..

The fiber has a high operating temperature, low loss, dual layer special polyimide coating, and excellent core/cladding concentricity. It can be useful for applications in avionics, military and oil and gas domain [3,65]. They can also be used for fiber sensor arrays to have multiple FBGs on the same fibers.

Table 3.5 Test parameters for polyimide coated FBG [9].

<i>Test Parameters</i>	<i>Specifications</i>
<i>Geometrical Properties</i>	
Cladding Diameter	125 ± 1.0 [μm]
Core Diameter	9.8 [μm]
Coating Diameter	145 ± 5 [μm]
<i>Mechanical Properties</i>	
Fiber proof test level	0.7 [GPa]
Operating Temperature Range	-50 to +430 [°C]
<i>Optical Properties</i>	
Attenuation	<0.5 [dB/km]
Cutoff Wavelength	<1300 ± 50 [nm]
Operating Wavelength	1300-1600 [nm]
Bend loss at 1550nm per 100 turns 25mm dia	<0.02 [dB]

3.1.3.1. Test Setup:

The experiment was performed to maintain reading, as the temperature increased, shifting of the FBG wavelength and the light transmission characteristics of the optical fiber in tandem were observed. Both fibers were introduced through a top opening of a Lindberg Blue box furnace with dimensions 30 x 30 x 30 cm and making a bend radius of approximately 1.5 cm (Figure 3.8). The temperature of the furnace was controlled with a

Eurotherm PID based controller having a resolution of $0.01\text{ }^{\circ}\text{C}$ reaching a limit temperature of 1100°C (Figure 3.9). A k-Type thermocouple was also dropped to the same height as of the two fibers to accurately depict temperature at that point. The inlet port was connected to an Amonics ® light source and the outlet was connected to a Yokogawa optical spectrum analyzer (OSA) through FC connectors. Light source is set at $P_{\text{out}} = 2.95\text{ mW}$ and $I_{\text{set}} = 135\text{ mA}$. Table 3.6 shows the characteristics of the FBG used in the experiment and the test conditions. Figure 3.10 gives a graphical representation of the superimposed spectra of the wavelength when observed for increase in furnace temperature, b) shows a linear trend for wavelength shift versus change in temperature. Error in temperature reading was $\pm 0.01^{\circ}\text{C}$.

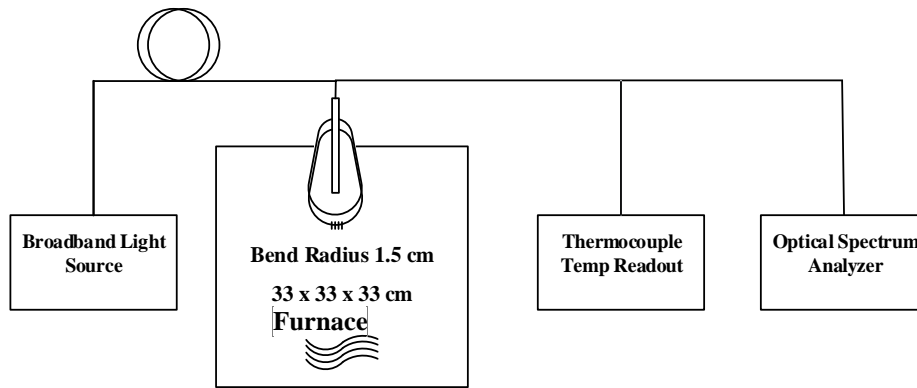


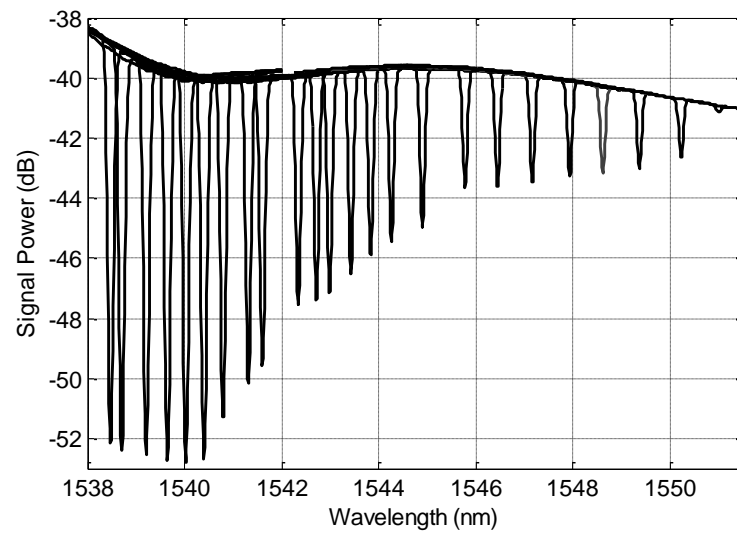
Figure 3.8 Schematic for test setup



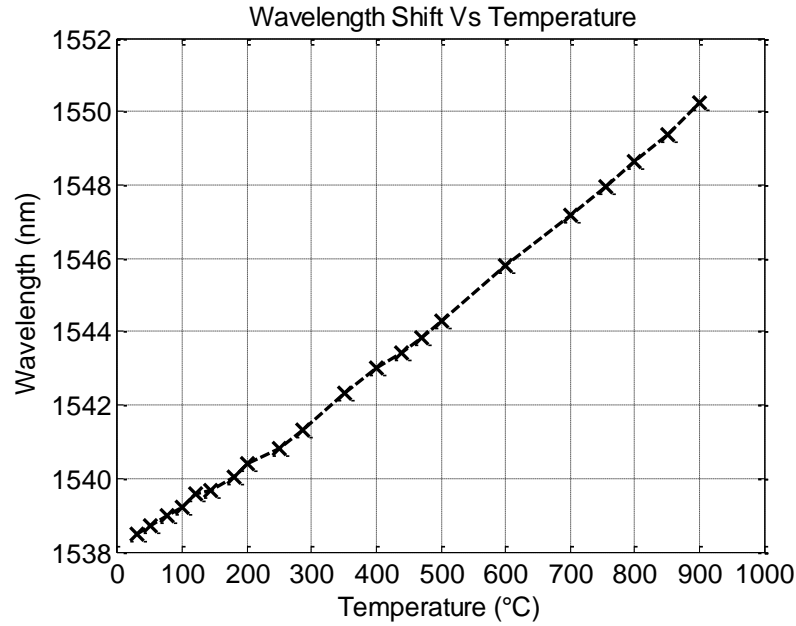
Figure 3.9 Lab setup showing connections and instruments/apparatus used

Table 3.6 Polyimide coated FBG properties.

Centre Wavelength	1537 [nm]
Bandwidth at 3dB	0.189 [nm]
SLSR	17.5 [dB]
Reflectivity	95.26 [%]
Grating Length	10 [mm]



(a)



(b)

Figure 3.10 (a) Superimposed spectra of wavelength shift with varying temperature ($^{\circ}\text{C}$) and effect on signal strength, (b) Linear response of wavelength shift to temperature variation

Table 3.7 Signal strength [dB] and output power [mW] for different fibers connected.

<i>Attachments</i>	<i>Broadband Source (BBS)</i>	<i>BBS + Transmission Fiber (TF)</i>		<i>BBS + FBG</i>
<i>Temperature [°C]</i>	23		938	956
<i>Signal Strength [dB]</i>	3.11	1.08	1.66	-14.77
<i>Power [mW]</i>	2.041	1.283	1.467	33.33e-3

3.1.3.2. Test Results (Analysis & Discussion):

Initially, the FBG central wavelength was recorded to be at 1538.5 nm at room temperature of 23°C . The test temperature was then raised with gradual steps and a corresponding wavelength shift was observed as shown in Figure 3.10 (a). The wavelength was almost

proportional to the increase of temperature as recorded in Figure 3.10 (b). The optical transmission loss remained negligible until the end of experiment with almost no sign of FBG wavelength peak at 956°C.

The relationship between Bragg wavelength of fiber grating and temperature change ΔT is expressed by equation (2) [10]

$$\frac{\Delta\lambda_B}{\lambda_B} = \xi_{eff}(1 - p_e)\alpha\Delta T + k_T\Delta T = K_T\Delta T \quad (2)$$

where ξ_{eff} is a constant between zero and one, p_e is effective photo-elastic coefficient of fiber, α is thermal expansion coefficient, ΔT is the change in temperature, k_T is a constant depending on thermal coefficient and thermal optic coefficient of glass fiber, and K_T is the temperature sensitivity of the packaged FBG as a total effect of temperature induced strain and thermal expansion of glass fiber.

The temperature sensitivity was recorded to be 0.02 nm/°C. The wavelength shift trend was linear corresponding to change in temperature. The signal almost disappears at the limit of 956°C, before which signal is readable and showing linear trend (Figure 3.10 (a)).

3.1.4. Pressure Test of FBG:

The pressure test was carried out in a test setup designed to evaluate pressure sensitivity of the FBG. A hydrostatic pump Rice Hydro HP10 was used to compress water inside a chamber cell (Figure 3.11) to a limit pressure of 3000 psi. The Fiber with FBG was assembled and sealed through a hole drilled in a bolt. The results from 3 runs with max pressures of 2600, 2850 and 2900 psi were performed (See Figure 3.12). All tests show a similar trend with an adjusted gage factor (GF) from the strain experiments to scale values

to μ strains. The pressure gage resolution is 100 psi (± 50 -psi reading error). The data acquisition was carried out for incremental pressure of every 20 sec allowing recording an average of readings for each pressure value and a strain activity from FBG. The average of 3 measurements with error bars is shown in Figure 3.14. The strain sensitivity due to the pressure is $\frac{\Delta\varepsilon}{\Delta p} = 0.152667 \mu\text{e/psi}$. The sensitivity of the FBG to hydrostatic pressure can be given by equation (3) [73] as

$$\frac{1}{\lambda} \frac{d\lambda}{dP} = -\frac{1}{E} \left((1 - 2\nu) - \frac{\nu^2}{2} (1 - 2\nu)(p_{11} + 2p_{12}) \right) \quad (3)$$

Where ν is the Poisson's ratio and p_{11} and p_{12} are components of the relevant strain-optic tensor for an isotropic solid. With reference to above equation, the first part in the parenthesis relates to the change in the period of the fabricated grating planes within the fiber core, whereas the second part relates to the refractive index change as a result of the strain optic effect.

Test Summary:

Response Time to Pressure Change:	0.003 [sec/psi]
Method of Calculation:	Linear fit for all 3 tests. Average of slope and intercepts of individual tests.
Nulling Wavelength:	1529.888 [nm]

Gage Factor:

$$GF = \frac{\Delta\lambda/\lambda}{\varepsilon} = 0.134$$

Where $\Delta\lambda$ is the change in wavelength and λ is the nominal wavelength. ε is the experienced strain.

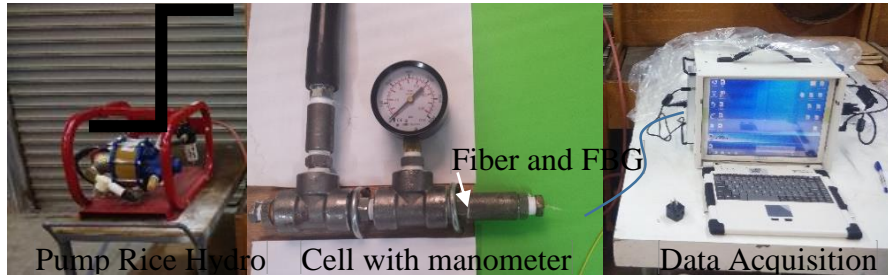


Figure 3.11 Pressure experimental setup

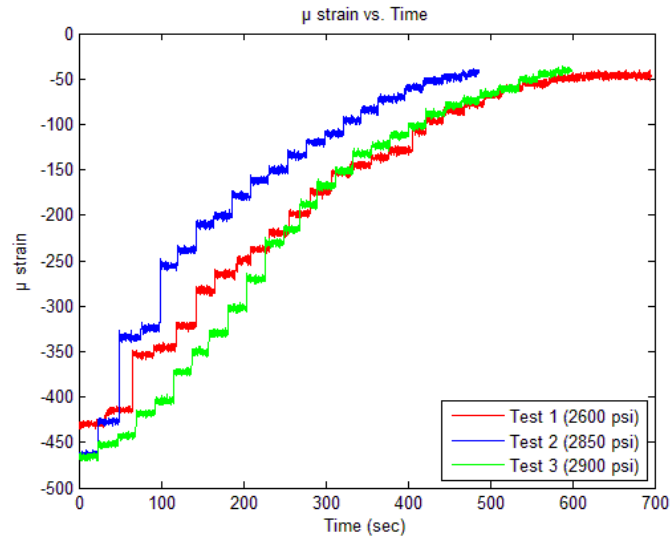


Figure 3.12 FBG strain measured with pressures reduced from 2600 [psi] (Test 1), 2850 [psi] (Test 2) and 2900 [psi] (Test 3)

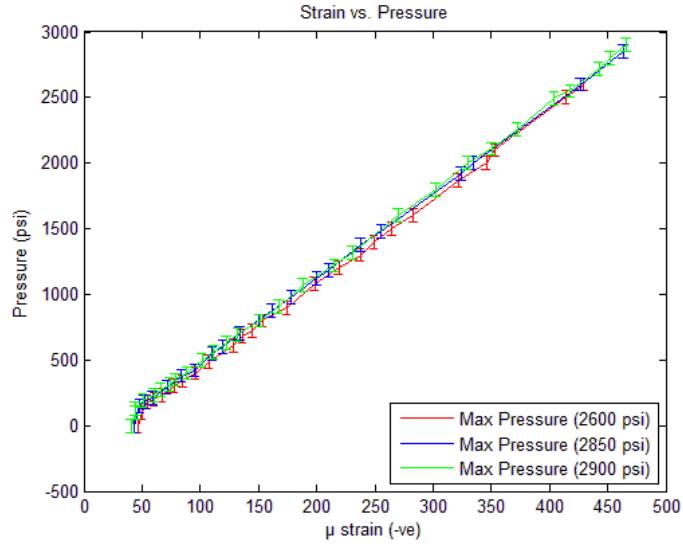


Figure 3.13 Compressive Strain vs Pressure (Error Plot ± 50 [psi])

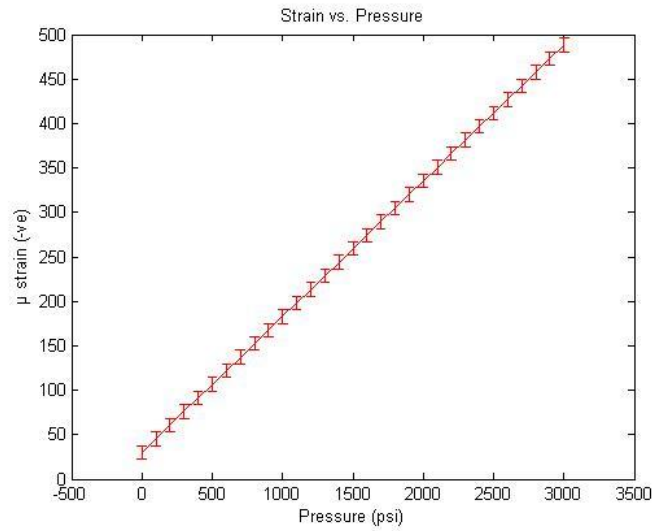


Figure 3.14 Average strain response from the three tests with ± 7.63 [$\mu\epsilon$] error

The sensitivity of the sensor to strain (Sec. 3.1.2.), temperature (Sec. 3.1.3.) and pressure (Sec. 3.1.4.) recorded for the conducted tests are summarized in Table 3.8.

Table 3.8 Summary for Strain, Temperature and Pressure Sensitivity

Measurand	Sensitivity
Strain	2.85e-4 [nm/ $\mu\epsilon$]
Temperature	2.00e-2 [nm/°C]
Pressure	3.13e-5 [nm/psi]

3.1.5. Bend Test (Corning SMF 28 Optical Fiber):

Optical fibers when carrying sensors like Fiber Bragg Grating (FBG) offer assistance in Structural Health Monitoring (SHM) of the structure. While embedded they experience hydrostatic state along with varying conditions of mechanical and thermal strain. The light transmission through the optical fiber is affected by the mentioned conditions and also the placement layouts. These layouts consists of bends to accommodate the sensors offering maximum coverage over the structure under investigation and attribute to the transmission loss. This loss leads to misinterpretation of the sensed signal and hence produce erroneous results unless corrections are made against such bend losses. An investigative method is presented to take into account two types of layout 1. Linear and 2. Circular. Multiple bends in the fiber are introduced to understand the effect of bends with an array FBG configuration for sensor coverage with a single embedded fiber.

The current work incorporates an optical fiber with multitude of bends (with layout of an array FBG) to investigate effects of bends and embedment on the loss of optical transmission. The study will help us identify the critical bend radius with the effects of

bend succession under embedment. The study applies to development of smart structures with embedded fiber optic sensors under different layouts.

Macro bending tests are performed as a standard to define the operational limits of the optical fiber and the losses due to such bends account for signal attenuation. Specialized investigative setups would require their own sets of tests to validate the performance in a new environment. Current work suggests a novel technique to investigate multiple bend scenario with embedded optical fibers. The objective is to study two different placement layouts for successive bends namely; 1. Linear and 2. Circular. This study would help identifying the critical bend radius and the corresponding power transmitted in structures with embedded optical fiber sensors. The tests for current study is performed in the following manner.

1. First, a Single Mode Fiber (Corning SMF 28) is attached to the test setup and the fiber is laid out in the linear and circular layouts.
2. Two different power inputs (Low and High) with wavelength setting at 1550 nm were given as input and the power transmitted through various bend patterns was investigated.
3. Based on the results, conclusion would be drawn on power loss due to different bend patterns.

3.1.5.1. Test Setup:

The bending of the fiber can be critical when embedded in materials as FBG arrays can be used in variety of host material with various layout shapes depending on the part e.g. square, triangle, circular etc. Hence, the corners will have sharp bending radiuses and can

result in breakage of the optical fiber causing loss in signal or low signal otherwise. The objective of this test is to evaluate the limits of bending that is under mandrel radius of 30 mm to keep fiber under proper operating conditions. The test setup is illustrated in Figure 3.15.

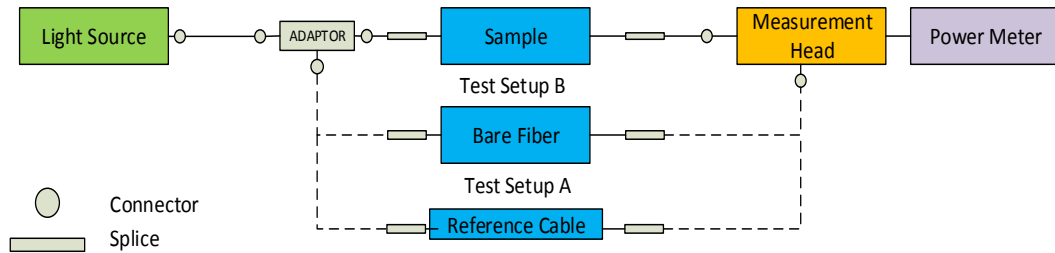


Figure 3.15 Setup configuration of the fiber optic tests with light measurement

3.1.5.2. Test 1: Individual Bend Radiuses (Circular):

This test was performed to test bend losses at different bending radiuses. The following bend radiuses of 5, 10, 15, 20, 25, 30 mm were applied on the SMF 28 as shown in Figure 3.16 (a). A broadband (1530-1565 nm) light source was transmitted through Amonics AEDFA 13-B-FA Optical Fiber Amplifier whereas the power loss was observed with an ILX Lightwave FBM 8220 Fiber Optic Power Meter. The signal loss increases with reduction of bending radiuses and becomes significant from diameter 10mm downward. It is worth mentioning that the fiber will manually break at less than 2 mm radius. This shows a clear obstruction of the light inside the fiber although relatively high power e.g. 1.61 mW was sent through. This power was measured using a reference fiber optic cable and also measured using a straight bare fiber giving 1.531 mW.

With tight bending e.g. 5 mm, the fiber optic material stretches with reduction in diameter as shown in Figure 3.16 (b) and hence light beam may split in point S and refract in various directions losing power.

Wavelength 1550 [nm]
Reference Power 1.61 [mW] (2.073 [dBm])
Bare Fiber Power 1.53 [mW] (1.842 [dBm])
Bend Radius Range 5 – 30 [mm]

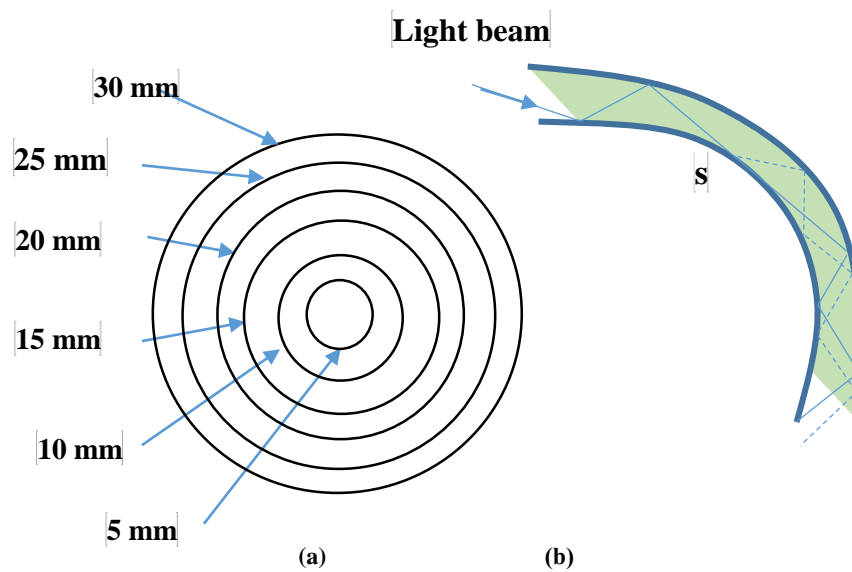


Figure 3.16 Bend pattern for (a) individual radiuses, (b) bending issue

Table 3.9 Power individual bends (Full Circle) – circular, signal Loss with different bend radiuses from 30 -

5mm

S/No.	Bend Radius [mm]	Power Out		Loss (Absolute)		Loss (Relative)		Percent Loss [%]	
		[mW]	[dBm]	[mW]	[dBm]	[mW]	[dBm]	[mW]	[dBm]
1	30	1.531	1.841	0.079	0.232	0.000	0.001	0.000	0.054
2	25	1.531	1.841	0.079	0.232	0.000	0.001	0.000	0.054
3	20	1.531	1.840	0.079	0.233	0.000	0.002	0.000	0.109
4	15	1.531	1.834	0.079	0.239	0.000	0.008	0.000	0.434
5	10	1.470	1.660	0.140	0.413	0.061	0.182	3.984	9.881
6	5	0.500	-3.050	1.110	5.123	1.031	4.892	67.342	265.581

Table 3.9 refers to the individual bend radiuses varying from 30 to 5 mm. The percentage loss does not show an increase until the bend radius as short as 10 mm is established.

3.1.5.3. Test 2: Spiral Pattern (Circular):

This spiral test was performed under similar conditions as previous test by recording bend losses with spiral progressing from 30-5 mm radius as indicated in Figure 3.17. Similar behavior was observed for power loss as shown in Figure 3.18 as expected compared to previous test since the nature of the bending is not very different.

Compared together e.g. circles and spirals, Figure 3.18 shows close power loss measurement agreement between bending in circles and in spiral with identical diameters.

Wavelength	1550 [nm]
Reference Power	1.61 [mW] (2.065 [dBm])
Bare Fiber Power	1.49 [mW] (1.732 [dBm])
Bend Radius Range	5 – 30 [mm]

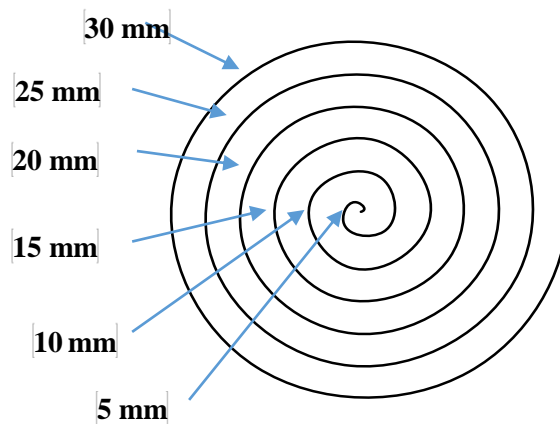


Figure 3.17 Spiral pattern for progressive bend test

Table 3.10 Power progressive bends (Full Circle) – circular, signal loss spiral pattern with progressive radiuses

S/No	Bend Radius [mm]		Power Out		Loss (Absolute)		Loss (Relative)		Percent Loss [%]	
	From	To	[mW]	[dBm]	[mW]	[dBm]	[mW]	[dBm]	[mW]	[dBm]
1	0	30	1.49	1.732	0.12	0.333	0.00	0.000	0.00	0.000
2	30	25	1.49	1.732	0.12	0.333	0.00	0.000	0.00	0.000
3	30-25	20	1.49	1.732	0.12	0.333	0.00	0.000	0.00	0.000
4	30-25-20	15	1.49	1.725	0.12	0.340	0.00	0.007	0.00	0.404
5	30-25-20-15	10	1.47	1.318	0.14	0.747	0.02	0.414	1.34	23.903
6	30-25-20-15-5	5	0.50	-6.068	1.11	8.133	0.99	7.800	66.44	450.346

Table 3.10 refers to the progressive bend radiuses varying from 30 to 5 mm. The percentage loss does not show an increase until the progressive bend radius reaches 10 mm.

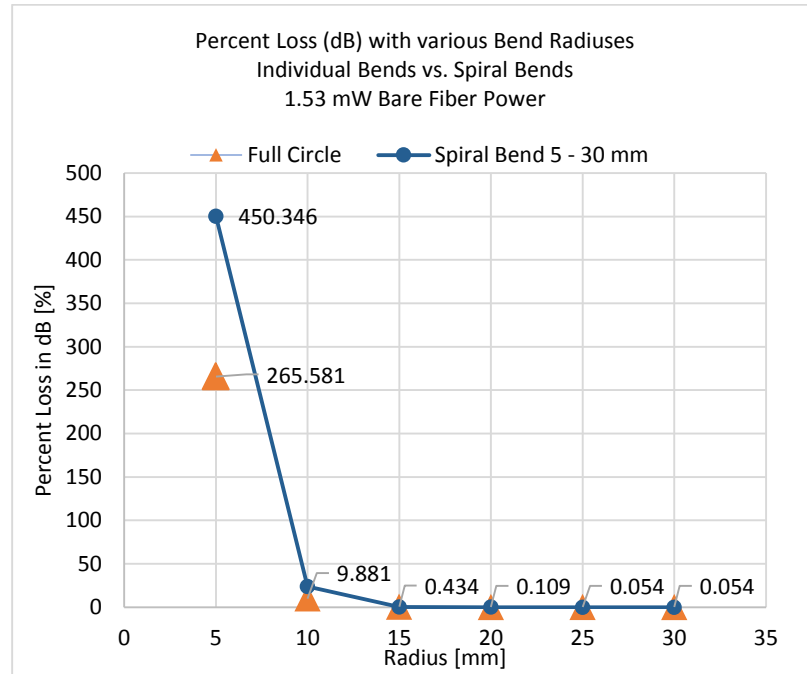


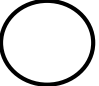


Figure 3.18 Percent loss [dBm] with various bend radiuses Individual Bends vs. Spiral Bends 1.53 [mW] Bare Fiber Power

Consecutive spiral bends tends to show a sharper increase in loss when moving to a smaller bend radius as compared to an individual circular bend of a similar size as shown in

Figure 3.18. Moreover power losses were also calculated for quarter, half and full bends as shown in Table 3.11.

Table 3.11 Bend shape comparison for power losses with bend radius 10 [mm] and power in 1.61 [mW] at 1550 [nm]

<i>Shape (Circle)</i>	<i>Power Loss [%]</i>	
	<i>[mW]</i>	<i>[dBm]</i>
 Quarter	1.316	2.423
 Half	2.516	5.602
 Full	3.984	9.881

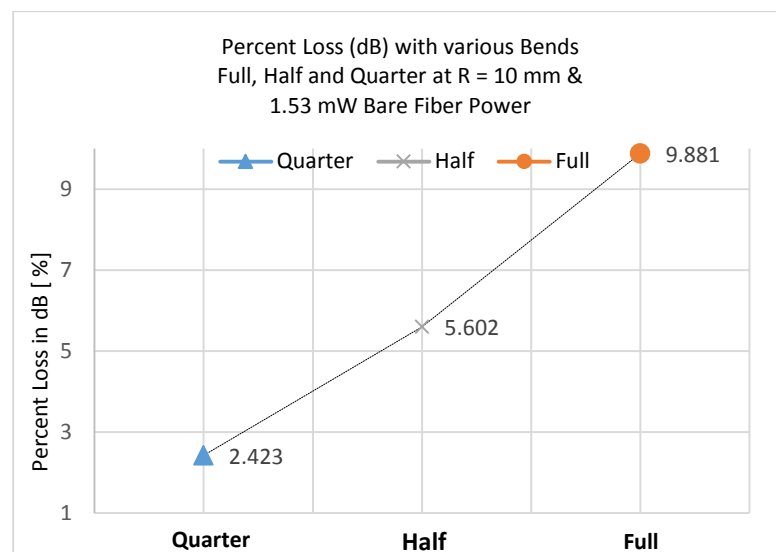


Figure 3.19 Percent loss [dBm] with Full, Half and Quarter circle bend radius (10mm) at 1.53 [mW] Bare Fiber Power

Figure 3.19 shows an increasing loss trend with bend profile moving from quarter to half to full.

3.1.5.4. Test 3: Zigzag Pattern (Linear):

The optical cable was bent in a zigzag pattern as shown in Figure 3.20. The bend radius is maintained at 10 mm and the bends were introduced progressively with 1-4 bends (Figure 3.20) and the signal loss was measured through the optical power meter. The results of the test are illustrated in Figure 3.21 showing the increase of signal loss as the number of bends increases. This test has been carried out with two level of powers (1.61 mW and 0.18 mW). It is worth noticing that interrogator usually power up the fibers at low power. It is observed that power loss is much lower with bends added to the fiber in low power compared to high power as shown in Figure 3.21. With this, it is recommended to optimize the number of bends when mapping fiber optics inside host materials.

Wavelength	1550 [nm]	
Power Range	High	Low
Reference Power	1.610 [mW] 2.059 [dBm]	0.180 [mW] -7.389 [dBm]
Bare Fiber Power	1.590 [mW] 2.017 [dBm]	0.170 [mW] -7.812 [dBm]
Bend Radius Range	10 [mm]	

Figure 3.21 shows a linear trend of power loss (low power) for increasing number of bends with a constant bend radius whereas for higher power input, bend losses tend to produce a nonlinear increase in power loss.

The losses for spiral bends increases exponentially beyond the 10 mm radius mark whereas the bend loss with an independent bend radius of less than 10 mm also shows an increasing

trend. While increasing the number of bends from 2 to 3 with constant bend radius of 10 mm, the losses start to increase drastically as shown in Figure 3.22.

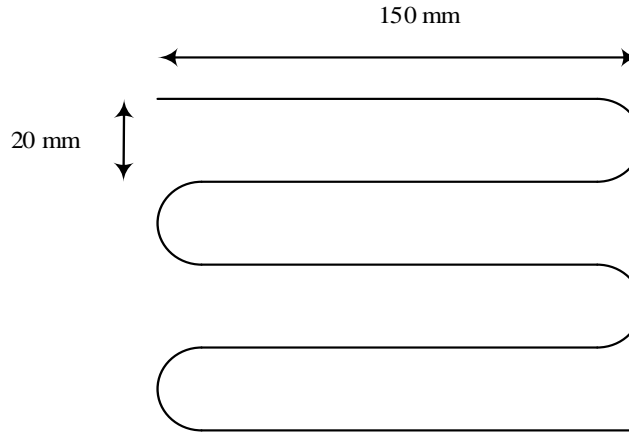


Figure 3.20 Zigzag pattern for bending test

Table 3.12 Signal loss zigzag pattern with multiple bends at R=10mm, a) high power, b) low power.

<i>Power Level</i>	<i>No. of Bends</i>	<i>Power Out</i>		<i>Loss (Absolute)</i>		<i>Loss (Relative)</i>		<i>Percent Loss (%)</i>	
		<i>[mW]</i>	<i>[dBm]</i>	<i>[mW]</i>	<i>[dBm]</i>	<i>[mW]</i>	<i>[dBm]</i>	<i>[mW]</i>	<i>[dBm]</i>
<i>High</i>	1	1.550	1.904	0.060	0.155	0.040	0.113	2.516	5.602
	2	1.520	1.814	0.090	0.245	0.070	0.203	4.403	10.064
	3	1.470	1.675	0.140	0.384	0.120	0.342	7.547	16.956
	4	1.450	1.617	0.160	0.442	0.140	0.400	8.805	19.831
<i>Low</i>	1	0.160	-7.860	0.020	0.471	0.010	0.048	5.882	0.614
	2	0.160	-7.941	0.020	0.552	0.010	0.129	5.882	1.651
	3	0.160	-8.042	0.020	0.653	0.010	0.230	5.882	2.944
	4	0.150	-8.142	0.030	0.753	0.020	0.330	11.765	4.224

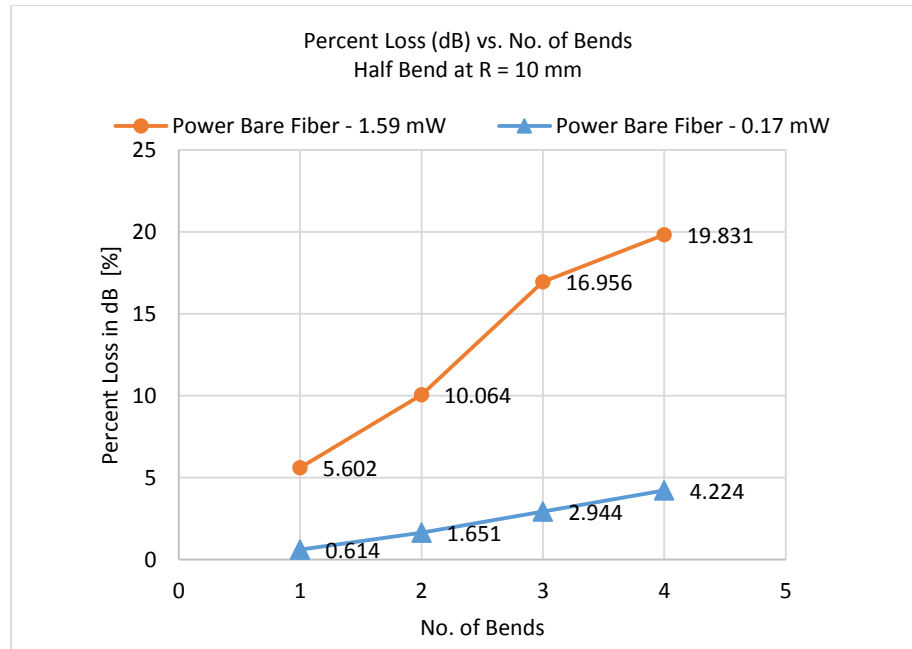


Figure 3.21 Percent Loss [dBm] with increasing number of bends (Bend Radius 10 [mm]) at low and high power input

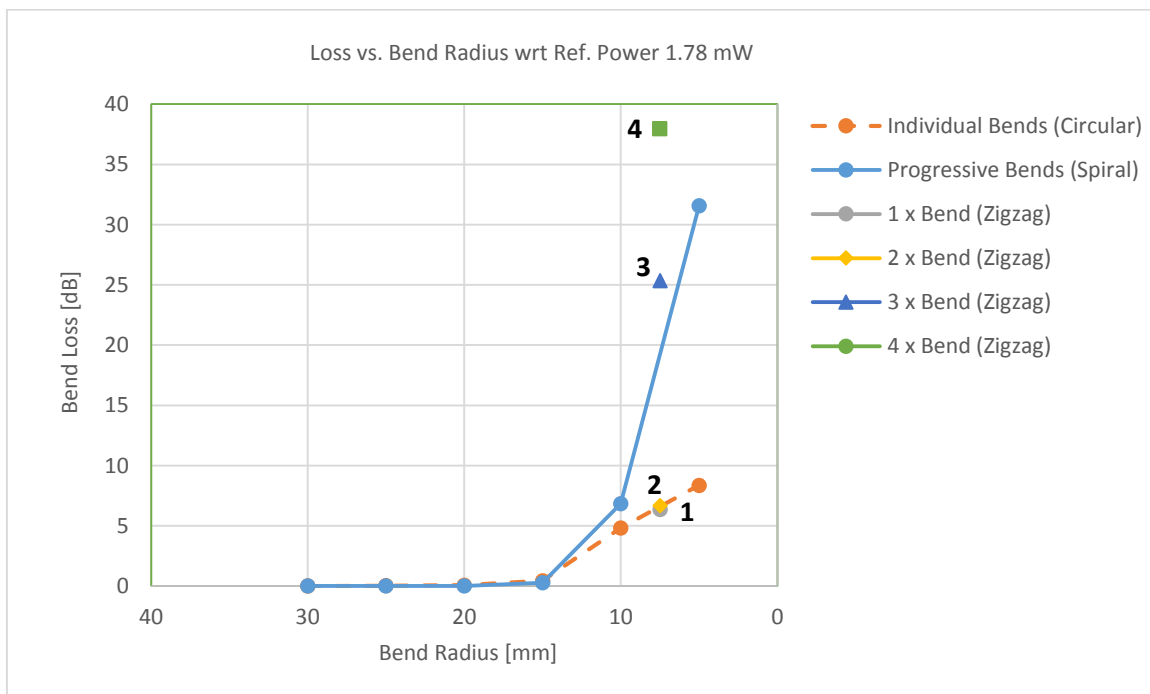


Figure 3.22 Comparison of power loss between Individual/progressive bends and the zig zag pattern on account of number of bends

3.2. FBG Calibration against LVDT:

A calibration study was performed for a cantilever beam with FBG embedded in a slot of 0.5 x 0.5 mm square running through the length of an aluminum beam (Figure 3.23). The purpose of this test is to compare and calibrate the FBG response in relation to Linear Variable Differential Transducer (LVDT) and Strain Gage activity. Also the prediction for modulus of Elasticity of the beam will give confidence to use calibration/gage factor (G.F.) in order to do further experimental investigation. The embedding was achieved using Loctite Epoxy Glue. The calibration was performed with the aid of strain gages and LVDT. In addition to previously obtained data for FBG G.F. under non-embedded conditions, we would like to see the effect of embedded conditions on the G.F.

3.2.1. Objective:

To find a calibration factor for FBG from the true displacement (LVDT Sensor) for known strains (Strain Gage).

3.2.2. Problem Description:

A cantilever beam with given dimension is loaded 25 mm from free end by weights 150, 250 and 350 g. The loading is achieved with a thread of negligible mass establishing a line contact. There are 3 strain gages (S1, S2 and S3) to record the strain at the shown location. The LVDT is used at positions $x=7.75$ mm (location of S1), $x=50$ mm (location of S2) and $x=100$ mm (tip of the beam) to read displacements upon loading as shown in Figure 3.23. Figure 3.24 shows the test setup developed to perform calibration studies.

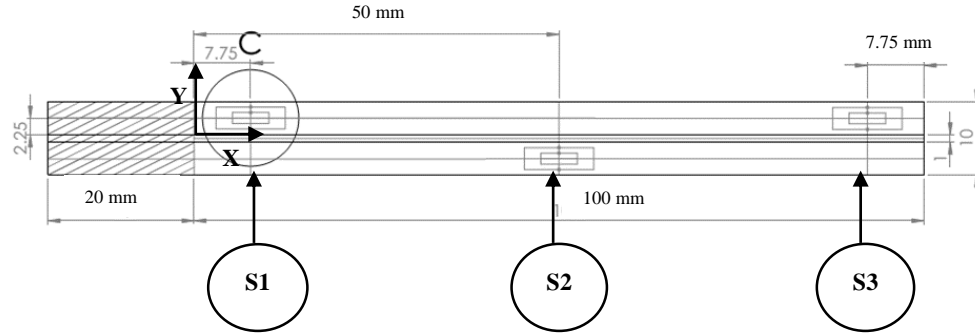


Figure 3.23 Beam with strain gage locations highlighted, FBGs are placed in slot next to the strain gages

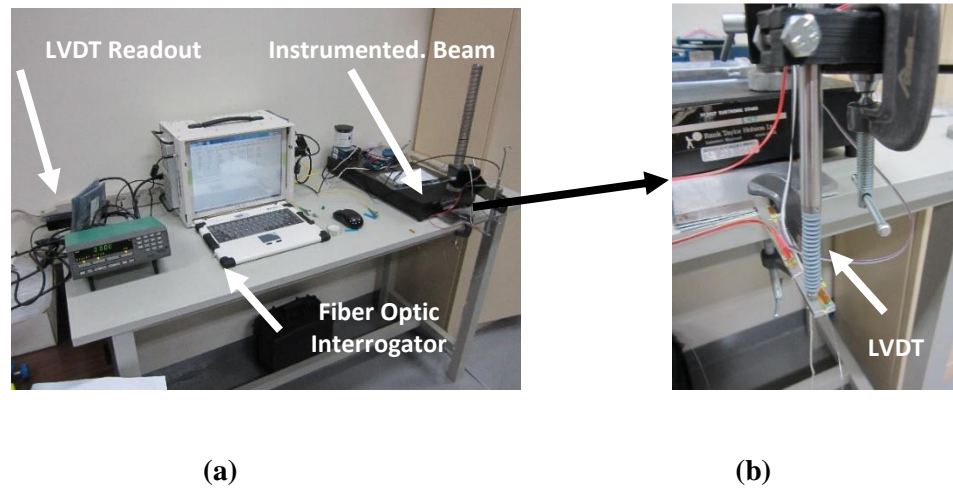


Figure 3.24 (a) Test setup for calibration, (b) instrumented beam with LVDT sensor on top

3.2.3. Test Description:

The test strain data was collected from strain gages and the LVDT. Later on the results were compared with analytical and FEM (COMSOL/ANSYS) solutions.

3.2.4. Analytical Solution:

Figure 3.25 shows the load 'P' applied at a distance 'a' from the fixed end of the cantilever beam. Table 3.13 shows the load conversion from grams to Newton. The following properties were used in the analytical calculations expressed in equation (4).

Distance of gage S1 & S2 from fixed end [m]	x	0.0075, 0.05
Applied Load [N]	P	
Distance btw gage center and P [m]	L	0.06725, 0.0425
Location of gage above NA [m]	c	1.53E-03
Moment of Inertia [m ⁴]	I	2.14E-11
Modulus of Elasticity [Pa]	E	7.0E+10
Distance of Load from fixed end [m]	a	0.075
Distance of Load from free end [m]	b	2.50E-02

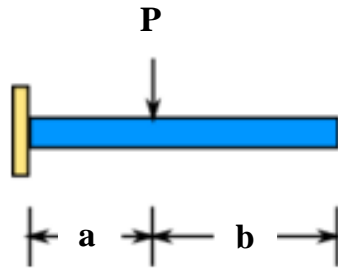


Figure 3.25 Load location on the cantilever beam

Table 3.13 Load conversion from [grams] to [Newton]

Load Approx. [g]	P-Load [N]
150.00	1.49
250.00	2.49
350.00	3.48

3.2.5. Theoretical Displacement:

Theoretical displacements for segment ‘a’ and segment ‘b’ can be separately calculated by

$$\delta_a = \frac{Px^2}{6EI}(3a - x)$$

$$\delta_b = \frac{Pa^2}{6EI}(3x - a) \quad (4)$$

Where ‘a’ is the segment to the left of the applied load ‘P’ and ‘b’ is to the right. The purpose to calculate theoretical displacement is to later compare the sensor based displacements to the ones obtained theoretically.

3.2.6. Theoretical Strain (Gage Location):

Theoretical strain in the beam experiencing bending moment can be shown by equation (5)

$$\varepsilon = \frac{PLc}{EI} \quad (5)$$

3.2.7. Indirect Measurements:

The purpose of taking indirect measurements is to cross check strain results from displacement data (LVDT) and displacement results from strain data (Strain Gage). Indirect measurements for strain and displacements taken against LVDT and Strain Gages are summarized in Table 3.14.

Table 3.14 Analytical formulas for strain and displacement

Sensor	Measurand	Analytical Formula
LVDT	Strain	$\varepsilon = \frac{6 Lc\delta_a}{x^2(3a - x)}$
Strain Gage	Displacement	$\delta_a = \frac{\varepsilon x^2(3a - x)}{6 Lc}$

Using the theoretical displacement formula, the unknown modulus ‘E’ was calculated as

$$E = \frac{Pa^2}{6I\delta_b}(3x - a) \quad (6)$$

Which is based on the results and was calculated to be

Modulus of Elasticity ‘E’= 70 [GPa]

NOTE: Calibration Factor used for S1 and S2 are 0.65 for Strain Gage and 1.52 for FBG.

Both the calibrations are calculated based on the readings from LVDT at S2. Test summary is presented in Table 3.15.

Table 3.15 Data calculated for LVDT, Strain gage and FBG

Sensor No.	Force [N]	Analytical δ [μm]	FEM δ [μm]	LVDT δ [μm]	ϵ _Analytical [$\mu\epsilon$]	ϵ _LVDT [$\mu\epsilon$]	ϵ _Strain Gage [$\mu\epsilon$]	ϵ _FBG [$\mu\epsilon$]
S1	0.1	2.03	2.28	6.00	102.52	94.70	150.00	90.08
	0.2	3.39	3.80	11.00	170.87	173.62	192.18	153.77
	0.3	4.74	5.32	16.00	239.21	252.54	224.46	225.07
S2	0.1	72.65	72.06	74.00	38.11	38.82	49.71	37.30
	0.2	121.09	120.11	126.00	63.52	66.10	66.07	68.51
	0.3	169.52	168.16	178.00	88.93	93.37	76.61	93.89
S3	0.1	210.17	208.00	182.00	N/A	N/A	-	2.17
	0.2	350.29	347.00	315.00	N/A	N/A	-	4.91
	0.3	490.41	486.00	436.00	N/A	N/A	-	0.36

Here strain gage S1 is located 7.75 mm from fixed end, gage S2 is 50 mm from fixed end and gage S3 is located 7.75 mm from the free end.

NOTE: Analytical Strain cannot be calculated at S3 as theoretical solution is applicable between fixed end and the load application point. Position of S3 is beyond load location near the free end. Strain Gage at S3 did not record data.

After obtaining the G.F., we are now in position to proceed with the experimental tests on the beam structure.

3.3. Conclusion:

The various tests carried out in this study have shown limitations not to exceed while keeping the integrity of the fiber optics. This gathered information would be useful in the design process of the nervous materials while embedding the fiber optics at the subsurface of the materials. It is expected that the fiber optic will fully report on the geometry change (bending) of the host part. All of these aspects are important for the study to prepare the fiber optic sensors that are embedded inside various materials to protect the sensors and to sense particular measurand from within the material. It is planned to add actuators along with the sensors to develop nervous materials for future work.

The tests were conducted to evaluate fiber optic performance in tensile loading, under different bending conditions and characterization for FBGs in terms of their sensitivity to strain and temperature. Different loading conditions such as heat and mechanical strain would influence the sensor output whether applied individually or combined. These characterization results would greatly benefit the proper deployment of the fiber optic

sensors inside a functional part allowing the extraction of critical information for the future smart structures. It is noted that limitation in terms of light transmission exist with multiple bending to be observed.

A calibration study was performed on a sample cantilever beam to utilize the extracted gage factor from the strain test and to evaluate the sensor in an embedded state (glued in to the slot). Calibration was done with reference to LVDT sensor that would give the displacement information relatable to strain at the sensor location.

After establishing practical considerations for embedding FBG sensors, we now converge to the issue of sensor placement for force prediction. Apart from the layout strategies mentioned previously, sensor positioning in key locations will be evaluated based on the dynamic characteristics of the structure obtained from a Finite Element Model. Discussion on feasible/optimum sensor selection will be discussed in the following chapter.

CHAPTER 4

SENSORS PLACEMENT TECHNIQUES

Optimal sensor placement (OSP) is a term frequently used nowadays in current research [41–45] which aims at introducing sensors with optimum positions to a system in order to observe the system status. OSP is a very demanding objective to design Structural Health Monitoring (SHM) systems as some systems would like to be installed with sensors in fixed position throughout their life time. One of the possibility is to have them embedded inside the structure which needs careful observation as the sensors need to extract desired information such as strain, temperature and pressure from critical locations.

OSP problems have been implemented with swarm algorithms recently and have shown tremendous research potential. These algorithms have helped install minimum sensors for vibration observation in bridge structures [42,43]. Also damage selection through optimal sensor in a cantilever beam were studied in [46] and improvement in swarm algorithms was implemented with sonar sensors in [47]. Swarm optimization is a computational method that optimizes a problem through iterative procedures to improve a candidate solution with regards to a certain defined objective. The objective can be accurate shape reconstruction or identifying the applied input to the system. Swarm technique solves a problem by having a population of candidate solutions (called particles) and moving these particles around in the search space towards the best solution. These techniques are based on artificial intelligence and requires some times intensive computations. Similarly researchers have also incorporated genetic algorithm (GA) for optimal sensor placement schemes [41,48].

Earlier attempts on Placement Index solutions to find optimal sensor placement have been presented in [45,49]. The potential of D-Optimal method for sensor/actuator placement studies are illustrated in [50,51].

The current work highlights the optimal embedded sensor placement techniques based on comparison of 1) Sensing/Control and 2) Numerical based optimization strategies. A list of similar attempts are mentioned in [74] where comparison of model reduction techniques from structural dynamics, numerical mathematics and systems and control have been summarized. To implement the above, we choose a) Placement Index and 2) D-Optimal method for sensor placement. The first method is based on identifying system norms which serve as a measure of intensity of a system's response to standard excitations, such as unit impulse, or white noise of unit standard deviation. Latter starts with strain extraction from predetermined load cases using the Finite Element Method. This method is useful when analytical/closed form solutions are not available in order to identify system. The sensor locations with minimum variance in force prediction are selected by calculating the strain response at candidate sensor locations due to a unity load. A Design of Experiment (DOE) tool, D-Optimal Method has been employed to minimize error in force prediction with least number of sensors. Both of the above methods operate on prior information of force application position(s).

The selected sensing article is an FBG (Fiber Brag Grating) sensor is capable to measure inline strain through pressure, mechanical and thermal means. The method is proposed to assist in optimal placement for the sensor in embedded conditions. For this reason two different placement criteria are observed whether both solutions are identical or otherwise. In the following passage, we now discuss the optimum sensor placement.

4.1. Optimum Sensors Placement:

The objective of the current work is to find the optimum number of strain sensors in order to predict magnitude of the static and dynamic load along with its acting position on the structure. The structure types under consideration are beams and plates. The sensors would also allow us to observe a set of structural modes when excited by a time varying load. The criteria for optimality is based on the true prediction of the structural shape determined by the strain sensors. The strain information collected from the sensors will allow us to convert it into the displacement of the structure. The displacement at positions other than the sensor positions need to be predicted in order to construct the complete structure shape.

To determine the optimum sensors placement, we would evaluate two different techniques namely a) Placement Index and b) D-Optimal Method. By comparing the two methods, we would like to obtain a better force prediction, sensor placement method.

4.1.1. Optimization via Placement Index:

The objective of the placement index is to observe the norm contribution from the sensor placement and excitation source. Thus prior information of force location is essential to define the problem and proceed with the solution procedure. System norms serve as a measure of intensity of its response to standard excitations, such as unit impulse, or white noise of unit standard deviation. The standardized response allows comparing different systems.

This specific method for optimum sensor placement ensures a balanced scheme where the system is equally observable and controllable meaning the locations are well suited to sense and actuate. The placement index also gives benefit in actuator placement strategy for a

given loading condition to respond to changing external stimulus. The gain calculation based on the placement criterion also helps to suggest required gain to either control the vibrations or an instant resistance to change in the structure when using actuators like Polyvinylidene difluoride (PVDF).

Objective function defined for optimal placement is based on the properties of two norms H_2 and H_∞ and calculations are done for large structures with high model order. Approach represented here is a suitable method for optimal actuator and sensor placement in large structures. This method is computationally less intensive.

The second order linear time invariant system can be expressed in the form

$$[M]\{\ddot{x}(t)\} + [C]\{\dot{x}(t)\} + [K]\{x(t)\} = \{f(t)\} \quad (7)$$

The state space representation can be shown for a linear time invariant system as

$$\begin{aligned} \dot{x} &= Ax + Bu \\ y &= Cx + D_{damp}u \end{aligned} \quad (8)$$

$$A = \begin{bmatrix} 0 & I \\ -M^{-1}K & -M^{-1}D_{damp} \end{bmatrix}$$

$$B = \begin{bmatrix} 0 \\ B_0 \end{bmatrix} \quad (9)$$

$$C = [C_{0q} \quad C_{0v}]$$

Equation (9) is a nodal representation of the structure with mass matrix $[M]$, damping matrix $[D_{damp}]$ and stiffness matrix $[K]$. Also A is the system matrix, B the input matrix, C is the output matrix with C_{0q} and C_{0v} as the nodal displacement and velocity vector respectively. D is the feedback matrix normally set equal to zero, x and u are the state and input vectors respectively whereas y is the output vector. Conversion of a nodal system to

a modal system reduces computational effort when modal reduction is utilized. The modal representation of the above matrices can be shown as

$$\begin{aligned}
 A_{mi} &= \begin{bmatrix} 0 & \omega_i \\ -\omega_i & -2\xi_i\omega_i \end{bmatrix} \\
 B_{mi} &= \begin{bmatrix} 0 \\ b_{mi} \end{bmatrix} \\
 C_{mi} &= \begin{bmatrix} \frac{C_{mqi}}{\omega_i} & C_{mvi} \end{bmatrix}
 \end{aligned} \tag{10}$$

Here ω_i and ξ_i are the i th natural frequency and damping ratio respectively. The entries b_{mi} , c_{mqi} and c_{mvi} are the i th input, displacement and velocity output to the system. The expressions can be calculated from the description of the full system by

$$B_m = M_m \Phi^T B_0, \quad C_{mq} = C_{0q} \Phi, \quad C_{mv} = C_{0v} \Phi \tag{11}$$

Here Φ is the mode shape matrix, B_m is the modal input matrix, B_0 the nodal input matrix and the modal mass matrix $M_m = \Phi^T M \Phi$.

4.1.1.1. Norms of Single Mode:

Norms for a single mode, and a structure with a set of actuators and sensors are explained below

4.1.1.1.1. H₂ norm of a single mode: The i th mode transfer function of the system is given by $G_i(\omega) = \mathbf{C}_{mi}(j\omega\mathbf{I} - \mathbf{A}_{mi})^{-1}\mathbf{B}_{mi}$, the H₂ norm of single mode is given by:

$$\|G_i\|_2 = \frac{\|b_{mi}\|_2 \|c_{mi}\|_2}{2\sqrt{\xi_i}\omega_i} \tag{12}$$

4.1.1.1.2. H_∞ norm of a single mode: H_∞ norm of the i th mode system with (A_{mi}, B_{mi}, C_{mi}) along with parameters $(\omega_i, \xi_i, b_{mi}, c_{mi})$ is given by

$$\|G_i\|_\infty = \frac{\|b_{mi}\|_2 \|c_{mi}\|_2}{2\xi_i \omega_i} \quad (13)$$

4.1.1.2. Norms of a Structure:

4.1.1.2.1. H_2 norm of a structure: H_2 norm of the structure with A_m, B_m, C_m is given by the root mean square of all the modal norms as

$$\|G\|_2 \cong \sqrt{\sum_{i=1}^n \|G_i\|_2^2} \quad (14)$$

where n represents the number of the modes, and G and G_i are the transfer function matrix of the structure and the i th mode, respectively.

4.1.1.2.2. H_∞ norm of a structure: It is approximately determined by the largest mode norms

$$\|G\|_\infty \cong \max \|G_i\|_\infty, \quad i = 1, \dots, n \quad (15)$$

Additive property holds for the H_2 and H_∞ norms for both a single mode and for a structure in case of a system including a set of actuators and sensor.

4.1.1.2.3. H_2 and H_∞ norms of a system with a set of actuators and sensors:

Norms corresponding to a single mode (i) and for a structure are given by

$$\|G\|_{2,\infty} \cong \sqrt{\sum_{j=1}^p \|G_{ij}\|_{(2,\infty)}^2}, \quad i = 1, \dots, n \text{ and } j = 1, \dots, p \quad (16)$$

Index i is the i th mode and should be omitted when dealing with the norm for a whole structure. Here p represents the number of actuators(s) or the number of sensors(r) and for a general case ($s \neq r$). Optimal locations are selected from a subset out of a given set of possible candidate locations. The candidate locations set consists of elements greater than the subset of locations to be optimized. Placement indices and matrices are defined to solve the actuator and sensor placements independently. Mode i norms are determined based on appropriate input (B_{mi}) and output (C_{mi}) matrices. If s represents the total number of defined inputs (actuators) $j = 1, \dots, s$, and r the total number of outputs (sensors) $k = 1, \dots, r$, the input and output matrices are shown to be

$$\begin{aligned} B_{mi} &= [B_{mi}^1 \quad B_{mi}^2 \quad \dots \quad B_{mi}^j \quad \dots \quad B_{mi}^s], \\ C_{mi}^T &= [C_{mi}^1 \quad C_{mi}^2 \quad \dots \quad C_{mi}^k \quad \dots \quad C_{mi}^r] \end{aligned} \quad (17)$$

Matrix B_{mi}^j is a 2×1 block of the j th actuator and C_{mi}^k is a 1×2 block of the k th sensor. Norm of a mode with a set of actuators (sensors) can be approximated by

$$\|G_i\|_{(2,\infty)}^2 \cong \sum_{j=1}^p \|G_i^j\|_{(2,\infty)}^2 \quad (18)$$

here $p = s$ (s —number of actuators) if dealing with actuators and $p = r$ (r —number of sensors) for sensors.

the i th mode H_2 norms with a single actuator corresponding to the j th position, and of the i th mode with a single sensor corresponding to the k^{th} position are given, respectively, by

$$\begin{aligned}\|G_i^j\|_2 &\cong \frac{\|B_{mi}^j\|_2 \|C_{mi}\|_2}{2\sqrt{\xi_i \omega_i}}, \\ \|G_i^k\|_2 &\cong \frac{\|B_{mi}\|_2 \|C_{mi}^k\|_2}{2\sqrt{\xi_i \omega_i}}\end{aligned}\tag{19}$$

Similarly the i th mode H_∞ norms of a single actuator corresponding to the j th position, and of a single sensor corresponding to the k th position can be shown as:

$$\begin{aligned}\|G_i^j\|_\infty &\cong \frac{\|B_{mi}^j\|_2 \|C_{mi}\|_2}{2\xi_i \omega_i}, \\ \|G_i^k\|_\infty &\cong \frac{\|B_{mi}\|_2 \|C_{mi}^k\|_2}{2\xi_i \omega_i}\end{aligned}\tag{20}$$

The optimal placement has been represented by Placement indices depending on H_2 or H_∞ norms for actuator and sensor placement. Index $\eta_{i(2,\infty)}^k$ evaluates the k th actuator (or sensor) for an i th mode in terms of the H_2 or H_∞ norm where $i = 1, \dots, n$, actuators $k = 1, \dots, s$ (or sensors $k = 1, \dots, r$)

$$\eta_{i(2,\infty)}^k = \frac{\|G_i^k\|_{(2,\infty)}}{\|G\|_{(2,\infty)}}\tag{21}$$

Where $\|G_i^k\|_{(2,\infty)}$ are determined accordingly and the transfer function G of the system is inclusive of candidate actuators (or sensors). The placement matrices for each norm type are represented as

$$N_{(2,\infty)} = \begin{bmatrix} \eta_{1(2,\infty)}^1 & \eta_{1(2,\infty)}^2 & \cdots & \eta_{1(2,\infty)}^k & \cdots & \eta_{1(2,\infty)}^p \\ \eta_{2(2,\infty)}^1 & \eta_{2(2,\infty)}^2 & \cdots & \eta_{2(2,\infty)}^k & \cdots & \eta_{2(2,\infty)}^p \\ \cdots & \cdots & \vdots & \cdots & \vdots & \cdots \\ \eta_{i(2,\infty)}^1 & \eta_{i(2,\infty)}^2 & \cdots & \eta_{i(2,\infty)}^k & \cdots & \eta_{i(2,\infty)}^p \\ \cdots & \cdots & \vdots & \cdots & \vdots & \cdots \\ \eta_{n(2,\infty)}^1 & \eta_{n(2,\infty)}^2 & \cdots & \eta_{n(2,\infty)}^k & \cdots & \eta_{n(2,\infty)}^p \end{bmatrix} \quad (22)$$

Each row of the placement matrix corresponds to the i th mode and each column to the k th actuator or sensor, and $p=s$ (for s actuators) or $p=r$ (for r sensors). Objective function in terms of the H_2 norm with actuator ‘a’ or sensor ‘s’, placement indices can be determined as root mean square sum of the column wise elements.

$$\eta_{(a,s)}^k = \sqrt{\sum_{i=1}^n (\eta_i^k)^2}, \quad k = 1, \dots, p \quad (23)$$

And $p=s$ (for s actuators) or $p=r$ (for r sensors). Objective function in terms of the H_∞ norm, the actuator/sensor placement index is the largest index over all modes

$$\eta_{(a,s)}^k = \max(\eta_i^k), \quad i = 1, \dots, n \quad k = 1, \dots, p \quad (24)$$

Where again $p=s$ (for s actuators) or $p=r$ (for r sensors). The placement indices $\eta_{(a,s)}^k$ determined highlights the importance of the k th actuator or sensor and acts as a criterion to place actuator/sensor individually.

In case of simultaneous placement, the placement index for an actuator or sensor is represented as

$$\eta_i^{jk} = \frac{\|G_i^{jk}\|}{\|G_m^i\|}, \quad i = 1, \dots, n \quad (25)$$

For each mode i , G_i^{jk} represents simultaneously placed actuator at the j th candidate location and of the sensor at the k th candidate location.

Above describes the mathematical formulation behind the placement index and the assessment is based on the concepts of control systems where the objective is to have a balanced system (equally controllable and observable). The balanced realization comes from the fact that the modal model produce Hankel Singular Values which are diagonally dominant. Proofs have shown that modal models are almost balanced [49].

Another advantage of utilizing the above technique is the determination of an actuator profile. The purpose to mention actuators here is that it will enable the future researchers to extend the utilization of the mentioned technique to develop SMART structures with an actuation capability.

4.1.2. Actuator Feasibility (PVDF Position, Gain and Shape Design):

Based on the analysis of Balanced systems (equally controllable/observable), candidate actuator positions for vibration suppression can be identified. Since in the case of collocated sensors and actuators, having sensors embedded allows the actuator to be applied on either side of the structure externally. Also from D-Optimal method, the strain sensors are not positioned according to the Placement Index results for displacement sensors. So as a result we have a non-collocated sensor/actuator combination.

Looking at modal actuators independently activated by the output of the strain sensors, one can utilize the benefit of running the optimal sensor/actuator placement through Placement Index method. While identifying Polyvinylidene difluoride (PVDF) as a candidate actuator for our current design, the actuator gains and locations can be implemented as a width shaped piezoelectric film. One of the advantages of using Placement Index is to excite not only a single mode but a selection of set of modes.

By setting Hankel singular values equal to 1 for modes to be excited and 0 for the rest unexcited modes leads us to arrive at the required modal actuators. Considering n_m modes out of n system modes and also assigning a zero (0) value to the i^{th} row b_{mi} of the modal input matrix B_m makes the i^{th} mode unexcited.

Given a modal matrix B_m , the nodal matrix B_0 can be derived in the following manner

$$B_m = RB_0 \quad (26)$$

Where

$$R = M_m^{-1}\Phi^T \quad (27)$$

The selected modes are controllable if the rank of R is nm , then the least square solution is given by

$$B_0 = R^+ B_m \quad (28)$$

In the above equation R^+ is pseudoinverse of R , $R^+ = V\Sigma^{-1}U^T$, where U , Σ and V are obtained from singular value decomposition of R i.e. $R = U\Sigma V^T$

The input matrix B_0 that defines the modal actuator can be determined also from

$$B_0 = M\Phi B_m \quad (29)$$

The result of implementing the above formulation is graphically presented in Figure 4.2 (a) with actuator gain profile over a Clamped-Clamped Beam (beam details illustrated in the following chapter, See Figure 4.1). A F.E. description of the structure with 60 elements and a known unit impulse load applied at node 40 of the structure, the piezo electric actuator shape in terms of its width is illustrated in Figure 4.2 (b). The '+' and '-' signs indicate the charge on the actuator in order to provide a specific mode shape.

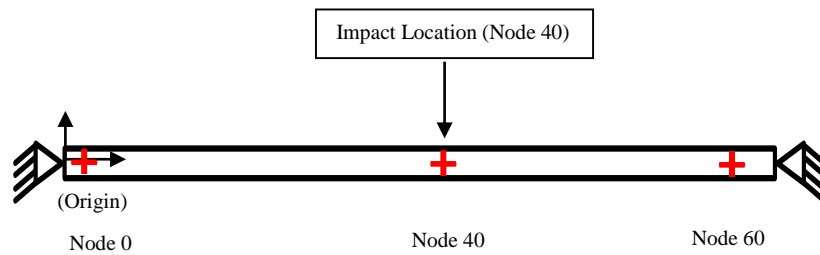
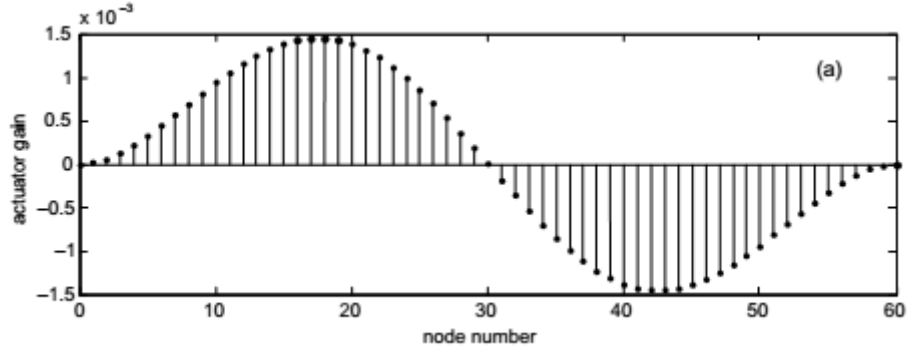
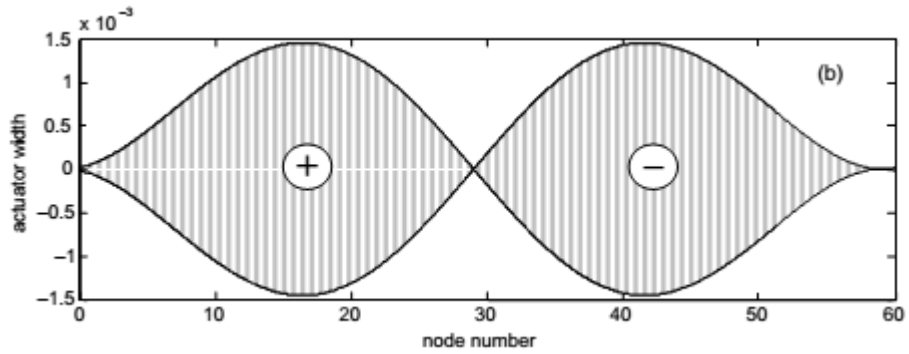


Figure 4.1 Load position on a clamped-clamped beam



(a)



(b)

Figure 4.2 (a) Actuator gain profile along the beam length, (b) Piezo electric actuator width profile to accomplish gains in (a)

With the description of the Placement Index technique, we now look into another technique for comparison and additional benefits achieved for force localization by the name of D-Optimal Method.

4.1.3. Optimization via D-Optimal Method:

The term D-Optimal means optimization through determinant maximization. We will look into the determinant types that would be considered for the D-Optimal Method in the following sections.

4.1.3.1. Static Load Identification:

For current study the matrix whose determinant needs to be maximized is constructed with matrix $[A]$ for static case and matrix $[\psi^e]$ for dynamic case where $[A]$ is a matrix with strain response at all candidate locations subjected to a unit load and $[\psi^e]$ is matrix of modal strains.

One method to recover Static loads is by using the equation below.

$$\{\varepsilon\} = [A]\{f\} \quad (30)$$

Where $\{\varepsilon\}$ is the strain vector of dimension $g \times 1$, where g is the required no of optimal sensors to recover the static load. Here $g \geq n_f$ (n_f is number of forces to be evaluated). It is assumed that this problem is linear and rules of superposition applies.

$[A]$ is a matrix of dimension $g \times n_f$, where each element a_{ij} represents the strain at location 'i' due to a unit load at 'j'. This matrix can be evaluated by collecting strain information at candidate sensor locations (accessible locations where sensors are not in direct contact with the applied load) with unit load applied at those points. The strain collection was done with the help of an FEM based software COMSOL.

$\{f\}$ is of the dimension $n_f \times 1$, where n_f represents the number of forces to be evaluated.

By the inverse principle we can write

$$\{f\} = ([A]^T[A])^{-1}[A]^T\{\varepsilon\} \quad (31)$$

In order to reach an optimal design, a Design of Experiment (DOE) tool called D-Optimal Design was used. This tool is available in MATLAB and can be used if we have a candidate

set 'C'. From the candidate set C, we form an optimum [A] such that the variance-covariance matrix is minimized given by

$$var(\{f\}) = \sigma^2([A]^T[A])^{-1} \quad (32)$$

In practice, the strain vector is prone to measurement errors. We have assumed here that errors in strain measurements are independently and identically distributed and the standard deviation of each of them is σ .

The D-Optimal design works towards maximizing the determinant $|[A]^T[A]|$ which would eventually lead to reduce the variance of $\{f\}$ to accurately estimate the applied load.

4.1.3.2. Dynamic Load & Mode Identification:

Known the dynamic equation of motion for a structure from equation (7)

$$[M]\{\ddot{x}(t)\} + [C]\{\dot{x}(t)\} + [K]\{x(t)\} = \{f(t)\}$$

The displacement of the structure $x(t)$ are related to the strains $\varepsilon(t)$ by the relation

$$\{\varepsilon(t)\} = D\{x(t)\} \quad (33)$$

It can be further shown that

$$\{\varepsilon(t)\} = [\psi^\varepsilon]\{q(t)\} \quad (34)$$

Where $[\Psi^\varepsilon]$ is the modal strain matrix. Since not all the modes can be accommodated and we can use reduction/truncation techniques such as Craig Bampton or the System Equivalent Reduction Expansion Process (SEREP), the solution can be expanded for the

unknown degrees of freedom to get a complete stress/strain profile. The reduced form due to limited sensor information, the above expression can be written as

$$\{\varepsilon(t)\} = [\tilde{\psi}^\varepsilon]\{\tilde{q}(t)\} \quad (35)$$

With reduced modal strain matrix, we have $\{\tilde{q}(t)\}$ defined here as the Modal Participation Factor (MPF). It is desired to determine the MPF with $[\tilde{\psi}^\varepsilon]$ known and measured $\{\varepsilon(t)\}$ with the least square estimate of the MPF as

$$\{\tilde{q}(t)\} = \left([\tilde{\psi}^\varepsilon]^T [\tilde{\psi}^\varepsilon]\right)^{-1} [\tilde{\psi}^\varepsilon]^T \{\varepsilon(t)\} \quad (36)$$

The inevitable truncation procedure for DOF is also accompanied by a modal order reduction and the modes with Mass Participation Factor (MPF_{mass}) above 90% need to be retained. The number of sensors g should be $g \geq m$ (m is the number of selected modes). The displacements $x(t)$ can then be determined with

$$\{x(t)\} = [\phi]\{q(t)\} \quad (37)$$

The expansion process used in the current work is based on SEREP. The purpose of expansion is two folds. One that the displacements at the untapped locations can be known from which force at each DOF can be evaluated. Two that the expansion of strain results can help identify the force location.

An interesting feature about usage of modal strain is that it does not require force location known priori rather the sensor position is targeted to observe the selected modes. Later it

will be shown that with the same dynamic sensors, static loads can also be recovered with force localization.

With the description of the Placement Index and the D-Optimal Method, we now focus on to the topic of force identification. Once the positions are determined for the strain sensors, the next step is now to identify the applied load. The following passage will elaborate on the concept of force localization as mentioned in [53].

4.2. Force Localization:

The force localization described in [53] requires that complete strain profile be known in addition to the strain response matrix $[A]$. With $[A]$ already known from the static load recovery, the expansion through SEREP would be suffice to provide the strains at locations without sensors.

A simple check to identify location of applied for would be to observe

$$[A_j]\{\varepsilon_i\} = [A_i]\{\varepsilon_j\} \quad i, j = 1, 2, \dots, N_s \quad (38)$$

Which in a better way can be calculated through

$$E = \min \sum_{i=1}^{N_s} \sum_{\substack{j=1 \\ j \neq i}}^{N_s} \frac{\| [A_j]\{\varepsilon_i\} - [A_i]\{\varepsilon_j\} \|^2}{\| [A_j]\{\varepsilon_i\} \|^2} \quad (39)$$

Here N_s represents the number of strain sensors with design variable x_e and y_e . The above equation will be defined as the ‘*Minimum Difference*’. After a brief description of force localization, description of the expansion process follows.

For dynamic force localization the above calculations are performed at each time step to constantly monitor whether the force is at the same location or has shifted based on the strain activity. Next the expansion procedure SEREP will be explained in detail.

4.3. System Equivalent Reduction Expansion Process (SEREP):

System Equivalent Reduction Expansion Process (SEREP) is an attractive tool when it comes to expansion of limited set of data to the complete set of DOFs of the structure. The proofs, merits and demerits are explained in [58–60]. The modal transformation can be shown by

$$\{x_n\} = \begin{Bmatrix} x_a \\ x_d \end{Bmatrix} = \begin{bmatrix} \phi_a \\ \phi_d \end{bmatrix} \{q\} \quad (40)$$

Here ϕ_i represents the modal matrix, ‘a’ stands for active DOFs (optimal sensors), ‘d’ stands for deleted DOFs (untapped locations) and q takes the form shown in the following equations depending on a general case where a (number of equations) is greater or equal to m (number of solution variables or modes).

$$\begin{aligned} \{x_a\} &= [\phi_a]\{q\} \\ [\phi_a]^T \{x_a\} &= [\phi_a]^T [\phi_a]\{q\} \\ ([\phi_a]^T [\phi_a])^{-1} [\phi_a]^T \{x_a\} & \\ &= ([\phi_a]^T [\phi_a])^{-1} [\phi_a]^T [\phi_a]\{q\} \end{aligned} \quad (41)$$

which leads to

$$\{q\} = ([\phi_a]^T [\phi_a])^{-1} [\phi_a]^T \{x_a\} = [\phi_a]^g \{x_a\} \quad (42)$$

The above method is a least squares method and the full set DOF (n) can be related to reduced set DOF (a) by

$$\{x_n\} = [\phi_n][\phi_a]^g \{x_a\} = [T_u]\{x_a\} \quad (43)$$

Where

$$[T_u] = [\phi_n][\phi_a]^g \quad (44)$$

This is the SEREP transformation matrix that is used for either the reduction of the finite element mass or stiffness matrices or for the expansion of the measured experimental modal vectors. The process relies on a finite element model or analytical model from which an Eigen solution is performed to develop the mapping between the full set of finite element DOF and the reduced set of 'a' DOF. The Eigen solution of the full set of system matrices yields a set of modal vectors which can be partitioned into those degrees of freedom that correspond to the active set of 'a' DOF and the inactive set of 'd' DOF. The partitioning can be shown in Figure 4.3.

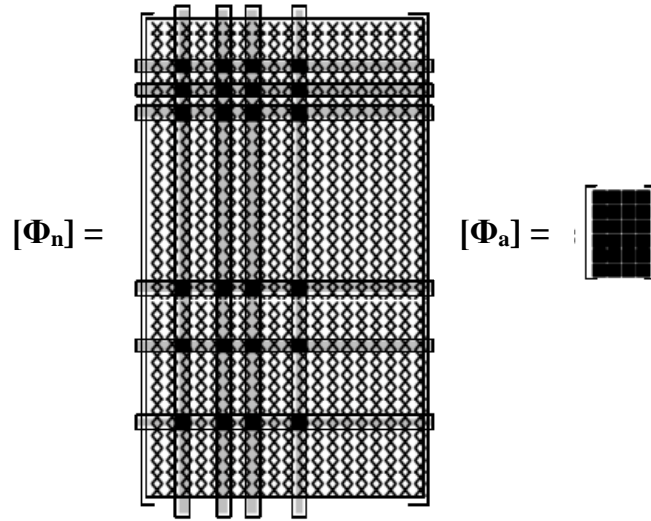


Figure 4.3 Mode Shape Reduction from full set 'n' to active DOFs 'a' [58]

Note that this process does not require the full set stiffness or mass matrix. The above method is useful for doing an expansion of the reduced set 'a' to full set 'n' as shown below.

The SEREP expansion technique is extremely accurate in regards to the expanded mode shapes, actually it is exact due to its inherent formulation. However, if the experimental mode shapes are not correlated well with regards to the analytical mode shapes, then the results can produce very poor expanded mode shapes. The SEREP process is very unforgiving of small errors that exist in the measured experimental data base. While the SEREP process is often looked at as being too harsh in the evaluation of modal vectors, this is exactly what is needed in order to more clearly identify where errors exist in the measured and/or analytical model.

The above described framework will guide us in the placement process. The above techniques will be applied upon two examples 1) beam (clamped-clamped & cantilever) and 2) plate (supported from all four edges) in the following chapter.

4.4. Comparison of SEREP to other Model Reduction Techniques:

The advantage of using SEREP in comparison to other reduction and expansion techniques like Guyan Reduction, Improved Reduced System (IRS) and Component Mode Synthesis is that the ability of the formulation to produce a reduced order system that depicts the complete dynamic behavior of the characteristic. A summary of the results [75] after comparison are presented in the following manner:

1. Guyan condensation always produces frequencies that are greater than those of the full model therefore dof selection is critical to its success.
2. IRS improves on Guyan by making adjustments to the inertial effects associated with the d_{dof} .
3. Dynamic condensation will preserve at most one of the eigenvalues of the original system
4. SEREP always produces the same frequencies and mode shapes as the full system.

A comparison was performed for different reduction techniques to evaluate the effect of inclusion of larger, fewer and sufficient number of a_{dof} selection on mode reconstruction (see Table 4.1). The SEREP was found to be robust despite using few sensors on an Aluminum frame (1 ½'' x 3 ½'' x 3/16'').

Table 4.1 Comparison of different reduction techniques Guyan, IRS and SEREP [75]

Selection Criterion	Reduction Techniques			
	Reference	Guyan	IRS	SEREP
	Identified Modes			
Poor (6 Sensors)		65.0	32.2	32.2
		109.6	109.6	109.4
		-	-	114.7
		129.7	129.4	129.5
		257.7	312.5	309.0
		792.6	367.0	354.5
Better (6 Sensors)	32.2	32.2	32.2	32.2
	109.4	111.1	111.5	109.4
	114.7	115.2	115.2	114.7
	129.5	131.6	130.3	129.5
	309.0	1168.0	577.4	309.0
	354.5	1584.5	688.5	354.5
Larger (10 Sensors)	456.1	32.3	48.0	32.2
	572.6	109.7	109.4	109.4
		117.5	114.7	114.7
		130.0	129.5	129.5
		321.7	318.7	309.0
		375.2	372.0	354.5
		483.3	480.8	456.1
		652.9	650.0	572.6
		701.4	697.3	598.0
		745.8	744.1	689.7

4.5. Conclusion:

A theoretical development has been presented for the two placement schemes namely; (a) Placement Index and (b) D-Optimal Method. The objective to achieve optimal placement is set to acquire information on unknown load magnitude and location using strain sensors.

To proceed with the objective to find optimum sensors and their location we would like to set an evaluation in such a way that the information collected from both the methods be expanded using SEREP technique. The expansion of the acquired data from these sensor positions will allow us to judge, which method is more appropriate for force identification.

It is stated again that to ensure accurate force prediction, an accurate shape construction of the structure is essential. The methodology for comparison is illustrated in Figure 4.4

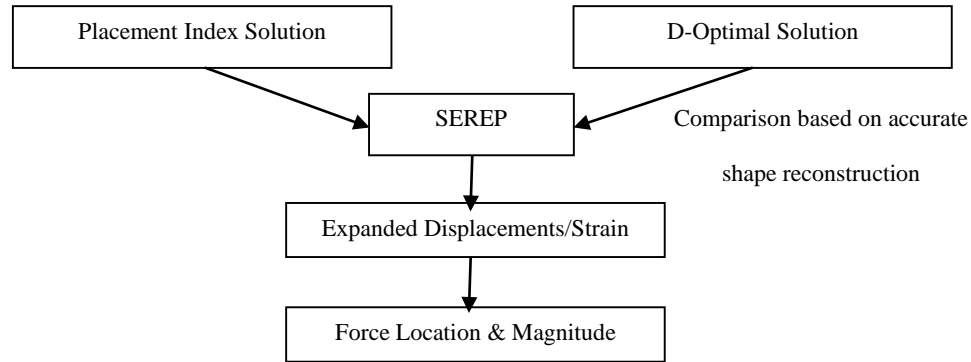


Figure 4.4 Graphical representation of implemented scheme

A force localization procedure has been explained once a complete strain profile of the structure is available. Based on accurate strain expansion and force position determination, we can arrive at the observation node in the structure to further evaluate force magnitude at that position. In addition actuator positioning, gain and size determination were presented in the actuator feasibility part to give closure on utilization of Placement Index for actuator placement as well. In the end a comparison of SEREP is made against contemporary model reduction techniques namely Guyan and IRS [75].

Both the Placement Index and the D-Optimal methods lead to investigate a reduced finite element model. Therefore a suitable reduction/expansion technique in the form of SEREP is selected to observe solution at non-sensor locations.

CHAPTER 5

SIMULATION RESULTS FOR STRUCTURAL EXAMPLES

This chapter will illustrate the application of the placement techniques while utilizing the SEREP expansion procedure to arrive at identifying the applied load on a structure (beam/plate) through its location and magnitude. The techniques discussed in the previous chapter are solved first by obtaining the pre requisite dynamic characteristic information from the Finite Element Model (FEM) developed in COMSOL and then further processing the mass matrix $[M]$ and stiffness matrix $[K]$ to obtain two sets of optimal placements namely; 1. Placement Index and 2. D-Optimal Design. Later on the expansion results using SEREP will be compared for both techniques to evaluate the scheme which produces better results for force location and magnitude prediction. An important aspect of a comparative assessment is to ensure a method that suits best to predict the structural motion and therefore evaluate the required unknown force. The methods have not been previously tested against a data expansion criteria and would provide a new insight into utilizing these methods.

Following assumptions will be made before analysis:

- The structural problems solved are linearly elastic and the principal of superposition is valid for modal studies.
- It is assumed that the all structures (beam/plate) are lightly damped with Rayleigh proportional damping.

- The applied force is at a single location only. Analysis for multiple force, force(s) with angular orientation and force(s) with varying locations over time are not covered in the scope of the work.
- Sensor placement is performed for identifying multiple modes and hence the number of sensors will be kept equal or greater than the observable modes.
- Model reduction and expansion is only performed with System Equivalent Reduction and Expansion Process (SEREP). The advantages of using SEREP over other model reduction techniques have been previously discussed.

The applied loads are of two nature 1. Static and 2. Dynamic. The Dynamic loads are further classified into a. Forced Harmonics and b. Impulse Force. In case of forced harmonics, the applied force is sinusoidal varying at a frequency set equal to any of the fundamental frequencies of the structure. The frequencies are purposely set equal to structure's natural frequency to test whether the placement helps identify the active frequency through mode participation factor (MPF). The MPF values help us identify the active mode by differentiating an active mode by its higher relative values from non-active ones.

It will be shown that better MPF assessment through strain information is the key to arrive at a better solution in terms of force prediction.

The objective of the analysis from simulated results is to test the two aforementioned placements schemes and comparing in terms of error produced from either results when identifying an unknown load magnitude along with its location. Later on in the following

chapter, an attempt to experimentally validate with FBG strain sensors embedded into a metal cantilever and clamped-clamped beam will be performed.

5.1. Simulated Examples:

The clamped-clamped beam example has been taken from [76], the revisited example will help us use the placement index method and to verify the solution. Once verified, we will apply the same method to a cantilever beam of the dimensions mentioned in

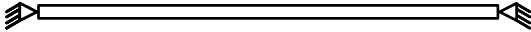
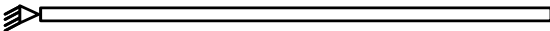
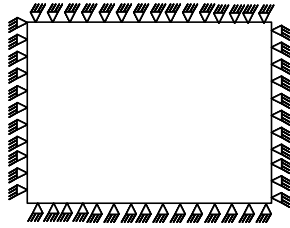
. The plate example has been selected in order to use the established placement index in [45] and to compare it with the D-Optimal method. Table 5.1 provides a summary of data for the structural examples implemented in the simulated study. The purpose of choosing these examples is to test the optimal schemes in reference to force prediction both magnitude and position. The position will be investigated using minimum difference scheme explained in chapter 4. The force magnitude will be solved using equation 7 once the displacements are expanded from the optimal sites to the complete nodal displacement of the complete structure. The equation of the motion of the structure is represented as.

$$[M]\{\ddot{x}(t)\} + [D_{damp}]\{\dot{x}(t)\} + [K]\{x(t)\} = \{f(t)\} \quad (45)$$

Equation (45) helps us evaluate the applied force once the mass matrix $[M]$, damping matrix $[D_{damp}]$ and stiffness matrix $[K]$ are known. The finite element procedure discretizes a structure into elements connected at nodes. Each node consists of a number of DOF that could range from 6 DOF ($x, y, z, \theta_x, \theta_y, \theta_z$) for 3D structures and 3 DOF (x, y, θ_z) for 2D representation of the structures. Say the displacement 'y' is available to us through the selected sensor which corresponds to 1 out of 3 DOF (x, y and θ), we would

need to obtain a reduced matrix form for [M] and [K] through SEREP as explained in chapter 4. The model reduction through SEREP will allow us to use minimum information to construct the force profile.

Table 5.1 Data for Beam and Plate examples

Structure Type	Beam Clamped-Clamped	Beam Cantilever	Plate All Edges Clamped
Geometry (x, y, z)	1500 x 5 x 5 [mm]	700 x 50 x 3 [mm]	900 x 600 x 1 [mm]
Beam Clamped-Clamped			
Beam Cantilever			
Plate All Edges Clamped			
Material			
Structural Steel: E =200 GPa, ρ = 7850 kg/m³, ν = 0.33 (Clamped-Clamped Beam & Plate)			
Aluminum: E=70 GPa, ρ = 2700 kg/m³, ν = 0.33 (Cantilever Beam)			
FEM Description			
	2D Beam	2D Beam	3D Shell
Nodes	16	71	31 x, 21 y
Elements	15	70	30 x, 20 y
Length/Element [mm]	100	10	30 x, 30 y

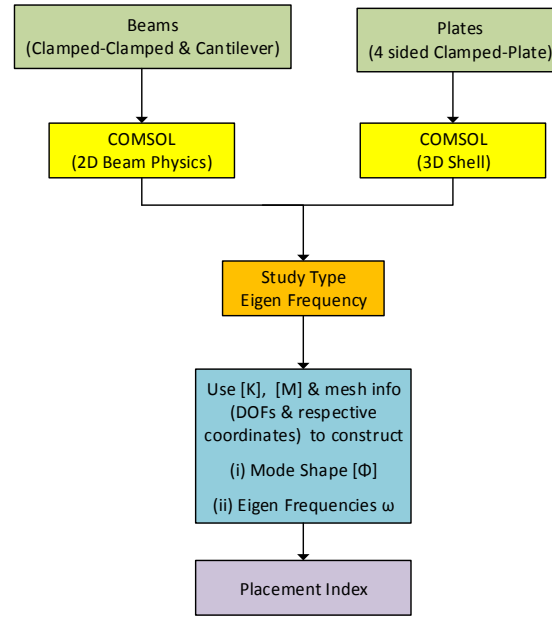
5.2. Problem Formulation & Solution Flow Chart:

The problem formulation has been set to investigate both static and dynamic load cases with structure type beam and plate (see Figure 5.1). The formulation part presented in Figure 5.1 (a) takes two structure types; beam and plate. The beam is investigated with the following boundary conditions (i) Clamped-Clamped & (ii) Cantilever. Whereas the boundary condition chosen for plate is all sides clamped. A major effort in the formulation

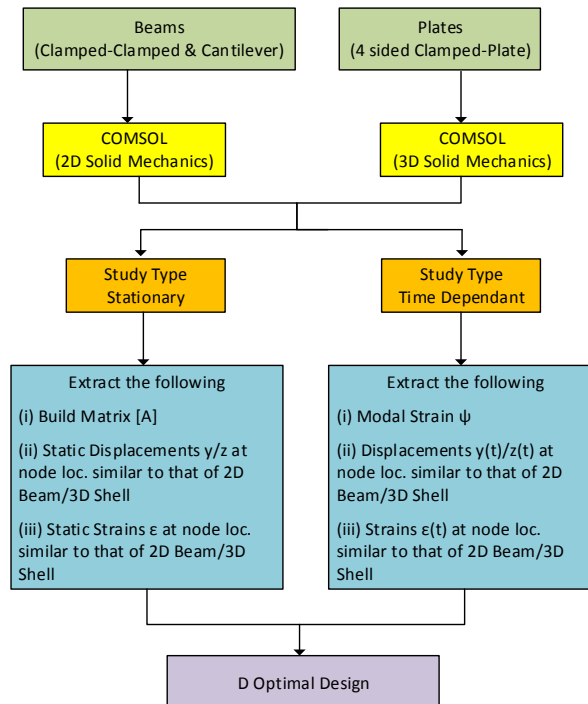
stage is to extract critical information such as mass matrix $[M]$ & the stiffness matrix $[K]$ for the development of a Placement Index solution. The extraction is performed with models constructed in COMSOL, an FEM software. Whereas in Figure 5.1 (b), steps have been shown to find the D-Optimal solution. The D-Optimal solution method is presented in detail in chapter 4.

After formulating the problem, the next stage is to devise a scheme to arrive at identifying the unknown applied load along with its magnitude and location. The strain response matrix $[A]$ and the SEREP expansion technique helps us arrive at the position of the load applied. This information can also be confirmed once the expanded solutions produce displacement, velocity and acceleration. The force at each node of the structure will help construct a shear force diagram, giving a visual reference to the applied load position. The problem solution flow chart is shown in Figure 5.2.

The chart in Figure 5.2 illustrates sequential steps in order to obtain an optimal configuration through both schemes (a) Placement Index and (b) D-Optimal Design once the problem has been formulated according to Figure 5.1. We would now start implementing the above mentioned routines on our examples tabulated in Table 5.1.



(a)



(b)

Figure 5.1 Problem formulation Flow Chart (a) Placement Index and (b) D-Optimal Design

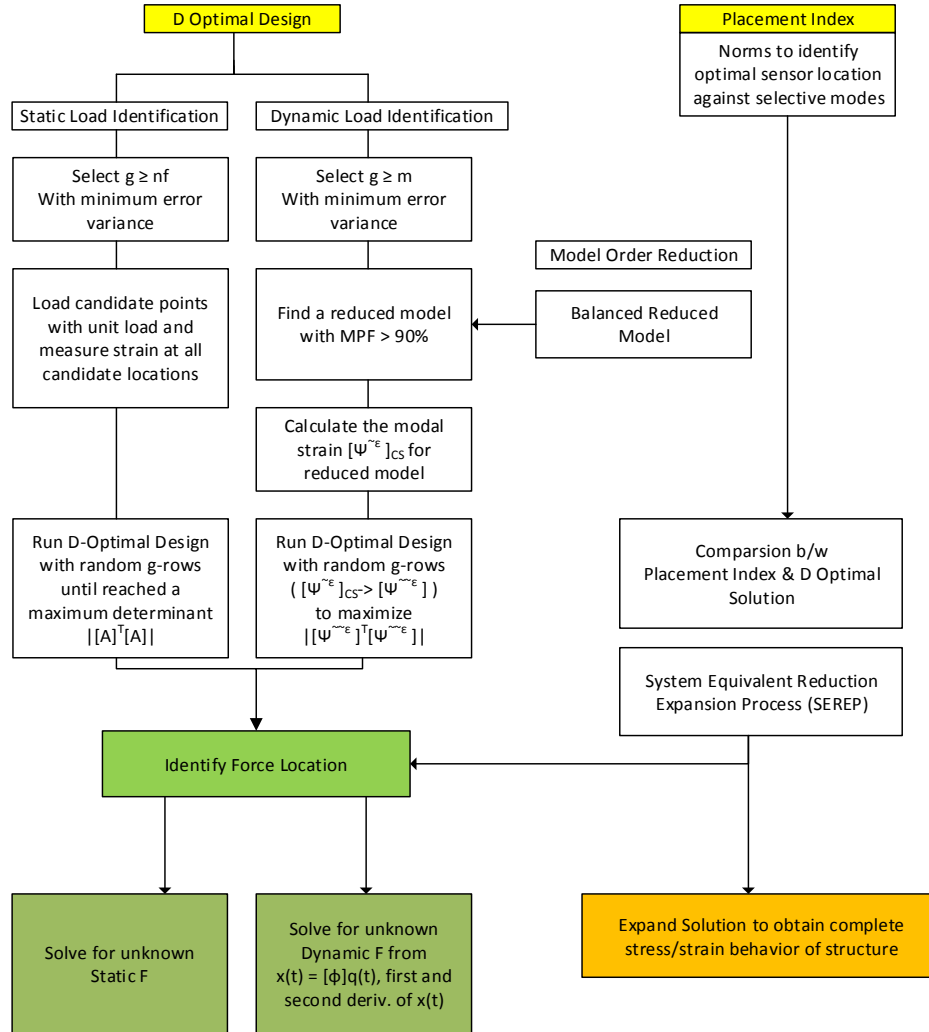


Figure 5.2 Problem solution Flow Chart

5.3. Example 1: Clamped - Clamped Beam under Static & Forced Harmonic

The geometric and material properties used for this example are presented in Table 5.1. Figure 5.3 shows the clamped-clamped boundary conditions and the node numbering. The red dots identify candidate positions whereas the blue plus sign indicates the sensor position obtained from D-Optimal solution. In the first phase we conclude our optimal positions both for Placement Index and D-Optimal Design. Later a sensor would be taken

out from the original configuration of the selected optimal design to observe the deviation of the extracted results from the ones obtained theoretically. A test will also be performed with a random sensor configuration.

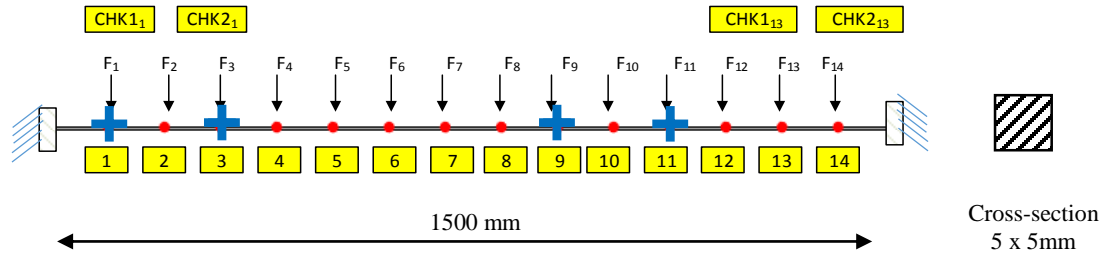


Figure 5.3 A clamped-clamped with cross locations identifying the position of D-Optimal sensors

Based on the problem formulation and solution flow chart (Figure 5.1 and Figure 5.2), sensor positions from the fixed end for both D-Optimal and Placement Index schemes are presented in Table 5.2.

Table 5.2 Sensor position tabulated with respect to optimization schemes

Optimization Scheme <i>Number of Sensors = 4</i>	D-Optimal Method	Placement Index
Position of sensors (from fixed end) [mm]	100, 300, 900, 1100	300, 400, 700, 800, 1100, 1200

An essential information for force determination is achieved by acquiring the Modal Participation Factor (MPF) using the sensor strain information based on equation (36). A major advantage here would be to qualitatively visualize the active mode based on our initial assessment of the structural dynamic characteristics which will be explained more clearly with mode identification.

5.3.1. Modal Identification:

Upon expansion of the displacement data collected at optimal sites e.g. D-Optimal sensors, we observe how the expanded displacement are similar to the actual ones. Figure 5.4 graphically shows the mode 2 shape at time $t = 0.1$ sec. It is important to mention that accurate expansion results are both based on the sensor position and the MPF values obtained from those positions.

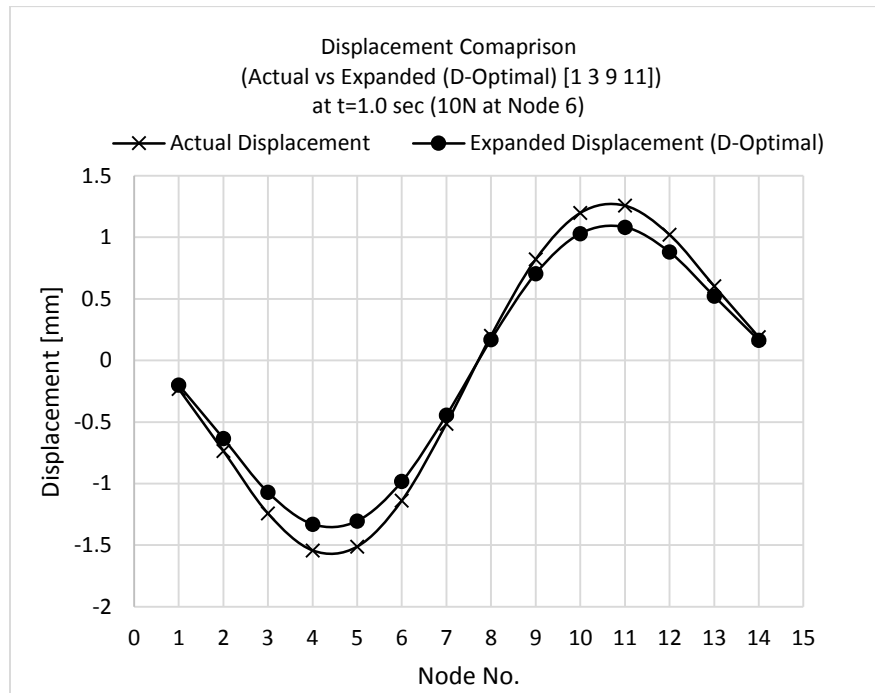


Figure 5.4 Displacement comparison of Actual vs Expanded data at D-Optimal locations [1,3,9,11] ($t=1.0$ [sec])

Another means for mode identification is through MPF values. Over the time interval, one can observe from Table 5.3 below that the MPF for the second mode remains dominant compared to the other modes. The MPF values over reported time helps us identify the i^{th} mode during a vibration test.

Table 5.3 Modal Participation Factors at T [0 1.0] sec with sensors at (1, 3, 9, 11)

Mode Participation Factor (MPF) <i>1e-3</i>	Mode	Elapsed Time (sec)				
		0.2	0.4	0.6	0.8	1
	1	-0.40	-0.44	0.91	-0.13	-1.07
	2	-0.75	5.56	-6.29	-2.19	11.75
	3	0.04	-0.02	-0.01	0.00	-0.03
	4	0.00	0.00	-0.02	0.00	0.12

Table 5.4 Mode switching observed based on the MPF calculations for sensors at [1 3 9 11]

Mode Participation Factor (MPF) <i>1e-3</i>	Mode	Elapsed Time (sec)			
		0.016	0.031	0.047	0.063
	1	-8.25	-7.19	1.87	8.75
	2	3.21	-6.42	9.57	-12.58
	3	0.06	0.09	0.14	0.17
	4	-0.03	0.03	-0.07	0.06

Mode switching can also be observed (Mode 1 to Mode 2 transition) in Table 5.4 if the time step is taken small enough depending on the excited modal frequency. Based on the *Nyquist* criteria, the sampling frequency was kept at 2xnatural frequency of the excited beam (2x32Hz).

5.3.2. Strain Expansion:

The strains are calculated through the available modal strains and the calculated MPF ‘q (t)’. The difference between optimal and non-optimal results are formed on the basis of the calculated MPF. Insufficient information from non-optimal sensors tends to ill predict the

expanded solution. The expansion results for strain will help determine the force location. Figure 5.5 shows the strain expansion results obtained from the D-Optimal selected sensors.

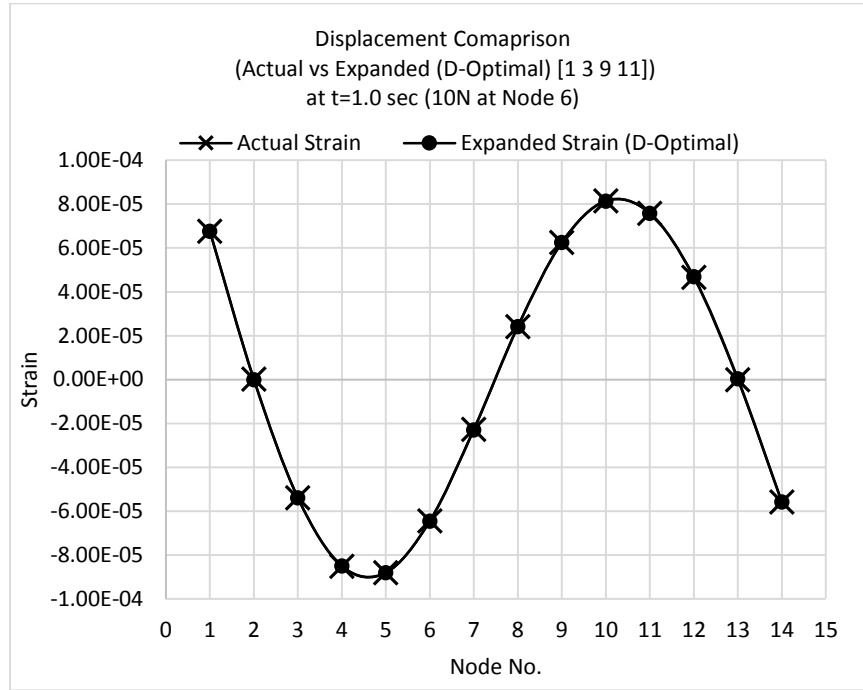


Figure 5.5 Strain comparison of Actual vs Expanded data at D-Optimal locations [1,3,9,11] (t=1.0 [sec])

5.3.3. Force Identification (Position):

The difference values in Table 5.5 Static Force identification are given against D-Optimal locations while using equation (39) from chapter 4. Significant details lie primarily in the vertical column sums of the product difference. Minimum value against a particular column highlights the possibility of the applied force location. Table 5.5 suggests that in the presence of all candidate strain sensors, it is location 6 which responds to the applied force. The strains were collected in COMSOL at candidate and optimal locations in the first principal direction which later can be compared and used in calibration of FBG and Strain

Gages. It also shows that despite lesser number of sensors (4), the strain response still helps us identify a single force originally applied at location 6.

Similarly for dynamic load identification, time varying strains are calculated firstly at all candidate locations and later on at optimal locations. Though originally subjected to a harmonic load of $10 \sin(2\pi 32) t$ at location 6, over a time period of 1 sec with 0.1 sec interval, the calculations show that force is applied at location 6. As a result of similar tables generated at different time intervals, force location was consistently found at node 6 position.

Table 5.5 Static Force identification

Difference Between	F1	...	F5	F6	F7	...	F14
S1 & S2	3.57E-01		1.94E+00	1.88E-17	5.51E-02		2.37E-01
S2 & S3	3.46E+00		6.98E-01	2.23E-16	3.70E+01		5.22E+00
S3 & S4	8.45E+00		1.25E+00	5.47E-17	5.02E-01		1.08E+02
S4 & S5	3.10E-01		2.81E-01	4.66E-18	1.07E-01		3.59E+00
S5 & S6	1.01E-03		1.09E-04	1.14E-17	8.71E-02		4.87E-01
S6 & S7	2.37E-03		1.79E-04	2.03E-18	2.31E-04		2.80E-01
S7 & S8	7.32E-05		5.46E-06	4.21E-21	7.10E-06		7.19E-03
S8 & S9	1.25E-02		7.59E-04	2.14E-18	6.93E-04		2.52E-01
S9 & S10	1.95E-01		6.67E-03	2.21E-17	4.50E-03		3.33E-01
S10 & S11	1.40E+00		4.01E+01	1.97E-15	2.44E-01		7.99E-01
S11 & S12	7.18E+00		1.28E+00	3.25E-15	3.94E+00		3.51E+01
S12 & S13	7.38E-02		9.86E-03	1.80E-17	1.86E-02		7.99E-01
S13 & S14	7.79E-03		9.33E-04	1.49E-18	1.53E-03		1.55E-01
SUM	2.15E+01		4.56E+01	5.57E-15	4.19E+01		1.56E+02

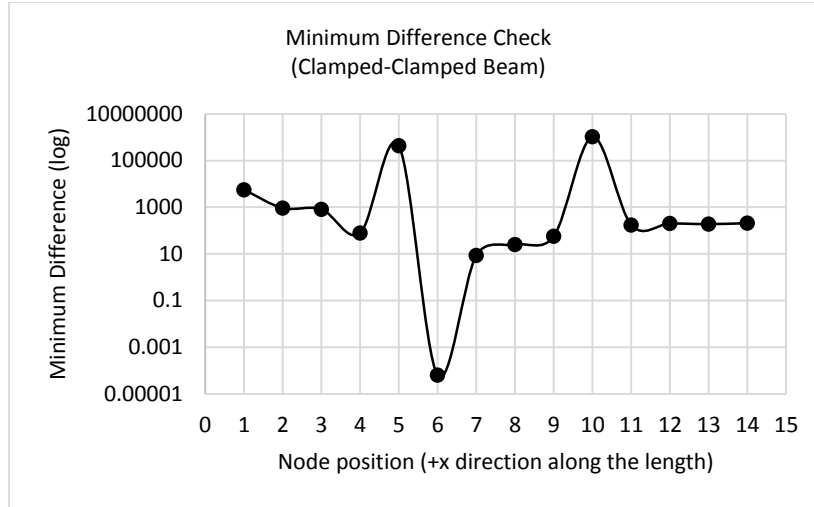


Figure 5.6 Minimum difference graphically illustrated for the Clamped-Clamped Beam example, highlighting node 6 as the position of load

Figure 5.6 illustrates the minimum difference for a clamped-clamped beam identifying position 6 as the load application point.

5.3.4. Force Identification (Magnitude):

The force identification would be split into two parts. 1) Static and 2) Dynamic. The inferences from the two analyses are explained below.

5.3.4.1. Static:

The case for static load recovery is straight forward once the method to identify force location explained in chapter 4 is applied. A load of 10 N downwards was applied at node 6 of the beam and was recovered with any of the optimal sensors.

5.3.4.2. Dynamic:

As explained earlier, the dynamic loads are recovered once the full field displacements are obtained through the expansion process explained in chapter 4. A load of 10 N was applied downwards with a frequency of 32 Hz (mode 2) at node 6 position.

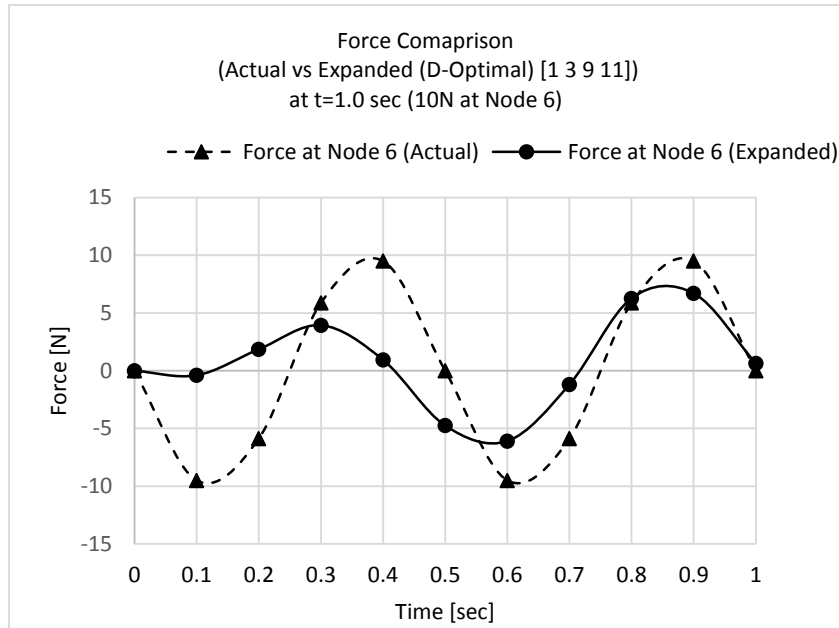


Figure 5.7 Force calculated through SEREP results expanded on D-Optimal sites at node 6 (t=0.0-1.0 [sec])

Figure 5.7 above shows the force experienced at node position 6 during time interval t [0.0-1.0] sec. Looking closely the value at node 6 (since the applied load location was previously determined), the force value seen at $t=0.9$ sec is 8.25 N which is short by 13.2% (9.51 N). From the above graph it can be learned that the force identification starts to develop at 0.6 sec mark and the interval 0.6-1.0 sec will be considered later for error analysis.

5.3.5. Comparison between Optimal and Non-Optimal Solutions

A comparison presented here is based on the solutions obtained in terms of expanded displacements, strains and forces for a) D-Optimal Solution, b) Placement Index Solution and c) Modified D-Optimal Solution. The original D-Optimal solution [1 3 9 11] was modified by taking out sensor at node 9 leaving the arrangement [1 3 11]. We named this arrangement Modified D-Optimal.

5.3.5.1. Displacement Comparison:

A displacement comparison is shown between different placement schemes in order to observe the effect of each sensor placement on displacement prediction of individual nodes.

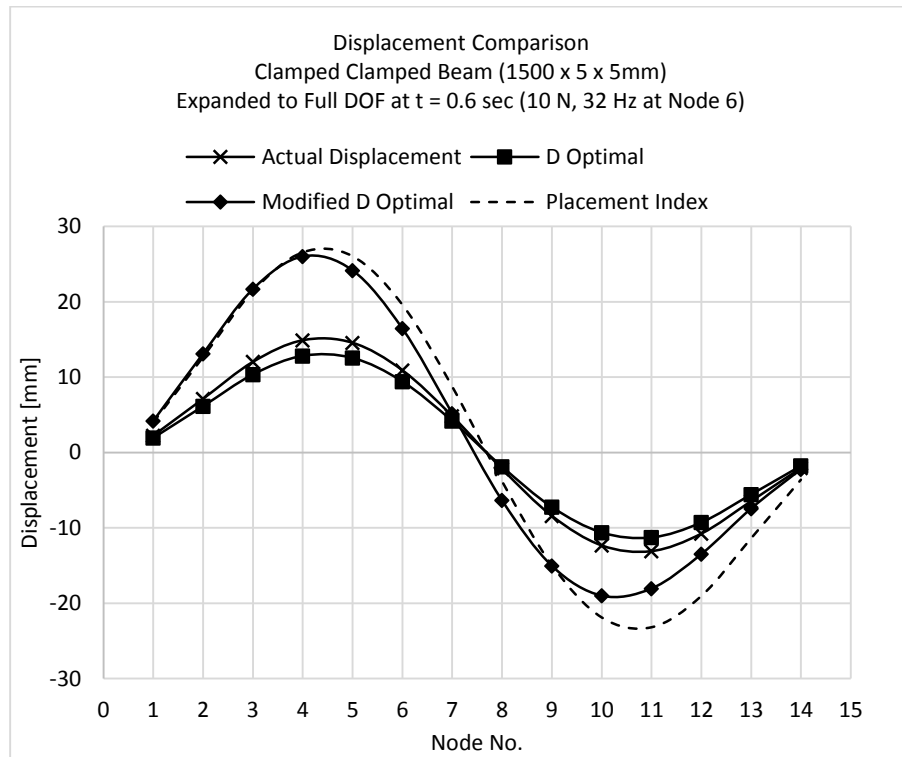


Figure 5.8 Comparison of the expanded displacement solution with the actual displacement of beam for sensor schemes (a) D-Optimal (b) Modified D-Optimal and (c) Placement Index

Figure 5.8 shows that the D-Optimal solution more accurately (13.82%-RMS error) follows the original displacements simulated earlier compared to the Placement Index and Modified D-Optimal approach. Sensor data comparison can be seen in A-1.

5.3.5.2. Strain Comparison:

A strain comparison is shown between different placement schemes in order to observe the effect of each sensor placement on strain prediction of individual nodes.

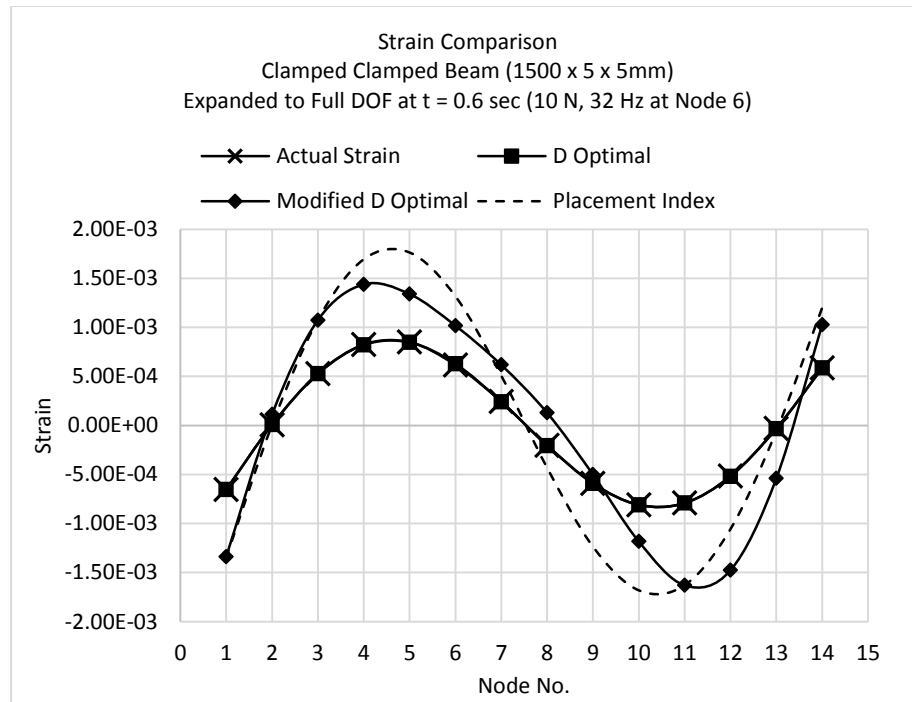


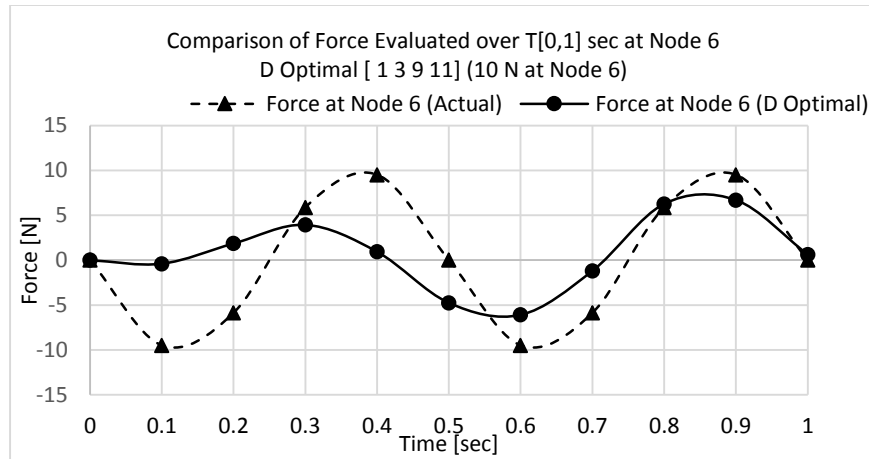
Figure 5.9 Comparison of the expanded strain solution with the actual displacement of beam for sensor schemes
(a) D-Optimal (b) Modified D-Optimal and (c) Placement Index

Figure 5.9 shows again that the D-Optimal solution more accurately (0.29%-RMS error) follows the original strains simulated earlier compared to the Placement Index and Modified D-Optimal approach. A summary of displacement and strain errors are presented in Table 5.6, Table 5.7 and Table 5.8.

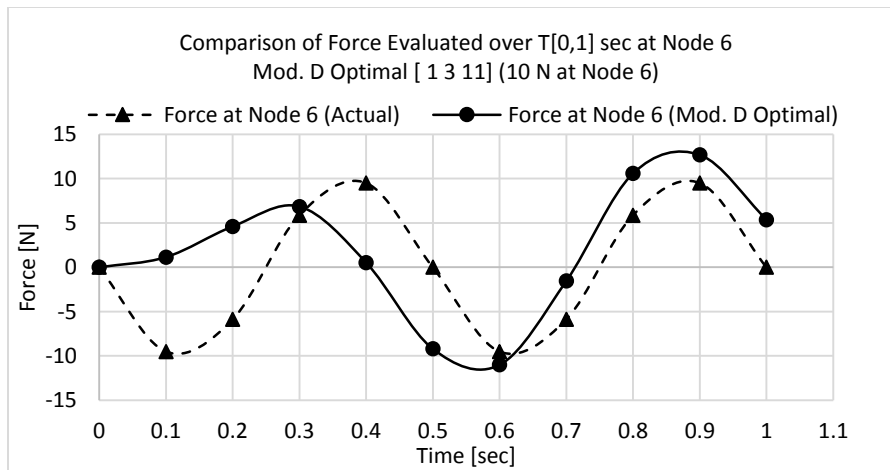
5.3.5.3. Force Comparison:

A force comparison for different placement schemes at node 6 of the clamped-clamped beam (See Figure 5.3) is shown in Figure 5.10. The D-Optimal sensors at [1 3 9 11] predict the force at node 6 as shown in Figure 5.10 (a). The effect of removing or switching off sensor 3 at node 9 is shown in Figure 5.10 (b). A comparison indicates that force identification with respect to the applied force is close to actual force input with (78 % RMS error), but not as close compared to the original 4 sensors contribution at [1 3 9 11] (56 % RMS error). The high error can be attributed to the missing sensor. 3 sensors using D-Optimal method was also considered for investigation with sensor positions [4 6 12]. The force comparison with the applied force is shown in Figure 5.10 (c). It was observed that the force prediction error with 3 sensors D-Optimal sensor was around 84% RMS error. The RMS error is calculated over time period $t = [0.6-1.0]$ sec.

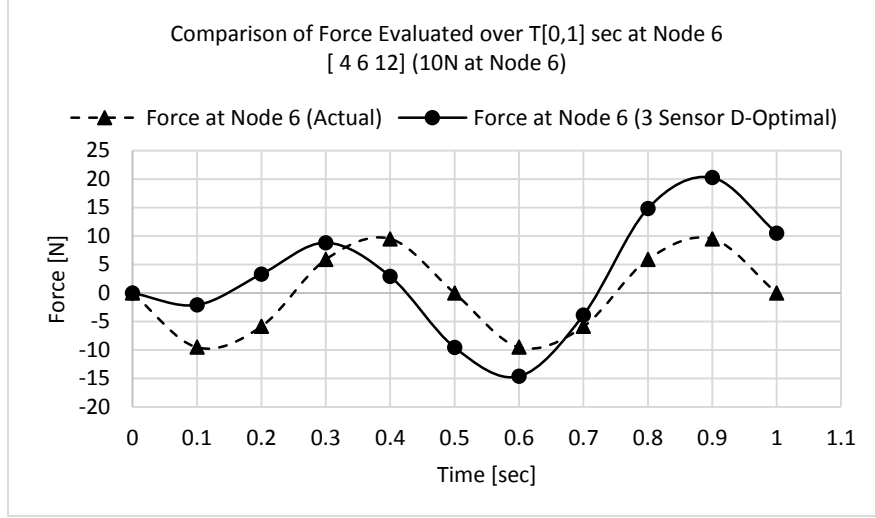
Figure 5.10 clearly indicates that the new positions fail to predict equal or better results. The D-Optimal solution for 3 sensors scheme [4 6 12] is implemented as if it could produce better results compared to the non-optimal solution. The modified D-Optimal solution though gives a poorer estimate for displacement but perform better than the 3 optimal sensors when predicting force. The D-Optimal solution for sensors lesser than the number of predicted modes tend to fail when determining the force. In future the D-Optimal sensors will be referred to as the optimal sensors.



(a) Force comparison D-Optimal Solution



(b) Force comparison Modified D-Optimal Solution



(c) Force comparison D-Optimal (3 Sensors) Solution

Figure 5.10 Comparison of the expanded force solution with the actual force on beam for sensor schemes (a) D-Optimal (b) Modified D-Optimal and (c) D-Optimal (3 sensors)

5.3.6. Error Analysis:

A number of cases as shown in Table 5.6 were tested against the optimal solution from the D-Optimal Method, Placement Index, Modified D-Optimal and also non-optimal position through a random selection. The criterion for optimality is now based on the best prediction of the unknown displacements which consequently help us determine the unknown applied force.

Different sensor positions will result in different solutions of the MPF. Based on the proper placement, the correct MPFs help in calculating the actual or close to actual displacements and forces. It was observed in our analysis that the force prediction starts to mature beyond the 0.6 sec time mark and hence all the errors are calculated for the interval $t [0.6 - 1.0]$ sec. The Root Mean Square (RMS) error is calculated using equation (46).

$$\%RMS\ Error = \frac{\sqrt{\sum (Actual_{ith\ data} - Predicted_{ith\ data})^2}}{\sqrt{\sum (Actual_{ith\ data})^2}} \quad (46)$$

5.3.6.1. Displacement Prediction Error:

Displacement errors are predicted for the expanded solution using the SEREP technique. The data in Table 5.6 has been compared to the simulated displacement results obtained from COMSOL Time Dependent Study. The results presented in Table 5.6 Displacement errors shown for different placement schemes shows that the solution expanded with D-Optimal method results in a better prediction of displacements (RMS Error less than 14%). The MPF calculated for all other cases resulted in strong or weak identification (Sensor Placement [3 12]) of mode 2.

Table 5.6 Displacement errors shown for different placement schemes. t=[0.6-1.0] [sec]

Method									
D-Optimal				Modified D-Optimal		Placement Index			
						H _∞		H ₂	
No. of Sensors									
4		3		3		6		2	
Sensor Positions									
1, 3, 9, 11		4, 6, 12		1, 3, 11		3, 4, 7, 8, 11, 12		3, 12	
Node	Error (%RMS)	Node	Error (%RMS)	Node	Error (%RMS)	Node	Error (%RMS)	Node	Error (%RMS)
1	13.69	4	10.72	1	8.66	3	13.43	3	60.74
3	13.82	6	7.67	3	11.88	4	13.35	12	57.09
9	14.01	12	19.32	11	33.49	7	11.46		
11	13.88					8	18.48		
						11	14.35		
						12	14.23		

5.3.6.2. Strain Prediction Error:

Table 5.7 Strain errors shown for different placement schemes show the strain errors for different sensor placement schemes.

Table 5.7 Strain errors shown for different placement schemes at t=0.6 [sec]

Method				
D-Optimal		Modified D-Optimal	Placement Index	
			H _∞	H ₂
No. of Sensors				
4	3	3	6	2
Sensor Positions				
1, 3, 9, 11	4, 6, 12	1, 3, 11	3, 4, 7, 8, 11, 12	3, 12
Error (%RMS)				
0.656	3.76	30.39	0.74	0.96

5.3.6.3. Force Prediction Error:

The forces are predicted based on the calculations presented in chapter 4. Attention is given to node 6 as the observation node as the force location was identified to be at node 6. The RMS Error for all other schemes are high as much as 379 % for H₂ Placement Index, compared to the D-Optimal Solution. The lowest error (56.81%) is observed at node 6 and also 2 with a 4 D-Optimal sensor arrangement [1 3 9 11]. Previous studies on the topic suggest number of sensor being equal or greater for better results.

Table 5.8 Force errors shown for different placement schemes

<i>Method</i>	<i>D-Optimal</i>		<i>Non-Optimal</i>	<i>Placement Index</i>	
				<i>H_∞</i>	<i>H₂</i>
<i>No. of Sensors</i>	4	3	3	6	2
<i>Optimal Positions</i>	1, 3, 9, 11	4, 6, 12	1, 3, 11	3, 4, 7, 8, 11, 12	3, 12
<i>Node</i>	<i>Error (%RMS)</i>				
6	56.81	84.11	78.04	57.35	379.93

5.3.6.4. Effect of Vibration Amplitude:

A study was also carried out to observe the effect of increase in vibrating load (10x times) on the prediction of displacements and forces. A comparison at $t = 0.6$ sec reveals that the displacement and force prediction errors between the two loadings (10 and 100 N) are almost identical.

Table 5.9 Force errors (RMS) after amplification, comparison between 10 and 100N dynamic load for sensors at [1 3 9 11], $t=0.6$ [sec]

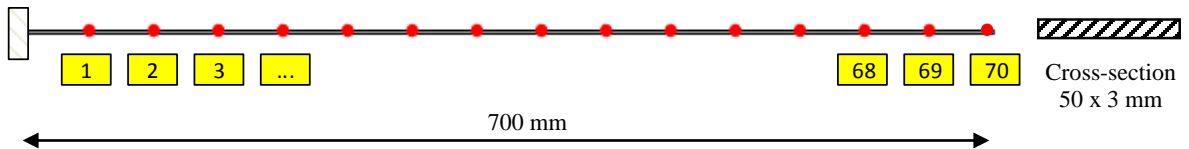
<i>Displacement</i>			<i>Force</i>		
<i>Load (N)</i>					
	<i>10</i>	<i>100</i>		<i>10</i>	<i>100</i>
<i>Node</i>	<i>Error (%RMS)</i>		<i>Node</i>	<i>Error (%RMS)</i>	
6	13.82	13.81	1	56.81	56.77

5.4. Example 2: Cantilever Beam under Impact

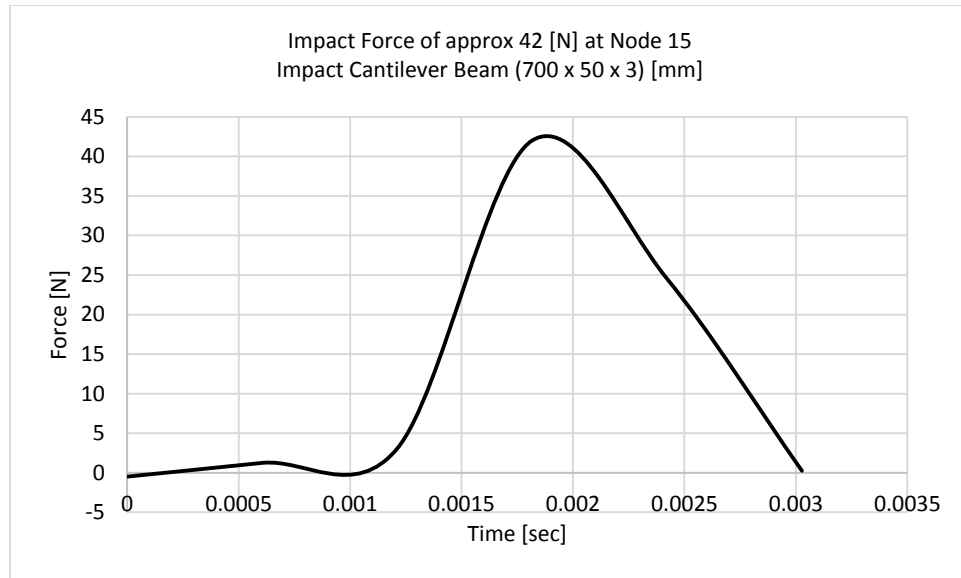
In this example an impact load is applied on the cantilever beam. The beam model with nodal representation is shown in Figure 5.11 (a). An impact force of 42 N (See Figure 5.11 (b)) is applied at a location of 150 mm (Node 15) from the fixed end as shown in Figure 5.13. The impact load is defined by a) amplitude, b) duration of impulse and c) shape of the impulse. In the presence of force measurement hardware like an impact hammer, we can directly use the hardware data indicating the true amplitude, span of impulse and the impulse shape,. The impulse shape is constructed with a cubic line approximation ($f(t) = a + bt + ct^2 + dt^3$) or a Gaussian Pulse ($f(t) = ae^{\frac{-(t-b)^2}{2c^2}}$) between data points. Here a, b and c are constants. The beam geometry and material description are presented in Table 5.1.

Contemporary impulse shapes as mentioned in [77] are shown in Figure 5.12 (a-d). These shapes can be used to approximate the impact loading on the structure (See Figure 5.12 (e)). These approximations need to be carefully made as the variations with respect to actual impulse shape profile, amplitude and impulse span may alter the results [78]. But the assumption is valid as long as the approximated shape average (area under the curve) is equal to impact hammer impulse shape average.

Two types of comparisons are presented. One is between the two optimization schemes and the second is based on the expansion results from both sensors placement. Though Placement Index results are based on the displacement sensor output and D-Optimal on strain, a basis of comparison is that strains are an indirect measure for displacements. High displacement points are also the ones with high strains but high strains do not correspond to high displacement values.

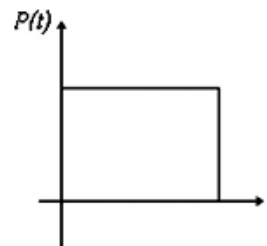


(a) Nodal representation of the cantilever beam

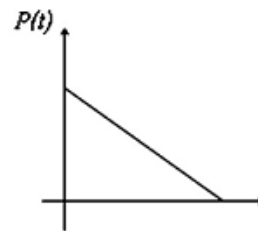


(b) Impact force of 42 [N]

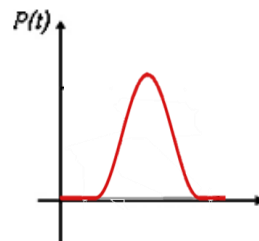
Figure 5.11 (a) Nodal representation of the cantilever beam, (b) Impact force of 42 [N]



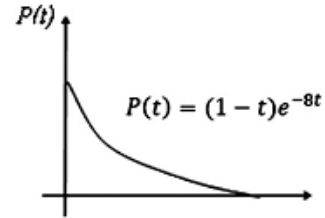
(b) Rectangular



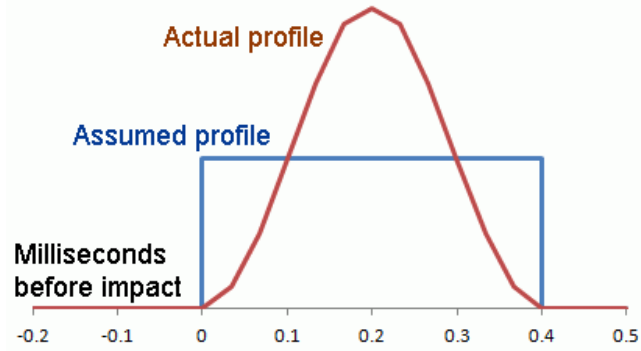
(a) Triangular



(d) Gaussian



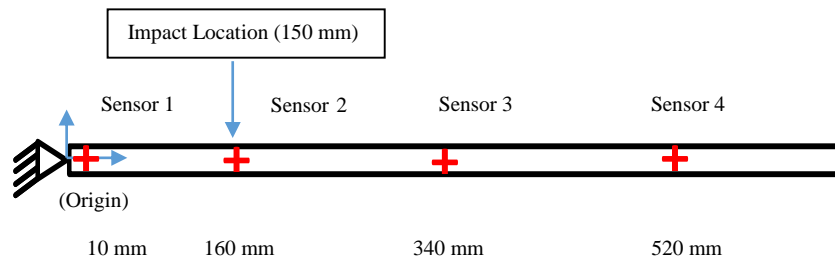
(c) Exponential



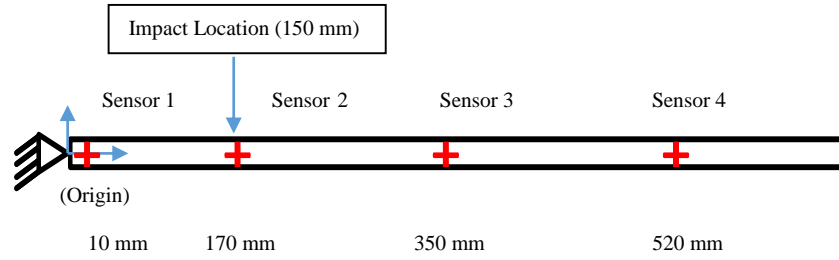
(e) Comparison of assumed profile with the actual profile (impulse)

Figure 5.12 (a-d) Characteristic loading functions for simple load pulses [77], (e) comparison of profiles

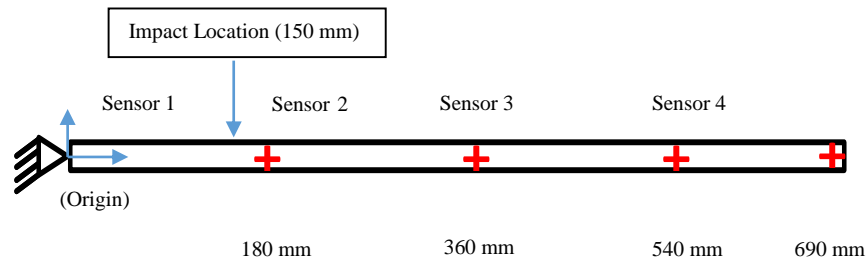
The optimum sensor positions against the presented cantilever beam are identified in Figure 5.13 below. The position will be later confirmed for their optimality in displacement, strain and force prediction of the untapped locations using the SEREP expansion.



(a) D-Optimal Positions



(b) Modified D-Optimal



(c) Placement Index Positions

Figure 5.13 Sensors positions with respect to (a) D-Optimal, (b) Modified D-Optimal and (c) Placement Index

Table 5.10 shows sensor positions tabulated with respect to optimization schemes.

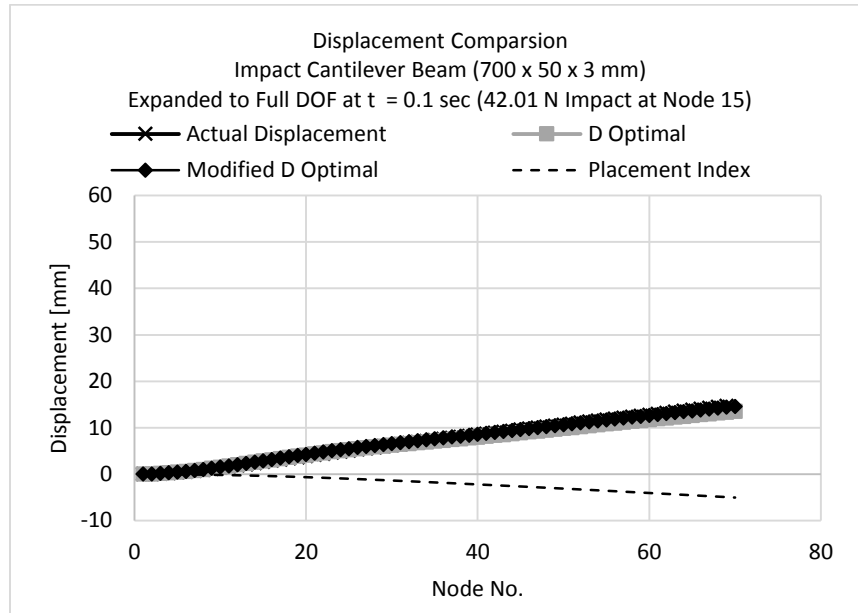
Table 5.10 Sensor position tabulated with respect to optimization schemes

Optimization Scheme <i>Number of Sensors = 4</i>	D-Optimal Method	Modified D-Optimal Method	Placement Index
Position of sensors (from fixed end) [mm]	10, 160, 340, 520	10, 170, 350, 520	180, 360, 540, 690

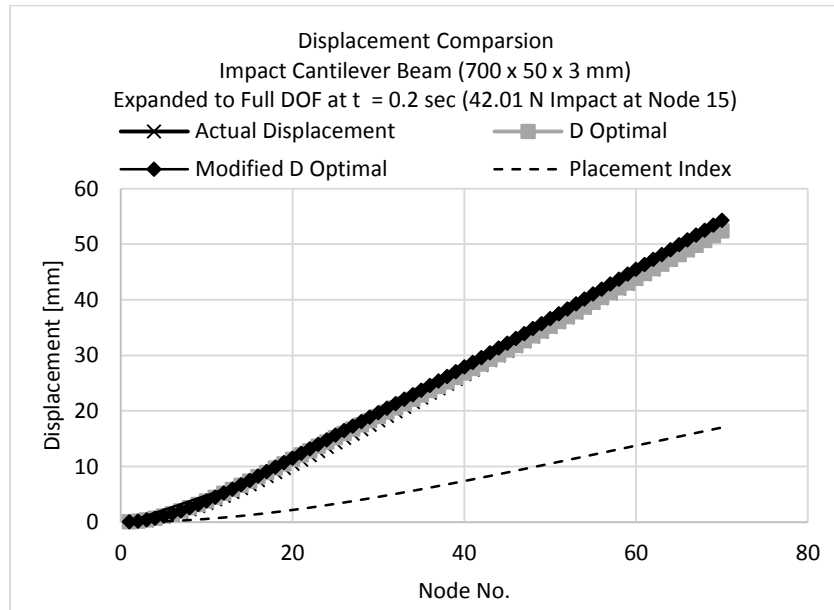
5.4.1. Displacement Comparison:

A displacement comparison is made among (a) D-Optimal [1 16 34 52], (b) Placement Index [18 36 54 69] and (c) Modified D-Optimal [1 17 35 52]. The node numbering is labelled from left to right as per convention used in Figure 5.3. The error analysis is

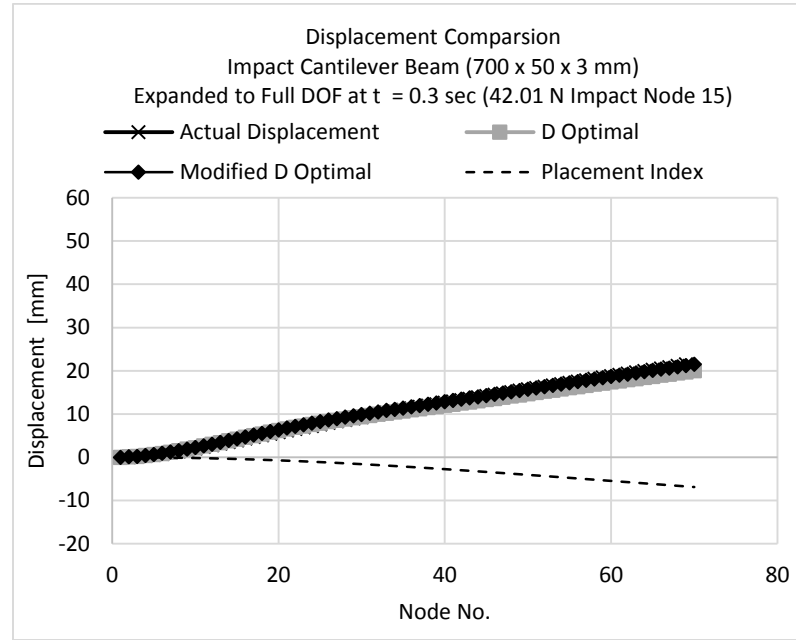
summarized later in Table 5.11 and Table 5.12. Sensor data comparison can be seen in A-2.



(a) Displacement comparison at $t = 0.1$ [sec]



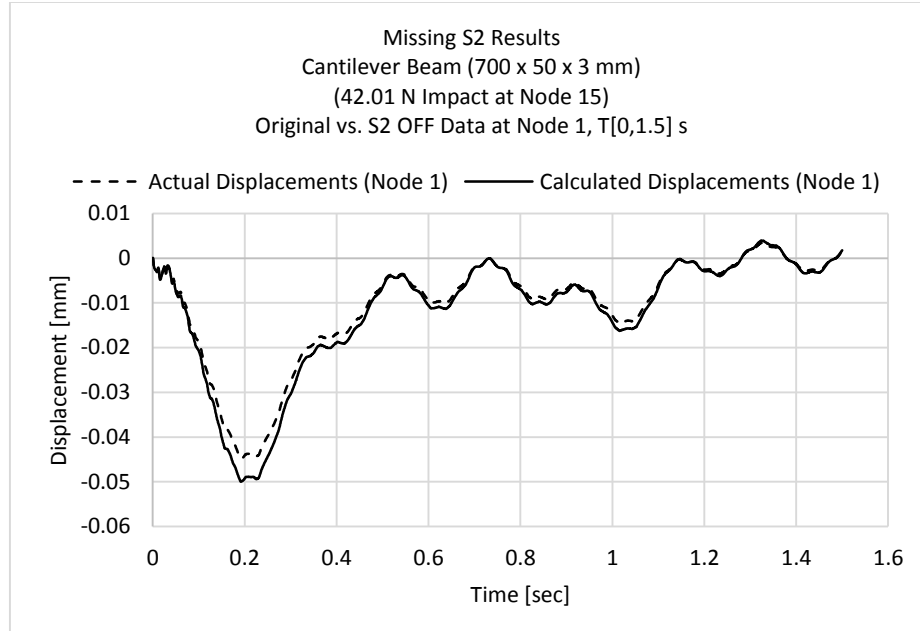
(b) Displacement comparison at $t = 0.2$ [sec]



(c) Displacement comparison at $t = 0.3$ [sec]

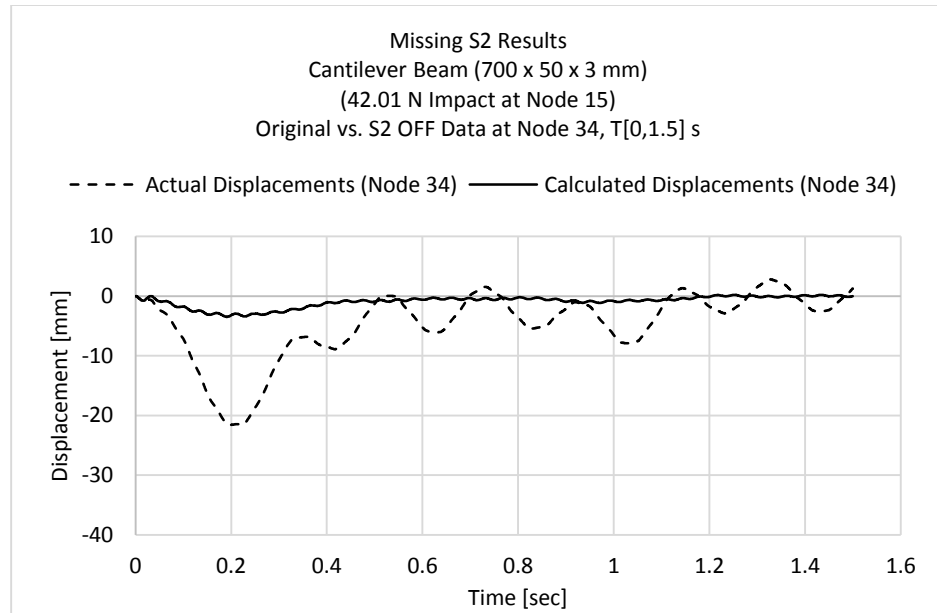
Figure 5.14 Comparison of the expanded displacement solution with the actual displacement of beam for sensor schemes (i) D-Optimal (ii) Modified D-Optimal and (iii) Placement Index at time (a) $t = 0.1$ [sec], (b) $t = 0.2$ [sec] and (c) $t = 0.3$ [sec]

Figure 5.14 shows that for observation times $t = 0.1$, 0.2 and 0.3 sec, the D-Optimal and the Modified D-Optimal solutions are accurately predicting the displacement profile. Whereas the Placement Index results are unsatisfactory. A scenario could develop where one of the sensors say Sensor 2 fails. In that case we will be left with the arrangement [1 34 52]. Figure 5.15 refers to implementing this situation. Sensor 1 at node 1 was able to fairly predict the results but when we made observation for node 34 and 52, the results were away from actual results. Thus force evaluation based on poor displacement predictions will always produce erroneous results.

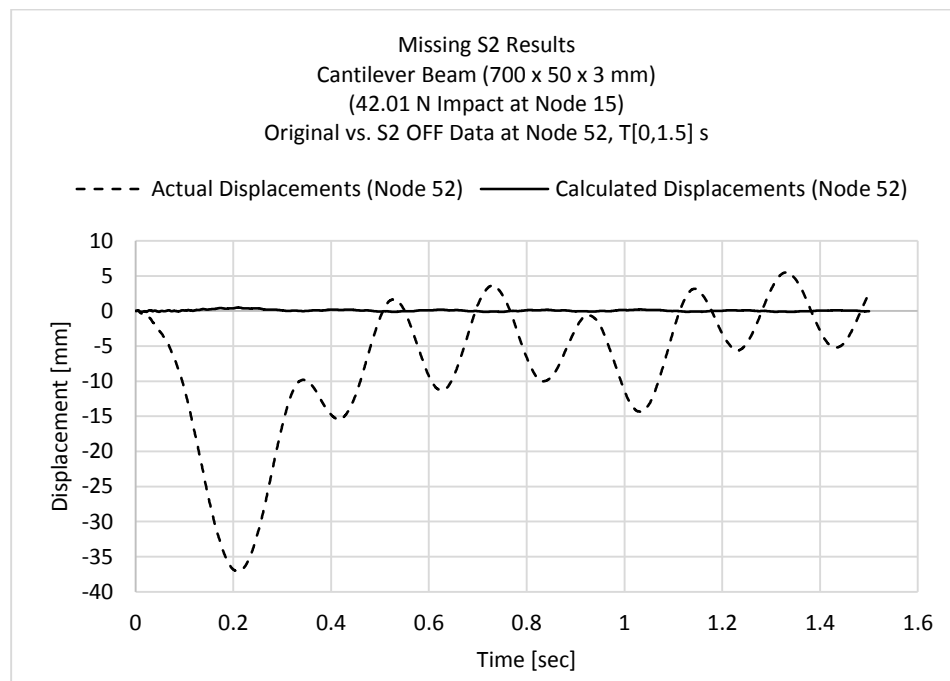


(a) **Displacement at Node 15 with sensor S2 turned off**

Figure 5.15 (a) shows that with sensor located near or at load application point, determines the displacement at the respective point fairly. Whereas Figure 5.15 (b) and (c) demonstrate the inability of the sensors at position 34 and 52 to record the actual displacements at these points. Detailed assessment for this case can be found in A-3 and A-4.



(b) Displacement at Node 34 with sensor S2 turned off

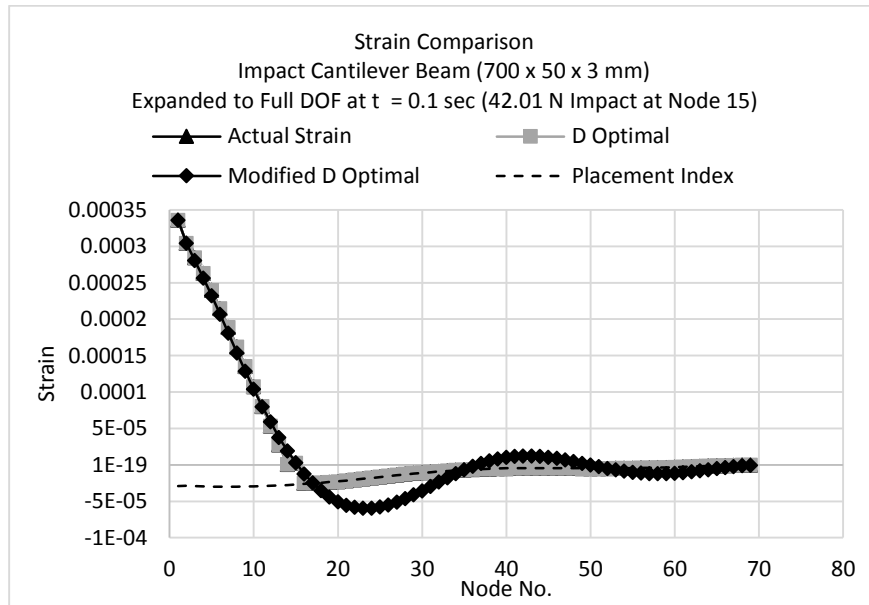


(c) Displacement at Node 52 with sensor S2 turned off

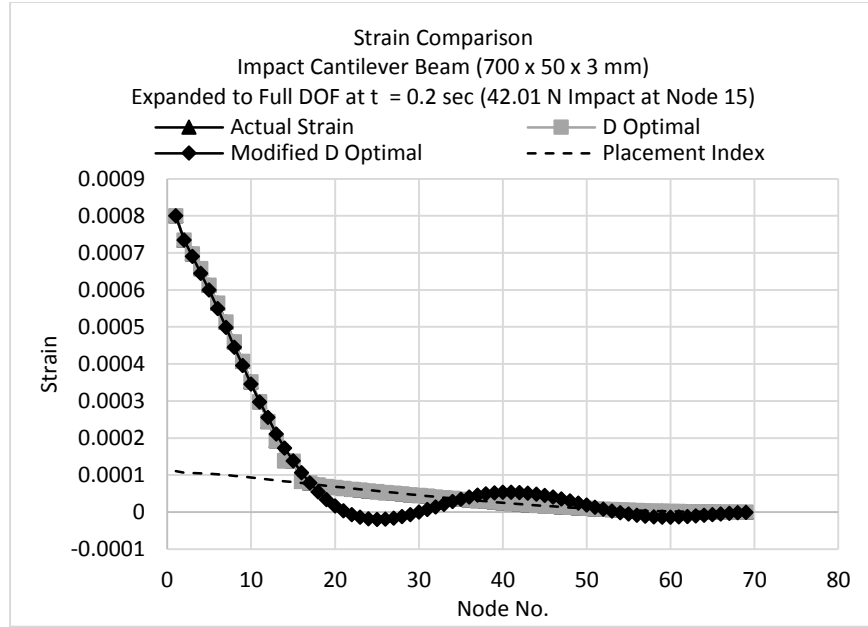
Figure 5.15 Displacements with S2 OFF (Cantilever Beam under impact), T [0-1.5] [s] (a) at Node 1, (b) at Node 34 and (c) at Node 52

5.4.2. Strain Comparison:

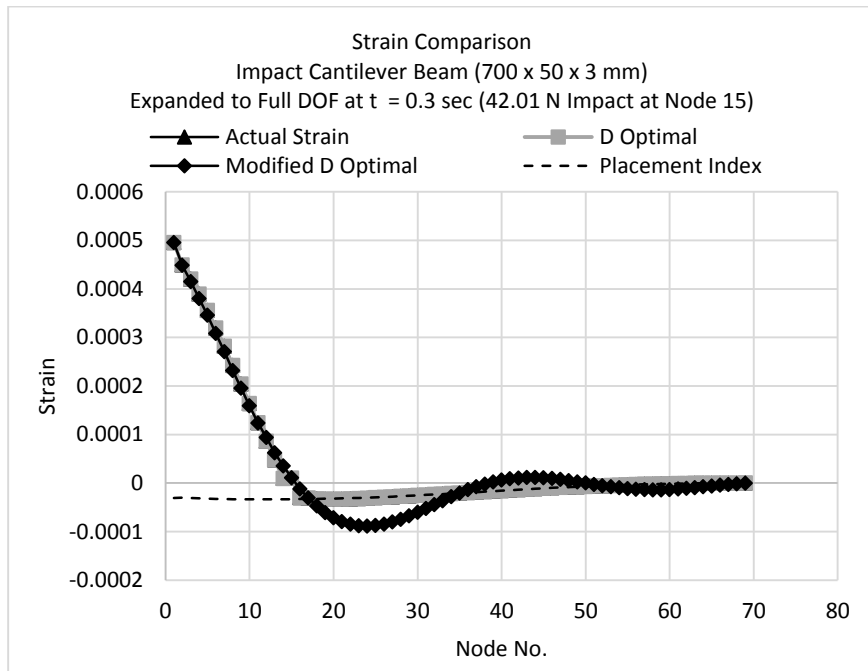
A strain comparison is shown in Figure 5.16 for different placement schemes against the original simulated strain data for $t = 0.1, 0.2$ and 0.3 sec. The strain data has been calculated after the expansion of strain at a) D-Optimal positions [1 16 34 52], b) Modified D-Optimal positions [1 37 35 52] and Placement Index positions [18 36 54 69]. The absence of the sensor in the region (Node 0-17) for Placemen Index scheme shows failed prediction of the actual strain.



(a) Strain comparison at $t = 0.1$ [sec]



(b) Strain comparison at t = 0.2 [sec]



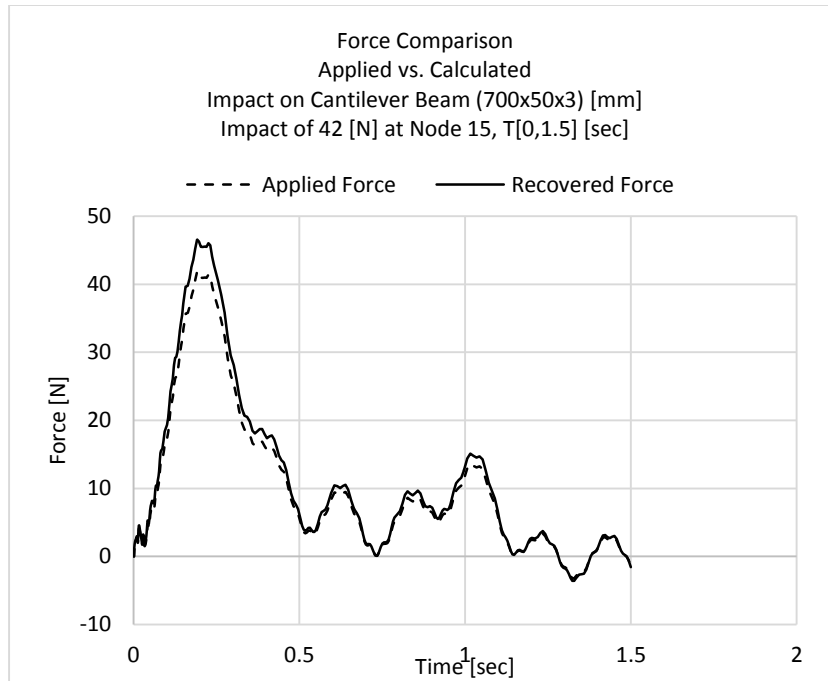
(c) Strain comparison at t = 0.3 [sec]

Figure 5.16 Comparison of the expanded strain solution with the actual displacement of beam for sensor schemes (i) D-Optimal (ii) Modified D-Optimal and (iii) Placement Index at time (a) t = 0.1 [sec], (b) t = 0.2 [sec] and (c) t = 0.3 [sec]

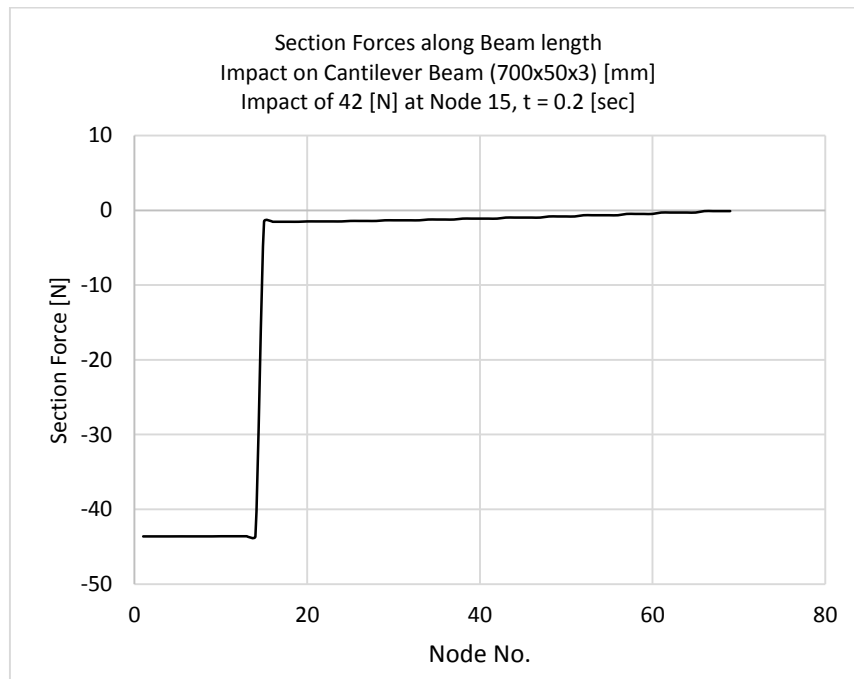
Strain comparison in Figure 5.16 shows yet again the ability of the D-Optimal expanded solution to be in good agreement with the actual strain.

5.4.3. Force Identification (Magnitude):

Similarly force comparison in Figure 5.17 (a) shows the error for force magnitude whose results are summarized in Table 5.11. It also shows that against an impact which spanned 0.02 sec resulted in the impact force detection at 0.2 sec. The numerical delay can be attributed to time stepping in dynamic analysis in COMSOL or the construction of the FEM model. This also signifies the importance of signal delays when using actual sensors. The data acquisition frequency should be fast enough to capture the impact at an effective time and predict accordingly otherwise the signal to be captured will be lost resulting in poor estimates. The force is calculated for D-Optimal Design only as it gave the lowest prediction error for displacement. Figure 5.17 (b) displays the shear force along the length of the beam calculated with the expansion from D-Optimal solution at $t = 0.2$ sec. This verifies the part (a) of the figure in terms of observation at 0.2 sec. Also the load position can also be determined based on the shear force diagram. Force location prediction will be primarily based on minimum difference.



(a) Force recovery over time $t = [0, 1.5]$ [sec]



(b) Force recovery over time $t = [0, 1.5]$ [sec]

Figure 5.17 Comparison of the expanded D-Optimal force solution with the actual force on beam and (b) Section forces developed at $t = 0.2$ [sec] along the beam length

5.4.4. Force Identification (Position):

Figure 5.18 shows the force position identification implemented with the force localization scheme mentioned in chapter 4. The observation was made at $t = 0.1, 0.2$ and 0.3 sec to arrive at identifying force position as node 18 contrary to the original load applied at node 15. Despite varying time, the force location identification was consistent. It was observed through finite element calculations that the maximum impact force magnitude was identified at $t = 0.2$ sec. For this reason the expanded strain solution was tested at $t = 0.2$ sec for the sensor positions identified by (a) D-Optimal, (b) Modified D-Optimal and (c) Placement Index methods.

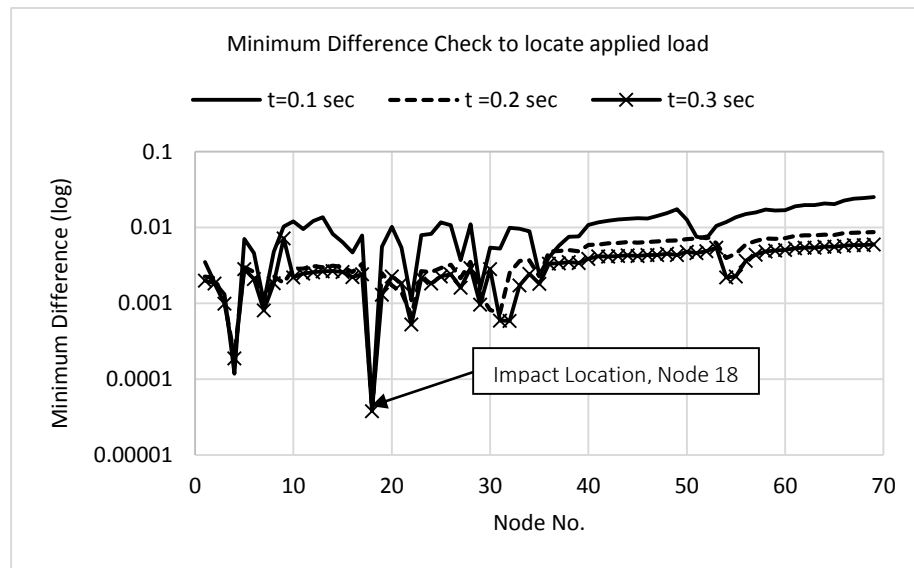


Figure 5.18 Minimum difference check to locate applied load, transition from $t = 0.1$ [sec] to $t = 0.2$ [sec]

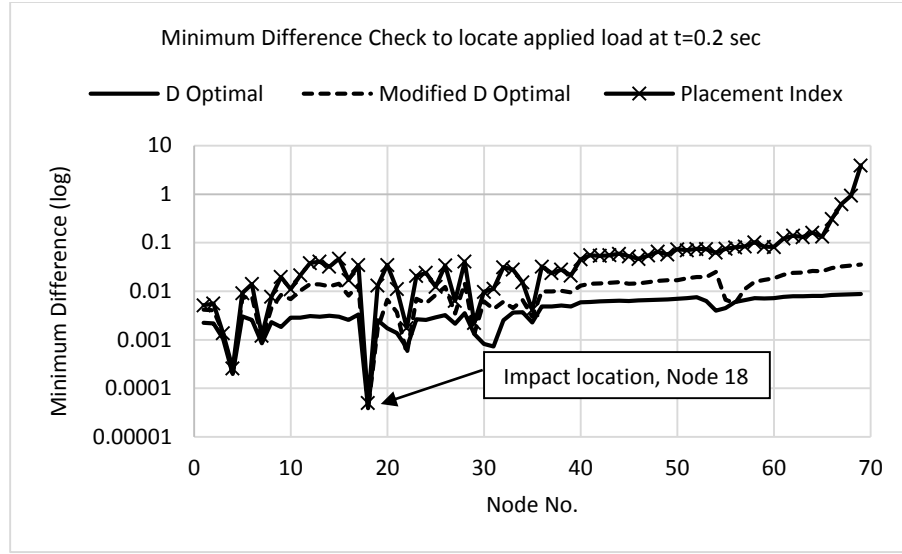


Figure 5.19 Minimum difference check to locate applied load at $t = 0.2$ [sec], comparison between (a) D-Optimal, (b) Modified D-Optimal and (c) Placement Index

Figure 5.19 shows the minimum difference check to locate applied load at $t = 0.2$ sec. A comparison between (a) D-Optimal, (b) Modified D-Optimal and (c) Placement Index shows that all these configurations produced the same impact location.

5.4.5. Error Analysis:

Table 5.11 presents RMS error for the displacement, Strain and Force profile matching at different time instances ($t = 0.1, 0.2$ and 0.3 sec). The RMS error for node 15 is also presented in Table 5.12 over the time span $T [0, 1.5]$ sec. Displacement & strain comparison in Figure 5.14 and Figure 5.16 shows that the error for shape matching remains less than 10 % compared to a slightly higher error from Modified D-Optimal results. Strains were recorded around 16%. The results are summarized in Table 5.11 and Table 5.12.

Table 5.11 % RMS error at $t = 0.1, 0.2$ and 0.3 [sec]

<i>% RMS Error at $t = 0.1, 0.2$ & 0.3 [sec]</i>									
Parameter	Optimization Schemes								
	D-Optimal			Modified D-Optimal			Placement Index		
Time [sec]	0.1	0.2	0.3	0.1	0.2	0.3	0.1	0.2	0.3
Displacement [mm]	7.52	1.56	6.45	2.68	4.63	2.65	129.28	81.34	126.16
Strain	22.41	15.56	20.89	18.45	12.87	17.26	112.20	69.81	108.62
Force (Magnitude) [N]	11.11			-			-		
Force Position (150 actual)	180			190			10		

Table 5.12 % RMS error (displacements) at Node 15 for $T [0, 1.5]$ [sec]

<i>% RMS Error for $T [0, 1.5]$ [sec]</i>	
D-Optimal Method	7.94
Modified D-Optimal Method	9.67
Placement Index	91.04

5.5. Example 3: All Edges Clamped, Rectangular Plate under Forced Harmonic

The plate geometry and material description for this example are presented in Table 5.1. The plate is subjected to a harmonic force of 10 N (46 Hz – Mode 3) in the center (450x, 300y). Figure 5.20 below shows a rectangular plate clamped on all sides. The distribution of candidate positions is set with an interval of 30 mm in both x and y direction. The red dot identifies the sensor obtained from Placement Index, yellow plus for D-Optimal and purple cross for random selection of 4 sensors on the plate.

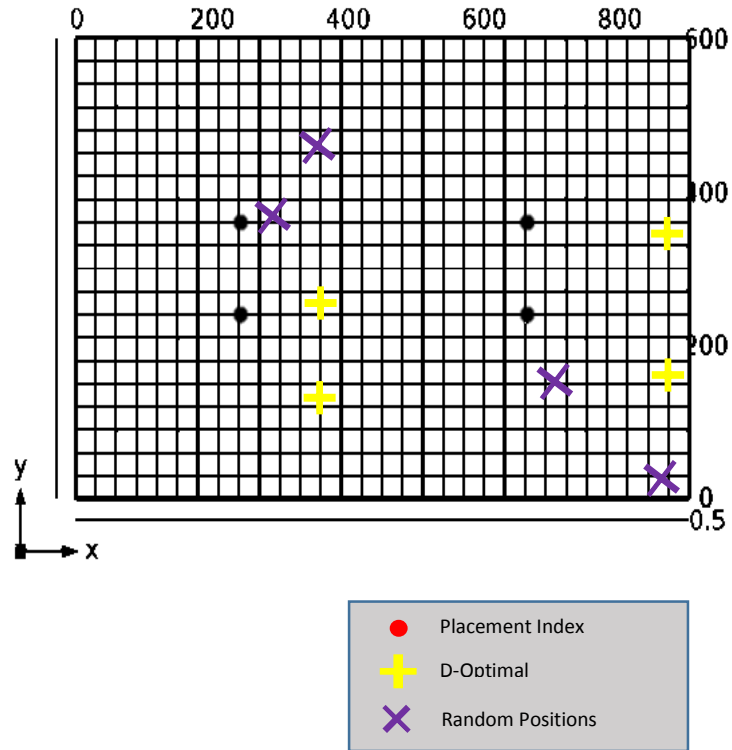


Figure 5.20 Identification of sensor positions on the all sides clamped rectangular plate

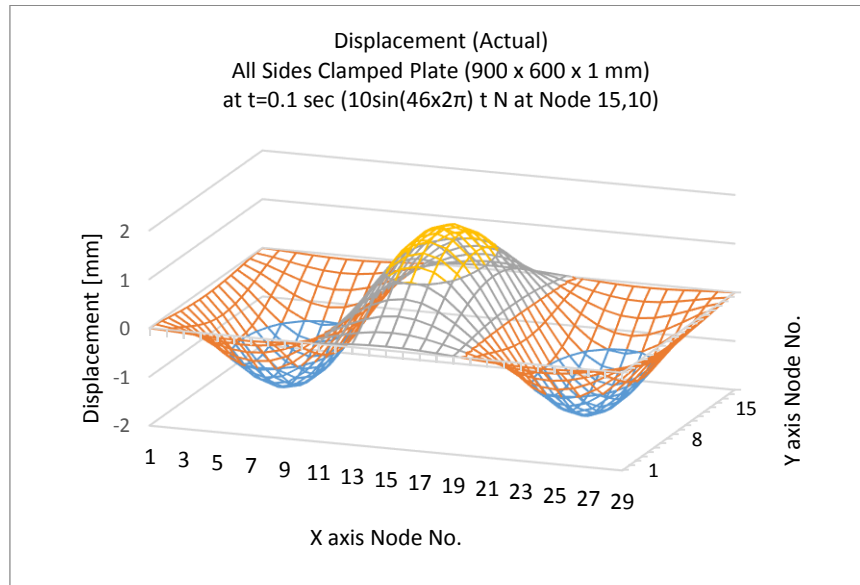
Table 5.13 below shows the sensor coordinate positions for all the schemes mentioned above. The coordinates are represented in (x, y) order.

Table 5.13 Sensor positions (coordinates) tabulated with respect to optimization schemes

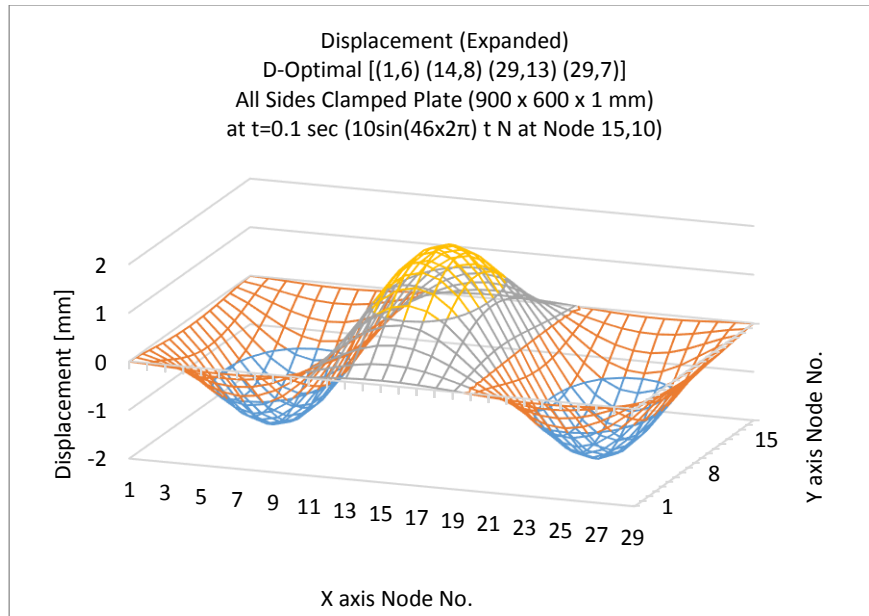
<i>S/No.</i>	<i>Placement Technique</i>	<i>Coordinate Position</i>
1.	Placement Index	(240,360), (240,240), (660,360), (660,240)
2.	D-Optimal	(390,180), (870,210), (390,300), (870,390)
3.	Random Positions	(330,390), (390,480), (720,180), (870,60)

5.5.1. Displacement Comparison

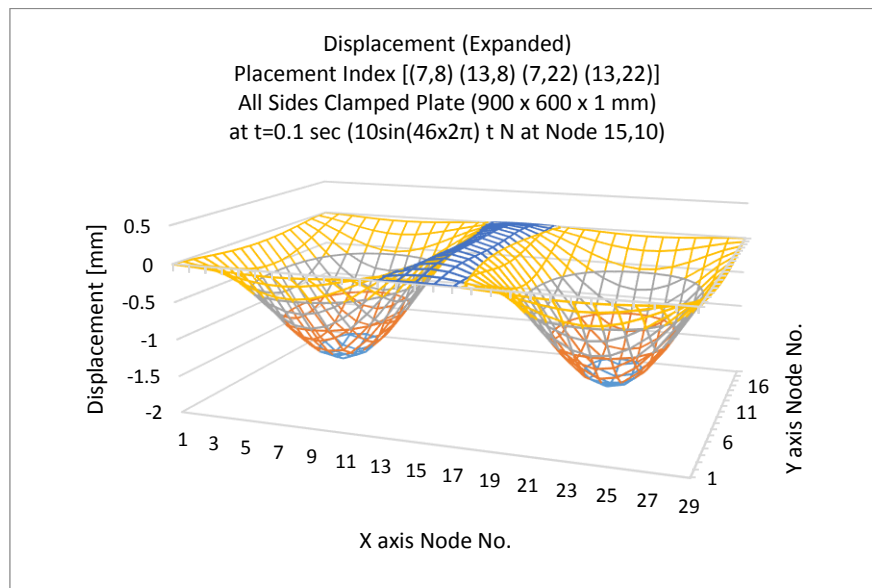
Figure 5.21 shows a complete displacement map for the example plate for different placement schemes namely; a) Placement Index, b) D-Optimal and c) Modified D-Optimal. The displacement maps have been generated by the SEREP expansion by using a limited number of 4 sensors placed in strategically positions. The map profiles from the Placement Index and Modified D-Optimal failed to come close to the original solution, also not been able to generate the specific mode shape (Mode 3). Time varying displacements for plate can be seen in A-5.



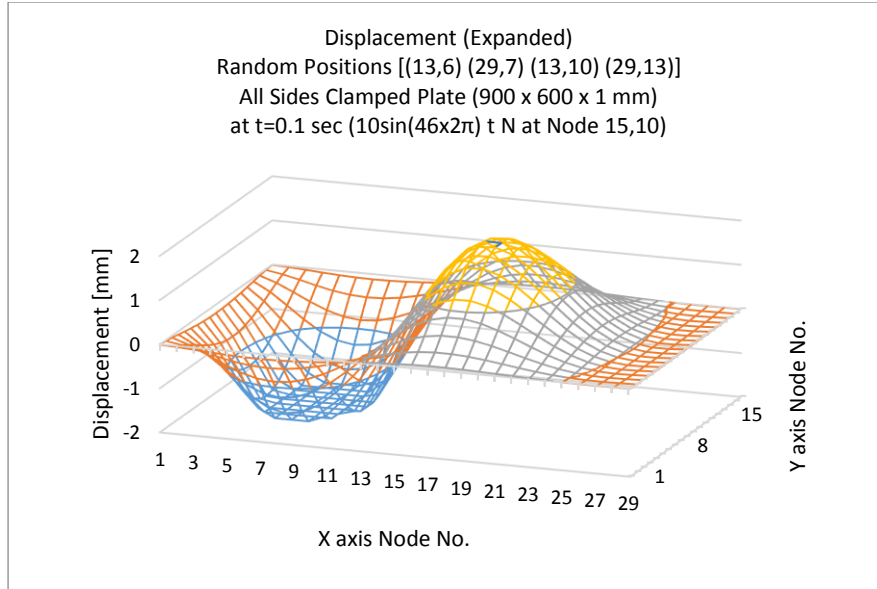
(a) Displacement (Actual) with plate excited in Mode 3 (46 Hz)



(b) Displacement, D-Optimal Expanded



(c) Displacement, Placement Index Expanded

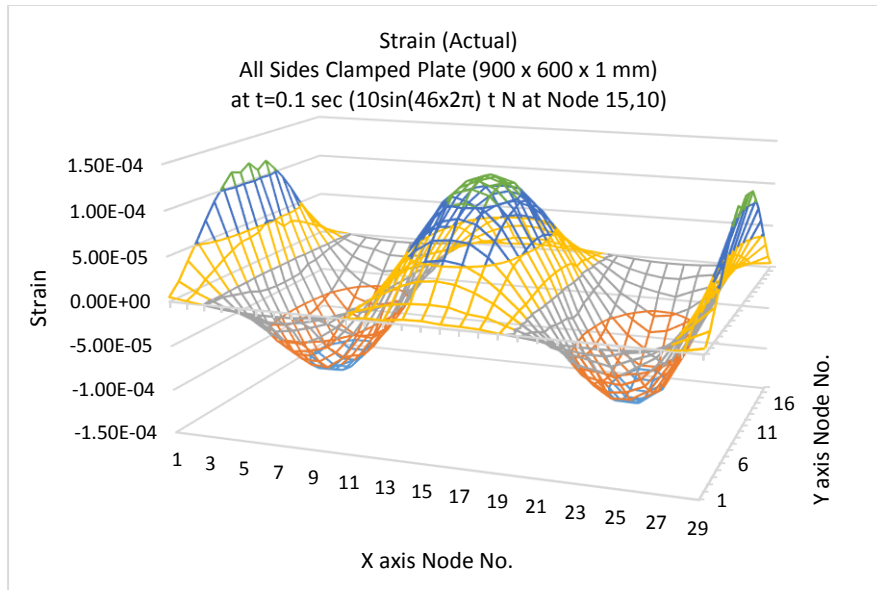


(d) Displacement, Random Positions Expanded

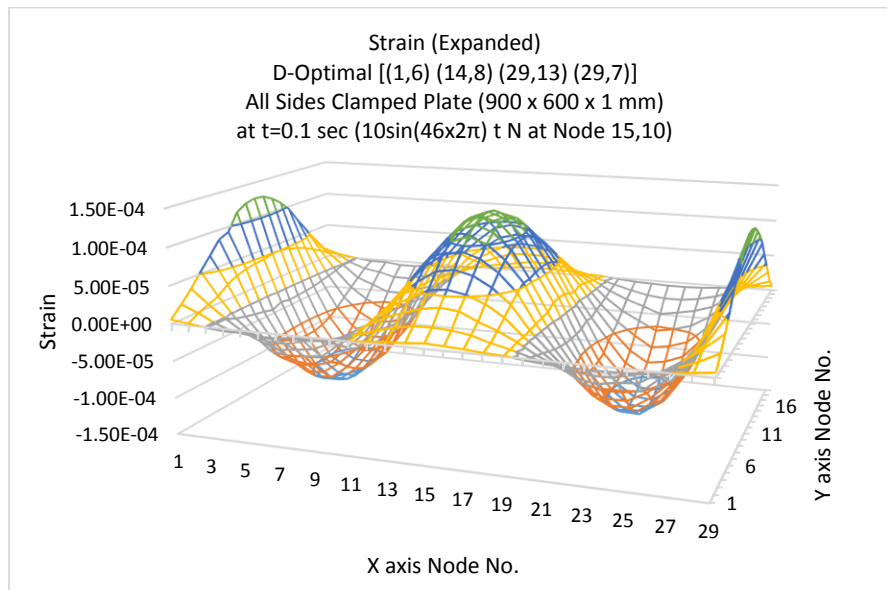
Figure 5.21 Comparison of the expanded displacement solution with the actual displacement of beam for sensor schemes (a) Actual Solution (b) D-Optimal (c) Placement Index and (d) Random Positions at time $t = 0.1$ [s]

5.5.2. Strain Comparison:

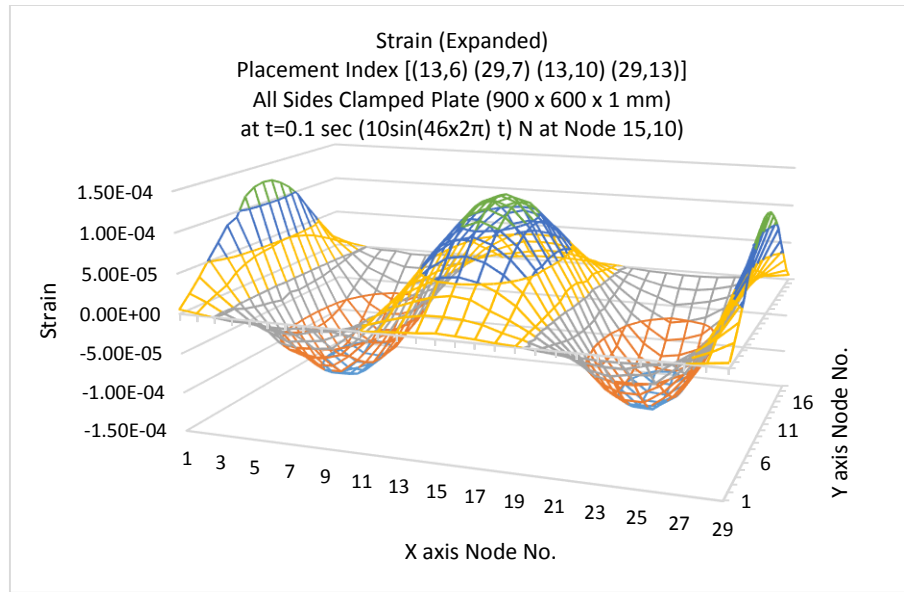
Contrary to displacement comparison, Figure 5.22 reveals that despite different position layout outs, the strain prediction was accurate. The expansion for displacements were based on SEREP expansion but for strains, expansion procedure was not applied rather using the modal strain matrix and the calculated MPFs. Figure 5.22 shows a complete strain map for the example plate for different placement schemes namely; a) Placement Index, b) D-Optimal and c) Modified D-Optimal against the original strain solution. All results accurately predict the distinctive mode 3 shape.



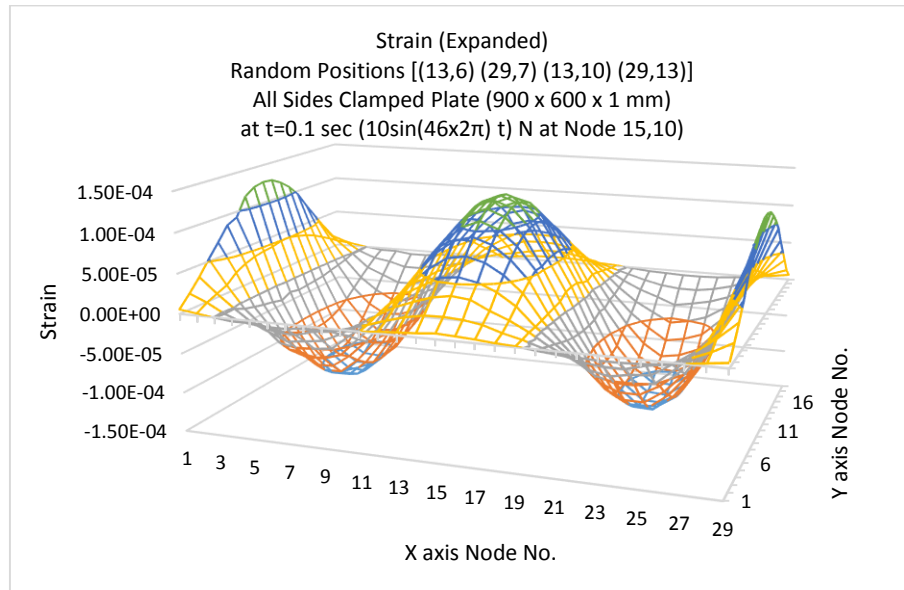
(a)



(b)



(c)



(d)

Figure 5.22 Comparison of the expanded strain solution with the actual displacement of beam for sensor schemes (a) Actual Solution (b) D-Optimal (c) Placement Index and (d) Random Positions at time $t = 0.1$ [s]

5.5.3. Error Analysis:

The error summary for displacements and strains are provided in Table 5.14.

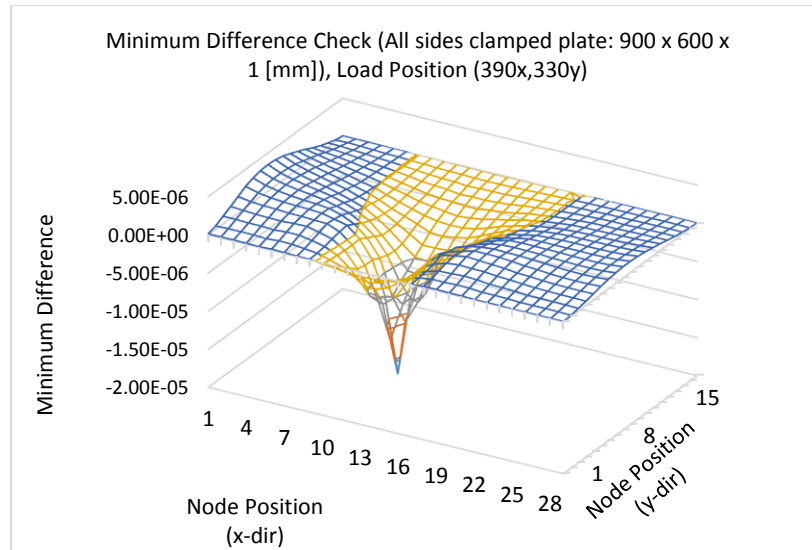
Table 5.14 % RMS error at $t = 0.1$ [sec] for displacements and strains against different optimization schemes.

Parameter	% RMS Error at $t = 0.1$ [sec]		
	Optimization Schemes		
	Placement Index	D-Optimal	Random Position
Displacement	25.90	1.12	82.25
Strain	5.83e-10	1.01e-09	9.61e-10

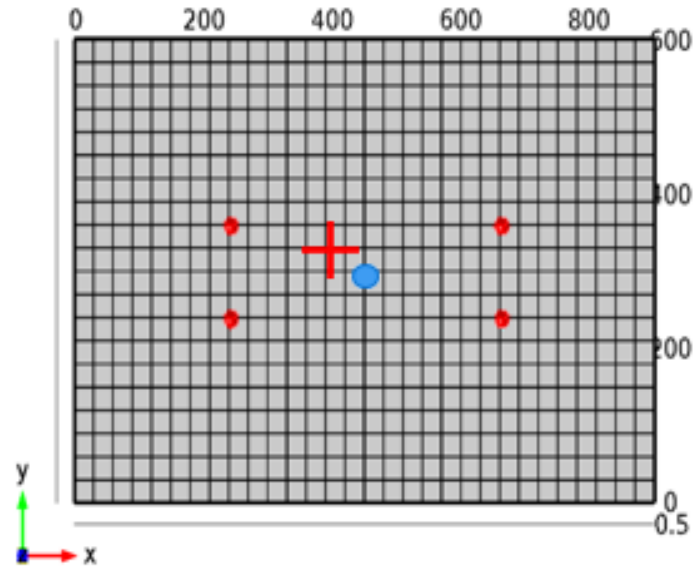
5.5.4. Force Identification (Position):

The force position is determined by the minimum difference scheme for force localization.

The actual impact was at 450 x and 300 y but the solution lead us to finding out position at 390 x and 330 y as shown in Figure 5.23. Though the location has not been identified accurately but since we have displacements at all locations, we can construct the shear force in the structure to reach at an accurate solution in terms of force position.



(a) Minimum Difference Check to obtain force location (390x, 330y)



(b) Force location (390x, 330y) '+' mark identified through D-Optimal

Figure 5.23 Minimum difference check to locate applied load at $t = 0.1$ [s], comparison between D-Optimal and original location

5.5.5. Force Identification (Magnitude):

Figure 5.24 shows a comparison between the theoretical force and the expanded data at D-Optimal sites. Force location was (15, 10) corresponding to (450 x, 300 y). The data starts to match after $t = 0.3$ sec. When observed over a period of 1 sec, the force errors were calculated to be around 13%.

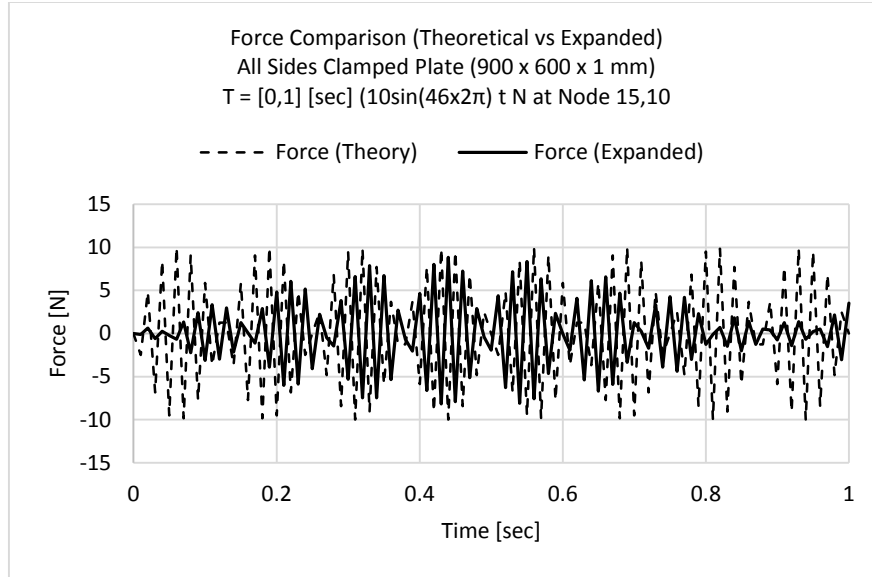


Figure 5.24 Comparison of the expanded D-Optimal force solution with the actual force (450 x, 300 y) on all sides clamped plate, $T = [0,1]$ [sec]

Table 5.15 summarizes on the structural examples used along with the mode shapes considered for optimal placement of sensors.

5.6. Conclusion:


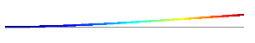
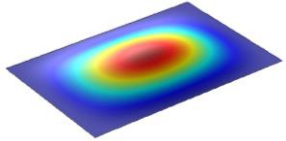
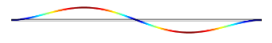

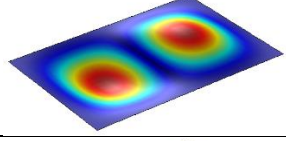
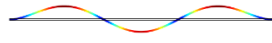
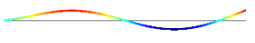
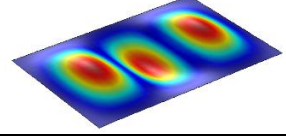
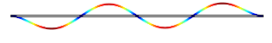
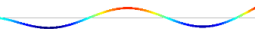
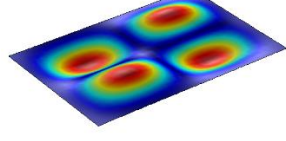
Based on the above work, strain data can be used from any strain sensors like FBG to extract unknown force and its location. There is a margin to improve by identifying multiple source of force uniquely. D-Optimal method has been shown to implement sensor placement for accurate force prediction with the aid of force localization.

The D-Optimal solution for Dynamic Sensor location was also compared with the Placement Index Technique (based on norms). Both solutions were compared on the basis of displacement and force prediction in the entire structure through the SEREP expansion

procedure. D-Optimal solution produced better results and other solutions were mostly able to identify the excited mode as well.

The utility of the above exercised technique is that it will help us use the embedded sensor strain data from the optimal sites and later on expand the solution using System Equivalent Reduction Expansion Process (SEREP). The expanded solution will give strain information at all untapped locations.

Table 5.15 Mode shapes for structural examples

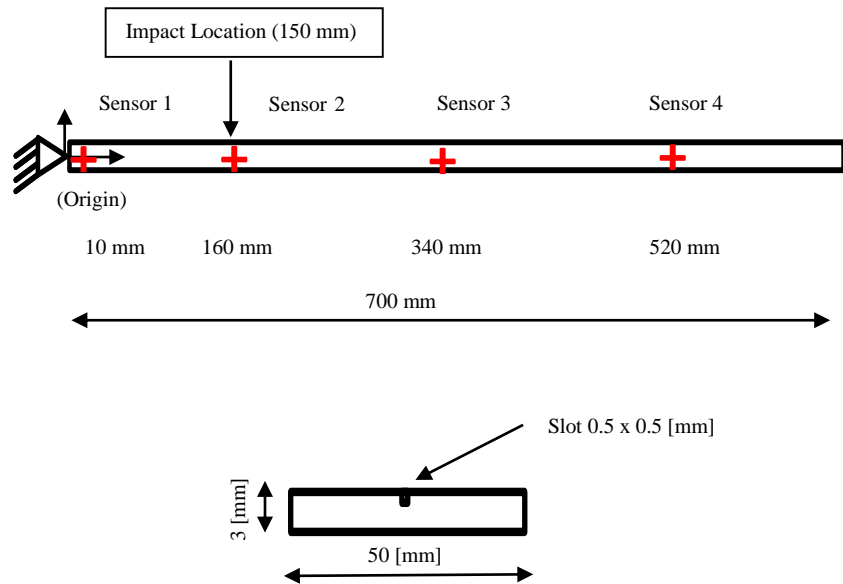
Type of Structure			
B.C	Beam, Clamped-Clamped	Beam, Cantilever	Plate, All Edges Clamped
Geometry (x, y, z)			
	1500 x 5 x 5 mm	700 x 50 x 3 mm	900 x 600 x 1 mm
Load Node			
	6	15	450 x, 300 y
Natural Frequency (Hz)			
Mode 1	11.53	5.04	18.54
Mode 2	31.78	31.56	28.66
Mode 3	62.31	88.37	46.04
Mode 4	103.03	173.16	55.34
Graphics			
Mode 1			
Mode 2			
Mode 3			
Mode 4			

CHAPTER 6

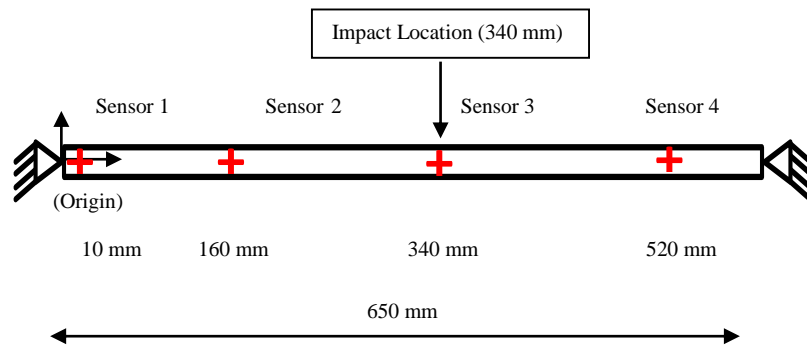
EXPERIMENTAL STUDY

In order to validate the concept through experimental means, we need to firstly select a system and identify the D-Optimal sites as per steps shown in Figure 5.1 and Figure 5.2. Later on, the structure would be instrumented with FBG sensors (single/array). The purpose of such test would be to validate the concepts previously explained in chapter 5 giving us confidence in using the strain sensors like FBG at optimal sites for complete construction of displacement and strain profile. The tests would give an insight to apply SEREP expansion procedure mentioned in chapter 4 on instrumented structures. Based on the accuracy of expansion on displacements and strains, we would be in a position to identify the applied force magnitude and location.

Validation work will be carried out on a cantilever beam of dimensions 700 x 50 x 3 mm as mentioned in example 2 of chapter 5. A square slot of dimensions 0.5 x 0.5 mm runs through the middle of the beam in length direction as shown in Figure 6.1 (a). The slot has been created to accommodate the FBG sensor (nominal diameter 250 μm). The FBGs are further brought in to their required optimal sites and secured with an epoxy glue, embedding the fiber in the created slot. Another example to implement the expansion procedure is illustrated through a cantilever beam of dimensions 650 x 50 x 3 mm with the sensors installed in location shown in Figure 6.1 (b).



(a) D-Optimal Positions, Cantilever Beam (Figure not to scale)



(b) Sensor Positions, Clamped-Clamped Beam (Figure not to scale)

Figure 6.1 Sensor positions, (a) D-Optimal sites, cantilever and (b) clamped-clamped beam with impact locations

The applied force is an impact which features force amplitude, duration of impact and the shape profile of the impact. The purpose to use an impact force is to collect information

through a force measurement device (impact hammer) and to be applied to the FEM model. The data collection can also be done in case of other force measurement device/instrument available.

The following paragraph will describe the strategy behind the experiment(s) in order to streamline data acquisition procedures to comply with the theoretical calculations performed with FEM.

6.1. Experiment Strategy:

The flow chart of experimental development is illustrated in Figure 6.2. This is presented as a route to determine the unknown applied impact and its location. The initial step is to determine the calibration/gage factor for the FBG sensors. The definition for calibration/gage factor have been detailed in chapter 3. The gage factor essentially helps setup the strain collection through the data acquisition hardware. Gage factor used for the experiment is 0.5. The data hardware characteristic will be explained in section 6.2. It is also very important to evaluate the structural dynamic characteristics in order to verify the conformity of the experimental data with the FEM model of the structure. Experimental Frequency Response Function (FRF) determination through an impact device and an accelerometer is a common practice to observe the excited modes of the structure under dynamic loading. Upon validation of the FRF, we install the sensors into the slot at optimal locations. The sensors are then connected to the data acquisition hardware to record the data. This data is then compared to the FEM results generated using the same impact force information from the experiment. The expansion on the strain and displacement data from the FBG strain sensors is then later evaluated to predict force location and magnitude.

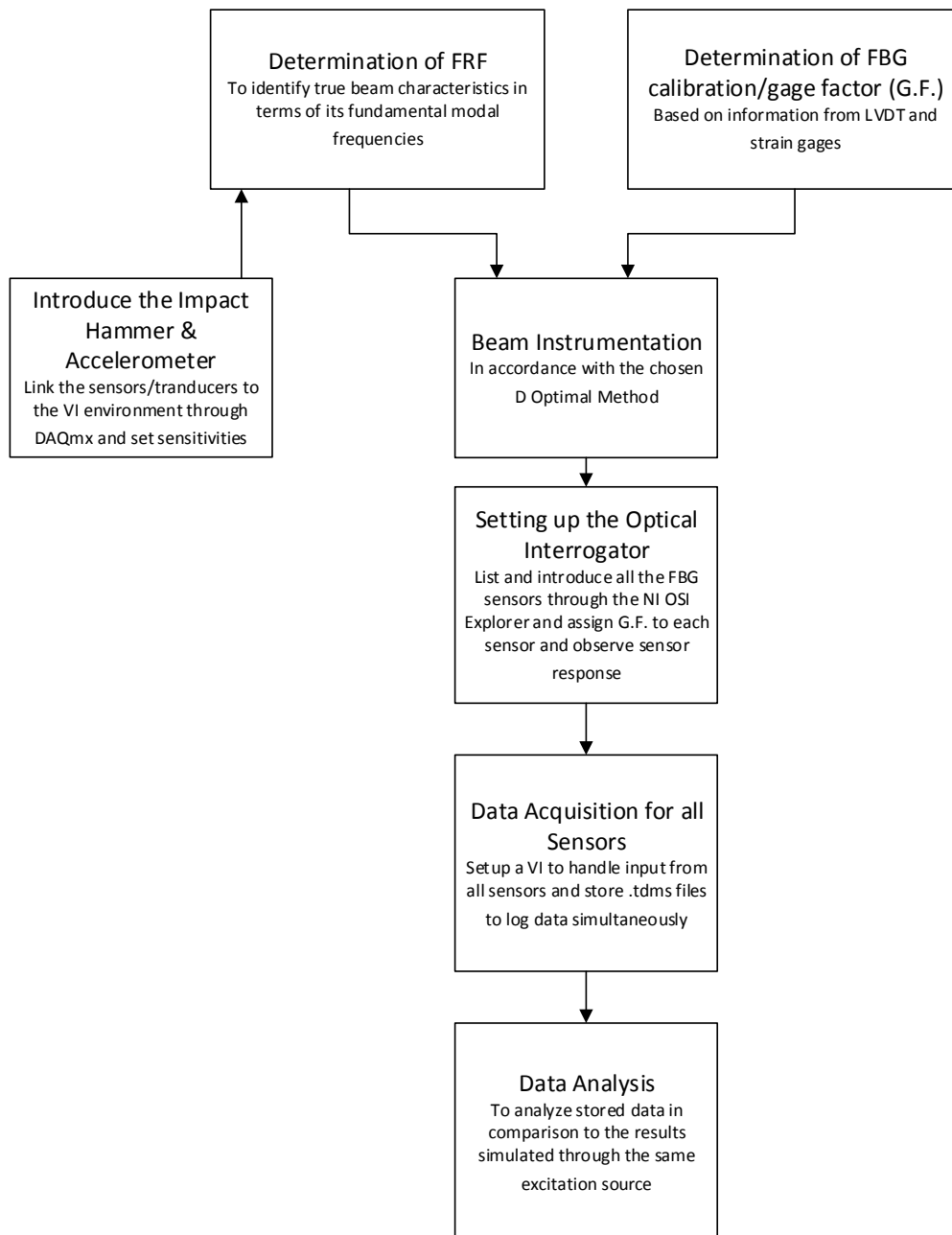


Figure 6.2 Experimental development flow chart

6.2. Equipment/Hardware Details:

Following is the list of experimental hardware and their associated characteristics for data acquisition.

Impact Hammer + Accelerometer Module:	NI 9234 (Sound & Vibration Input Module, 51.2 k Sample/s/ch)
Strain Gage Module:	NI 9235 (Quarter Bridge Module, 8 Channel 10k Sample/s/ch) along with NI cDAQ 9171
FBG Interrogator:	NI PXIe 4844 4 Channel Optical Sensor Interrogator, Sampling Rate 10 Hz, $\lambda=1510-1590$ [nm]
FBG:	1 Single and 3 Array FBGs, length 10 [mm]
Strain Gage:	Omega, Steel Wire, 9.5 x 3 [mm], 120 [Ω]
Impact Hammer:	Bruel & Kjaer-8602-002, Sensitivity 2.27 [mV/N]
Accelerometer:	PCB, 352C04, Single Axis, Sensitivity 10 [mV/g]

The purpose to use the impact hammer is to quantify the amount of force delivered to the system and we could later compare whether the sensors were able to predict the magnitude and position of this impact. A single axis accelerometer has been included in order to verify the structural dynamics response through Frequency Response Function. This will

give us confidence in knowing whether the FEM model has been constructed to represent the actual system.

The data acquisition hardware should be able to collect adequate data samples in an observation time T $[0, t]$. The number of samples collected in one time $t = 1$ sec is called the '*sampling frequency*'. The sampling frequency should be at least or more than 2 times the frequency of the object under observation (Nyquist Criteria). It was observed that the lowest vibration mode (Mode 1) for the vibrating cantilever structure is 5 Hz. With the FBG interrogator of 10 Hz sampling frequency, we would only be able to see the mode 1 activity of the beam. From our observation of results from example 2, chapter 5, we could see that the impact at location 150 mm from the fixed end excited the structure in mode 1 (see Figure 5.14). Hence, we could use the FBG interrogator to observe the dynamic performance of the beam.

We now proceed to explain the Graphical User Interface (GUI) built for data acquisition. The data acquisition is handled in a National Instruments (NI) software LabVIEW. The GUIs built in LabVIEW are called Virtual Instruments (VI's). The VI's can be programmed to connect to data acquisition hardware and process the collected information to present the sensor information according to our choice.

6.3. VI Development & Data Acquisition:

The data is obtained by customizing a NI LabVIEW, VI to handle simultaneous input from the impact hammer, accelerometer, FBG and the strain gage. The VI used for data acquisition is provided in appendix A-6. Apart from the data acquisition part, it is also essential to setup the FBGs through a setup called NI OSI Explorer. The sensors require

gage factor information and sensor indexing before proceeding with the data acquisition. Figure 6.3 presents the GUI displaying signature wavelengths of 3 FBG array in the NI OSI Explorer.

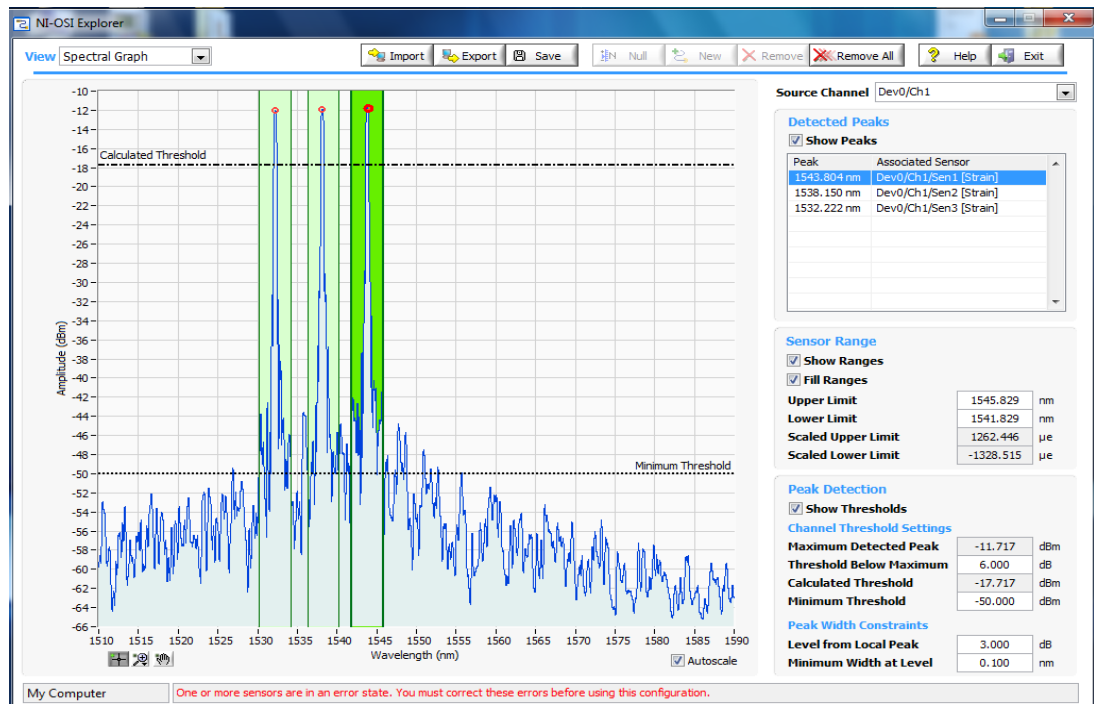


Figure 6.3 NI OSI Explorer GUI displaying signature wavelengths of individual sensors in array and the effect of strain

We now proceed to explain the steps in order to experimentally evaluate the Frequency Response Function (FRF).

6.4. Frequency Response Function (Experimental):

A frequency response was evaluated using the impact hammer and accelerometer in order to (a) verify the COMSOL model against experimental results and (b) to see the effect of

damping on the natural frequencies. The response of accelerometer to impact is immediate while the strain gage responded with a delay of approximately 2.459 ms and FBG with a delay of 2.5 ms. A strain gage was installed as a part of strain calibration with the FBG. FBG and strain gages responded to impact in the same manner. Figure 6.4 shows the hardware used for FRF and the resulting output.

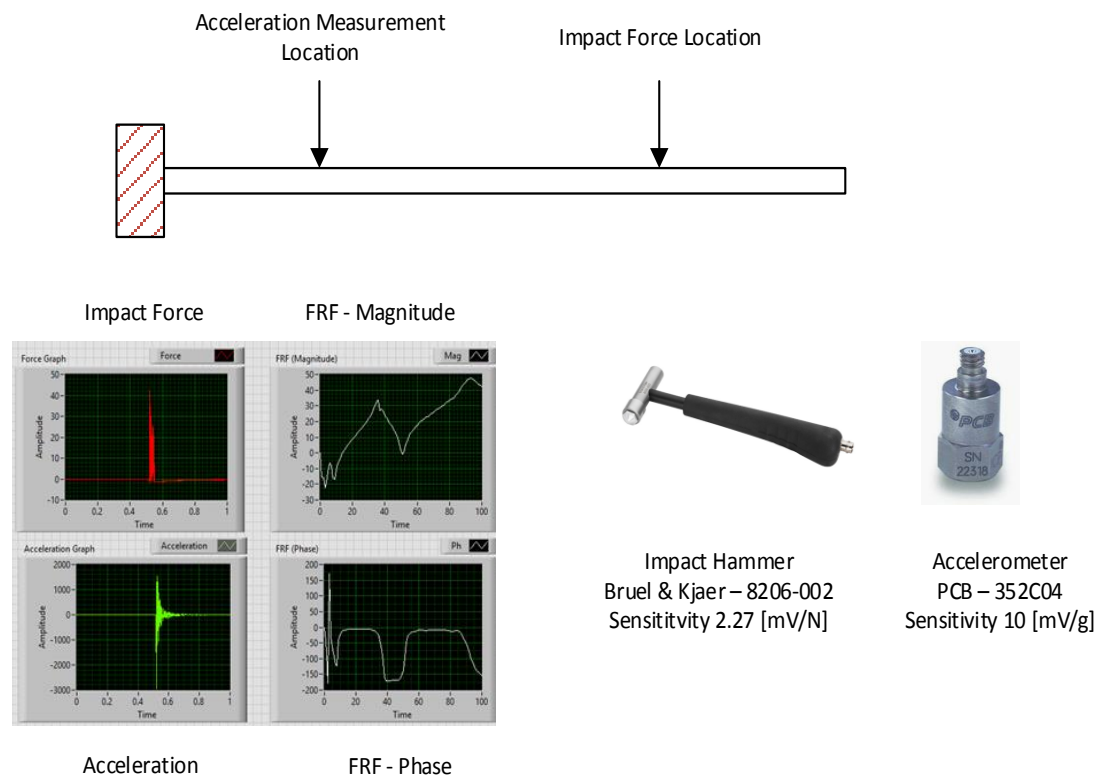


Figure 6.4 Impact hammer and accelerometer used in experiment to generate FRF

Figure 6.5 shows the response from the individual sensors; impact hammer and the accelerometer and the associated frequency response function generated as a result of an impact of 10.01 N producing a max acceleration of 20.54 g. The frequency response thus

produced is close to the analytical and simulated results for an identical beam geometry with similar boundary conditions. The accelerometer mass has not been considered while comparing the experimental results with the FEM.

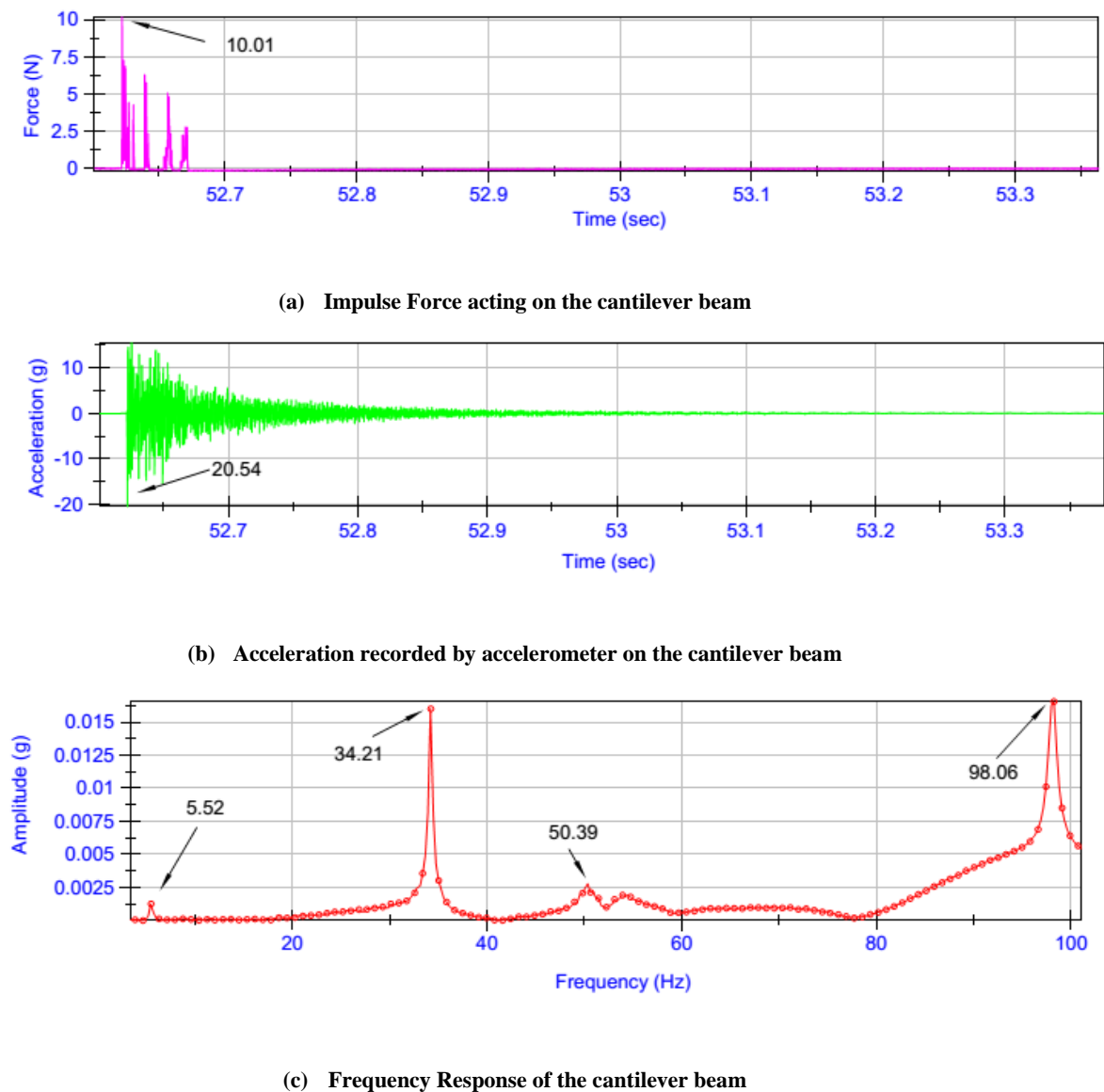


Figure 6.5 (a) Force data and (b) acceleration data to produce (c) frequency response of the impact on the cantilever beam

Listed in Table 6.1 are the first four Eigen frequencies for the beam modeled in COMSOL

a) 2D Beam Physics and b) 3D Solid Mechanics. Comparing to the experimental results

there is a reasonable agreement when compared to the theoretical values. The validation encourages us to use the mode shape matrix and associated dynamic characteristics obtained through FEM for expansion of experimental strain and displacement data.

Table 6.1 Modal frequencies obtained from FEM against (a) 2D Beam Physics and (b) 3D Solid Mechanics

Mode No.	Frequency (Hz)	
	2D Beam Physics	3D Solid Mechanics
1	5.04	5.064
2	31.56	31.77
3	88.37	89.57
4	173.16	175.36

6.5. Experimental Impact Test (Cantilever Beam):

This section will present the steps involved in obtaining experimental strains from the FBG sensors installed on a cantilever beam. Later the strain data will be expanded using SEREP with the help of FEM matrices and dynamic characteristic information.

6.5.1. Experimental Setup:

The experimental investigation has been designed to assist in acquiring the true characteristics of the system through proper implementation of device/senor setup and to gather information from FBG strain sensors to identify location and magnitude of an unknown impact.

The sensor positions for the embedded FBG under impact are illustrated in Figure 6.6. The actual setup along with instrumented beam, Fiber Optic interrogator and associated hardware are shown in Figure 6.7.

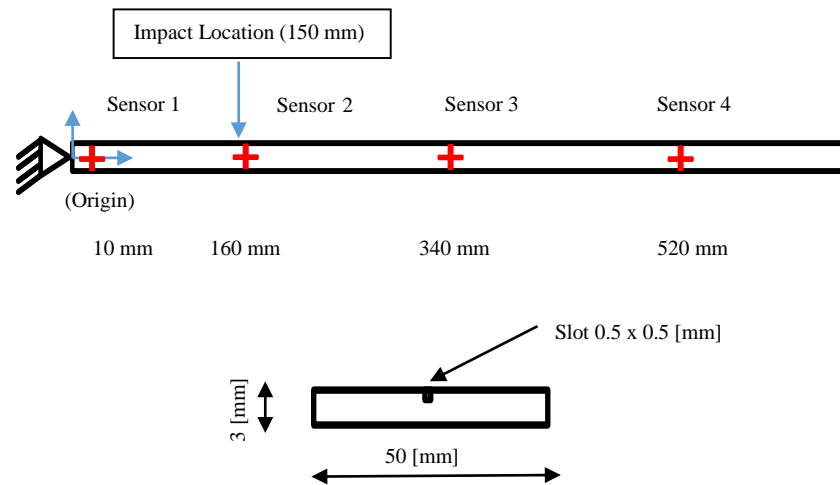


Figure 6.6 Beam dimensions and sensor positions (cantilever)

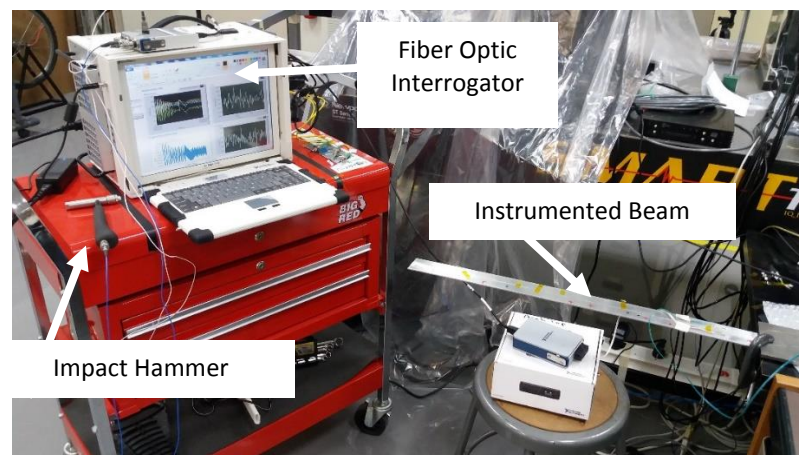


Figure 6.7 Complete experimental setup along with instrumented beam with embedded FBG array

6.5.2. Strain Results:

The experimental strains from FBGs are obtained as a result of impact of approximately 20.07 N at a location 150 mm from fixed end is shown in Figure 6.8.

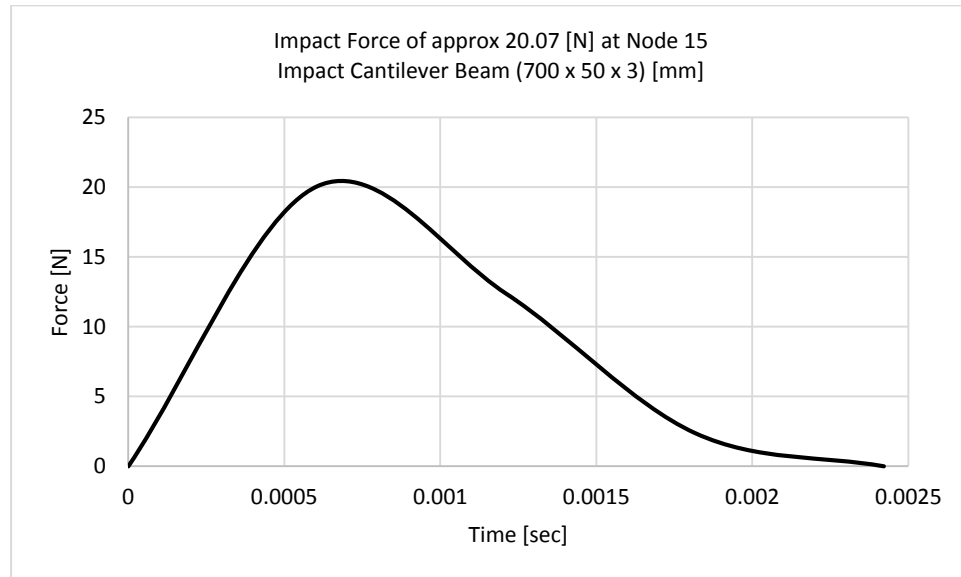


Figure 6.8 Experimental impact force 20.07 [N]

The impact force data shows that the peak amplitude (20.07 N) occurred at 0.7 ms and the span of impulse is 2.5 ms. Figure 6.9 shows the strain data obtained from FBG sensors at the specified D-Optimal locations. These strains need to be calibrated according to the theoretical strain from the FEM, the gage factor used was 0.5. Strain data also reveals that the response of the FBGs in their respective locations is appropriate as the sensor closest to fixed end has high strain compared to the ones farther away.

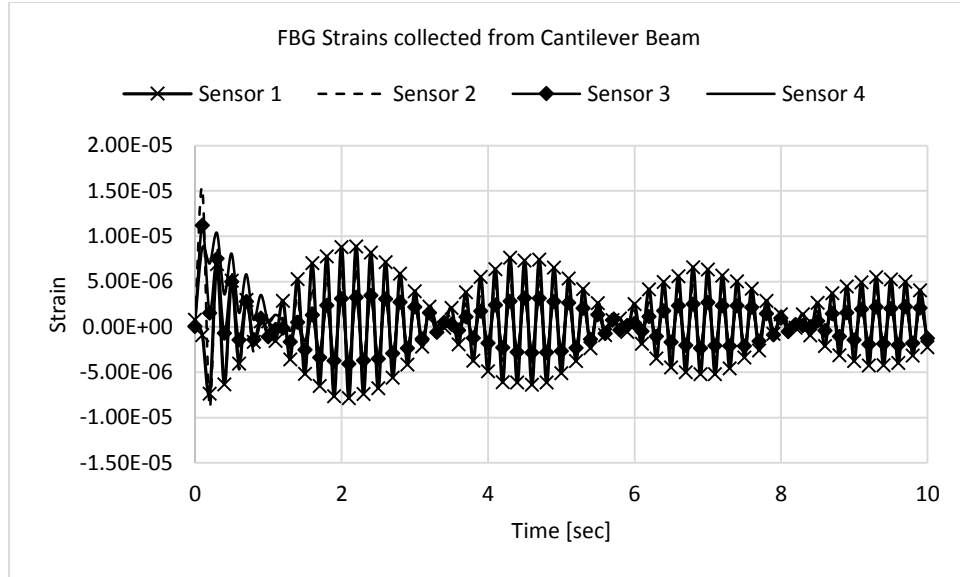
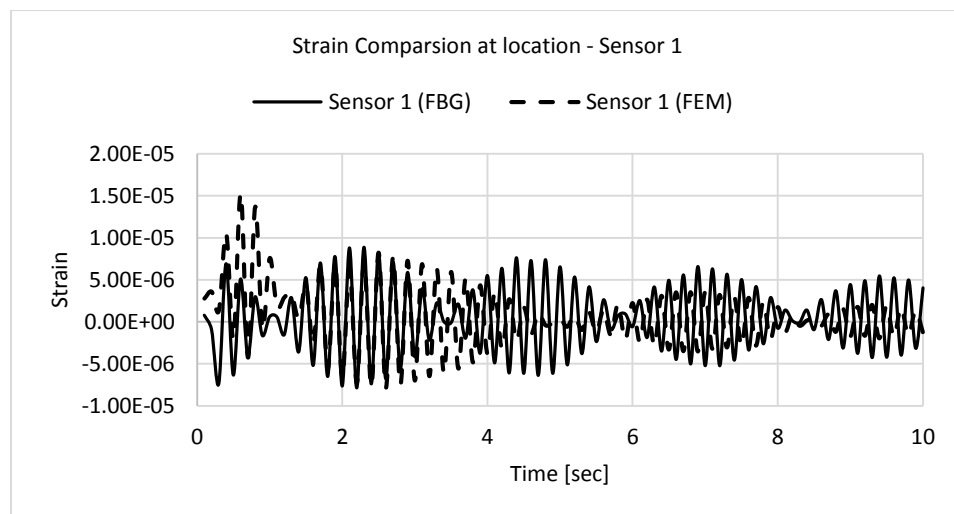
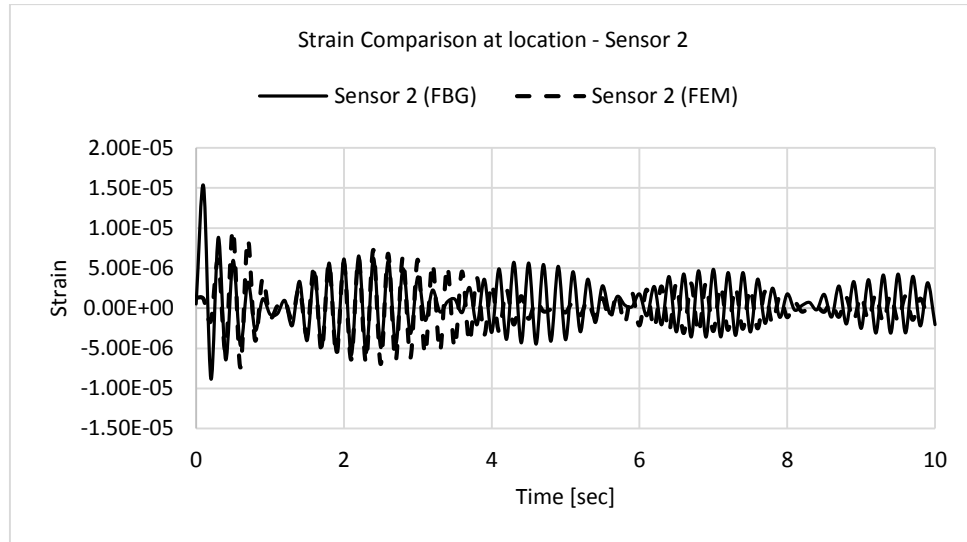


Figure 6.9 FBG strains recorded at sensor position 1-4

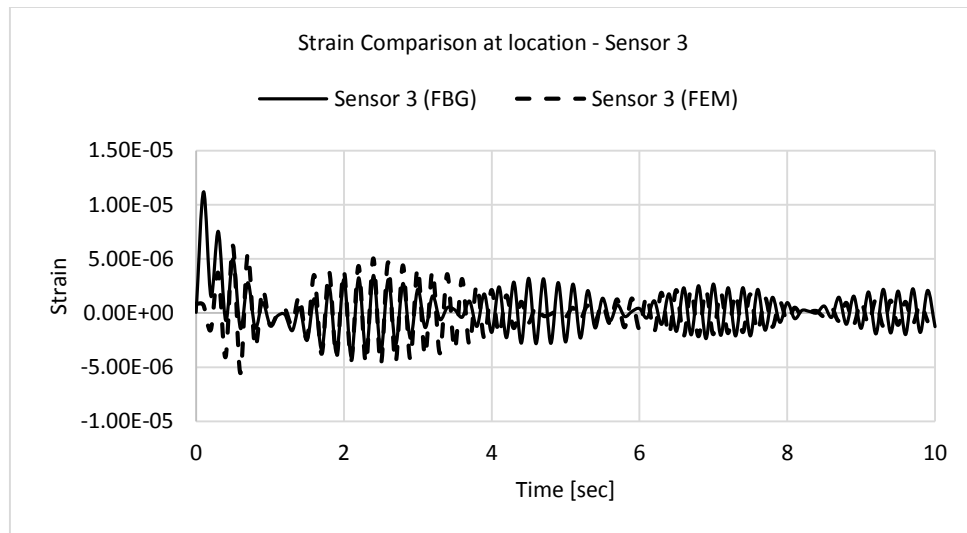
The experimentally obtained strains were compared with the results of the FEM based model. The force input for the beam was used from the impact hammer force data to simulate the same impact at a location of 150 mm from fixed end. The resulting strains are compared with the FBG strains in Figure 6.10



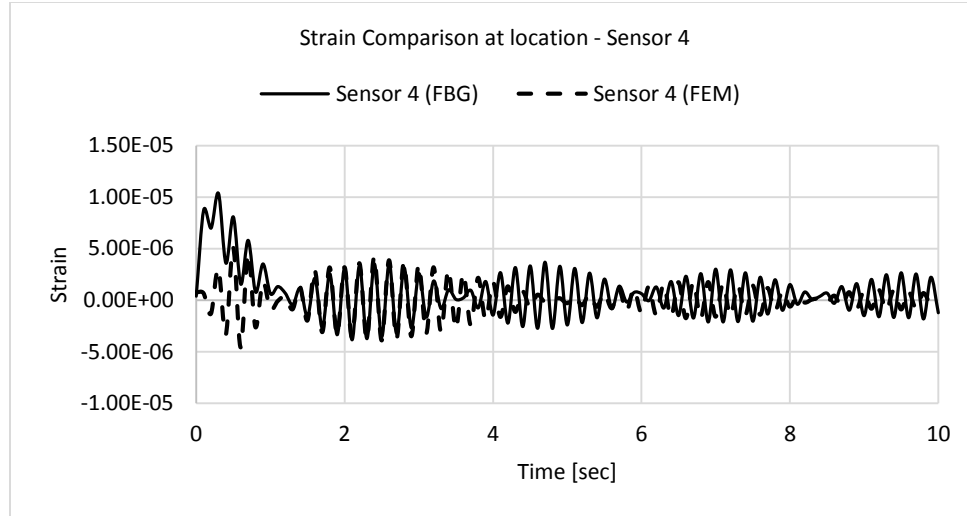
(a) Strain comparison between FBG data and FEM at sensor 1



(b) Strain comparison between FBG data and FEM at sensor 2



(c) Strain comparison between FBG data and FEM at sensor 3



(d) Strain comparison between FBG data and FEM at sensor 4

Figure 6.10 (a-d), Comparison of experimental results to simulated (cantilever)

Upon comparison, the difference between the experimental and the simulated results through FEM were found to have an RMS error around 20%. The source of discrepancies can be attributed to variation in boundary condition, sensor mounting and sensor data. These errors could affect the force prediction and we would like to see the impact of such errors on the result. The static strain evaluated in response to the peak impact load (20.07 N) produced results similar to the dynamic strain at experimental peak load.

6.5.3. Displacement Prediction:

Displacement profile is predicted after expanding the displacements known at optimal sites and applying SEREP. Expansion results for the entire beam would result in a complete displacement profile of the structure based on all available nodal displacements as shown in Figure 6.11. It was observed in the FEM solution that the applied force is recognized at a time mark of 0.6 sec. Modifying the impact profiles (amplitude, span and shape profile) resulted in different reaction times to the actual applied load in FEM

simulations. When compared to the theoretical solution, the experimental results provided an RMS error of around 11% at 0.6 sec (see Table 6.2).

Table 6.2 % RMS error for displacements at different times (Cantilever Beam)

<i>% RMS Error at different times</i>				
Time	t = 0.1 [sec]	t = 0.2 [sec]	t = 0.3 [sec]	t = 0.6 [sec]
Displacement	1.86	9.86	7.18	10.85

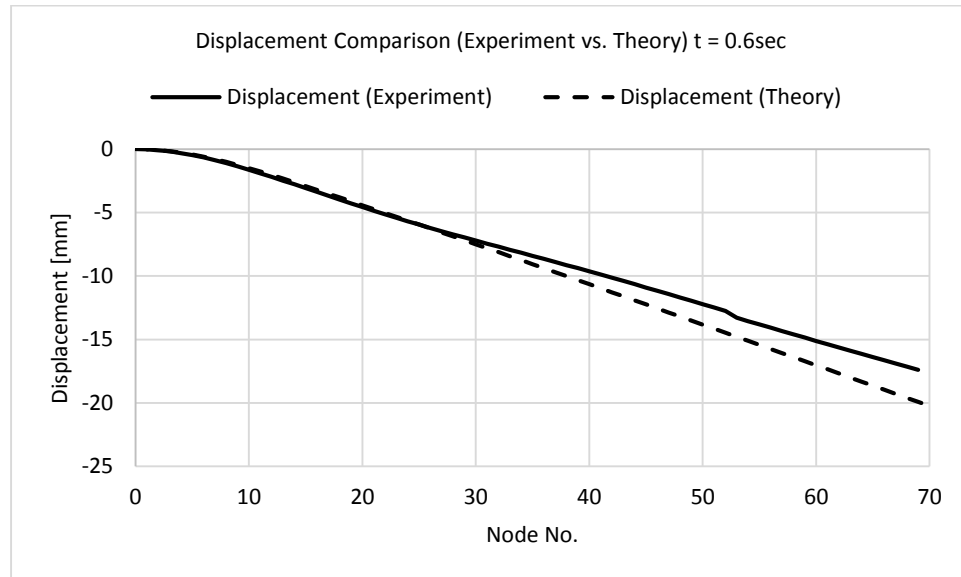


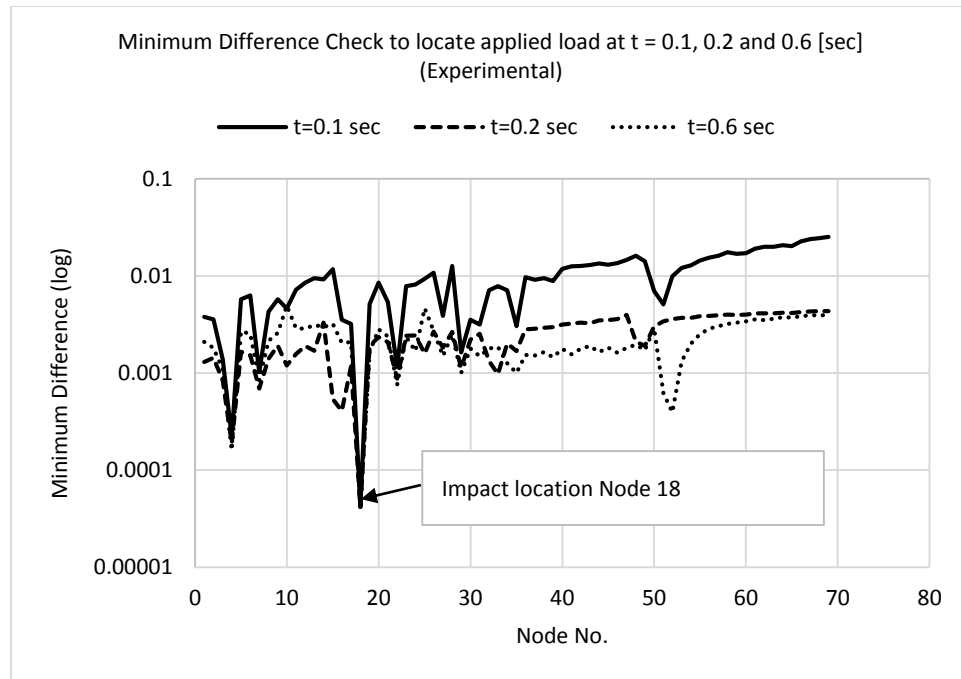
Figure 6.11 Expanded displacement profile from D-Optimal sensors at t = 0.6 [sec]

6.5.4. Force Identification (Position and Magnitude):

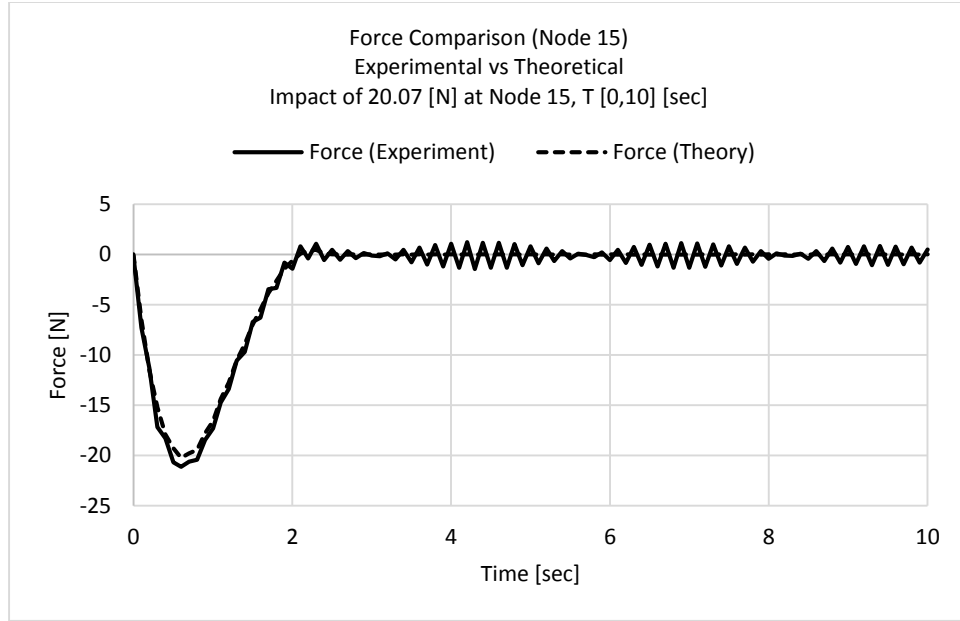
After performing expansion of strains, we proceed to identify the load position. Figure 6.12 (a) shows the impact location determination using minimum difference as explained in chapter 4. It also shows that at all times (t = 0.1, 0.2 and 0.6 sec), position is

identified as node 18. Figure 6.12 (b) shows a force magnitude 23.12 N determined experimentally compared to an applied 20.07 N (error of 15.23%). \

We conclude that with a strain error of around 20 % we get a force position at node 18 for all times ($t=0.1, 0.2 \dots 0.6$ sec). Despite being unable to predict the accurate force location, the magnitude was predicted with an error of around 15 % and a displacement prediction error of around 7% at 0.6 sec. We now proceed to perform an impact test on a clamped-clamped beam with the same sensor configuration to observe whether we can still predict the applied force despite sensors not being present at all optimal sites for the clamped-clamped beam.



(a) Force position identification through minimum difference

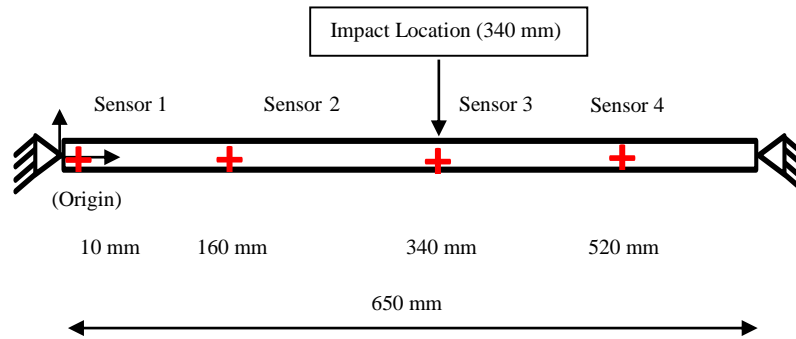


(b) Time history of the force, experimental vs theoretical

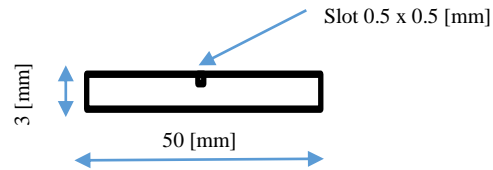
Figure 6.12 (a) Location identification at different times (b) Comparison of the expanded D-Optimal force solution with the actual force on beam at Node 15

6.6. Experimental Impact Test (Clamped-Clamped Beam):

The same beam earlier used as a cantilever is now tested with a clamped-clamped boundary condition. The beam has been shortened by 50 mm and the test beam specifications are shown in Figure 6.13. The D-Optimal sites were calculated to be [1 20 54 and 62] which are in the vicinity of the installed sensors. The instrumented beam is shown in Figure 6.14.



(a) Sensor Positions, Clamped-Clamped Beam (Figure not to scale)



(b) Cross-section, Clamped-Clamped Beam (Figure not to scale)

Figure 6.13 Beam dimensions and sensor positions (clamped-clamped)

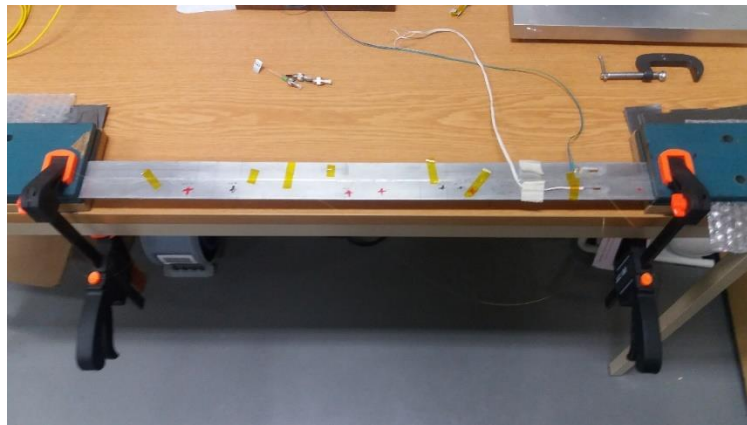


Figure 6.14 Instrumented clamped-clamped beam

6.6.1. Strain Results:

The experimental strains are obtained as a result of impact of approximately 28 N at a location of 340 mm from the left fixed end as shown in Figure 6.15. The impact force maximum amplitude was recorded at 0.5 ms with the impulse span of 1 ms. The FBG strains collected at sensor positions are shown in Figure 6.16.

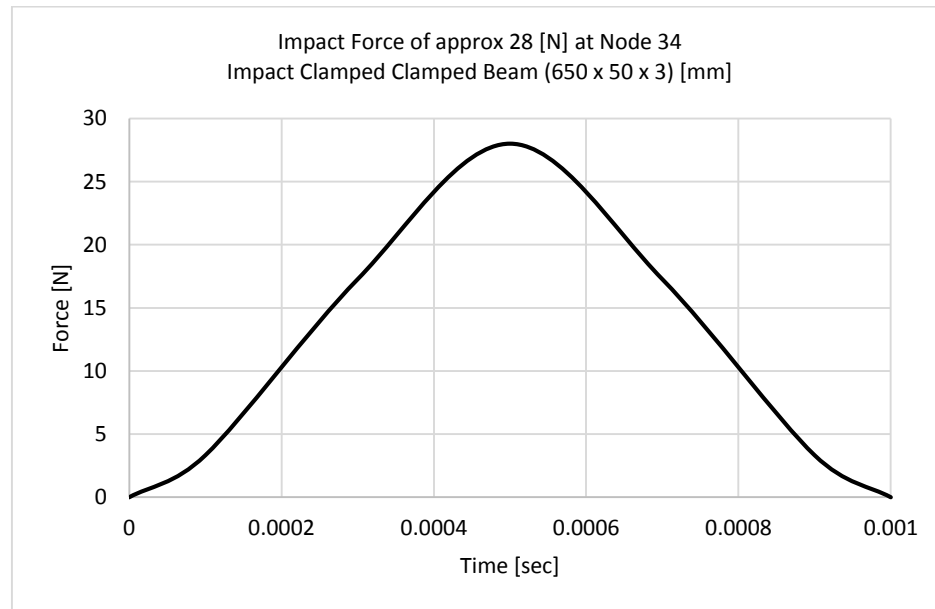


Figure 6.15 Experimental impact force 28 [N]

Upon comparison of experimental strain data to FEM, it was found that the RMS error was found to be 30 %. Since the sensors are not at the optimal sites (using the cantilever, embedded sensor beam), we would like to see the effect of the non-optimal sensor position data on the results. The strain comparison is shown in Figure 6.17.

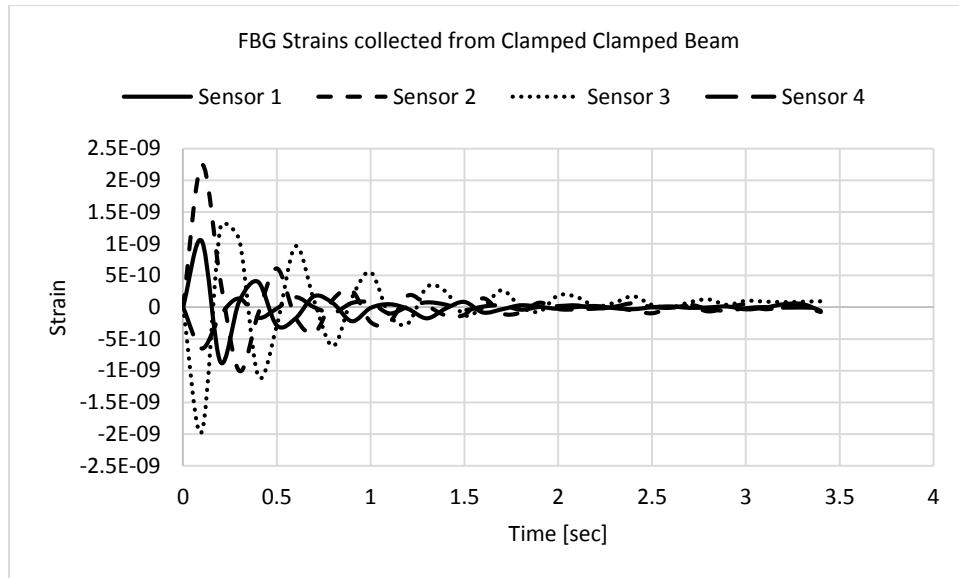
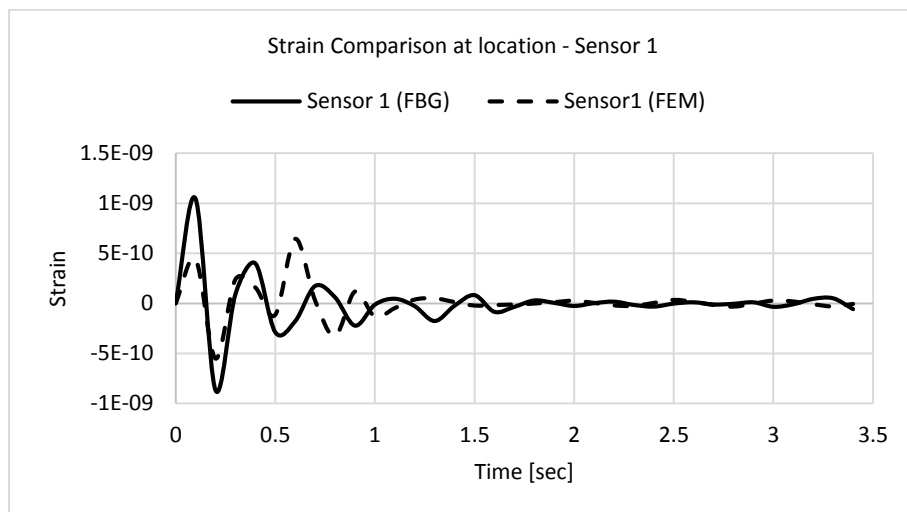
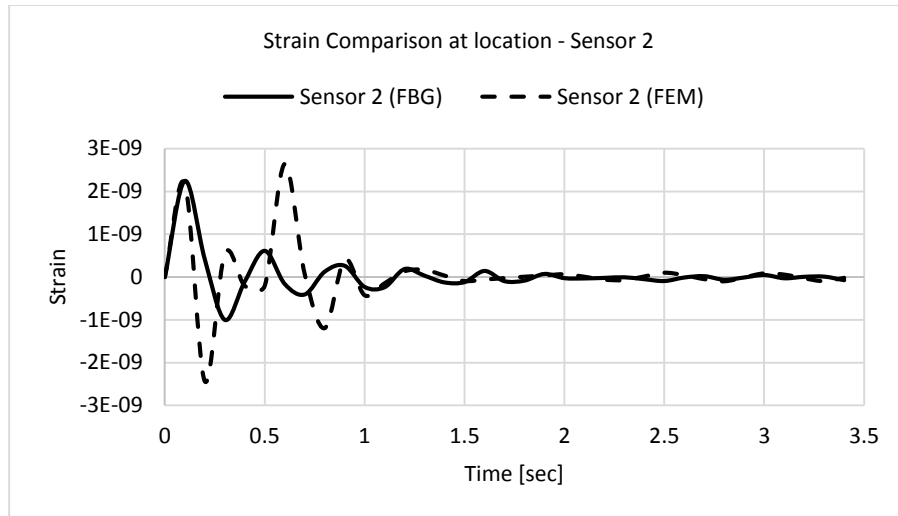


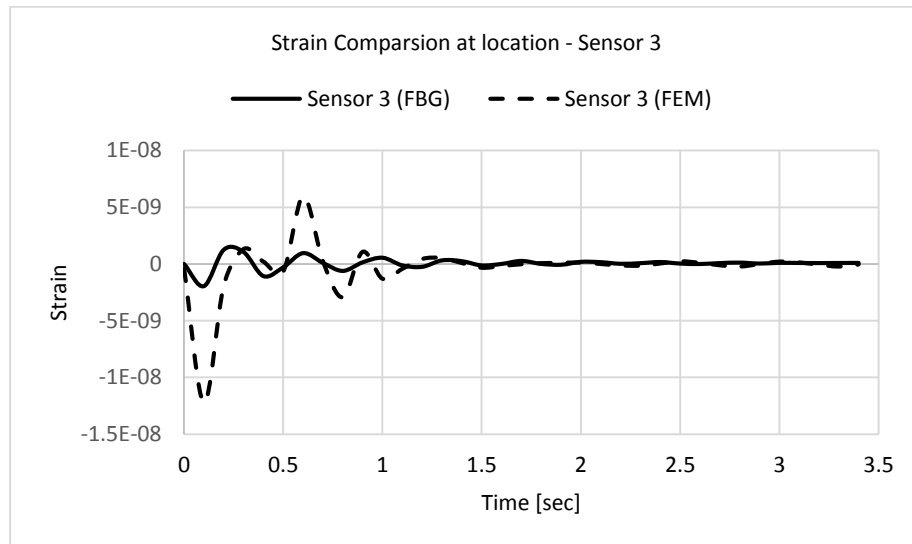
Figure 6.16 FBG strains recorded at sensor position 1-4



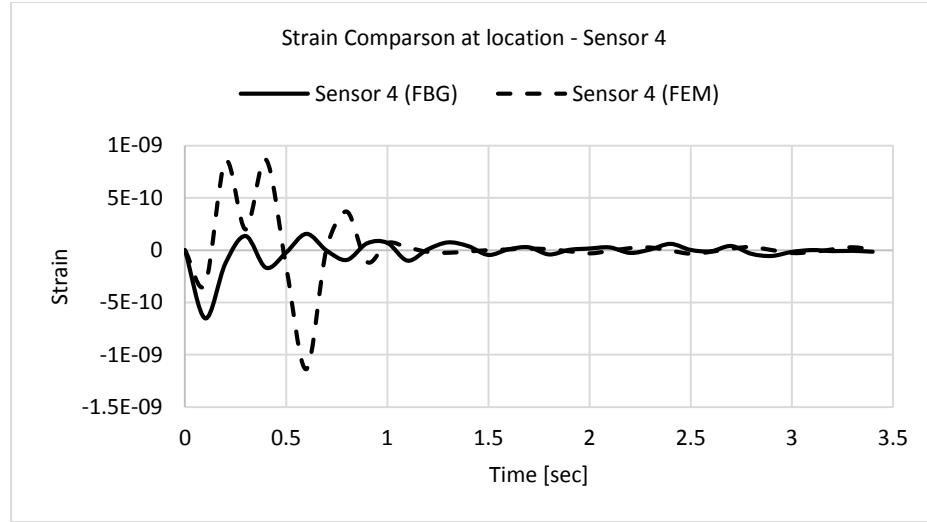
(a) Strain comparison between FBG data and FEM at sensor 1



(b) Strain comparison between FBG data and FEM at sensor 2



(c) Strain comparison between FBG data and FEM at sensor 3



(d) Strain comparison between FBG data and FEM at sensor 4

Figure 6.17 (a-d), Comparison of experimental results to simulated (clamped-clamped)

6.6.2. Displacement Prediction:

After performing expansion on the sensor sites, the expanded displacement results were compared to the theoretical displacements. The displacement profile produced after expansion resulted in an 18% error at $t=0.1$ sec (see Table 6.3) when compared to the theoretical displacements. Theoretical calculations suggest that the maximum force amplitude will be visible at $t = 0.1$ sec mark. The impact profile modification in the clamped-clamped case has resulted in a different time to observe maximum force. Figure 6.18 shows a comparison of expanded displacements, experiment versus theory.

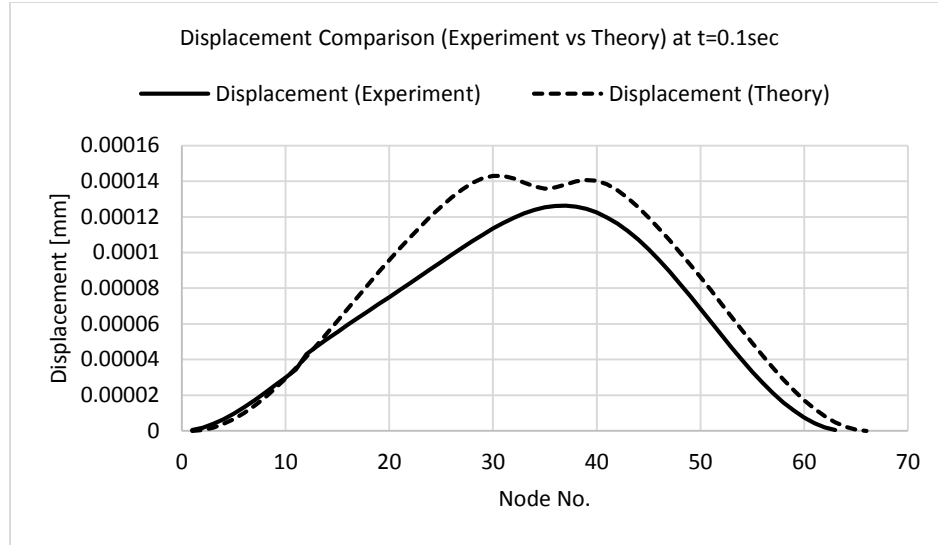


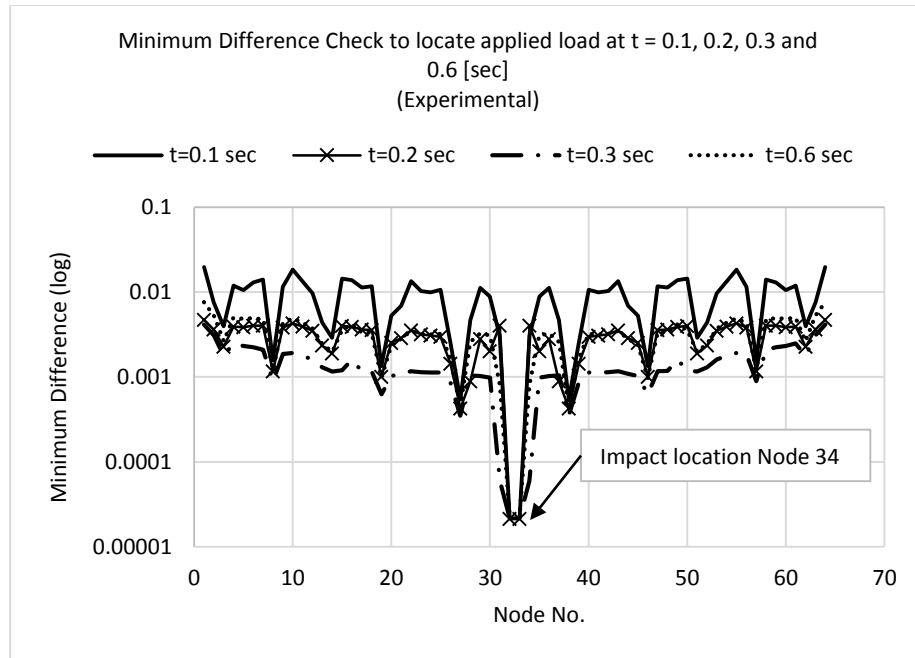
Figure 6.18 Comparison displacements (Theoretical vs Experimental), clamped-clamped beam

Table 6.3 % RMS error for displacements at different times (Clamped-Clamped Beam)

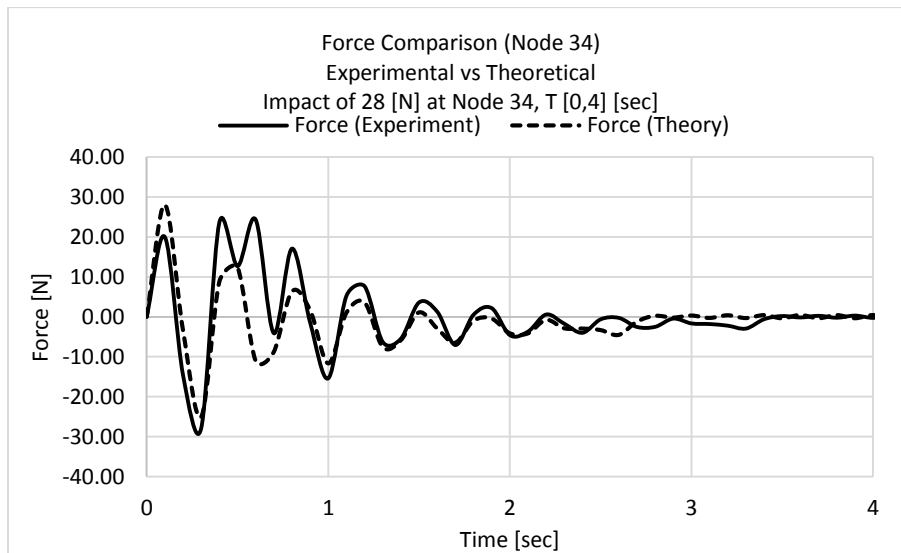
<i>% RMS Error at different times</i>				
Time	t = 0.1 [sec]	t = 0.2 [sec]	t = 0.3 [sec]	t = 0.6 [sec]
Displacement	18.15	18.71	67.14	19.95

6.6.3. Force Identification (Position and Magnitude):

Figure 6.19 (a) shows the impact location determination through minimum difference calculation. The force identified through the non-optimal sensor were able to locate the applied load location at 340 mm which is same as actual. It also shows that for $t = 0.1$, 0.2, 0.3 and 0.6 sec, the identified position remains identified as node 34. Figure 6.19 (b) shows the force comparison, experimental versus theoretical at node 34 showing a difference of around 31.79 % at $t = 0.1$ sec. The reason for higher error (67.14%) was unidentified.



(a) Force position identification through minimum difference



(b) Time history of the force, experimental vs theoretical

Figure 6.19 (a) Location identification at different times (b) Comparison of the expanded D-Optimal force solution with the actual force on beam at Node 34

6.7. Conclusion:

The experimental study has allowed us to implement the sensors placement scheme and carry out analysis with respect to force identification. The FBG strain calibration issues were resolved by comparing the FEM and experimental results. Impact hammer force data was useful to implement a numerical force description as opposed to theoretical impact force description (square, triangle, exponential etc.). The impact data produced a known discretized force profile to be added to the model in FEM. Accurate geometry construction was obtained for the instrumented cantilever beam as was also highlighted in chapter 5 with D-Optimal sites. The same sensor scheme when applied to a clamped-clamped beam were able to yield comparable results as most sensors (3/4 sensors) were located in the vicinity of the D-Optimal sites. The analysis performed for the cantilever beam was in transient state of the beam and the lobe formation for strain data can be attributed to the transient phase and limitation of data acquisition frequency.

CHAPTER 7

ANALYSIS, CONCLUSION & RECOMMENDATIONS

7.1. Analysis:

The objective of the research was to find out the optimal number of sensors and their corresponding positions to identify an unknown applied load on a structure in terms of its magnitude and position. Later on full field strain in the structure was evaluated through displacements and strain at the sensor locations. The idea is to incorporate a placement method so that a smart structure with embedded strain sensor like an FBG can be made useful due to its advantageous features. On route to the desired objective of force identification, investigative path led to selecting appropriate sensor(s), understanding the sensor behavior through characterization and calibration studies

Upon carrying out the literature review, it was identified that the current research for smart structures with embedded sensors is gaining wide attention with FBG sensors. Conventional strain sensor like the strain gage lacks the potential for embeddability due to difficulty in embedding, survivability and electromagnetic interference which effects the measurand. But allows us to compare with the standard strain measurements obtained from FBG. All the strain activities were monitored through National Instruments (NI) hardware and software (LabVIEW).

The mentioned FBG sensors due to their requirement of embedding were interrogated under different scenarios such as tensile test, mechanical strain, temperature and pressure.

These results helped in order to observe the sensitivity of the sensor to mechanical strain, pressure and temperature. Later on light transmission tests were carried out in order to investigate effect of different bend radiuses and layout geometries to observe the loss of optical power and effect of bending. The bend test results helped us identify critical bend radius under which the array FBG can take different layout forms (circular/regular grid).

A calibration study was performed on a slotted aluminum beam with an array FBG sensor (3 Sensors) to observe strain activity in the slot. The calibration was accompanied by strain gages (strain measurement) and LVDT (displacement measurement). The beam was investigated under different static loads and compared with the FEM results of the beam under similar conditions. The Fiber Optic Interrogation System requires that the Gage Factor for the FBG be known. This factor was evaluated based on the characterization study mentioned in the previous paragraph.

A theoretical study for the optimal placement was also performed to find the optimal locations of the strain sensors in order to capture the static as well as the dynamic load magnitudes and their position. Two methods namely 1) Placement Index and 2) D-Optimal Design were compared to see the effect of different placement schemes on achieving the required objective. The utility of the exercised technique is that it helps us to use the embedded sensor strain data to first build up the optimal sites and later on expand the solution using techniques like Craig Bampton Method or System Equivalent Reduction Expansion Process (SEREP) to find displacements, strains and forces along with their locations. The expanded solution gives strain information at all untapped locations. Analysis on the optimal locations help us judge whether the optimal sensors are

optimal in the true sense while capturing the un-identified forces and modes at the same time.

7.2. Conclusion:

The outcomes of this research can be concluded as follows:

- The development of a force localization scheme based on the inputs of the D-Optimal Design method that allows us to design a smart structure with embedded FBGs in structures of different types (beam and plate).
- A comparative study between D-Optimal Design method and Placement Index to evaluate for a better performing scheme identifying the applied structural load (Static/Dynamic) from strain sensors and its location through SEREP expansion process. An experimental validation of the concept was achieved with FBG embedded in an aluminum cantilever and clamped-clamped beam.
- Characterization study that enables us to have knowledge about the geometrical and physical constraints on the use of the FBG.

We conclude that the sensors placement schemes implemented individually as the 1) Placement Index and 2) D-Optimal method were dependent on prior information on force location. The SEREP expansion applied to both techniques helped us identify D-Optimal method as a better placement method for force identification (load and position). The implemented expansion technique with SEREP in combination with Minimum Difference method were useful to locate force position and magnitude.

7.3. Future Recommendations:

An enormous potential exists based on the implementation of the current research in the area of smart structure development. Incorporation of actuation to form a closed loop system will add value to the smart system with response. Correct sensor and actuator placement is expected to improve structural behavior monitoring and control. These structures can be of simple or complex geometries. Proposed sensor placement and force identification technique can also be exploited for complex geometry structures. Also the effects of hardware issues on prediction error further needs investigation. Hardware measurement characteristic issues with better data acquisition frequency (data sampling) is important in minimizing the prediction errors for structural behavior.

Aerospace and biomedical fields will experience maximum benefit out of such design studies as there is an immense need to cope up with the future trends and demands to develop intelligent and smart systems with sensors in embedded state.

REFERENCES

- [1] Mattar, E., 2013, “A survey of bio-inspired robotics hands implementation: New directions in dexterous manipulation,” *Rob. Auton. Syst.*, 61, pp. 517–544.
- [2] Gibson, R. F., 2010, “A review of recent research on mechanics of multifunctional composite materials and structures,” *Compos. Struct.*, 92(12), pp. 2793–2810.
- [3] Lopez, I., and Sarigul-Klijn, N., 2010, “A review of uncertainty in flight vehicle structural damage monitoring, diagnosis and control: Challenges and opportunities,” *Prog. Aerosp. Sci.*, 46(7), pp. 247–273.
- [4] Ramly, R., Kuntjoro, W., and Rahman, M. K. A., 2012, “Using Embedded Fiber Bragg Grating (FBG) Sensors in Smart Aircraft Structure Materials,” *Procedia Eng.*, 41(Iris), pp. 600–606.
- [5] Luyckx, G., Voet, E., Lammens, N., and Degrieck, J., 2011, “Strain measurements of composite laminates with embedded fibre bragg gratings: Criticism and opportunities for research,” *Sensors*, 11(1), pp. 384–408.
- [6] Li, Y., Liu, W., Feng, Y., and Zhang, H., 2012, “Ultrasonic embedding of nickel-coated fiber Bragg grating in aluminum and associated sensing characteristics,” *Opt. Fiber Technol.*, 18(1), pp. 7–13.
- [7] Zubel, M. G., Sugden, K., Saez-Rodriguez, D., Nielsen, K., and Bang, O., 2016, “3D printed sensing patches with embedded polymer optical fibre Bragg gratings,” 9916, p. 99162E.

- [8] Mekid, S., and Kwon, O. J., 2009, “Materials: A New Approach for Better Control, Reliability and Safety of Structures,” *Sci. Adv. Mater.*, 1(3), pp. 276–285.
- [9] Koecher, M. C., Pande, J. H., Merkley, S., Henderson, S., Fullwood, D. T., and Bowden, A. E., 2015, “Composites : Part B Piezoresistive in-situ strain sensing of composite laminate structures,” *Compos. PART B*, 69, pp. 534–541.
- [10] Beard, S. J., 2005, “Practical issues in real-world implementation of structural health monitoring systems,” *Proc. SPIE*, (408), pp. 196–203.
- [11] Qing, X., Beard, S., Kumar, a, Chan, H., and Ikegami, R., 2006, “Advances in the development of built-in diagnostic system for filament wound composite structures,” *Compos. Sci. Technol.*, 66(11–12), pp. 1694–1702.
- [12] Sun, M., Staszewski, W. J., and Swamy, R. N., 2010, “Smart Sensing Technologies for Structural Health Monitoring of Civil Engineering Structures,” *Adv. Civ. Eng.*, 2010, pp. 1–13.
- [13] Farrar, C. R., Worden, K., Lieven, N. a J., and Park, G., 2007, “Structural Health Monitoring for Aerospace Applications,” *Aerospace*, (November), pp. 1–12.
- [14] Simpson, B., Hoult, N. A., Asce, M., Moore, I. D., and Asce, M., 2010, “Distributed Sensing of Circumferential Strain Using Fiber Optics during Full-Scale Buried Pipe Experiments,” pp. 1–10.
- [15] Sofla, a. Y. N., Meguid, S. a., Tan, K. T., and Yeo, W. K., 2010, “Shape morphing of aircraft wing: Status and challenges,” *Mater. Des.*, 31(3), pp. 1284–1292.
- [16] Park, Y. L., Chau, K., Black, R. J., and Cutkosky, M. R., 2007, “Force sensing robot

fingers using embedded fiber Bragg grating sensors and shape deposition manufacturing,” Proc. - IEEE Int. Conf. Robot. Autom., pp. 1510–1516.

- [17] Al-Fakih, E., Osman, N. A. A., and Adikan, F. R. M., 2012, “The use of fiber bragg grating sensors in biomechanics and rehabilitation applications: The state-of-the-art and ongoing research topics,” *Sensors (Switzerland)*, 12(10), pp. 12890–12926.
- [18] Yang, Y., Annamdas, V. G. M., Wang, C., and Zhou, Y., 2008, “Application of Multiplexed FBG and PZT Impedance Sensors for Health Monitoring of Rocks,” *Sensors*, 8, pp. 271–289.
- [19] Pille, D. C., 2010, “In-Process Embedding of Piezo Sensors and RFID Transponders into Cast Parts for Autonomous Manufacturing Logistics,” (March), pp. 23–24.
- [20] Alemohammad, H., and Toyserkani, E., 2011, “Metal Embedded Optical Fiber Sensors: Laser-Based Layered Manufacturing Procedures,” *J. Manuf. Sci. Eng.*, 133(June 2011), p. 31015.
- [21] Ghoshal, A., Prosser, W. H., Kim, H. S., Chattopadhyay, A., and Copeland, B., 2010, “Development of embedded piezoelectric acoustic sensor array architecture,” *Microelectron. Reliab.*, 50(6), pp. 857–863.
- [22] Lin, M., 2001, “SMART Layer and SMART Suitcase for structural health monitoring applications,” *Proc. SPIE*, 4332(408), pp. 98–106.
- [23] Measures, R., and Abrate, S., 2002, “Structural Monitoring with Fiber Optic Technology,” *Appl. Mech. Rev.*, 55, p. B10.
- [24] Measures, R. M., 1989, “Smart structures with nerves of glass,” *Prog. Aerosp. Sci.*,

26, pp. 289–351.

- [25] Majumder, M., Gangopadhyay, T. K., Chakraborty, A. K., Dasgupta, K., and Bhattacharya, D. K., 2008, “Fibre Bragg gratings in structural health monitoring- Present status and applications,” *Sensors Actuators, A Phys.*, 147, pp. 150–164.
- [26] <http://www.ni.com/white-paper/11821/en/> (2017)
- [27] Liu, W., and Giurgiutiu, V., 2007, “Finite element simulation of piezoelectric wafer active sensors for Structural Health Monitoring with coupled-field elements,” *SPIE Vol. 6529*, 6529, p. 65293R–65293R–13.
- [28] Boller, C., 2000, “Next generation structural health monitoring and its integration into aircraft design,” *Int. J. Syst. Sci.*, 31(June 2012), pp. 1333–1349.
- [29] <https://en.wikipedia.org/wiki/Piezoelectricity> (2017)
- [30] Moore, L., and Barrett, J., 2012, “Embedded module for 3-D mechanical strain measurement,” *IEEE Trans. Components, Packag. Manuf. Technol.*, 2(6), pp. 1002–1011.
- [31] Siggard, E. J., Madhusoodanan, a. S., Stucker, B. E., and Eames, B., 2006, “Structurally Embedded Electrical Systems Using Ultrasonic Consolidation (UC),” *Proc. 17th Solid Free. Fabr. Symp.*, pp. 70–83.
- [32] Saheb, N., and Mekid, S., 2015, “Fiber-embedded metallic materials: From sensing towards nervous behavior,” *Materials (Basel)*, 8(11), pp. 7938–7961.
- [33] Mekid, S., Saheb, N., Daraghma, H., Butt, A., and Qureshi, K., 2015,

- “SMASIS2015-8859 upscaling sensing materials with challenges of sensors,”
Conference on Smart Systems, Adaptive Structures & Intelligent Systems,
Colorado, USA, pp. 1–7.
- [34] Mekid, S. Butt, A. M., Qureshi, K. 2015, “SMASIS 2015-8860 Characterization of
fiber optics integrity under several embedding parametrs,” Conference on Smart
Systems, Adaptive Structures & Intelligent Systems, Colorado, USA, pp. 1–6.
- [35] Zhu, Z., Zhang, Y., Zeng, C., and Xiong, Z., 2011, “Preliminary investigation on
embedding FBG fibre within AA6061 matrices by ultrasonic welding,” *Lect. Notes
Electr. Eng.*, 88 LNEE, pp. 375–381.
- [36] Li, Y., Hua, Z., Yan, F., and Gang, P., 2009, “Metal coating of fiber Bragg grating
and the temperature sensing character after metallization,” *Opt. Fiber Technol.*,
15(4), pp. 391–397.
- [37] Yulong Li, Hua Zhang, Yan Feng, and Gang Peng, 2009, “A plating method for
metal coating of fiber Bragg grating,” *Chinese Opt. Lett.*, 7(2), pp. 115–117.
- [38] Li, X., 2001, “Embedded Sensors in Layered Manufacturing,” (Thesis).
- [39] Willis, K., Brockmeyer, E., Hudson, S., and Poupyrev, I., 2012, “Printed optics: 3D
printing of embedded optical elements for interactive devices,” *Proc. 25th Annu.
ACM Symp. User interface Softw. Technol. - UIST '12*, pp. 589–598.
- [40] Liacouras, P., Grant, G., Choudhry, K., Strouse, G. F., and Ahmed, Z., 2015, “Fiber
Bragg Gratings Embedded in 3D-Printed Scaffolds.” (Research Article)
- [41] He, C., Xing, J., Li, J., Yang, Q., Wang, R., and Zhang, X., 2015, “A New Optimal

Sensor Placement Strategy Based on Modified Modal Assurance Criterion and Improved Adaptive Genetic Algorithm for Structural Health Monitoring,” 2015.

- [42] Li, J., Zhang, X., Xing, J., Wang, P., and Yang, Q., 2015, “Optimal sensor placement for long-span cable-stayed bridge using a novel particle swarm optimization algorithm,” *J. Civ. Struct. Heal. Monit.*, 5(5), pp. 677–685.
- [43] Peng, Z., Zhao, Y., Yin, H., and Pan, A., 2015, “Artificial Fish Swarm Algorithm Based Optimal Sensor Placement,” 8(4), pp. 287–300.
- [44] Chang, M., and Pakzad, S. N., 2014, “Optimal Sensor Placement for Modal Identification of Bridge Systems Considering Number of Sensing Nodes,” *J. Bridg. Eng.*, 19(6), pp. 1–10.
- [45] Nestorović, T., and Trajkov, M., 2013, “Optimal actuator and sensor placement based on balanced reduced models,” *Mech. Syst. Signal Process.*, 36, pp. 271–289.
- [46] Abdalla, M. O., and Al-Khawaldeh, E., 2011, “Optimal Damage Detection Sensor Placement Using PSO,” *Appl. Mech. Mater.*, 110–116, pp. 5336–5341.
- [47] Ngatchou, P. N., Fox, W. L. J., and El-Sharkawi, M. a., 2005, “Distributed sensor placement with sequential particle swarm optimization,” *Proc. 2005 IEEE Swarm Intell. Symp. 2005. SIS 2005.*, pp. 385–388.
- [48] Guo, H. Y., Zhang, L., Zhang, L. L., and Zhou, J. X., 2004, “Optimal placement of sensors for structural health monitoring using improved genetic algorithms,” *Smart Mater. Struct.*, 13, pp. 528–534.
- [49] Ling, F. F., 2004, *Advanced Structural Dynamics and Active Control of Structures*,

Springer-Verlag. ISBN 0-387-40649-2

- [50] Kincaid, R. K., and Padula, S. L., 2002, “D-optimal designs for sensor and actuator locations,” *Comput. Oper. Res.*, 29, pp. 701–713.
- [51] Gupta, D. K., and Dhingra, A. K., 2013, “Input load identification from optimally placed strain gages using D-optimal design and model reduction,” *Mech. Syst. Signal Process.*, 40(2), pp. 556–570.
- [52] Ma, C.-K., Tuan, P.-C., Lin, D.-C., and Liu, C.-S., 1998, “A study of an inverse method for the estimation of impulsive loads,” *Int. J. Syst. Sci.*, 29(6), pp. 663–672.
- [53] Kawabata, N., Hayata, H., Hu, N., and Fukunaga, H., 2003, “Inverse Problems in Engineering Mechanics IV,” *Inverse Probl. Eng. Mech.* IV, pp. 85–94.
- [54] West, R. L., 2005, “Inverse Problems in Structural Mechanics Inverse Problems in Structural Mechanics,” (Thesis).
- [55] Gombi, S. L., and Ramakrishna, D. S., 2012, “A Solution to the Inverse Problem of Impact Force Determination from Structural Responses,” 1(3), pp. 192–196.
- [56] Gupta, D. K., 2013, “Inverse Methods for Load Identification Augmented By Optimal Sensor Placement and Model Order Reduction,” (Thesis).
- [57] Jiang, H., van der Veen, B., Kirk, D., and Gutierrez, H., 2013, “Real-Time Estimation of Time-Varying Bending Modes Using Fiber Bragg Grating Sensor Arrays,” *AIAA J.*, 51(1), pp. 178–185.
- [58] Pingle, P., Avitabile, P., and Lowell, M., 2011, “Full-Field Dynamic Stress / Strain

from Limited Sets of Measured Data.” (Research Article)

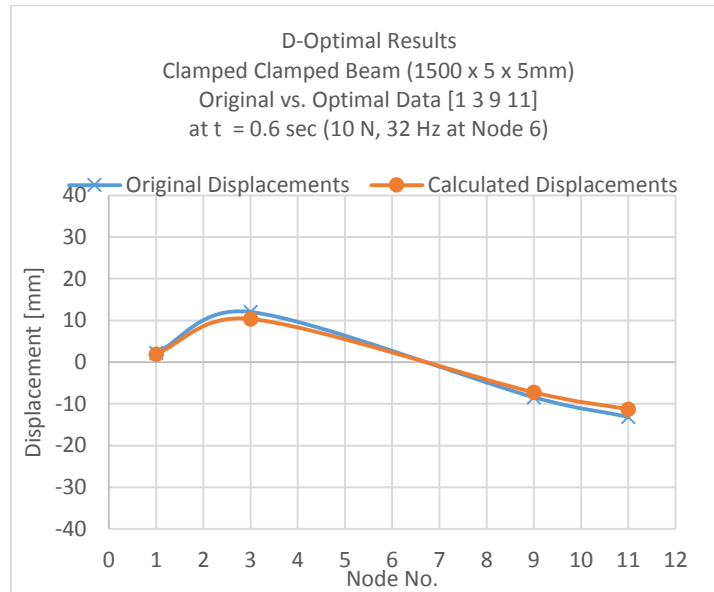
- [59] Avitabile, P., and Pingle, P., 2012, “Prediction of full field dynamic strain from limited sets of measured data,” *Shock Vib.*, 19(5), pp. 765–785.
- [60] Avitabile, P., Nonis, C., and Obando, S. E., 2014, “System model modes developed from expansion of uncoupled component dynamic data,” *Stroj. Vestnik/Journal Mech. Eng.*, 60(5), pp. 287–297.
- [61] Leng, J., and Asundi, A., 2003, “Structural health monitoring of smart composite materials by using EFPI and FBG sensors,” *Sensors Actuators A Phys.*, 103(3), pp. 330–340.
- [62] Kerrouche, a., Boyle, W. J. O., Sun, T., and Grattan, K. T. V, 2009, “Design and in-the-field performance evaluation of compact FBG sensor system for structural health monitoring applications,” *Sensors Actuators, A Phys.*, 151, pp. 107–112.
- [63] <http://www.ni.com/en-lb/support/model.pxie-4844.ht>.(2017)
- [64] <http://www.pi-us/blog/piezo-sensors-pzt-vs-fib>.(2017)
- [65] Udoh, S., Njuguma, J., and Prabhu, R., 2014, “Modelling and Simulation of Fiber Bragg Grating Characterization for Oil and Gas Sensing Applications.”, 2014 First International Conference on Systems Informatics, Modelling and Simulation
- [66] Park, Y.-L., Seok Chang, R., Black, R. J., Moslehi, B., and Cutkosky, M. R., 2008, “Fingertip force control with embedded fiber Bragg grating sensors,” *Robot. Autom.* 2008. ICRA 2008. IEEE Int. Conf., pp. 3431–3436.

- [67] Jung, E. J., Kim, C.-S., Jeong, M. Y., Kim, M. K., Jeon, M. Y., Jung, W., and Chen, Z., 2008, "Characterization of FBG sensor interrogation based on a FDML wavelength swept laser.," *Opt. Express*, 16(21), pp. 16552–16560.
- [68] Romaniuk, R., 2000, "Tensile strength of tailored optical fibres," *Opto-electronics Rev.*, 8, pp. 101–116.
- [69] Incorporated, C., 2011, "Corning ® SMF- 28 e +® LL Optical Fiber," (July), pp. 2010–2011. (Technical Document)
- [70] Knight, M. J., Felli, I. C., Pierattelli, R., Bertini, I., Emsley, L., Herrmann, T., and Pintacuda, G., 2012, "Sample preparation," (Sem 141), pp. 1–5.
- [71] Ilankeeran, P., Mohite, P., and Kamle, S., 2012, "Axial Tensile Testing of Single Fibres," *Mod. Mech. Eng.*, 2(November), pp. 151–156.
- [72] Jin, L. J. L., Zhang, W. Z. W., Zhang, H. Z. H., Liu, B. L. B., Zhao, J. Z. J., Tu, Q. T. Q., Kai, G. K. G., and Dong, X. D. X., 2006, "An embedded FBG sensor for simultaneous measurement of stress and temperature," *IEEE Photonics Technol. Lett.*, 18(1), pp. 154–156.
- [73] Johnson, I. P., Webb, D. J., and Kalli, K., 2012, "Hydrostatic pressure sensing using a polymer optical fibre Bragg gratings," *Proc. SPIE*, 8351, pp. 835106-835106–7.
- [74] Besselink, B., Tabak, U., Lutowska, A., Wouw, N. Van De, and Nijmeijer, H., 2013, "A comparison of model reduction techniques from structural dynamics , numerical mathematics and systems and control \$," 332, pp. 4403–4422.
- [75] <http://higherdbcs.wiley.com/legacy/college/craig/>. (2017)

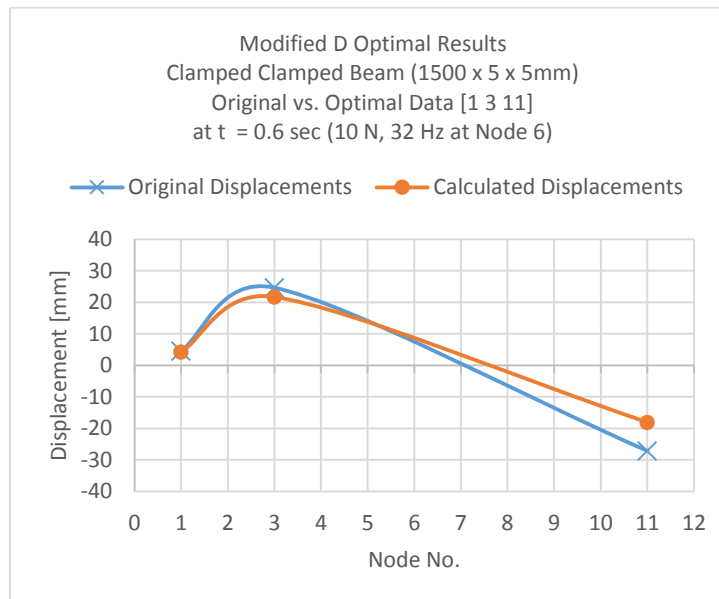
- [76] Ling, F. F., 2004, *Advanced Structural Dynamics and Active Control of Structures*, Springer New York, New York, NY. ISBN: 0387406492
- [77] Tsai, Y. kuan, and Krauthammer, T., 2015, “Energy based load-impulse diagrams,” *Eng. Struct* (Article in Press).
- [78] Inoue, H., Harrigan, J. J., and Reid, S. R., 2001, “Review of inverse analysis for indirect measurement of impact force,” *Appl. Mech. Rev.*, 54(6), p. 503.

APPENDIX

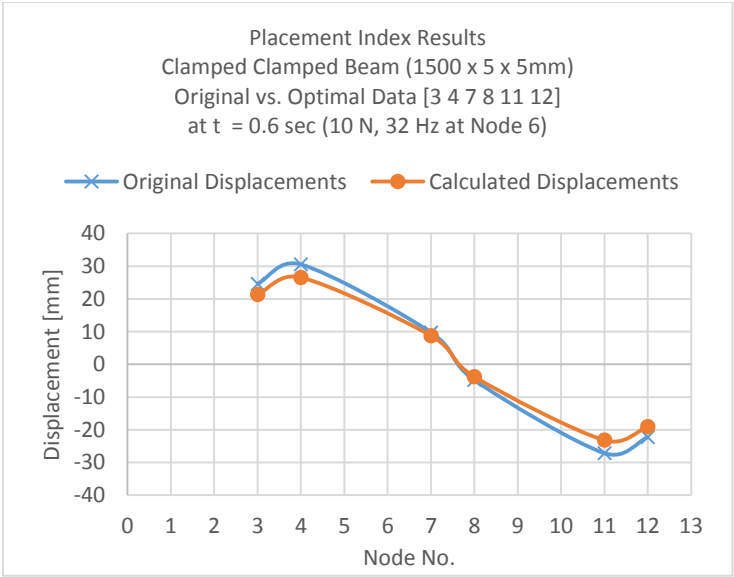
A-1. Clamped-Clamped Beam Data:



(a)



(b)

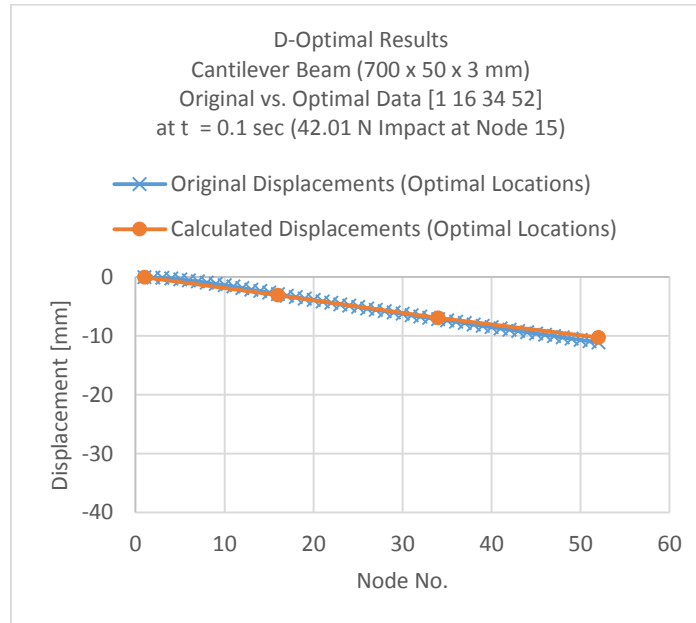


(c)

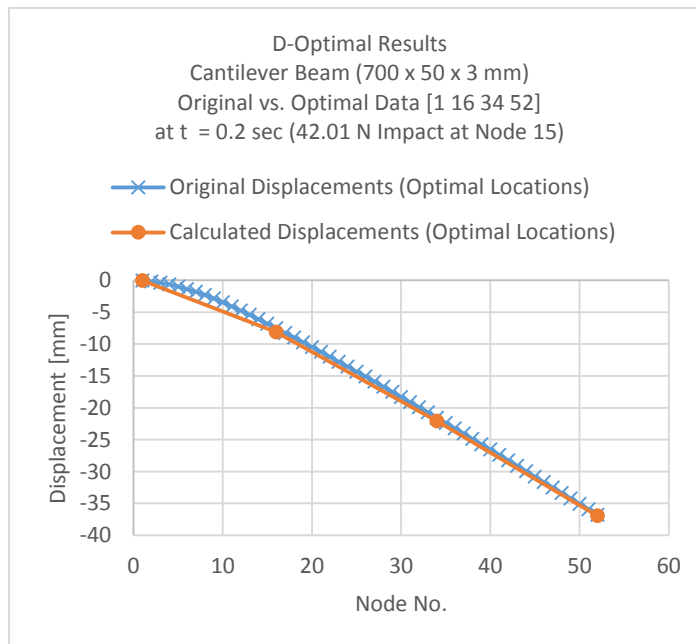
Fig. A.1. Displacements at D-Optimal sites (Clamped-Clamped Beam under harmonic force) (a) at $t = 0.1$ [s], (b) at $t = 0.2$ [s] and (c) at $t=0.3$ [s]

A-2. Cantilever Beam Data:

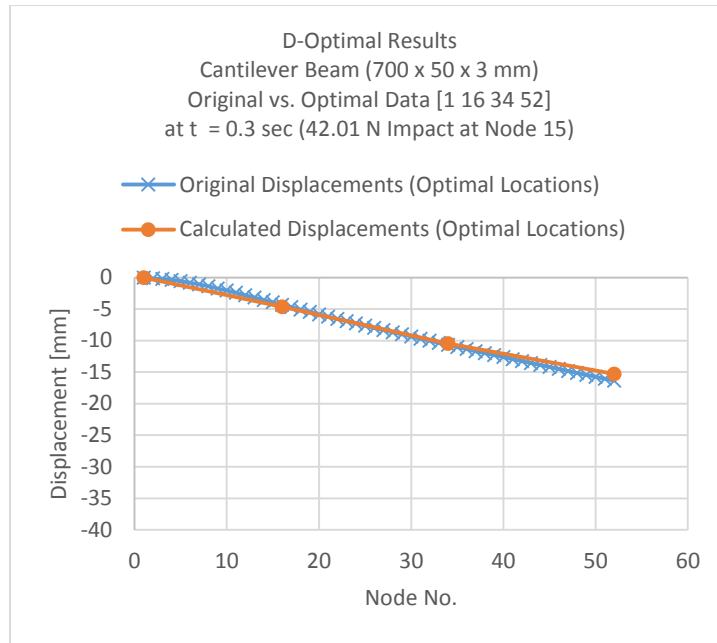
D-Optimal Results [1 16 34 52]:



(a)



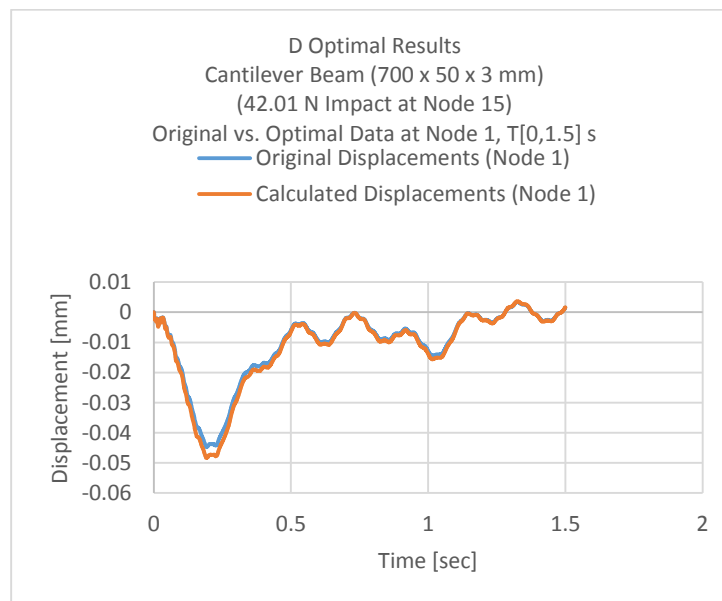
(b)



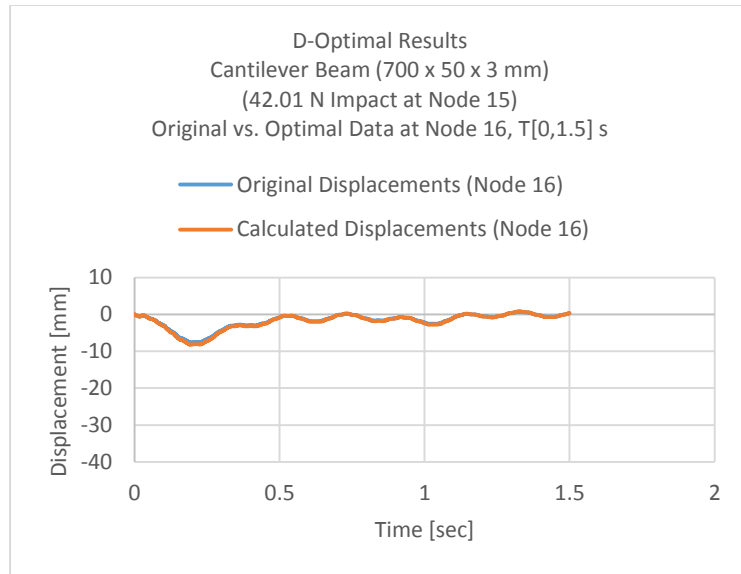
(c)

Fig. A.1 Displacements at D-Optimal sites (Cantilever Beam under impact) (a) at t = 0.1 [s], (b) at t = 0.2 [s] and (c) at t=0.3 [s]

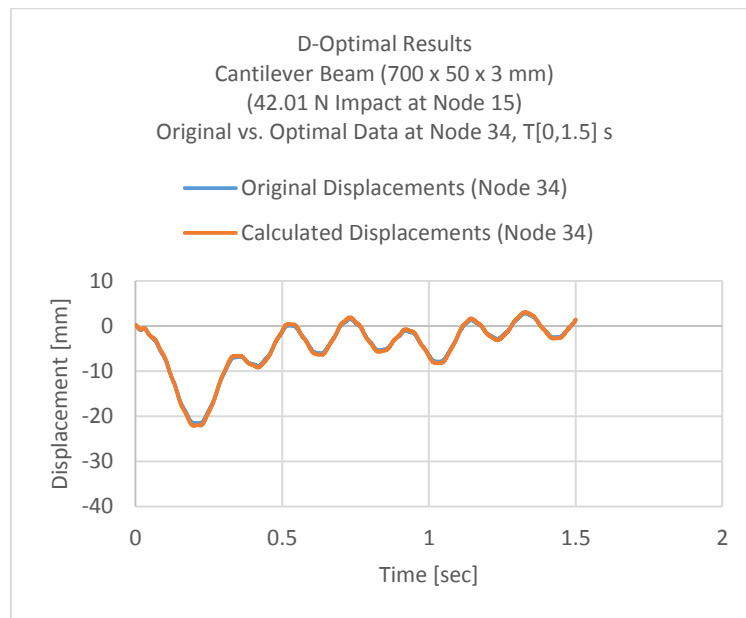
D-Optimal Results (Time History) [1 16 34 52]:



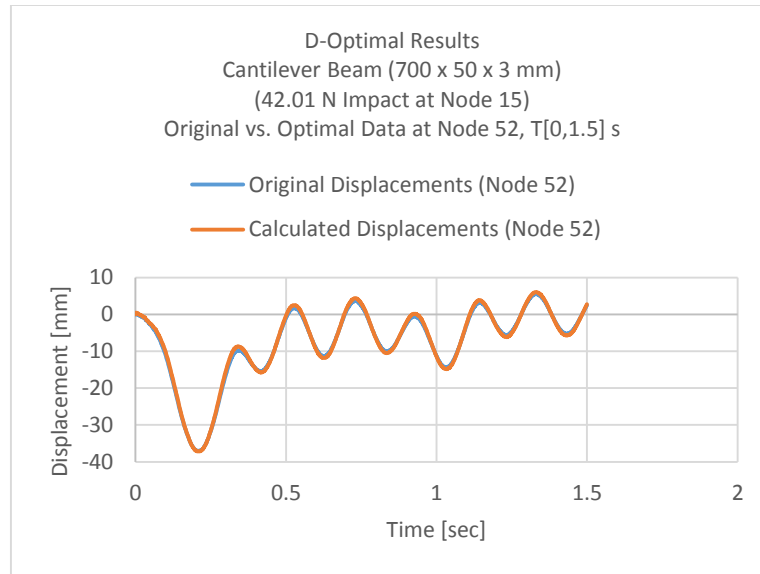
(a)



(b)



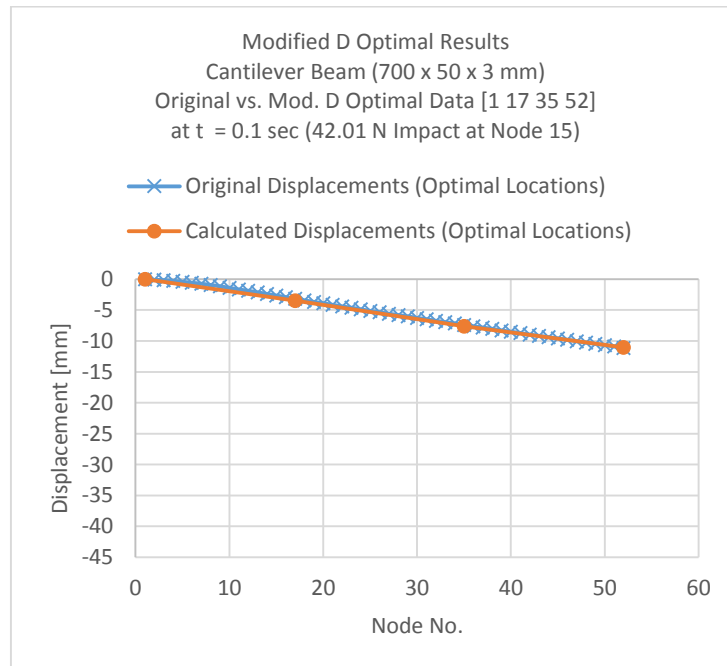
(c)



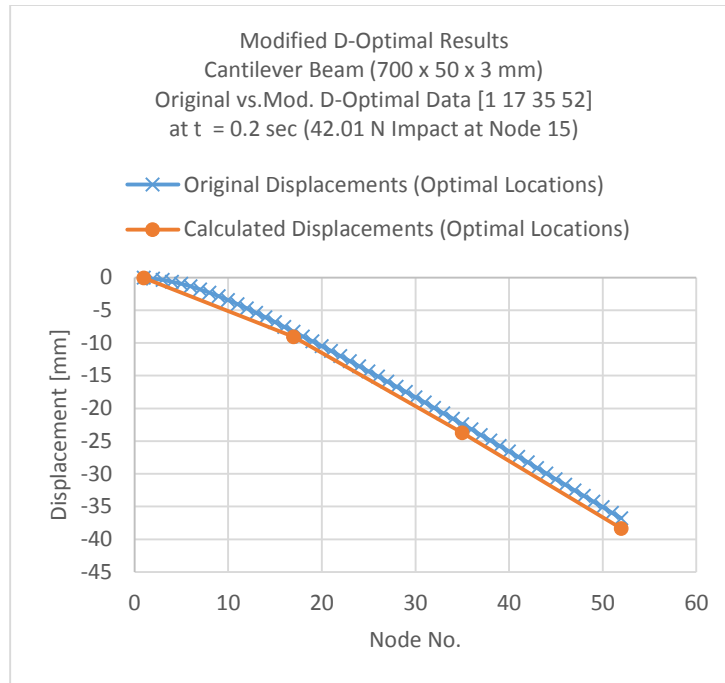
(d)

Fig. A.2. Displacements at D-Optimal sites (Cantilever Beam under impact), T [0-1.5] [s] (a) at Node 1, (b) at Node 16 (c) at Node 32 and (d) at Node 54

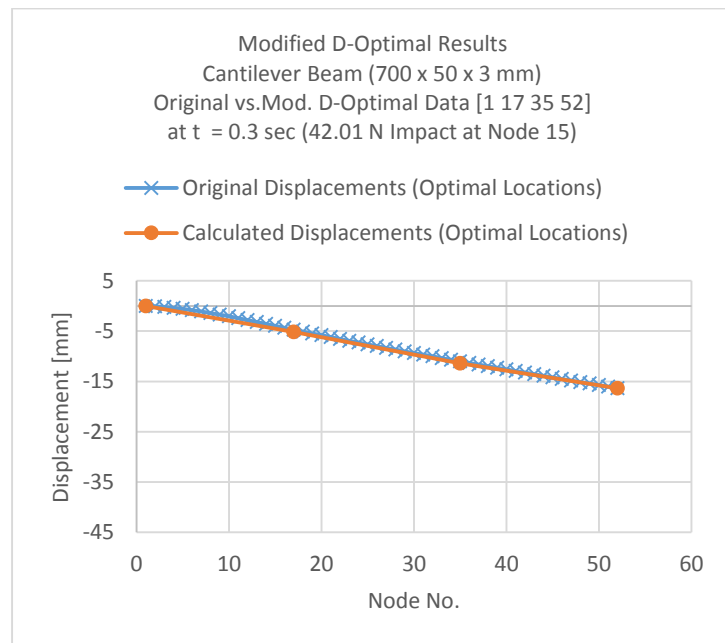
Modified D-Optimal Results [1 17 35 52]:



(a)



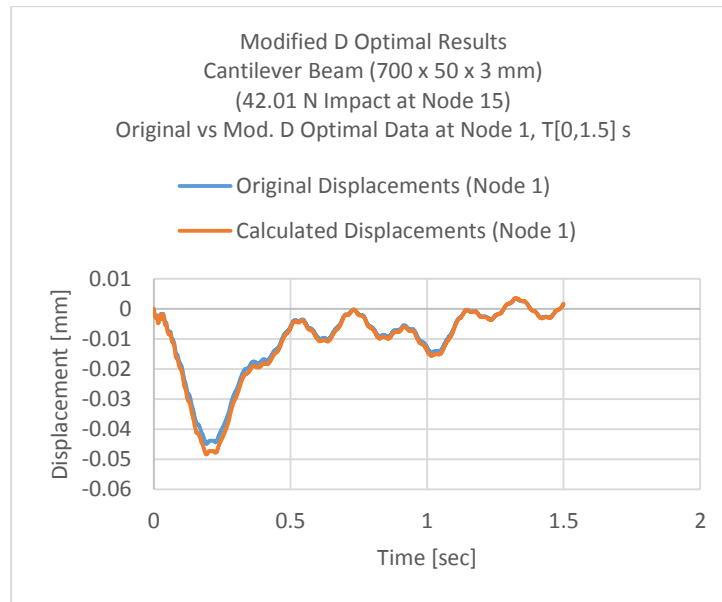
(b)



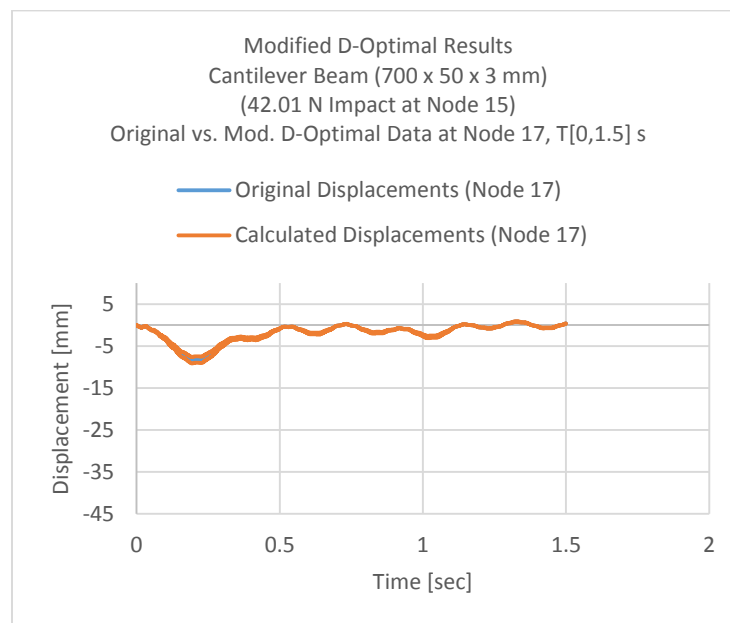
(c)

Fig. A.3. Displacements at Modified D-Optimal sites (Cantilever Beam under impact) (a) at $t = 0.1$ [s], (b) at $t = 0.2$ [s] and (c) at $t = 0.3$ [s]

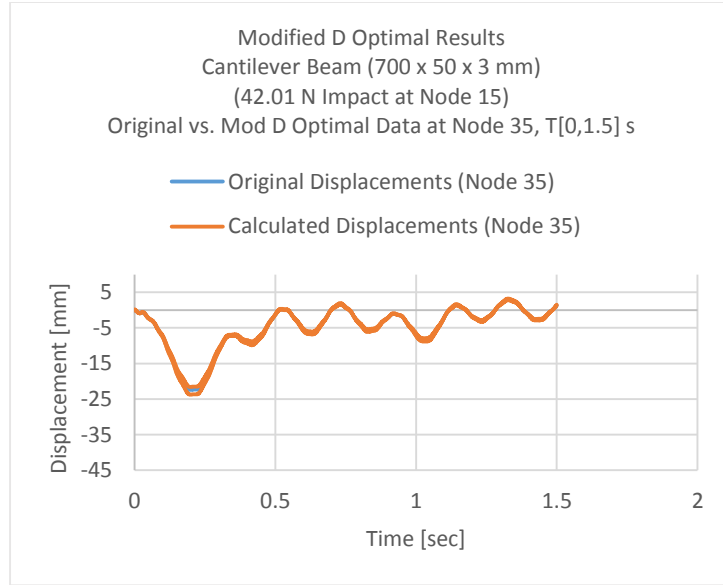
Modified D-Optimal Results (Time History) [1 17 35 52]:



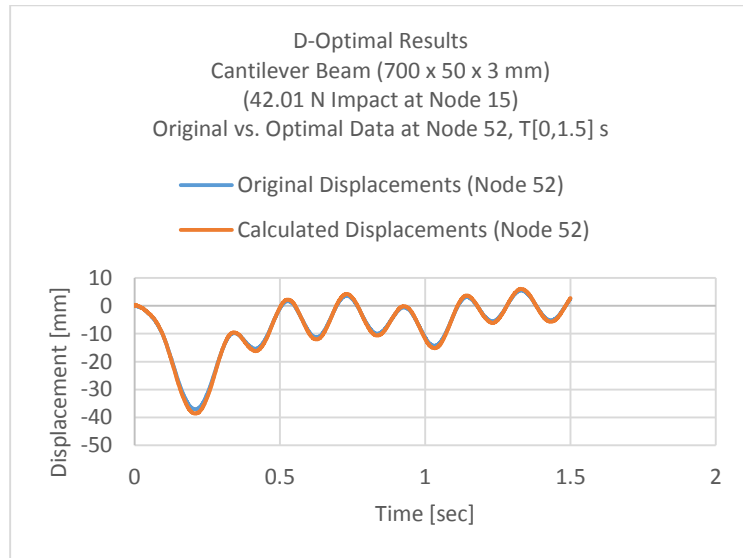
(a)



(b)



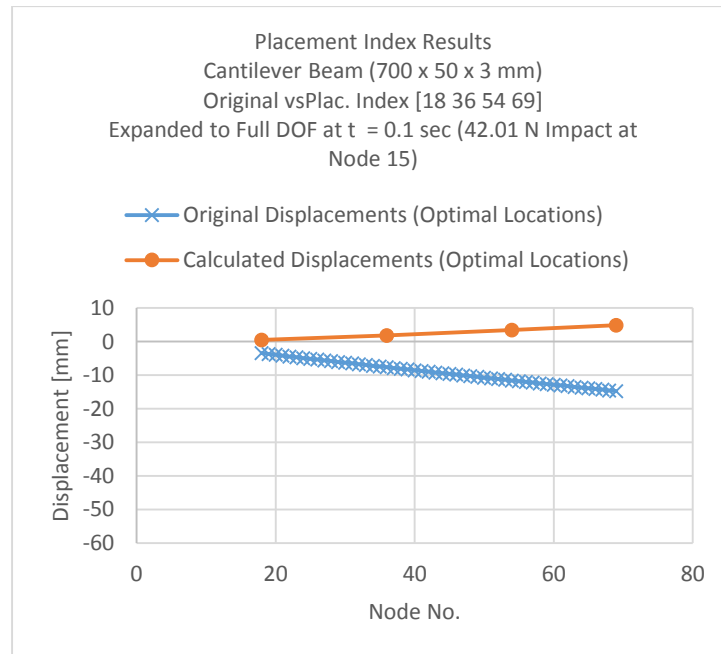
(c)



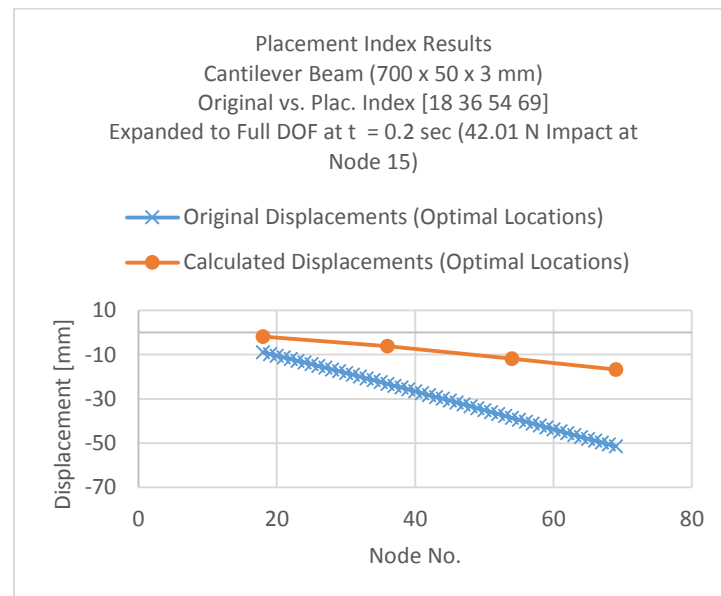
(d)

Fig.A.4. Displacements at Modified D-Optimal sites (Cantilever Beam under impact), T [0-1.5] [s] (a) at Node 1, (b) at Node 17 (c) at Node 35 and (d) at Node 54

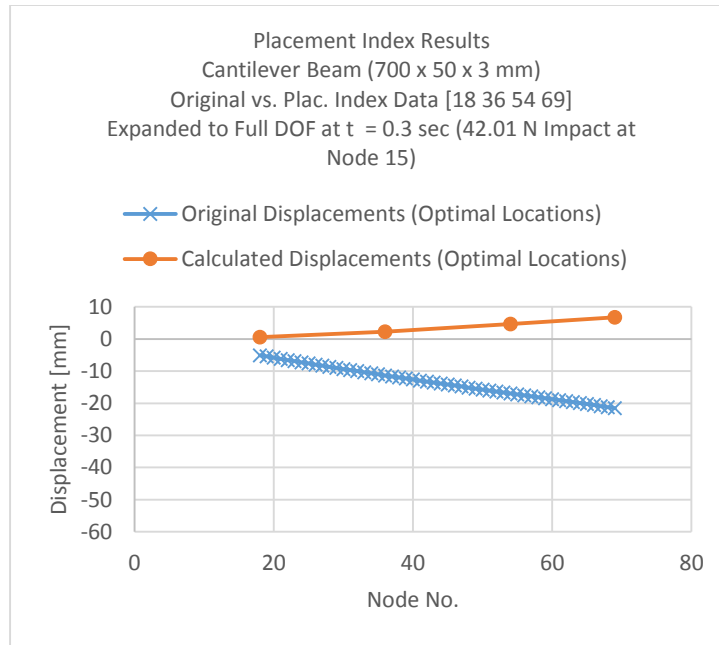
Placement Index Results [18 36 54 69]:



(a)



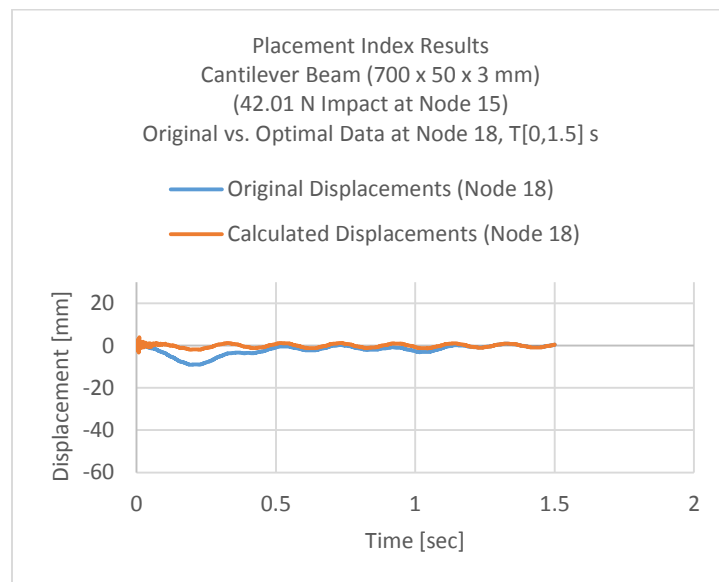
(b)



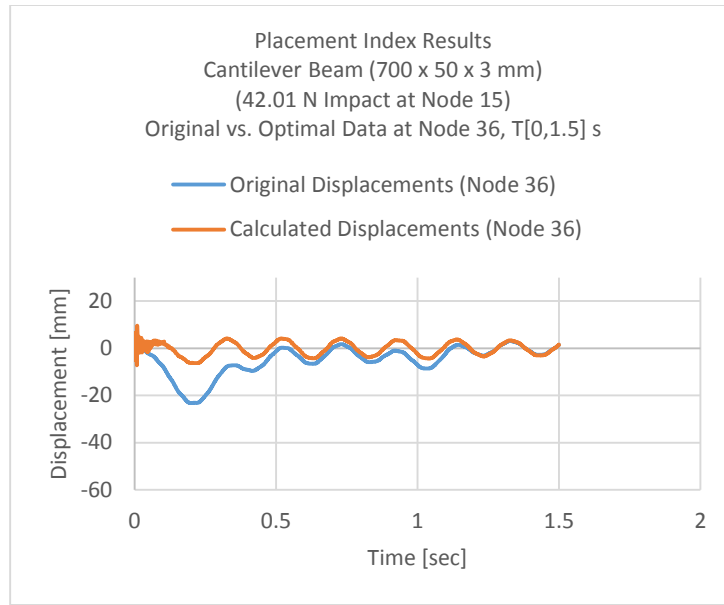
(c)

Fig.A. 5 Displacements at Placement Index sites (Cantilever Beam under impact) (a) at $t = 0.1$ [s], (b) at $t = 0.2$ [s] and (c) at $t = 0.3$ [s]

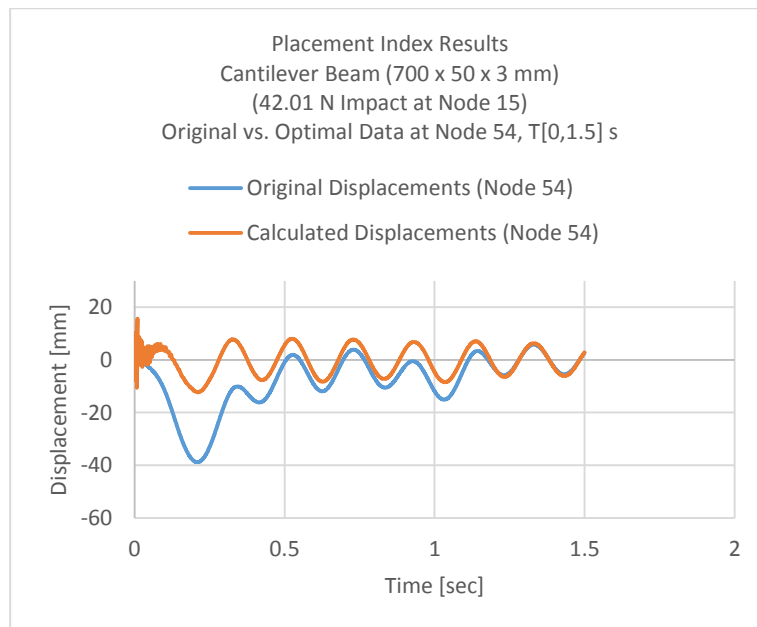
D-Optimal Results (Time History) [1 16 34 52]:



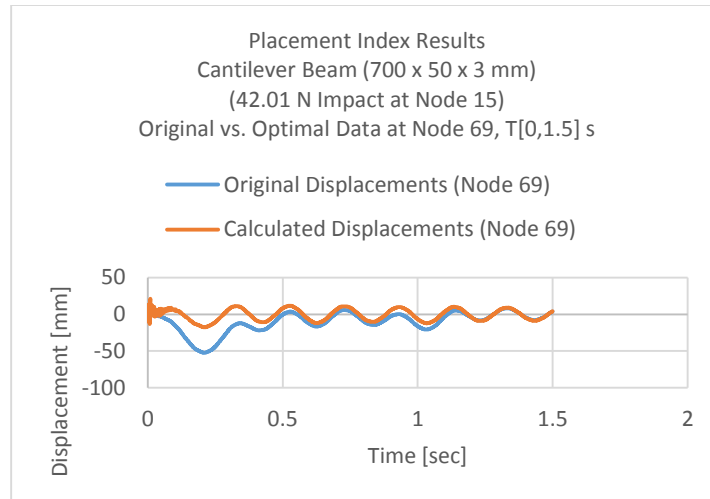
(a)



(b)



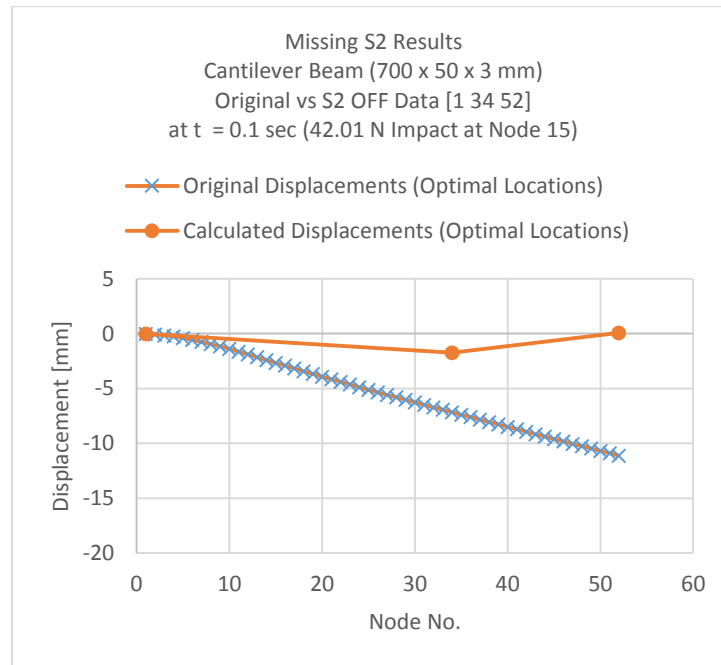
(c)



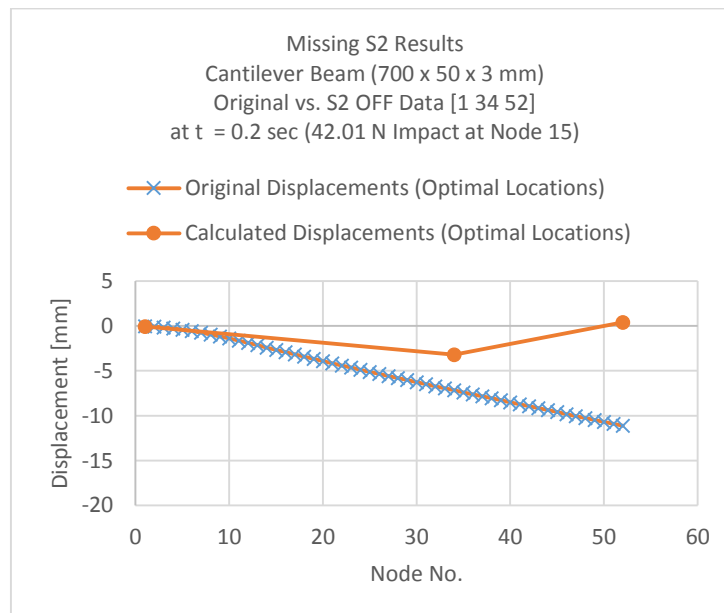
(d)

Fig.A.6 Displacements at Modified D-Optimal sites (Cantilever Beam under impact), T [0-1.5] [s] (a) at Node 18, (b) at Node 36 (c) at Node 54 and (d) at Node 69

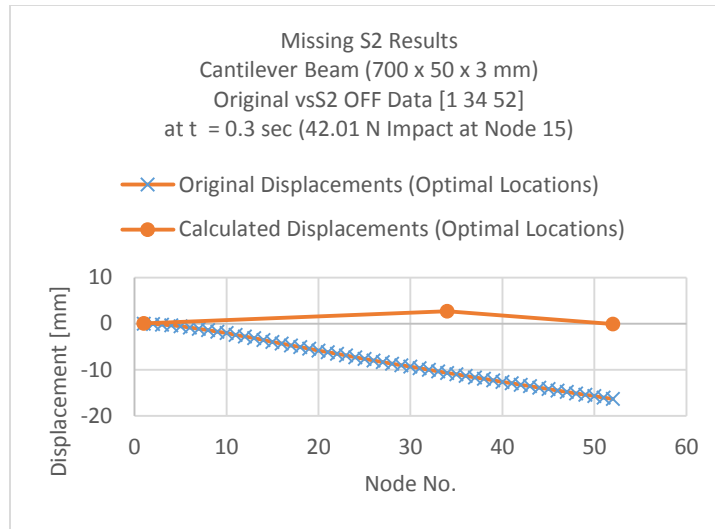
A-3. S2 OFF Results [1 34 52]:



(a)



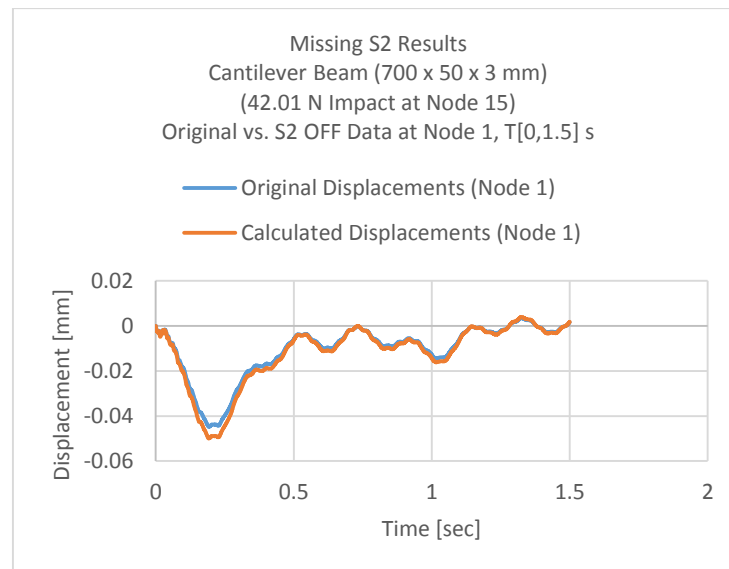
(b)



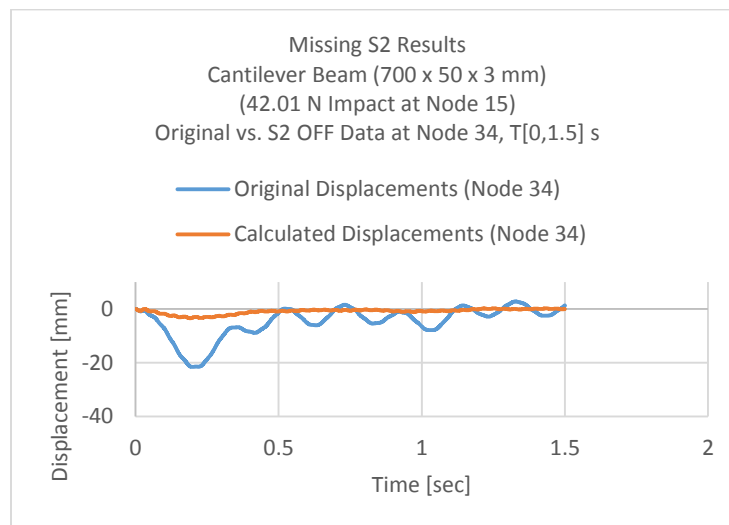
(c)

Fig.A. 7 Displacements with S2 OFF (Cantilever Beam under impact) (a) at $t = 0.1$ [s], (b) at $t = 0.2$ [s] and (c) at $t=0.3$ [s]

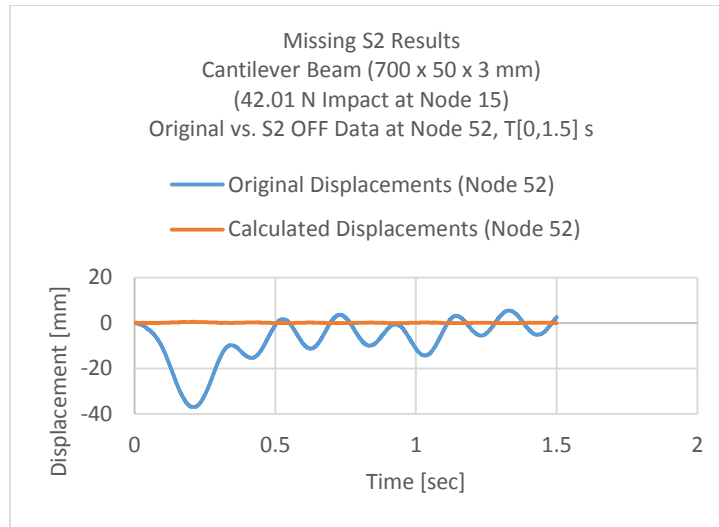
A-4. S2 OFF Results (Time History) [1 34 52]:



(a)



(b)

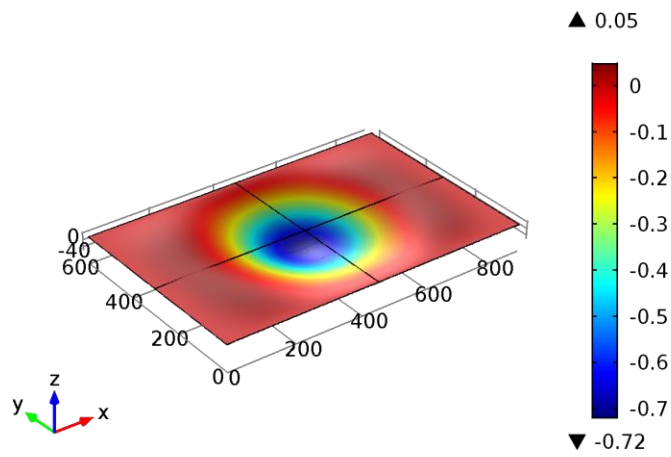


(c)

Fig.A. 8 Displacements with S2 OFF (Cantilever Beam under impact), T [0-1.5] [s] (a) at Node 1, (b) at Node 34 and (c) at Node 52

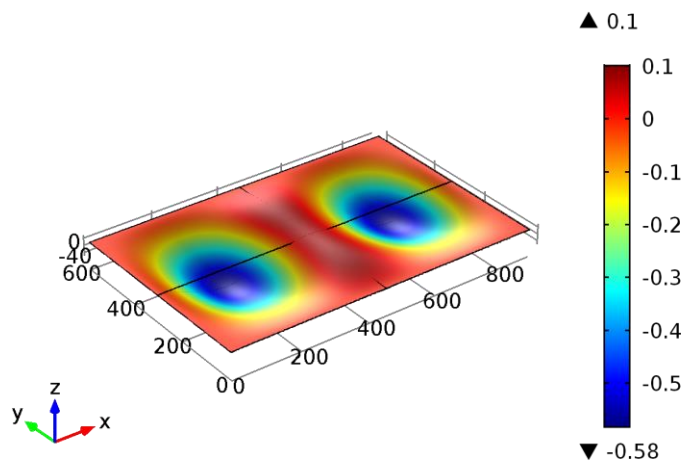
A-5. All Edges Clamped Plate, Development of Mode Shapes over time:

Time=0.010967 s Surface: Displacement field, Z component (mm)



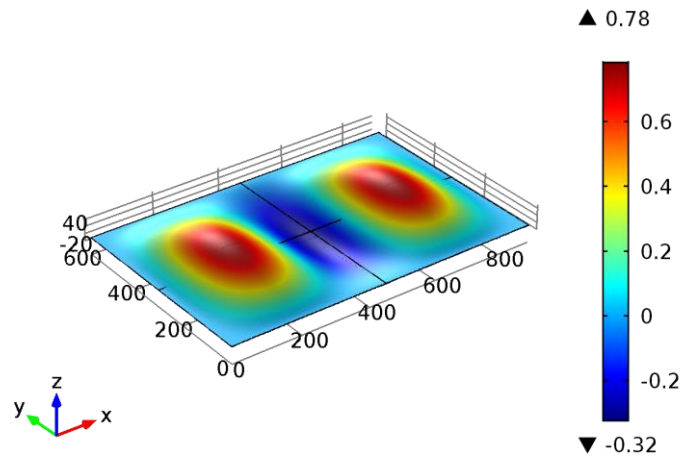
(a)

Time=0.021935 s Surface: Displacement field, Z component (mm)



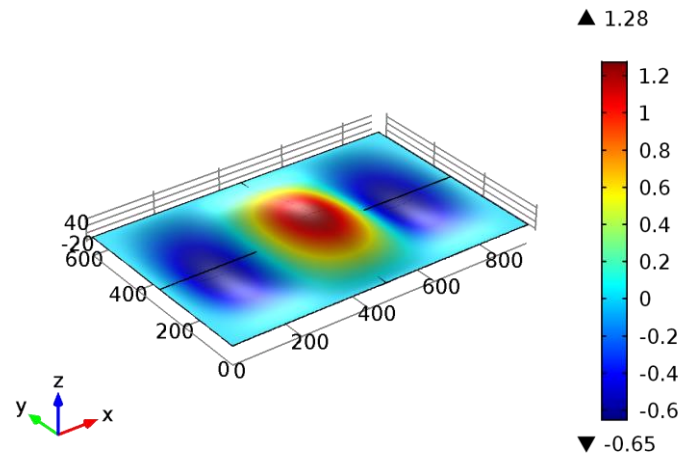
(b)

Time=0.032902 s Surface: Displacement field, Z component (mm)



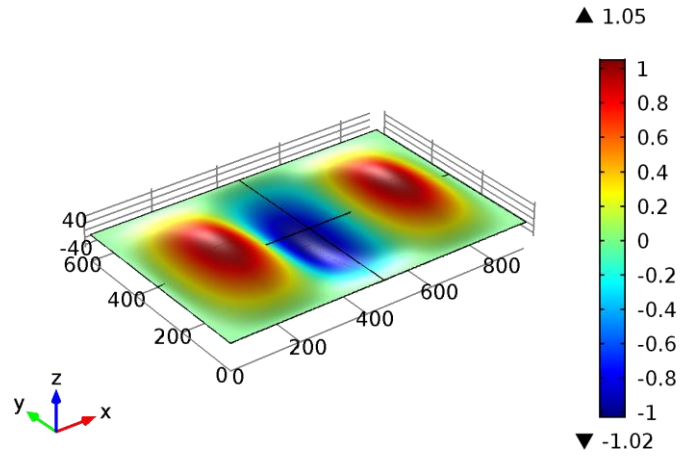
(c)

Time=0.043869 s Surface: Displacement field, Z component (mm)



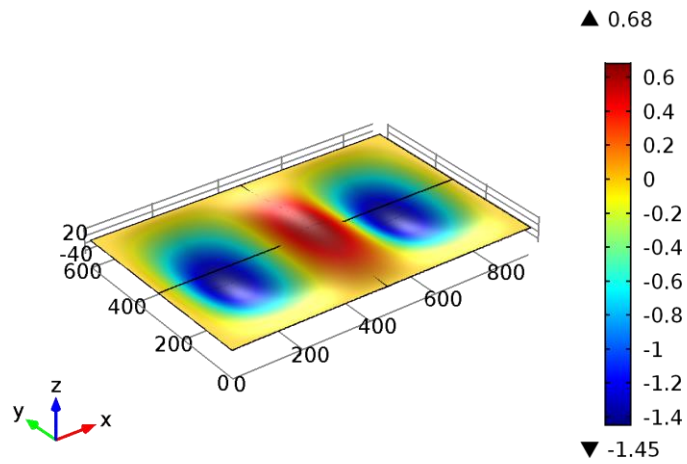
(d)

Time=0.054837 s Surface: Displacement field, Z component (mm)



(e)

Time=0.065804 s Surface: Displacement field, Z component (mm)



(f)

Fig.A. 9 Development of Mode Shapes over time for All sides clamped Rectangular Plate

A 6. LabVIEW VI for Simultaneous Data Acquisition from numerous sensors:
Acquisition VI for Impulse, Strain (Strain Gage and Array FBG) and Acceleration:

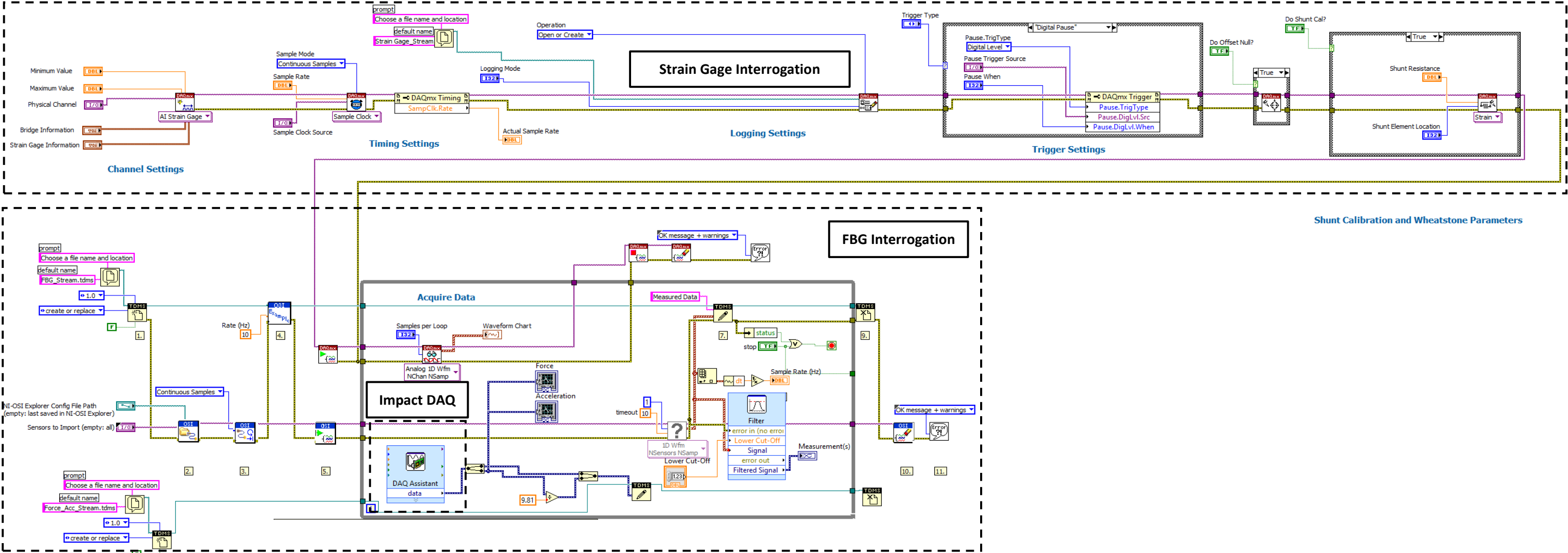


Fig.A.10 VI for simultaneous measurements from (a) Impact Hammer, (b) Strain Gage and (c) Array FBGs and (d) Accelerometer

VITAE

Name: Asad Muhammad Butt

Date of Birth: March 16, 1984

Present Address: KFUPM P. O. Box 8405, King Fahd University of Petroleum and Mineral, Dhahran-31261, Saudi Arabia.

Permanent Address: H. No. 30 A/1, Street 12, Afshan Colony, Rawalpindi-46000, Pakistan.

Email Address: asadbutt@kfupm.edu.sa
asad_aero@hotmail.com

Educational Qualification:

M.S (Mechanical Engineering)

May, 2009

National University of Sciences & Technology,

Islamabad, Pakistan

B.S. (Aerospace Engineering)

Aug, 2006

Institute of Space Technology,

Islamabad, Pakistan

Publications

Journal Papers

1. Mekid, S., **Butt**, A. and Qureshi, K. 2017, “Integrity Assessment under Various Conditions of Embedded Fiber Optics Based Multi-Sensing Materials”, Optical Fiber Technology, Vol. 36, pp. 334-343

Conference Proceedings

1. **A. Butt** and S. Mekid, Development Smart/Nervous Material with Novel Sensor Embedding Techniques - A Review - SMASIS2015-8940, Proceedings of the ASME 2015 Conference on Smart Materials, Adaptive Structures and Intelligent Systems (SMASIS2015), September 21-23, 2015, Denver, Colorado, USA.
2. S. Mekid, **A. Butt** and K. Qureshi, Characterization of Fiber Optics Integrity under several Embedding Parameters in Smart Materials - SMASIS2015-8860, Proceedings of the ASME 2015 Conference on Smart Materials, Adaptive Structures and Intelligent Systems (SMASIS2015), September 21-23, 2015, Denver, Colorado, USA.
3. S. Mekid, N. Saheb, H. Daraghma, **A. Butt** and K. Qureshi, Upscaling Sensing Materials with Challenges of Sensors Embedding in Powder based Materials and Polymers - SMASIS2015-8859, Proceedings of the ASME 2015 Conference on Smart Materials, Adaptive Structures and Intelligent Systems (SMASIS2015), September 21-23, 2015, Denver, Colorado, USA.
4. **A.M. Butt** and S.W. ul Haq, *Comparative Study for the Design of Optimal Composite Pressure Vessels*, Key Engineering Materials Vol. 442 (2010) pp 381-388, Trans Tech Publications, Switzerland.